THE INFLUENCE OF COLLAGEN-GAG SCAFFOLD ARCHITECTURAL AND BIOLOGICAL CUES ON TENOCYTE AND MESENCHYMAL STEM CELL BIOACTIVITY FOR MUSCULOSKELETAL TISSUE ENGINEERING

BY

STEVEN RICHARD CALIARI

DISSERTATION

Submitted in partial fulfillment of the requirements
for the degree of Doctor of Philosophy in Chemical Engineering
in the Graduate College of the
University of Illinois at Urbana-Champaign, 2013

Urbana, Illinois

Doctoral Committee:

Assistant Professor Brendan Harley, Director of Research
Professor Jonathan Higdon
Associate Professor Hyunjoon Kong
Associate Professor Christopher Rao
Associate Professor Ryan Bailey

ABSTRACT

While many tissue engineering strategies focus on repair of single tissues, orthopedic injuries often occur at the interface between soft tissue and bone. The tendon-bone junction (TBJ) is a classic example of such an interface, and contains overlapping patterns of growth factors, extracellular matrix (ECM) proteins, and mineral content that serve to minimize stress concentrations and enable normal locomotion. Clinical strategies to treat TBJ injuries forsake biological integration for mechanical fixation, resulting in high failure rates. Modern tissue engineering requires the design of new biomaterials permitting simultaneous control of microstructural, mechanical, and biochemical properties in a spatially-defined manner. This thesis describes a suite of studies undertaken to better understand microenvironmental regulators of cell bioactivity and the application of this knowledge to the design of a multi-compartment scaffold for engineering the TBJ. The studies here use collagen-glycosaminoglycan (CG) scaffolds, regulatory compliant analogs of the native ECM that have been applied to the regeneration of dermis, peripheral nerve, and osteochondral tissue. Chapter 2 quantifies the role CG scaffold relative density plays in directing tenocyte bioactivity and maintaining transcriptomic stability. Chapter 3 describes an investigation elucidating the influence of the dose and mode of presentation (soluble, sequestered) of five biomolecules (SDF-1α, PDGF-BB, IGF-1, bFGF, and GDF-5) on the recruitment, proliferation, collagen synthesis, and genomic stability of tenocytes within anisotropic CG scaffolds. Chapter 4 uses selective modification of our standard CG scaffold to probe the combined influences of structural and biochemical instructive cues to drive human bone marrow-derived mesenchymal stem cell (MSC) differentiation down tenogenic, osteogenic, and chondrogenic lineages respectively. Chapter 5 utilizes a series of CG scaffolds that were inspired by elements of distinct components of

orthopedic interfaces (cartilage, tendon/ligament, and bone) to examine the role of biomaterial physical properties (relative density, mineral content) on biasing MSC phenotype in the presence of mixed soluble signals to drive osteogenesis or chondrogenesis. Finally, chapter 6 adapts the CG scaffold system to provide a pathway towards engineering the TBJ. 3D scaffolds with coincident gradients of pore anisotropy and mineral content to drive spatially-graded MSC differentiation were fabricated for the first time. Together, these studies present the framework for building instructive biomaterials to regulate stem cell fate in the context of musculoskeletal tissue repair.

ACKNOWLEDGMENTS

This thesis would not have been possible without the contributions of many friends and colleagues. I would like to start by acknowledging everyone who contributed directly to the research covered in this thesis: Dan Weisgerber (Chapters 2, 4-6, Appendix C), Doug Kelkhoff (Chapter 2, Appendix B), Manny Ramirez (Chapter 2, Appendix B), Bill Grier (Chapter 6), Ziad Mahmassani (Chapter 6), Emily Gonnerman (Appendix A), and Rebecca Hortensius (Appendix C). Many others also contributed: Professors Matt and Allison Stewart provided tendon cells, Dr. Sandra McMasters prepared media, Karen Doty and Donna Epps helped with histological analysis, Drs. Jim Mabon and Catalin Chiritescu assisted with electron microscopy, Dr. Shiv Sivaguru helped tremendously with confocal microscopy, and Professors Charles Schroeder, Hyunjoon Kong, Paul Kenis, and Marni Boppart generously shared their laboratory's equipment.

I'd also like to thank all of my lab mates for being great work colleagues and for helping keep things light with Sporcle and bags in the office, trips to Murphy's, etc: Sunny, Bhushan, Dan, Emily, Sara, Jackie, Laura, Rebecca, Bill, Doug, Manny, Peter, Lisa, Kwaku, Paul, and everyone else that has passed through the lab over the last five years.

I've also been fortunate to interact with some wonderful faculty and staff here at the University of Illinois. Professor Wilfred van der Donk and Nan Holda were great mentors during my time in the CBI training program. Thank you to Christy Bowser and Cathy Paceley for always helping with paperwork and reimbursements. I'd especially like to thank my thesis committee: Professors Ryan Bailey, Chris Rao, Joon Kong, Jon Higdon, and my advisor Brendan Harley. When I came to Illinois five years ago I didn't know what to expect, but I can honestly say that I

can’t imagine things working out any better than they did, and that is in large part due to the people I’ve been fortunate enough to interact with since I came here. It’s been a wonderful experience to help Brendan start his laboratory and watch it grow to where it is today.

The work described here was funded by the Chemistry-Biology Interface Training Program NIH T32GM070421, NSF 1105300, the Drickamer and Mavis Future Faculty Fellowships, the IGB-OTM Proof-of-Concept Award, the Chemical and Biomolecular Engineering Department, and the Institute for Genomic Biology at the University of Illinois at Urbana-Champaign. This research was carried out in part in the Frederick Seitz Materials Research Laboratory Central Facilities, University of Illinois, which are partially supported by the U.S. Department of Energy under grants DE-FG02-07ER46453 and DE-FG02-07ER46471.

Finally, I am grateful and blessed to have great friends and family that give me balance in my life. In particular, I would like to give a heartfelt thanks to my Mom, Dad, my brothers Jonathan and Daniel, and my sister Erika as well as the rest of my family for always being there for me. I love you all.

TABLE OF CONTENTS

LIST OF SYMBOLS AND ABBREVIATIONS

Abbreviation	Term, Definition
A	Cross-sectional area
ACAN	Aggrecan
ACI	Autologous chondrocyte implantation
ACL	Anterior cruciate ligament
ALP	Alkaline phosphatase
ANOVA	Analysis of variance
AR	Aspect ratio
ASC	Adipose-derived stem cell
BMP-x	Bone morphogenetic protein; relevant isoforms include BMP-2 and BMP-7
BP	Benzophenone
BSA	Bovine serum albumin
BSE	Backscatter electron
BSP	Bone sialoprotein
C2C12	Mouse myoblast cell line
CaP	Calcium phosphate
cDNA	Complementary DNA (deoxyribonucleic acid)
CG	Collagen-glycosaminoglycan co-precipitate
CGCaP	Collagen-glycosaminoglycan-calcium phosphate triple co-precipitate
CNTF	Ciliary neurotrophic factor
COL1A1	Collagen I alpha 1
COL1A2	Collagen I alpha 2
COL2A1	Collagen II alpha 1
COL3A1	Collagen III alpha 1
COMP	Cartilage oligomeric matrix protein
ConA-biotin	Biotinylated concanavalin A
COOH	Carboxyl group
d	Scaffold pore size
DCN	Decorin
DHT	Dehydrothermal crosslinking
DMEM	Dulbecco's modified Eagle's media
DRT	Dermal regeneration template
ECM	Extracellular matrix
E_s	Elastic modulus of individual scaffold strut
E^*	Elastic modulus of the entire cellular material
E_sI	Scaffold strut flexural rigidity
ε	Compressive strain
EDC	1-Ethyl-3-(3-dimethylaminopropyl) carbodiimide hydrochloride
EDTA	Ethylenediaminetetraacetic acid
EDX	Energy-dispersive X-ray spectroscopy
ERK	Extracellular signal-related protein kinase
ESC	Embryonic stem cell
FAM	Fluorescently-labeled with 5(6) carboxyfluorescein
FBS	Fetal bovine serum

FE	Finite element
FGF	Fibroblast growth factor
GAGs	Glycosaminoglycans
GAPDH	Glyceraldehyde 3-phosphate dehydrogenase; used as housekeeping gene
GDF-x	Growth/differentiation factor; relevant isoforms include GDF-5, 6, and 7
GDNF	Glial cell line–derived neurotrophic factor
GelMA	Gelatin methacrylate
HA	Hyaluronic acid OR hydroxyapatite
H&E	Hematoxylin and eosin
HPLC	High-performance liquid chromatography
HUVEC	Human umbilical vein endothelial cell
IGF-1	Insulin-like growth factor-1
Ihh	Indian hedgehog
k	Scaffold permeability; units: m^2
l	Height of scaffold under compression
LIF	Leukemia inhibitory factor
MAPK	Mitogen-activated protein kinase
MC3T3-E1	Mouse pre-osteoblast cell line
MCL	Medial cruciate ligament
MMP	Matrix metalloproteinase
MRI	Magnetic resonance imaging
MSC	Mesenchymal stem cell or marrow stromal cell
MTJ	Muscle-tendon or myotendinous junction
NGF	Nerve growth factor
NHS	*N*-hydroxysulfosuccinimide
NRT	Nerve regeneration template
NSC	Neural stem cell
OC	Osteocalcin
OP	Osteopontin; late marker of bone formation
σ_{el}^{*}	Compressive plateau stress
P	Pressure head
PBS	Phosphate-buffered saline
PCL	Poly(ε-caprolactone)
PCR	Polymerase chain reaction
PDGF-BB	Platelet-derived growth factor-BB
PDMS	Poly(dimethylsiloxane)
pDTEc	Poly(desaminotyrosyl-tyrosine ethyl ester carbonate)
pDTOc	Poly(desaminotyrosyl-tyrosine octyl ester carbonate)
PEG	Poly(ethylene glycol)
PEO	Poly(ethylene oxide)
PGA	Poly(glycolic acid)
pHEMA	Poly(2-hydroxyethyl methacrylate)
PLGA	Poly(lactic-co-glycolic acid)
PLLA	Poly(L-lactic acid)
Ptc1	Patched-1
PTFE	Poly(tetrafluoroethylene)

PVA	Poly(vinyl alcohol)
ρ^*/ρ_s	Relative density (1 – porosity)
Q	Flow rate
r	Scaffold-membrane composite radius
RGDS	Arg-Gly-Asp-Ser; sequence often added to synthetic materials to promote cell attachment
RhoA	Ras homolog gene family, member A
RIPA	Radio immunoprecipitation assay
RNA	Ribonucleic acid
ROCK	Rho-associated protein kinase
RPC	Retinal progenitor cell
RUNX2	Runt-related transcription factor 2
SAM	Self-assembled monolayer
SA/V	Specific surface area; total surface area per unit volume for a given unit cell
SBF	Simulated body fluid
SCXB	Scleraxis; a transcription factor highly expressed in tendon
SDF-1α	Stromal cell-derived factor-1α
SE	Secondary electron
SEM	Scanning electron microscopy
SHG	Second harmonic generation
Shh	Sonic hedgehog
siRNA	Small interfering ribonucleic acid
SIS	Small intestine submucosa
SIX1	Sine oculis-related homeobox 1
SMAD	Portmanteau of SMA and MAD (mothers against decapentaplegic) genes
SMC	Smooth muscle cell
SOX9	Sry-related homeobox gene 9; transcription factor involved in chondrogenesis
TBJ	Tendon-bone junction
TC	Tendon cell
TGF-βx	Transforming growth factor-βx; relevant isoforms include TGF-β1, TGF-β2, and TGF-β3
TNC	Tenascin-C
UV	Ultraviolet light (crosslinking)
μ	Viscosity
μCT	Micro-computed tomography
V	Volume
VEGF	Vascular endothelial growth factor; a chemical signal produced by cells that stimulates the growth of new blood vessels (angiogenesis)
Wnt	Wingless type
XRD	X-ray diffraction

CHAPTER 1: INTRODUCTION AND BACKGROUND: BIOMATERIALS TO ENGINEER MULTI-TISSUE JUNCTIONS AND REGULATE STEM CELL FATE[1]

1.1 Thesis overview

This chapter introduces CG materials as regenerative templates for a wide range of tissue engineering applications and reviews the latest in the interconnected fields of multi-tissue junction engineering and stem cell fate regulation through controlled presentation of material and biological cues. The remainder of the thesis will focus on the development of a CG composite material for tendon-bone junction (TBJ) engineering, including optimization of scaffold architectural and biological cues to induce spatially-defined lineage specification of stem cell phenotype. Some of the materials used often in this thesis were developed and outlined in my master's thesis, including a highly aligned CG scaffold that mimicked the native anisotropy of tendon (Caliari and Harley 2011) as well as a scaffold-membrane composite material that was inspired by mechanically efficient natural structures such as porcupine quills (Caliari, Ramirez et al. 2011). We also previously developed a fabrication method for spatially-patterning multiple biomolecules in CG scaffolds in a manner that preserved the native bioactivity of the scaffold (Martin, Caliari et al. 2011). For more information on these foundational studies the reader is referred to the cited manuscripts.

In this thesis, Chapter 2 will describe the influence of scaffold relative density and maintenance of aligned contact guidance cues on promoting and maintaining tenocyte phenotype. Chapter 3 presents the results of a systematic screen of five candidate soluble factors and their dose-dependent effects on tenocyte chemotaxis, proliferation, collagen synthesis, and gene expression

[1] This chapter has been adapted from the following publication:
Caliari, S. R. and B. A. C. Harley (in preparation). "Biomaterials to engineer multi-tissue junctions and regulate stem cell fate."

while also introducing a simple method to present immobilized growth factors while maintaining bioactivity. Chapter 4 uses selective modification of CG scaffold architectural and biological cues to influence the differentiation of mesenchymal stem cells (MSCs) down tenogenic, chondrogenic, and osteogenic lineages. Chapter 5 reveals the influence of scaffold biophysical cues on the biasing of MSC differentiation in the presence of mixed soluble signals. Finally, Chapter 6 covers the development of a multi-compartment CG scaffold with distinct compartments of mineralization and pore anisotropy for TBJ engineering. This chapter includes characterization of the material, integration with a Flexcell bioreactor system, and initial cell results. Chapter 7 will conclude this thesis with a summary of results and recommendations for ongoing and future work.

1.2 Chapter overview

While many tissue engineering approaches focus on the repair of a single tissue, orthopedic injuries often occur at the interface between two tissues, underscoring the need for multi-tissue regenerative strategies. Current clinical repair approaches are often inadequate, providing rudimentary mechanical fixation instead of biological re-integration while failing to recapitulate the elegant patterns of proteins and biomolecules seen in native interfaces. In this review, we highlight emerging technologies to design spatially and temporally dynamic biomaterials that regulate stem cell fate in the context of multi-tissue repair. We begin by introducing unique challenges to engineering tissue interfaces and regulating stem cell fate in a spatially-defined manner. We will summarize fabrication strategies for creating dynamic biomaterials to deliver growth factors, genes, and cells with precise spatial resolution. We will then review approaches

for repairing the more extensively studied osteochondral (cartilage-bone) interface and cover emerging research on other clinically relevant junctions including tendon/ligament-bone and muscle-tendon. Finally, we will close with a perspective on how to better integrate knowledge gleaned from fundamental microscale studies into the design of next generation regenerative templates.

1.3 Introduction

Tissue engineering and regenerative medicine have emerged in recent years as burgeoning fields that aim to repair tissues and organs (Langer and Vacanti 1993). In particular, the design of novel biomaterials to guide tissue repair is increasingly being recognized as an integral component to most tissue engineering strategies. While the normal wound healing process in adults leads to scar tissue formation with a poorly organized, mechanically-inferior extracellular matrix (ECM), evidence has accumulated that biomaterials can fundamentally alter this process. In fact, materials designed to block wound contraction have shown clinical success for partial regeneration of skin and peripheral nerves (Yannas, Lee et al. 1989; Soller, Tzeranis et al. 2012). Biomaterials can also controllably present instructive microstructural, mechanical, and biochemical cues to drive regeneration. While designing materials to repair a single tissue is already a daunting task, injuries often occur at the junction between dissimilar tissue types, especially in orthopedics. These junctions, termed multi-tissue junctions here, contain a heterogeneous set of architectural, mechanical, and compositional cues that together are critical for maintaining the integrity of the musculoskeletal system during normal locomotion.

Therefore, biomaterial strategies to repair these junctions must be able to recapitulate salient features of these heterogeneous, graded tissues.

This review will have a dual focus on materials to regulate stem cell fate as well as an overview of current tissue engineering strategies for repairing three classes of multi-tissue junctions: cartilage-bone (osteochondral), tendon/ligament-bone (osteotendinous), and muscle-tendon (myotendinous). While some reviews have focused on model material systems to regulate stem cell fate (Fisher, Khademhosseini et al. 2010; Cha, Liechty et al. 2012) while others have covered tissue engineering strategies for orthopedic interfaces (Mikos, Herring et al. 2006; Moffat, Wang et al. 2009; Yang and Temenoff 2009; Lu, Subramony et al. 2010; Sahoo, Teh et al. 2011; Seidi, Ramalingam et al. 2011; Castro, Hacking et al. 2012), this review serves as a bridge between those two communities. Orthopedic interface engineering represents a wonderful clinically-relevant field to apply many of the emerging techniques to create patterned, gradient materials. Since multi-tissue junction engineering requires the regeneration of multiple tissue types on ideally a single scaffold material, an increasingly attractive approach is to spatially pattern or grade instructive cellular cues onto these materials to drive site-specific lineage specification of a progenitor cell type such as mesenchymal stem cells (MSC).

This review will begin with an overview of interface tissue organization and biology. It will continue with a rundown of technologies to fabricate patterned, gradient materials, paying close attention to how these systems might inform biomaterial design for orthopedic interface engineering. We will then overview the latest advances in the design, fabrication, and *in vitro* as well as *in vivo* evaluation of biomaterials to repair the aforementioned three classes of multi-

tissue junctions. Finally, we will conclude with a perspective on how the biomaterials, stem cell biology, and orthopedics communities can come together to pursue optimal regenerative strategies moving forward.

1.4 Interface tissue organization and biology

1.4.1 Cartilage-bone

Cartilage-bone (osteochondral) interfaces are the most common target of multi-junction tissue engineering strategies. This review will focus on models of osteochondral repair pertaining to the knee, although other joints such as the hip are potential regenerative targets with their own unique mechanical microenvironment (Hodge, Fijan et al. 1986). The most common malady requiring osteochondral repair is osteoarthritis. Osteoarthritis is estimated to afflict 250 million people worldwide (Vos, Flaxman et al. 2012) with prevalence increasing with age and in women. Notably, osteoarthritis affects the entire joint with hyaline cartilage damage, subchondral bone remodeling, and weakening of the periarticular muscles; damage to these non-cartilage tissues is likely to be the source of patient pain since cartilage is aneural (Felson 2006). Osteoarthritis also occurs in a non-uniform, focal manner with autocatalytic loss of cartilage tissue and bony remodeling. Current surgical treatment options include arthroscopic debridement, autologous chondrocyte implantation (ACI), microfracture, and mosaicplasty. Engineered biomaterials to serve as osteochondral grafts have found utility in conjunction with several of these approaches, including as carriers for autologous cell implantation or to fill defects created during microfracture or mosaicplasty procedures.

Cartilage is primarily composed of type II collagen and the proteoglycan aggrecan, with chondrocytes interacting with type II collagen through integrins α1β1 and α2β1 (Camper, Heinegård et al. 1997). The primary cartilage cell type is the chondrocyte. Adult cartilage is relatively acellular with chondrocytes comprising about 2% of the mature tissue by volume (Mitrovic, Quintero et al. 1983). Articular cartilage is typically thought of as having four distinct but continuous layers: *i)* superficial zone, *ii)* middle zone, *iii)* deep zone, and *iv)* calcified cartilage zone overlaying the subchondral bone (Poole, Kojima et al. 2001).

The superficial zone consists of type II collagen fibers arranged parallel to the articular surface with flattened chondrocytes interspersed in the matrix. The collagen fibrils are thin (~ 20 nm diameter) in this region while aggrecan content is lowest in this zone. The parallel arrangement of the collagen fibers and the production of lubricin, both from the resident chondrocytes as well as from the surrounding synovial fluid, give this zone the highest tensile strength out of all the cartilage zones (Kempson, Muir et al. 1973; Akizuki, Mow et al. 1986). The elevated tensile strength in this zone helps the tissue deal with shearing encountered during articulation. The proteoglycans decorin and biglycan are also found at their highest levels in this zone and play a role in fibrillogenesis (Poole, Rosenberg et al. 1996).

The middle zone contains an aggrecan-rich ECM embedded with rounder chondrocytes that is more isotropic in organization compared to the superficial zone. The pericellular regions around chondrocytes are about 2 μm and contain decorin and type VI collagen (Poole, Kojima et al. 2001). The deep zone has a lower cell density than the top two zones, but higher aggrecan content and thicker collagen fibrils (70-120 nm) (Venn 1978). The ECM in the deep zone is

longitudinally aligned (perpendicular to organization of superficial zone). Finally, the calcified cartilage layer serves as the buffer between cartilage proper and the subchondral bone. This zone is populated with hypertrophic chondrocytes that produce type X collagen and mineral (Poole, Kojima et al. 2001). Together, these zones harbor patterns of ECM (content and organization) and cellular content. Mechanical properties of the osteochondral interface show a strong depth dependence. While the compressive modulus for full thickness articular cartilage has been measured as 0.38 MPa, the moduli of individual zones ranges from 0.079 MPa for the superficial layer to 2.1 MPa for the deep zone (Schinagl, Gurskis et al. 1997).

1.4.2 Tendon/ligament-bone

Designing materials for the regeneration of tendon and ligament junctions with bone represents an emerging area of research at the intersection of biomaterials, orthopedics, and stem cell biology. Common tissue engineering targets for tendon/ligament-bone include the anterior cruciate ligament (ACL, both femoral and tibial insertions), the patellar tendon (ligament), and the rotator cuff (in particular the supraspinatus-humerus junction). Tendons and ligaments are hierarchical, mechanically and geometrically anisotropic tissues composed primarily of type I collagen fiber bundles. These fiber bundles show a characteristic crimp pattern that helps the tissue adapt to normal loading. Tendons and ligaments can be up to an order of magnitude stiffer in the plane longitudinal to collagen fiber alignment compared to the transverse plane (Quapp and Weiss 1998). While tissue engineering strategies to repair tendons and ligaments are often very similar, there are some key differences between the two tissues. Tendons connect skeletal muscle to bone, transferring muscle-generated forces to the skeletal system to enable everyday locomotion (Wang 2006). Ligaments connect bone to bone, restricting their movements and

stabilizing joints. In general, tendons have higher elastic moduli than ligaments and have a higher type I/type III collagen ratio as well as less elastin than ligament (Gross and Hoffmann 2013). Tendon tissue is 70% water, with collagen comprising 75-85% of the dry weight, of which 95% is type I with the remainder being types III and V (Wang 2006). In contrast, ligaments have much more types III and V collagen (~ 20% of total collagen weight) (Birk and Mayne 1997). Tendon elastin content is less than 3% (ligaments are 10-15%) while proteoglycans constitute about 2%, although this amount varies widely and is typically higher in tendons that must withstand significant compressive stress (Martin, Burr et al. 1998). Tendons and ligaments are both populated primarily by fibroblastic cells. In tendon, these cells are called tenocytes and are interspersed throughout the collagen fibers in the tissue. Although relatively sparse in mature tendon, tenocytes can stretch to great lengths (> 100 μm) and communicate with each other via connexins 32 and 43 (McNeilly, Banes et al. 1996). Collagen fiber bundles are bound together by the endotenon, which in turn is integrated with the peritenon, which surrounds the whole tissue (Gross and Hoffmann 2013). Peritenon is composed of an inner layer called the epitenon and an outer layer called the paratenon. Some tendons, especially in the hands and feet, are enclosed by synovial sheaths to enable smooth gliding during movement (Gross and Hoffmann 2013). Type III collagen is typically localized to the endotenon and epitenon, although it can also appear in mechanically dynamic regions such as the supraspinatus (Duance, Restall et al. 1977).

Tendons and ligaments can insert into bone through either a direct or indirect enthesis. Indirect, or fibrous, entheses are made up of essentially tendon and bone zones only and will not be extensively covered in this review. A direct enthesis contains four continuous zones: *i)*

tendon/ligament proper, *ii)* non-mineralized fibrocartilage, *iii)* mineralized fibrocartilage, and *iv)* bone (Thomopoulos, Williams et al. 2003; Thomopoulos, Marquez et al. 2006; Genin, Kent et al. 2009). The fibrocartilage zones are rich in type II collagen and aggrecan, making them biochemically similar to articular cartilage. As in articular cartilage, the ECM composition at the interface holds water to resist compression, which aids in dissipating stress concentrations between the mechanically dissimilar tendon and bone (Gross and Hoffmann 2013). The tidemark found at the interface of zones 2 and 3 is similar to the tidemark in osteochondral tissue. Like the osteochondral interface, the tendon/ligament-bone junction shows graded mechanical properties. Moffat *et al.* demonstrated compressive mechanical properties strongly correlated with mineral content across both the tibial and femoral insertions of the ACL (Moffat, Sun et al. 2008). Moving from tendon proper to bone, there is a linear gradient of mineralization but interestingly, not a linear gradient of mechanical properties (Genin, Kent et al. 2009). In fact, there is a decrease in tangent modulus at the onset of the junction due to misalignment of the collagen fibers (Thomopoulos, Williams et al. 2003). This dip in stiffness is rapidly made up by increasing mineral content.

1.4.3 Muscle-tendon

As with the cartilage-bone (osteochondral) and tendon/ligament bone (osteotendinous) junctions, the muscle-tendon (myotendinous) junction is a common injury site. In fact, the majority of muscle injuries occur at the fibers near the interface with tendon (Tidball, Salem et al. 1993). Commonly injured muscles include the hamstrings and quadriceps (Sullivan and Best 2005). Skeletal muscle injuries and diseases are pervasively common in patients of many backgrounds ranging from elite athletes and soldiers to the elderly. Muscle generated force is transmitted via

tendons to the skeletal system in order to enable locomotion. Even though muscle tissue shares some key physiological similarities with tendon, exhibiting a hierarchical organization of muscle fiber bundles and a significant degree of geometrical and mechanical anisotropy, muscle is much less stiff than tendon (elastic modulus 2-3 orders of magnitude less than tendon (Ladd, Lee et al. 2011)) and includes a significantly higher density of vascular and neural components. Skeletal muscle makes up 40-50% of total body mass and, unlike smooth and cardiac muscle, is voluntarily contracted via the central nervous system (Sullivan and Best 2005). Skeletal muscle is a fibrous tissue where individual fibers are composed of multinucleated myocytes surrounded by plasma membrane called the sarcolemma. Muscle fibers have characteristic "light" (I-band) and "dark" (A-band) bands known as striations. Myosin and actin filaments corresponding to dark and light bands respectively are contractile proteins that generate force to enable muscle contraction (Sullivan and Best 2005). Skeletal muscle is composed of multiple collagen types (I-V), laminin, and elastin among other components. Like tendons and ligaments, muscle is a hierarchical tissue where individual muscle fibers are surrounded by endomysium to promote integration with collagen fibers (Sullivan and Best 2005). Muscle fibers bundle into fascicles with the aid of the perimysium, which also directs vascular and neural components of the tissue. Finally, the entire muscle tissue is covered by the epimysium (Sullivan and Best 2005).

The myotendinous junction is characterized by folding of the tendon collagen fibers into 'finger-like' processes generated by myocytes in the muscle, permitting transmission of muscle-generated forces by contractile proteins such as actin and myosin to the tendon. The junction also contains a population of muscle stem (satellite) cells (Benjamin and Ralphs 2000). The attachment of the muscle cells to the collagen fibers of tendon at the myotendinous junction is

analogous to focal adhesions; in fact, localization of focal adhesion-associated proteins at the junction such as paxillin, vinculin, and talin has been observed (Turner, Kramarcy et al. 1991). While some collagen fibers attach directly to muscle fibers (cells), others penetrate endomysium and are terminated at the muscle basal membrane, which is significantly thickened at the myotendinous junction (Khoroshkov 1975). Other ECM proteins have been implicated as being critical for myotendinous patency including dystrophin and laminin 2, a ligand for the α7β1 integrin (highly expressed at the junction) (Trotter 2002). Together, this multi-modal folding integration of muscle and tendon increases the surface area by over an order of magnitude at the junction (Trotter 2002), reducing stress concentrations during muscle contraction and subsequent tendon loading (Gross and Hoffmann 2013). Despite this, the myotendinous junction is generally considered the weakest part of the muscle, making it an important target for tissue engineering applications.

1.5 Technologies for fabricating patterned, gradient biomaterials

1.5.1 Patterned materials to assess and regulate cell functions

Combinatorial biomaterials to rapidly assess multiple combinations of biophysical and biochemical regulators are necessary to deconvolute the complex set of cell-ECM interactions encountered in tissues. When considering the engineering of multi-tissue junctions containing heterogeneous ECM protein, mineral, and soluble factor content it is critical to understand how spatiotemporal presentation of these factors affects stem cell lineage specification.

1.5.1.1 Combinatorial biomaterial arrays

In one of the first approaches to rapidly fabricate arrayed biomaterials on the nanoscale, Anderson *et al.* produced slides spotted with 576 combinations of 25 different acrylate, diacrylate, dimethacrylate, and triacrylate monomer with a radical initiator on a poly(hydroxyethyl methacrylate) (pHEMA) substrate (Anderson, Levenberg et al. 2004). They used these arrays to rapidly probe the differentiation of human embryonic stem cells (ESCs) down epithelial or mesenchymal lineages. They found that certain monomers inhibited spreading, leading to an almost pure population of epithelial cells while the absence of retinoic acid in culture reduced epithelial differentiation. Another approach assayed combinations of ECM proteins and soluble factors to drive ESC differentiation down the cardiac lineage (Flaim, Teng et al. 2008). The multi-well microarray platform permitted 1200 experiments with 240 unique microenvironments simultaneously. Data from fluorescent images was collected using a DNA microarray scanner, which proved to be much more time-efficient than traditional fluorescence microscopy. Cosson *et al.* used microfluidics (hydrodynamic flow focusing) to generate coincident and overlapping gradients of multiple proteins on PEG hydrogels (Cosson, Allazetta et al. 2013). As a proof of concept, a gradient of tethered leukemia inhibitory factor (LIF) was created to show that formation of self-renewing colonies by ESCs required a baseline concentration of 85 ng cm^{-2}. Qi *et al.* used a hybrid microgel setup to culture embryoid bodies at the interface between two or four microgels composed of gelatin methacrylate (GelMA) and PEG (Qi, Du et al. 2010). The authors found that vasculogenic differentiation was preferentially promoted in the GelMA substrates in a spatially dependent manner and that this effect could be abrogated by the addition of a matrix metalloproteinase (MMP) inhibitor.

Combinatorial approaches have also been applied to direct adult stem cell differentiation. Nakajima *et al.* used photo-assisted patterning of alkanethiol self-assembled monolayers (SAMs) to immobilize combinations of ECM proteins and growth factors to assess the role those environmental components play in neural stem cell (NSC) differentiation (Nakajima, Ishimuro et al. 2007). They found that while certain growth factors generally drove specific cell behaviors (*e.g.* ciliary neurotrophic factor (CNTF) led to astroglial differentiation), these effects were altered depending on the composition of the underlying ECM, suggesting a role of the ECM itself in the transduction of growth factor signals during differentiation. Gobaa *et al.* combined robotic protein spotting with micropatterning of PEG hydrogel microwells with tunable stiffness to probe the combined influence of biochemical and biophysical cues on regulating stem cell fate, focusing specifically on adipogenic and osteogenic MSC differentiation as well as neural stem cell differentiation (Gobaa, Hoehnel et al. 2011). This group has also developed methods to spot mammalian cells with nanowells using DNA microarray technology (Woodruff, Fidalgo et al. 2013).

While the above technologies have cultured cells on top of planar substrates, progress has been made on developing arrays of 3D scaffolds where cells can be encapsulated or cultured within a 3D matrix to more accurately mimic the architectural milieus encountered *in vivo*. Yang *et al.* used a dual syringe pump system to fabricate combinatorial arrays of 3D macroporous salt-leached polymer scaffolds consisting of gradient combinations of poly(desaminotyrosyl-tyrosine ethyl ester carbonate) (pDTEc) and poly(desaminotyrosyl-tyrosine octyl ester carbonate) (pDTOc) (Yang, Bolikal et al. 2008). They assessed the suitability of the scaffolds for bone tissue engineering using MC3T3 cells, demonstrating that increased pDTEc content enhanced

cell adhesion and proliferation. The same group used a gradient maker to fabricate a combinatorial array of 3D PEG hydrogels over a stiffness range of 10-300 kPa to assess the role 3D of gel stiffness in driving encapsulated MC3T3 osteoblastic maturation, finding that gels stiffer than 225 kPa enhanced osteogenesis (Chatterjee, Lin-Gibson et al. 2010).

1.5.1.2 Technologies to create biomolecular patterns in 3D materials

The last decade has seen an explosion of techniques to create gradients and patterns of biomolecules in 3D biomaterials. While many of these studies have not progressed past the proof-of-concept stage, these patterning technologies could be useful in the creation of gradient scaffolds for the engineering of multi-tissue junctions. An early technique to fabricate gradient PEG hydrogels using a microfluidic gradient maker was developed that enabled the formation of adhesive ligand (RGDS) and crosslinking density gradients that were shown to affect human umbilical vein endothelial cell (HUVEC) adhesion (Burdick, Khademhosseini et al. 2004). Another technique to generate relatively large (cm-scale) gradients in microfluidic channels containing PEG-DA hydrogels was pioneered by combining passive-pump-induced forward flow and evaporation-induced backwards flow (He, Du et al. 2010). Gradients of RGDS adhesion ligand and PEG-DA concentration were created to demonstrate that HUVECs would preferentially adhere in RGDS-rich areas while their spread area was increased in the stiffer, higher PEG-DA concentration sections of the gradient.

In addition to gradients, technologies to develop discrete spatiotemporally controlled patterns in hydrogel systems have been pioneered largely by the Anseth and Shoichet groups. Luo and Shoichet created cysteine-modified agarose hydrogels that provided a photolabile substrate

amenable to the patterning of biochemical cues (Luo and Shoichet 2004). In this work, they demonstrated immobilization of the adhesion ligand GRGDS in discrete volumes of gel to guide 3D cell migration and neurite outgrowth. This same group used their photolabile agarose gel system to guide endothelial cell migration and differentiation through the presentation of immobilized VEGF (Aizawa, Wylie et al. 2010). While patterning of single biochemical factors was achieved with this method, controlling the spatial organization of multiple proteins has proven to be more difficult. Wylie *et al.* addressed this issue by taking advantage of orthogonal binding pairs barnase-barstar and streptavidin-biotin respectively to immobilize two different fusion proteins (barstar-sonic hedgehog (SHH) and biotin-CNTF) (Wylie, Ahsan et al. 2011). These proteins were sequentially patterned in coumarin-derivatized agarose hydrogels and shown to maintain activity as well as modulate the differentiation and migratory capacity of retinal progenitor cells (RPCs).

Other techniques to pattern and immobilize proteins have used click chemistry. In one approach, copper-free click chemistry was used to directly encapsulate cells within modified PEG hydrogels while in parallel thiol-ene photocoupling was used to enable patterning of biological moieties in real time (DeForest, Polizzotti et al. 2009). Another approach from the same group used wavelength-specific photochemical reactions to allow orthogonal and dynamic spatiotemporal control of photocleavage and photoconjugation events (DeForest and Anseth 2011).

These approaches can be exploited to drive specific cell behaviors. A strategy to create photodegradable PEG-based hydrogels through the incorporation of photolytic nitrobenzyl

groups was developed to enable on-demand degradation for the creation of various features and the release of pendant functionalities (Kloxin, Kasko et al. 2009; Kloxin, Tibbitt et al. 2010). This approach enabled directed cell migration and allowed for the promotion of MSC chondrogenic differentiation via photolytic removal of RGDS ligands. A follow up to these studies further demonstrated the utility of this system by showing that, in a well-based culture platform, 3D shapes inspired by native alveolar structures affected lung epithelial cell differentiation (Kloxin, Lewis et al. 2012).

While many techniques have been described for patterning biomolecules in hydrogel systems, fewer investigations have focused on spatial patterning in 3D macroporous scaffolds more amenable to orthopedic tissue engineering applications. Martin *et al.* developed a technique to biomolecularly pattern 3D macroporous collagen scaffolds using benzophenone-based chemistry (Martin, Caliari et al. 2011). Benzophenone groups were conjugated to free amines in the collagen scaffold and then exposed to UV light through a photomask in the presence of a biomolecule of interest. UV irradiation creates a transient diradical on the benzophenone that permits abstraction of a proximal C-H bond from the biomolecule to form a new C-C covalent bond. Importantly, if a biomolecule is not inserted the diradical will relax back to its ground state, allowing it to be re-excited in the presence of a different biomolecule through a different photomask if desired. This technique allows for the creation of multiple discrete and overlapping patterns of multiple biomolecules with the only biomolecular requirement being the presence of a C-H bond. Additionally, this patterning technique was shown to not harm collagen triple helical integrity, mechanical properties, or MC3T3 viability (Martin, Caliari et al. 2011).

1.5.1.3 Micropatterned substrates to drive stem cell differentiation

Micropatterned substrates are increasingly being utilized to assess the influence of architectural and mechanical cues on stem cell differentiation. In a classic demonstration of the influence of substrate geometry on cell fate, McBeath *et al.* cultured MSCs on fibronectin-coated PDMS islands of different shapes and sizes (McBeath, Pirone et al. 2004). MSCs allowed to spread underwent osteogenesis while MSCs that were rounded and unspread became adipocytes. This process was RhoA-dependent with activation of the RhoA-ROCK pathway inducing osteogenesis regardless of shape. The same group investigated the influence of cell shape on driving TGF-β-mediated chondrogenic versus smooth muscle cell (SMC) fate (Gao, McBeath et al. 2010). They found that spread cells up-regulated SMC genes while rounded cells up-regulated chondrogenic genes. For these lineages, the effect was not Rho-A dependent but rather driven by Rac1 and N-cadherin activation in the case of promoting SMC differentiation. Inspired in part by this work, Kilian *et al.* showed that shapes with increasing aspect ratio and subcellular curvature promoted increased actomyosin contractility and osteogenesis while small molecule cytoskeletal inhibitors abrogated these effects (Kilian, Bugarija et al. 2010). Contractile MSCs undergoing osteogenesis were shown to have elevated activation of the c-Jun N-terminal kinase (JNK), extracellular signal-related kinase (ERK1/2), and wingless-type (Wnt) signaling pathways. The same researchers demonstrated that altering the density and affinity of cell adhesion ligands could affect MSC lineage specification with higher densities promoting osteogenesis, lower affinity driving myogenesis, and low density/low affinity mediating neurogenesis (Kilian and Mrksich 2012).

Micropatterned mechanical cues can also have a profound effect on stem cell differentiation processes. In one study, sequentially-crosslinked hyaluronic acid (HA) hydrogels were used to investigate the role of crosslinking density in driving MSC fate (Khetan and Burdick 2010). The introduction of non-degradable kinetic chains in hydrogels that underwent UV-mediated secondary crosslinking inhibited MSC spreading and remodeling, resulting in preferential adipogenesis despite the increase in elastic modulus induced by secondary crosslinking. A follow up to this study concluded that MSC differentiation was driven by generation of degradation-mediated cellular traction forces, independent of MSC cytoskeletal organization and hydrogel modulus (Khetan, Guvendiren et al. 2013). Interestingly, when MSCs were grown on top of, instead of encapsulated within, these HA hydrogels osteogenesis was induced by secondary crosslinking, underscoring the important of culture dimensionality in regulating MSC fate (Guvendiren and Burdick 2012).

1.5.1.4 Materials to modulate stem cell fate via growth factor signaling

A host of material systems have been applied to understand and manipulate growth factor signaling in the context of regulating multi-potent cell fate. In the previous section, it was suggested that the composition of the ECM could affect the transduction of soluble factor signals (Nakajima, Ishimuro et al. 2007). Several studies have shown that substrate stiffness can also influence growth factor signaling. The Picart group has utilized polyelectrolyte multi-layers constructed via layer-by-layer assembly (Schneider, Francius et al. 2006; Ren, Crouzier et al. 2008) to probe the combined influence of stiffness and growth factor signaling on cell fate on both monolithic (Crouzier, Ren et al. 2009; Crouzier, Fourel et al. 2011) and gradient (Almodovar, Crouzier et al. 2013) versions of the films. One study in particular investigated the

roles of soluble or bound BMP-2 on soft (~ 200 kPa) or stiff (~ 350 kPa) polyelectrolyte films on C2C12 adhesion, spreading, and differentiation (Crouzier, Fourel et al. 2011). This study showed that bound BMP-2 was required for cell spreading on the soft films, that bound BMP-2 promoted increased activation of canonical BMP signaling pathways compared to soluble BMP-2, and that activation of BMP signaling was higher on softer films compared to stiff films. Together, these data suggest that the mode of presentation (soluble versus bound) as well as the substrate physical properties can differentially affect the way biochemical signals are processes by cells. Substrate stiffness also affects growth factor signaling in relation to other tissues, including cartilage. Allen *et al.* demonstrated that cartilage cells expressed elevated levels of chondrogenic genes when cultured on 0.5 MPa substrates and that there was a synergistic effect of exogenous TGF-β supplementation on promotion of chondrogenic phenotype (Allen, Cooke et al. 2012). The response to stiffness was shown to be ROCK-dependent, affecting autocrine production of TGF-β. The synergy of stiffness and growth factor supplementation acted through a p38-MAPK-dependent mechanism (Allen, Cooke et al. 2012).

The native ECM acts a reservoir for soluble factors and sequesters them through a range of mechanisms. Understanding the role of biomaterials in sequestering soluble factors is therefore a critical design parameter. The Murphy group has designed a variety of modular peptides in order to investigate this important area of research. Hudalla *et al.* showed that surfaces presenting a heparin-binding peptide could sequester heparin from culture media supplements such as fetal bovine serum, which in turn could promote the binding of growth factors to the heparin-trapped surfaces (Hudalla, Koepsel et al. 2011). This led to amplified growth activity which in turn promoted MSC proliferation and osteogenesis via sequestration of FGF and BMP-2 respectively

(Hudalla, Kouris et al. 2011). Modular peptides can also be designed to adhere to specific ECM proteins. Lee *et al.* designed a multi-functional peptide with one end inspired by the HA-binding region of osteocalcin and the other end inspired by the "knuckle" epitope of BMP-2 (Lee, Wagoner-Johnson et al. 2009). HA surfaces modified with the modular BMP-2 peptide were shown to promote improved osteogenic activity in terms of ALP activity, osteocalcin expression, and mineral deposition.

1.5.2 Patterned materials towards engineering multi-tissue junctions

1.5.2.1 Material with graded mineral structure

One approach to recapitulate the compositional and mechanical heterogeneity found in soft tissue-bone junctions is to engineer materials with gradations in mineralization. Phillips *et al.* created a mineral gradient on a collagen scaffold using a dipping method to manufacture a gradient of immobilized retrovirus encoding for the osteogenic transcription factor RUNX2 (attached to poly(L-lysine) groups) (Phillips, Burns et al. 2008). Zonal organization of osteoblastic and fibroblastic phenotypes was observed both *in vitro* and *in vivo* with increased mineralization and expression of osteogenic factors observed coincident with the RUNX2 pattern.

Another approach utilized a hybrid electrospinning process to fabricate graded poly(caprolactone) (PCL) meshes incorporating tricalcium phosphate nanoparticles (Erisken, Kalyon et al. 2008). When seeded with MC3T3 preosteoblasts, the graded scaffold supported gradations of ECM protein synthesis, mineralization, and mechanical properties after 4 weeks of culture. Electrospinning was also used to create PLGA scaffolds with a linear gradient in calcium

phosphate content (Li, Xie et al. 2009). The linear gradient was created by partially submerging the PLGA scaffold (at an angle) in a solution of 10x simulated body fluid (SBF). The mineral gradient resulted in a quasi-linear gradient of mechanical properties and influenced the proliferation of MC3T3 cells with higher cell numbers observed on the more mineralized scaffold sections after 3 days of culture. This same group has also adapted their submersion protocol to attach opposing linear gradients of MC3T3 preosteoblasts and tendon fibroblasts, representing an important step towards making scaffolds with coincident gradations of mineral content and cell type (Liu, Zhang et al. 2012). More recently, electrospinning was used again to make a nanofiber scaffold out of PCL containing a gradient of amorphous calcium phosphate nanoparticles (Ramalingam, Young et al. 2012). Adhesion, proliferation, and osteogenic response of MC3T3 cells were enhanced in scaffold regions containing increased calcium phosphate content.

CG scaffolds have also been created with gradations of mineral content using a liquid phase co-synthesis method (Harley, Lynn et al. 2010). Suspensions corresponding to a cartilage phase (type II collagen, chondroitin sulfate in acetic acid) and a bone phase (type I collagen, chondroitin sulfate, calcium salts in phosphoric acid) were created separately. Using a titrant-free concurrent mapping technique (Lynn, Best et al. 2010), collagen-GAG-calcium phosphate (CGCaP) suspensions can be created with a mineral content ranging from 0-80 wt% with the calcium phosphate phase easily converted to the biologically-relevant hydroxyapatite via hydrolysis (Harley, Lynn et al. 2010). The CG (cartilage) and CGCaP (bone) suspensions were carefully layered on top of one another and allowed to interdiffuse prior to freeze-drying. The freezing process locked the diffusion gradient in place at the interface of the two suspensions.

Following sublimation, this resulted in a multi-compartment scaffold displaying distinct regions of mineral content as observed via microCT and EDX analysis, but continuity of the collagen fibers at the interface as shown by SEM. This was critical in order to prevent delamination of the construct under loading. Moreover, the compartment-specific differences in mechanical properties allowed the scaffold to exhibit deformation properties under loading similar to that of native articular joints (compression primarily confined to the non-mineralized cartilage phase).

1.5.2.2 Graded pore anisotropy

While less attention has been paid to making materials with gradations in pore alignment (anisotropy), this is critical design parameter for engineering junctions between highly anisotropic tissues such as tendons and ligaments with a more amorphous tissue such as bone. This need was addressed in part by Xie *et al.* in the creation of a nanofiber scaffold with a gradient of aligned and randomly oriented fibers (Xie, Li et al. 2010). The PLGA scaffolds were created by electrospinning onto a unique collector composed of two metal plates with an air gap between them. Fibers were isotropically oriented on the metal plate while the fibers in the gap were uniaxially stretched to promote alignment during collection. This graded setup supported the attachment and proliferation of tendon fibroblasts with the cells conforming to the contact guidance cues provided on both the aligned and non-aligned portions of the scaffold.

1.5.2.3 Graded soluble factor distribution

In additions to gradations of microstructure, mechanics, and composition, multi-tissue junctions contain heterogeneous distributions of biomolecules such as growth factors during development, homeostasis, and following injury. One effort towards recapitulating this graded presentation of

growth factors involved the creation of a PLGA microsphere-based scaffold where microspheres loaded with different molecules were arranged in a spatially-tunable manner and then joined together as a continuous scaffold via ethanol sintering (Singh, Morris et al. 2008). Although this study only used model dyes instead of actual growth factors, it represents an intriguing approach to organizing biomolecule presentation in spatially-tunable manner within a 3D material. The same group was able to create scaffolds with gradations of stiffness as a potential method to drive graded differentiation through the incorporation of mechanical cues. Singh *et al.* fabricated a macroporous 3D scaffolds containing a gradient of PLGA microspheres with a subset of the microspheres incorporating calcium carbonate or titanium dioxide nanoparticles to increase stiffness (Singh, Dormer et al. 2010).

More recently, a method to create 3D PCL/Pluronic scaffolds with a gradient of growth factor content was developed using centrifugation (Oh, Kim et al. 2011). The study was able to create overlapping gradients of the growth factors BMP-7, TGF-β2, and VEGF in the longitudinal plane of the scaffold and show sustained release profiles over 35 days. One drawback of this study was that the increase of growth factor concentration correlated with increased matrix density (due to centrifugation), which may negatively impact cell viability.

Micropatterning and printing technologies have also been used to create patterns and gradients of growth factors. Phil Campbell's group has used inkjet bioprinting to drive spatially-graded stem cell differentiation (Phillippi, Miller et al. 2008). In one approach, C2C12 cells were seeded onto fibrin-coated glass coverslips with printed patterns of tenogenic (FGF-2) and osteogenic (BMP-2) factors. Areas with printed FGF-2 and BMP-2 showed localized expression of the tenogenic

marker scleraxis and the osteogenic marker ALP respectively, with spontaneous myogenic differentiation in the non-patterned areas (Ker, Chu et al. 2011). Importantly for translation to multi-tissue junction engineering applications, this printing process is compatible with biomaterials such as aligned nanofiber scaffolds (Ker, Nain et al. 2011).

1.6 Engineering cartilage-bone (osteochondral) interfaces

1.6.1 Design considerations

Although some approaches to osteochondral tissue engineering have used scaffold-free constructs for regeneration (Brehm, Aklin et al. 2006), this section will focus on the development of novel, bioactive scaffolds towards the repair of osteochondral defects. Osteochondral grafts are often designed as separate chondral and osseous layers that are later integrated by co-culture or via an adhesive such as fibrin glue. The chondral layer is typically hydrogel-based with a high cell density to promote condensation and chondrogenesis while the osseous layer is often a macroporous composite containing a calcium phosphate phase such as hydroxyapatite. Due to the availability of stromal cells from the bone marrow, osteochondral grafts are often implanted acellularly or with cells (chondrocytes, MSCs/chondrocytes) embedded in the chondral layer only. In this section we will summarize *in vitro* and *in vivo* applications of various biomaterials designed for osteochondral repair. We will survey strategies to drive MSC differentiation with biomaterial-based instructive cues as well as soluble (growth factors and/or genes) cues.

1.6.2 Current tissue engineering approaches

1.6.2.1 In vitro applications

1.6.2.1.1 MSC lineage specification driven by material-based cues

Helen Lu's group has pioneered several innovative scaffold designs to help elucidate the role of material properties in driving cell fate for osteochondral repair. One study used an agarose hydrogel and composite microspheres of PLGA/bioactive glass to create a biphasic scaffold with a pre-integrated interface (Jiang, Tang et al. 2010). Co-culture of chondrocytes and osteoblasts resulted in the formation of calcified cartilage at the interface between the two cell types that was dependent on the presence of the PLGA/bioactive glass. Higher cell density improved chondrogenesis and graft mechanical integrity. Using a similar agarose-based system, Khanarian *et al.* examined the effects of hydroxyapatite incorporation and particle size on the activity of both non-hypertrophic and hypertrophic chondrocytes (Khanarian, Haney et al. 2012). Hypertrophic chondrocytes showed increased mineralization and improved composite mechanics with micron-scale hydroxyapatite particle incorporation. Another study by the same authors similarly looked at the effects of HA incorporation in an alginate gel system on the response of embedded chondrocytes, focusing on mineralization and hypertrophy (Khanarian, Jiang et al. 2012). HA incorporation was shown to promote chondrocyte hypertrophy, type X collagen deposition, and improved mechanics.

Recently, a sphere-templating approach was used to fabricate a bi-layered poly(hydroxyethyl methacrylate) hydrogel scaffold (Galperin, Oldinski et al. 2012). In a reversal of many osteochondral tissue engineering strategies, the material used relatively small (38 μm) pores in the osseous compartment with larger (200 μm) pores in the chondral compartment. Chondrocyte pellets and MSCs were seeded in the cartilage and bone compartments respectively and cultured

in standard growth medium for 4 weeks, demonstrating compartment-specific profiles of proteoglycan and mineralization.

1.6.2.1.2 MSC lineage specification driven by soluble-based cues

Wang *et al.* used a gradient-making system to create single concentration or reverse gradients of microspheres (PLGA or silk fibroin) incorporating chondrogenic (IGF-I) or osteogenic (BMP-2) growth factors in alginate or porous silk scaffolds (Wang, Wenk et al. 2009). They found that MSCs cultured in the gradient system for 5 weeks showed osteogenic differentiation in response to the BMP-2 gradient, but not chondrogenic differentiation in response to the IGF-1 gradient. This was likely due to the ability of the silk microspheres to more efficiently deliver BMP-2.

In a creative approach, Sheehy *et al.* sought to create osteochondral constructs through spatial control of endochondral ossification (Sheehy, Vinardell et al. 2013). Bilayer agarose constructs were seeded with MSC-derived chondrocytes and MSCs on the chondral and osseous layers respectively and cultured in chondrogenic medium for 21 days. Subsequent culture in hypertrophic medium resulted in endochondral ossification that was restricted to the osseous layer of the scaffold.

Allan *et al.* developed an *in vitro* method to induce graded regions of mineralized and non-mineralized interfacial fibrocartilage by seeding chondrocytes on top of a porous calcium polyphosphate substrate and growing them in the presence of beta-glycerophosphate (Allan, Pilliar et al. 2007). After 8 weeks cartilage tissue displayed a zonal organization of mineral

content with improved interfacial shear strength compared to controls grown without beta-glycerophosphate.

Other strategies have considered integrating distinct chondral and osseous compartments following *in vitro* conditioning to create osteochondral constructs. Chen *et al.* used MSC-seeded silk fibroin scaffolds cultured separately in osteogenic and chondrogenic media and then joined together via peptide conjugation (Chen, Shi et al. 2013). Although the MSCs near the interface expressed higher levels of hypertrophic markers type X collagen and MMP-13, concerns about the mechanical integrity at the interface of two compartments remain.

1.6.2.2 In vivo applications

Seminal work from the Caplan group helped shape the now established field of osteochondral tissue engineering. An early approach used rat MSCs that were separately cultured in osteogenic and chondrogenic induction media followed by seeding onto separate, phenotype-specific materials: a hyaluronan sponge and a porous calcium phosphate ceramic for the chondral and osseous layers respectively (Gao, Dennis et al. 2001). The materials were joined with fibrin glue and implanted subcutaneously in rats, resulting in integration of the two compartments and ECM synthesis appropriate for each compartment. The same group followed up this study with an injectable composite of hyaluronan and calcium phosphate to repair rat osteochondral defects (Gao, Dennis et al. 2002). The two components of the composite were injected separately and layered on top of one another in the defect site. After 12 weeks there was clear zonal arrangement of the repair tissue with good integration into the healthy cartilage and subchondral bone as well as a layer of calcified cartilage between the chondral and osseous layers.

Demineralized bone matrix has also been considered as a promising material for engineering osteochondral defects. Gao *et al.* evaluated the use of demineralized cortical and trabecular bone separately in the repair of rabbit osteochondral defects, hypothesizing that intrinsic cytokines harbored in the matrix would guide stratified osteochondral regeneration (Gao, Knaack et al. 2004). While the trabecular bone graft resulted in poorly organized repair tissue, the cortical graft supported the formation of distinct articular cartilage and subchondral bone layers that integrated into the surrounding native tissue. Li *et al.* used demineralized bone matrix gelatin as an *in vitro* scaffolding material to support rabbit chondrocytes in culture, producing 1.3 mm thick neo-cartilage after 6 weeks (Li, Jin et al. 2006).

1.6.2.2.1 Osteochondral regeneration directed by material-based cues

The *in vivo* performance of the aforementioned CG-CGCaP multi-compartment scaffold was evaluated in a 26 week goat model (Getgood, Kew et al. 2012). In the study, the CG-CGCaP scaffold was compared to a biphasic synthetic (PLGA) material as well as empty defect controls. After 26 weeks, the total histology score was significantly improved over the PLGA or empty defect groups with lower occurrence of subchondral bone cysts and markedly more hyaline-like cartilage.

Zhang *et al.* produced a composite material consisting of collagen and electrospun poly(L-lactic) acid (PLLA) nanofibers to drive osteochondral regeneration in a rabbit model (Zhang, Chen et al. 2013). The presence of the nanofiber phase resulted in improved osteogenic response as

measured by OCN, RUNX2 expression as well as calcium production while pre-seeding the composite with MSCs improved overall construct integrity.

A recent study demonstrated the development of a low density PVA nanofiber mesh incorporating chondroitin sulfate (Coburn, Gibson et al. 2012). PVA-chondroitin sulfate composites supported higher levels of chondrogenic gene expression compared to pellet cultures *in vitro*, and when implanted acellularly into rat osteochondral defects were able to recruit cells and support the synthesis of cartilage-like tissue.

A biphasic material composed of PLGA (impregnated with beta-tricalcium phosphate in the osseous phase) was developed as a scaffold for autologous chondrocyte implantation in osteochondral defects created in the femoral condyles of mini-pigs (Jiang, Chiang et al. 2007). After 6 months, repair tissue had similar mechanical properties to the native tissue with hyaline-like cartilage in the chondral phase and good integration with native subchondral bone in the osseous phase.

Pore size is also a critical scaffold design parameter to consider for multi-tissue engineering. Duan *et al.* initiated a study to investigate the role of compartment-specific (chondral or osseous) pore size on the regeneration of rabbit osteochondral defects using bilayered PLGA scaffolds (Duan, Pan et al. 2013). Optimal results were achieved with pores in the 100-200 μm range for the chondral layer and 300-450 μm range for the osseous layer as shown by histology and gene expression analyses.

1.6.2.2.2 Osteochondral engineering via spatially-graded growth factor and gene delivery

Reyes *et al.* created bilayer scaffolds consisting of a TGF-β1-loaded PLGA/polyurethane chondral layer and a BMP-2-loaded macroporous PLGA osseous compartment to guide osteochondral repair in a rabbit model (Reyes, Delgado et al. 2013). Although the growth factors displayed zero order release kinetics, the incorporation of both growth factors did not appear to enhance the regenerative response. Another approach utilized oligo(poly(ethylene glycol) fumarate) (OPF) hydrogels loaded with gelatin microparticles to assess the dual role of IGF-1 and TGF-β3 delivery in the regeneration of rabbit osteochondral defects (Kim, Lam et al. 2013). Although both growth factors improved cartilage morphology compared to the control, single delivery of IGF-1 resulted in better subchondral bone integration as well as GAG synthesis compared to the dual release groups. Re'em *et al.* described an acellular graded growth factor delivery system using sulfated-alginate gels to deliver spatially-stratified affinity-bound TGF-β1 and BMP-4 in the chondral and osseous layers respectively (Re'em, Witte et al. 2012). Implanted constructs in a rabbit model were able to recruit cells and support the synthesis of layer-specific ECM components after 4 weeks. In addition to the delivery proteins such as growth factors, spatially-graded delivery of genes encoding for ECM proteins and growth factors has been considered as a strategy for osteochondral regeneration. One approach utilized a bilayered gene-activated chitosan-gelatin scaffold consisting of a chondral layer with a TGF-β1-encoding plasmid and an osseous layer containing hydroxyapatite mineral as well as a BMP-2-encoding plasmid (Chen, Chen et al. 2011). The bilayer system was shown to support MSC lineage specification and simultaneous articular cartilage and subchondral bone repair in a rabbit model.

An approach to engineering articular condyles was described using bone marrow-derived MSCs in a PEG-based hydrogel (Alhadlaq and Mao 2005). MSCs were induced to differentiate down chondrogenic and osteogenic lineages, suspended in separate PEG gels, and then combined using sequential photopolymerization. Following 12 weeks of implantation in nude mice, stratified layers of chondral and osseous tissue were observed with chondrocytes at the osteochondral interface staining positive for hypertrophic markers (type X collagen).

Shao *et al.* used a 3D porous PCL scaffold that incorporated tricalcium phosphate in the osseous region to promote repair of osteochondral defects in a rabbit model (Shao, Goh et al. 2006). MSC-seeded groups showed superior repair compared to acellular controls after 6 months with good integration of the osseous layer with native subchondral bone and moduli approaching that of normal cartilage.

The Detamore group applied their gradient microsphere system (see previous sections) to deliver spatially-graded material and biological based cues in a rabbit osteochondral defect model. Opposing gradients of PLGA microspheres loaded with TGF-β1 (chondral region) and BMP-2 with or without nanophase HA (osseous region) were evaluated after 12 weeks implantation in a rabbit model with coincident gradients of material (HA) and biological (growth factor) cues inducing the best functional response in terms of ECM synthesis and graft integration (Mohan, Dormer et al. 2011). A related study by the same group validated the benefit of incorporating growth factors into their continuous scaffold design and suggested that pre-seeding of scaffolds with MSCs prior to implantation also improved regenerative outcomes (Dormer, Singh et al. 2011).

Based on a previously designed scaffold for osteochondral repair consisting of three sutured layers of type I collagen sponges containing graded amounts of HA (Tampieri, Sandri et al. 2008), Kon *et al.* performed a pilot clinical study in twenty-eight human patients over two years (Kon, Delcogliano et al. 2011). MRI and Tegner scores showed steady improvement in knee function from baseline with complete filling of cartilage and integration of the graft in 70% of the cases.

1.6.3 Summary and future challenges

The approaches presented in this section can be broadly fractioned into two camps: one where material-based cues were the primary drivers of cell phenotype, and the other where soluble factor cues were used to govern regeneration. Material-based approaches typically used hydrogels for the chondral layer and macroporous, HA-containing composites for the osseous layer. Some of these approaches were combined with soluble factor delivery, where chondrogenic (usually TGF-β1, TGF-β3, or IGF-1) and osteogenic (BMP-2, 4, or 7) were presented to enhance regeneration. In general, material-based approaches seem to be more successful than strategies that used soluble factors alone, especially *in vivo*.

Despite the relative maturity of the osteochondral repair field, there is still much room for growth. Many materials-based approaches still use materials with hard or abrupt interfaces that do not mimic native articular joints. Cell source is also a challenging problem; while acellular bone grafts have shown good performance, seeding chondrocytes in the chondral scaffold layer improves performance. Chondrocytes are difficult to acquire in large numbers, so efforts towards

generating large populations of these cells, either through differentiation of stem cells, co-culturing with primary chondrocytes, or other approaches, will be important. Integration with the native tissue continues to be a challenge as well. Injectable scaffolds that can simultaneously fill abnormally shaped defects and present a graded set of instructive cues may represent a path forward.

1.7 Engineering tendon/ligament-bone junctions

1.7.1 Design considerations

The primary design consideration for tendon and ligament tissue engineering is mechanical integrity. As a result, most scaffolds are designed as electrospun mats (Moffat, Kwei et al. 2009) or knitted, woven structures (Altman, Horan et al. 2002; Altman, Horan et al. 2002; Cooper, Sahota et al. 2007) that can be fabricated as dense, fibrous constructs while still supporting adequate cell viability, characteristic fibroblastic (elongated) morphology, ECM biosynthesis, and some level of cellular ingrowth. However, conventional approaches to ligament/tendon-bone repair have not used biomaterials, instead focusing on hybridized tendon grafts (Mutsuzaki, Sakane et al. 2011) and injectable carriers to deliver cells, growth factors, and/or compounds to promote bony integration (Rodeo, Suzuki et al. 1999; Tien, Chih et al. 2004; Huangfu and Zhao 2007). Zhang *et al.* used fibrin glue combined with BMP and a bone xenograft to promote healing of the rabbit ACL (Zhang, Pan et al. 2011). They found that the combination of BMP and the xenograft promoted formation of a cartilaginous interfacial region, higher mineral density in the bony insertion, and improved mechanical properties 12 weeks after surgery. Another approach used a heparin/fibrin-based delivering system to controllably release TGF-β3, a factor

that is known to promote scarless healing in fetal development (Manning, Kim et al. 2011). This delivery system, when applied to rat supraspinatus repair, accelerated the wound healing process and led to significant improvement in structural and material properties of the junction. While these approaches had some level of success, this section will focus on the emergence of biomaterial approaches, both *in vitro* and *in vivo*, to drive tendon/ligament-bone phenotypic stability and integration.

1.7.2 Current tissue engineering approaches

1.7.2.1 In vitro applications

A recent review by Derwin *et al.* summarized the mechanical and biochemical properties of several commercially-available ECM scaffolds for rotator cuff repair (Derwin, Baker et al. 2006). This study analyzed two small intestine submucosa (SIS)-based materials (Restore and CuffPatch) as well as two scaffolds derived from dermis (GraftJacket and TissueMend), with the CuffPatch being the only graft that was chemically crosslinked. The two SIS materials displayed better mechanical properties than their dermis-based counterparts, although all four grafts were an order of magnitude less stiff than the native canine infraspinatus tendon. Notably, the Restore graft had a substantial amount of sulfated and non-sulfated GAG content while the TissueMend scaffold still had a significant amount of residual DNA (~800 ng/mg). The GraftJacket and Restore materials also harbored residual DNA. This study indicates that there is still much work to do in the design of materials to repair rotator cuffs as far as mimicking the mechanical and biochemical properties of native tissue.

One of the first approaches to creating a stratified scaffold design for engineering the ligament-bone interface was pioneered by Spalazzi *et al.*. In their first study, the researchers designed a triphasic scaffold for the 3D co-culture of osteoblasts and fibroblasts towards engineering the ACL-bone interface (Spalazzi, Doty et al. 2006). The scaffold consisted of polyglactin, PLGA, and PLGA/bioactive glass layers corresponding to the ligament, fibrocartilage, and bone phases respectively. Fibroblasts and osteoblasts were seeded in the ligament and bone phases respectively and co-cultured over 4 weeks, over which time direct interactions between the two cell types were successfully limited to the middle fibrocartilage phase. In a related study by the same group it was demonstrated that scaffold-induced compression of a patellar tendon explant led to the up-regulation of fibrocartilagenous genes expressed at the ligament-bone interface including type II collagen, aggrecan, and TGF-β3 (Spalazzi, Vyner et al. 2008). Another *in vitro* co-culture study examined a tri-lineage setup where MSCs were cultured between fibroblasts and osteoblasts on a hybrid silk scaffold to drive fibrocartilagenous differentiation (He, Ng et al. 2012). PCR and immunohistochemistry revealed that the MSCs did indeed differentiate down a fibrocartilagenous lineage with a graded calcified cartilage region on the osteoblast-seeded side of the scaffold. TGF-β3 supplementation was shown to inhibit the fibrocartilage mineralization process.

Paxton *et al.* developed *in vitro* models of bone-ligament-bone grafts using poly(ethylene glycol) diacrylate (PEGDA) anchors functionalized with hydroxyapatite (HA) and the RGD peptide for cell adhesion (Paxton, Donnelly et al. 2009). These anchors were used to form the bony ends of a contracting fibroblast-loaded fibrin gel representing the ligament component of the construct. The researchers found that incorporating HA improved the mechanics of the scaffold while RGD

addition improved cell adhesion. The combination of HA and RGD improved cell attachment and interface formation, although adding too much HA (> 5wt%) made the constructs brittle. A follow up to this study evaluated the suitability of cast brushite anchors to serve as the bony ends of the construct (Paxton, Grover et al. 2010). This system, in conjunction with ascorbic acid, proline, and TGF-β supplementation, produced an *in vivo*-like tidemark with a ligament elastic modulus of 5.46 MPa and interface strength of 42 kPa. Other studies have examined the impact of differential mineral content on modulation of osteogenic and fibroblastic differentiation. Samavedi *et al.* used a co-electrospinning approach to create a PCL scaffold with a gradient in nano-hydroxyapatite particle content (Samavedi, Guelcher et al. 2012). MSCs cultured on the scaffold were shown to be metabolically active with elevated expression of osteogenic genes encoding for BMP-2 and osteopontin observed in the mineralized scaffold region.

1.7.2.2 In vivo applications

Spalazzi *et al.* sought to validate their triphasic scaffold design in an subcutaneous athymic rat model (Spalazzi, Dagher et al. 2008). One important change from the initial *in vitro* study was the introduction of third cell type (chondrocytes) added to the middle scaffold layer, leading to a tri-culture set-up with fibroblasts and osteoblasts. Cell-seeded groups showed good tissue infiltration and superior mechanical properties compared to acellular controls. Calcification was limited to the bone phase of the scaffold while fibrocartilage was observed in both the ligament and fibrocartilage scaffold phases, possibly due to the higher porosity in the ligament phase.

Ma *et al.* fabricated a 3D engineered bone-ligament-bone construct using a similar method to the one used by Paxton *et al.* discussed previously. Here, separate bone and ligament sections were

first created by growing MSCs on laminin-coated dishes (Ma, Goble et al. 2009). Once the constructs reached maturity, they were co-cultured and then implanted in a rat MCL model. After 1 month the constructs contained type I collagen, elastin, and a vascular network with improved mechanics over *in vitro* controls. While this is a promising approach, there are scale-up concerns with this type of model that make it questionable whether this type of system would be useful for larger animal or human trials. In order to address some of these concerns, this group followed up their MCL replacement study with the development of a 3D construct for ACL replacement in a larger animal (sheep) model (Ma, Smietana et al. 2012). In this study, the researchers were able to scale up the size of their constructs by using larger culture dishes and then fusing several of the constructs together to form large (60 mm length x 3 mm diameter) bone-ligament-bone grafts. Following 6 months *in vivo*, the constructs showed good integration with native bone and mechanical properties close to that of the native ACL.

A creative approach to engineering osteotendinous junctions was developed by manipulating BMP signaling in MSC-seeded type I collagen sponges implanted subcutaneously or intramuscularly in mice (Shahab-Osterloh, Witte et al. 2010). Canonical BMP signaling is mediated by the Smad proteins 1, 5, 8 where Smad1 and 5 are hypothesized to be more important for osseous and chondral development while Smad8 plays an integral role in mediating tenogenic phenotype (Hoffmann, Pelled et al. 2006; Retting, Song et al. 2009). In this study, viral expression of Smad8 and/or BMP-2 was induced in MSCs to promote a tenogenic and osteogenic/chondrogenic phenotype respectively. The combination of induced Smad8 and BMP-2 expression led to the formation of tendinous and osseous structures joined together with a fibrocartilage-like interface (Shahab-Osterloh, Witte et al. 2010).

Approaches for ligament-bone repair could have substantial implications beyond orthopedics. One important area of clinical need is the reconstruction of oral and craniofacial defects, specifically the tooth-ligament-bone connections. Park *et al.* demonstrated the creation of a PCL-poly(glycolic acid) (PGA) co-polymer scaffold via 3D printing to guide formation of BMP-7-transduced human gingival fibroblast-derived tooth dentin-ligament-bone tissue in a nude mouse model (Park, Rios et al. 2010). This group followed up that study with development of biomimetic fiber-guiding scaffolds to recapitulate the anisotropy of native ligamentous structures (Park, Rios et al. 2012). This approach led to improved fiber organization, greater mineralization, increased periostin expression, and better overall interfacial organization compared to randomly ordered scaffolds. Another group created a biphasic scaffold composed of a fused deposition modeling scaffold and an electrospun mat to regenerate bone and periodontal ligament respectively (Vaquette, Fan et al. 2012). The group seeded osteoblasts in the bone compartment and sheets of periodontal ligament cells on the electrospun ligament compartment followed by implantation on a dentin block for 8 weeks in a rat subcutaneous model. Results showed that cell sheet incorporation improved attachment of the scaffold to the dentin surface while higher ALP activity and mineralization was observed in the bone phase.

1.7.3 Summary and future challenges

While the studies presented show promise, much progress must still be made. The constructs outlined here fail to recapitulate the mechanics of native tendon/ligament-bone interfaces. Additionally, biomaterial designers must work with surgeons to find the best way to make constructs that can be integrated in a minimally invasive manner. Although many rotator cuff

repairs are performed arthroscopically, large tears necessitating biomaterial intervention would likely be implanted during open surgery. In this setting, the tendon end would likely be sutured to the torn tendon while the bone end would be integrated into the native bone using cement or screws. Working closely with surgeons will be necessary to determine the best methods for promoting integration with the native tissues.

Another challenge with tendon and ligament engineering is from a developmental biology standpoint tendons and ligaments are relatively poorly characterized, making it difficult to assess induction of a proper fibroblastic phenotype in engineered materials. This is starting to the change with the identification of scleraxis as a potent marker of tendon (Schweitzer, Chyung et al. 2001) as well as other studies that are elucidating the roles of different signaling pathways in tendon development (Brent, Schweitzer et al. 2003; Pryce, Watson et al. 2009; Liu, Aschbacher-Smith et al. 2012) and wound healing, both at the fetal (Kuo, Petersen et al. 2008) and adult (Kinneberg, Galloway et al. 2013) levels. Gleaning knowledge from these studies to inform the design of next generation materials will be critical.

1.8 Engineering muscle-tendon (myotendinous) junctions

1.8.1 Design considerations

The myotendinous junction (MTJ) is the least studied of the three junctions covered in this review. However, it shares some important similarities as far as design criteria to the other two junctions. One important shared feature is the graded interface between the two tissues. Although there is no gradient in mineral content between the two tissues, the MTJ contains a significant

amount of interdigitation. This interconnectivity increases the surface area at the junction, allowing for reduced stress concentrations. In addition, the ECM networks of both tissues interconnect with each other to promote strong, focal adhesion-like junctions between muscle myocytes and collagen fibers from tendon to permit force transfer and locomotion. Tissue engineering strategies for the MTJ will therefore need to include an open, continuous interface between the tendon and muscle sides while approaches to increase the interfacial surface area and interconnectivity are critical.

1.8.2 Current tissue engineering approaches

Engineering strategies for repairing the muscle-tendon junction are not nearly as well-developed as the other junctions covered in this review, but increasing attention is being paid to fabricating materials that integrate functional neural and vascular elements in engineered skeletal muscle to their corresponding tendon in order to enable normal locomotion. Early efforts from Swasdison *et al.* focused on engineering *in vitro* models of the myotendinous junction (Swasdison and Mayne 1991; Swasdison and Mayne 1992). The first paper outlined an effort to create a model culture system to understand the connection of myotubes to collagen fibers in tendon (Swasdison and Mayne 1991). The model included two type I collagen gels: one gel encapsulated quail skeletal muscle cells and supported the formation of myotubes while the other gel served as a "tendon" where the myotubes could interact with collagen fibrils. While the development of sarcolemmal invaginations was observed, direct association of the collagen fibers with muscle fibers was sporadic, suggesting that other proteins may modulate this interaction during development. One drawback of this paper was that the muscle fibers that formed were randomly oriented, making it difficult to track attachments to the ECM. The authors followed this up with

an approach to make highly aligned muscle fibers by culturing quail myoblasts in the center of an aligned membrane with tendon fibroblasts on either end; this culture system either persisted in 2D or was transferred to a 3D collagen gel for further culture (Swasdison and Mayne 1992). Muscle fibers were observed to make strong connections to the neighboring ECM that were reminiscent of the native MTJ.

The importance of integrating muscle-tendon connections has been recognized in industrial and surgical settings. Devices such as the OrthoCoupler have been developed in order to attach muscle to bone. In an a goat semitendinosus tendon model the OrthoCoupler was compared to a standard braided suture approach with fatigue strength evaluated. Fatigue strength was higher by a factor of 2.5 in OrthoCoupler group, where the muscle actually tore as the OrthoCoupler remained attached (Melvin, Litsky et al. 2010).

Recently, more renewed efforts have been made towards the development of materials to model and replace the MTJ. Larkin *et al.* used a commonly-applied anchored gel system to promote contraction-mediated formation of aligned myotendinous tissue constructs (Larkin, Calve et al. 2006). Constructs were formed by seeding muscle stem cells in a monolayer around anchors composed of engineered or native tendon. The engineered constructs were mechanically robust, failing primarily in the muscle region. There was also evidence of paxillin expression, a marker highly expressed in the native MTJ, in the engineered MTJs made here.

More recently, one of the first biomaterials engineered specifically for MTJ regeneration was fabricated by Ladd *et al.* (Ladd, Lee et al. 2011). This biomaterial system consisted of co-

electrospun PCL/collagen and PLLA/collagen nanofibers to create two mechanically distinct regions corresponding to muscle and tendon respectively along with an overlap region representing the junction. Mechanical tests indicated the material had regionally-specific mechanical properties similar to that of the native porcine diaphragm MTJ. Scaffolds also supported C2C12 myoblast and NIH3T3 fibroblast attachment and function, including the formation of myotubes by the C2C12 cells. This material represents an exciting step forward for the field of MTJ engineering, but *in vivo* validation is still necessary.

1.8.3 Summary and future challenges

The field of MTJ engineering is, at this point, in its infancy. Clearly one of the largest challenges in this field right now is the lack of researchers working in it. The study by Ladd *et al.* (Ladd, Lee et al. 2011) is one of the first to design a biomaterial scaffold specifically for muscle-tendon junction engineering. Before even designing these new materials, better *in vitro* models of the junction must be established that permit co-culture of both myocytes and tenocytes with interactions between the different cell types and ECM proteins that are reminiscent of the native junction. Much of the inspiration for future biomaterial designs will likely come from the more established tendon/ligament engineering communities, although some important considerations will have to be taken. One, the optimal approach to MTJ healing may be a minimally invasive, injectable material. Although most tendon/ligament scaffolds are not injectable, the advent of injectable, preformed scaffolds with shape memory may guide future applications in this area (Bencherif, Sands et al. 2012).

1.9 Overall summary and future perspective

The fields of tissue engineering and regenerative medicine have grown exponentially over the past 20 years. An emerging subfield of tissue engineering is focusing on the design of graded materials to regenerate heterogeneous multi-tissue junctions that are common injury sites in orthopedics. In parallel, much research has been undertaken to gain fundamental understanding of the microstructural, mechanical, and biochemical cues that drive stem cell differentiation. There are several important areas where moving forward these two camps can mutually benefit each other:

i) Creation of macroscale gradient materials

Many of the multi-compartment biomaterials designs outlined in this review employ disparate constructs that are separately cultured for a period of time and then integrated together through co-culture or an adhesive. Other approaches used scaffolds with hard interfaces dividing the compartments. While these approaches have shown some measure of success, these disparate materials do a poor job of mimicking the soft, continuous interfaces found in native articular joints. This can lead to problems such as excess shear at the compartment interface as well as inadequate transport and cellular crosstalk at the interface, factors that are critical in orthopedic interfacial development and homeostasis. One avenue to combat this would be to utilize microscale gradient-making technologies and scale up to the length scales (1-10 mm) needed for orthopedic tissue engineering. Several of the approaches outlined in this review would seem to be amenable to this, including the work by He *et al.* to generate cm-scale microfluidic gradients (He, Du et al. 2010) and the approach by Singh and co-workers to make continuous microsphere gradients (Singh, Morris et al. 2008).

ii) Combinatorial arrays to screen regulators of cell behavior

A general challenge for the tissue engineering community is the proper identification of the most important instructive cues to integrate into biomaterials towards achieving optimal regenerative outcomes. Combinatorial approaches as outlined in this review to screen hundreds or thousands of different microenvironments in parallel have begun to emerge as tools to enable this process. These studies are particularly important to the multi-tissue junction engineering community where biomaterials must present distinct, graded sets of instructive cues on a single platform. Studies such as the one by Chatterjee *et al.* that used material arrays to identify the optimal stiffness for driving MC3T3 osteogenesis (Chatterjee, Lin-Gibson et al. 2010) are particularly relevant. These studies should continue to inform the design of macroscale constructs.

iii) Spatially-patterning instructive cues into macroscale biomaterials

The patterning methods discussed in this review should be useful for making macroscale gradients to recapitulate native interfacial structures. Patterning of ECM proteins, growth factors, and other biomolecules may also provide a pathway around having to consider the integration of discrete biomaterial compartments, an issue with many of the designs discussed here. Methods such as the one discussed by Martin *et al.* are amenable to the creation of multiple, overlapping patterns of biomolecules with no inherent limits to the size of the construct being patterned (Martin, Caliari et al. 2011).

To conclude, these three focus areas represent common ground for future multi-disciplinary work that can enhance the efficacy of biomaterials-based regenerative strategies for multi-tissue

junctions while providing a tangible field of application for scientists designing methods to create patterns and gradients to drive cell fate.

CHAPTER 2: THE INFLUENCE OF COLLAGEN-GLYCOSAMINOGLYCAN SCAFFOLD RELATIVE DENSITY AND MICROSTRUCTURAL ANISOTROPY ON TENOCYTE BIOACTIVITY AND TRANSCRIPTOMIC STABILITY[2]

2.1 Chapter overview

Biomaterials for orthopedic tissue engineering applications must balance mechanical and bioactivity concerns. This work describes the fabrication of a homologous series of anisotropic collagen-GAG (CG) scaffolds with aligned tracks of ellipsoidal pores and a consistent degree of anisotropy but three different relative densities (ρ^*/ρ_s = 0.005 - 0.016). We subsequently quantified the role scaffold relative density plays in directing tenocyte bioactivity. Scaffold permeability and mechanical properties, both in tension and compression, were significantly influenced by relative density in a manner predicted by cellular solids modeling techniques. Equine tenocytes showed greater levels of attachment, metabolic activity, soluble collagen synthesis, and alignment as well as less cell-mediated scaffold contraction in anisotropic CG scaffolds of increasing relative density. Notably, the lowest density scaffolds experienced significant cell-mediated contraction with associated decreases in tenocyte number as well as loss of microstructural integrity, aligned contact guidance cues, and preferential tenocyte orientation over a 14 day culture period. Gene expression analyses suggested tenocyte de-differentiation in the lowest density scaffold while indicating that the highest density scaffold supported significant increases in COMP (4-fold), tenascin-C (3-fold), and scleraxis (15-fold) expression as well as significant decreases in MMP-1 (9-fold) and MMP-13 (13-fold) expression at day 14 compared to tenocytes in the lowest density scaffold. These results suggest that anisotropic scaffold relative density can help to modulate the maintenance of a more tendon-like

[2] This chapter has been adapted from the following publications:
Caliari, S. R., D. W. Weisgerber, et al. (2012). "The influence of collagen-glycosaminoglycan scaffold relative density and microstructural anisotropy on tenocyte bioactivity and transcriptomic stability." J Mech Behav Biomed Mater **11**: 27-40.

microenvironment and aid long-term tenocyte transcriptomic stability. Overall this work demonstrates that relative density is a critical scaffold parameter, not only for insuring mechanical competence, but also for directing cell transcriptomic stability and behavior.

2.2 Introduction

Collagen-glycosaminoglycan (CG) scaffolds have been fabricated for a variety of regenerative medicine application including dermis, peripheral nerves, cartilage (Yannas, Lee et al. 1989; Yannas 2001; Harley, Spilker et al. 2004), and most recently tendon (Caliari and Harley 2011; Caliari, Ramirez et al. 2011). CG scaffolds are fabricated by freeze-drying a suspension of collagen and glycosaminoglycans (GAGs), resulting in a highly porous (> 99%) sponge-like material with interconnected pores defined by CG fibers, termed struts. However, these scaffolds are typically fabricated at extremely low relative densities (ρ^*/ρ_s), the ratio of the scaffold density (ρ^*) to the density of the solid from which the scaffold material is composed (ρ^*/ρ_s). Scaffold relative density and porosity are also related (ρ^*/ρ_s: 1 – porosity). Scaffolds with low ρ^*/ρ_s typically present reduced mechanical properties that are not suitable for orthopedic tissues such as tendon, though recent work has incorporated high-density CG membranes into a low density CG scaffold in order to improve scaffold mechanical performance (Caliari, Ramirez et al. 2011). Previous work with CG scaffolds has demonstrated that these materials can be fabricated with relative densities as high as 0.18 (82% porosity) using techniques such as plasticating extrusion (Harley, Spilker et al. 2004) and vacuum filtration (Kanungo and Gibson 2009; Kanungo and Gibson 2010), but comprehensive analyses of the specific impact of scaffold relative density on cell bioactivity are still needed. Scaffold relative density is likely a critical biomaterial parameter

due to its significant effect on construct mechanics, permeability, specific surface area, and potential for steric hindrances to cell motility among other key properties (Kanungo and Gibson 2009; Kanungo and Gibson 2010; Istrate and Chen 2011). However, the effect of relative density on the properties of anisotropic biomaterials for tendon tissue engineering is unknown.

Musculoskeletal injuries account for over 100 million office visits per year (Mishra, Woodall et al. 2009) with about half of these injuries involving soft tissues such as tendons and ligaments (James, Kesturu et al. 2008). Tendon injuries affect people from all walks of life from the elderly to elite athletes with substantial costs accrued, both financial ($30 billion annually in the US alone (Butler, Juncosa-Melvin et al. 2008)) and quality-of-life related. While considerable progress has been made in the development of biomaterials for tendon tissue engineering (Juncosa-Melvin, Matlin et al. 2007; Li, Xie et al. 2009; Moffat, Kwei et al. 2009; Doroski, Levenston et al. 2010; Sahoo, Toh et al. 2010), there is a critical need for improved, innovative strategies. We have recently developed fabrication methods for anisotropic CG scaffolds with aligned tracks of ellipsoidal pores (Caliari and Harley 2011) and CG scaffold-membrane core-shell composites for increased mechanical competence (Caliari, Ramirez et al. 2011) for tendon tissue engineering. While scaffold-membrane composites show improved mechanical competence, the scaffold core used for this work had a relative density of ~ 0.5%. This is the typical relative density for many previous applications of CG scaffolds for soft tissue repair, but is not suitable for tendon repair due to its inability to withstand tenocyte-mediated contraction (Torres, Freyman et al. 2000; Caliari and Harley 2011).

This chapter describes the microstructural, mechanical, and biophysical properties of a homologous series of anisotropic CG scaffolds as a function of relative density. While increasing relative density was hypothesized to decrease construct permeability, it was also hypothesized to increase mechanical properties and ability to withstand tenocyte-mediated contraction, preserving the anisotropic contact guidance cues provided by the scaffold microstructure. Furthermore, it was hypothesized that the more dense anisotropic CG scaffolds would foster a more tendon-like microenvironment for tenocytes, resulting in elevated gene expression of tendon extracellular matrix (ECM) markers such as collagen I and cartilage oligomeric matrix protein (COMP) as well as tendon phenotypic markers including scleraxis and tenascin-C. While the effects of relative density on CG scaffold mechanical properties and early cell attachment have previously been elucidated (Kanungo and Gibson 2009; Kanungo and Gibson 2010), its effects on permeability, gene expression, long-term cell viability and its role in the functionality of anisotropic biomaterials for tendon tissue engineering have not been rigorously explored.

2.3 Materials and methods

2.3.1 Anisotropic CG scaffold fabrication and crosslinking

2.3.1.1 CG suspension preparation

CG suspension was produced from a homogenized blend of type I microfibrillar collagen from bovine tendon (Sigma-Aldrich, St. Louis, MO) and chondroitin sulfate from shark cartilage (Sigma-Aldrich, St. Louis, MO) in 0.05 M acetic acid (Yannas, Lee et al. 1989; O'Brien, Harley et al. 2004; Caliari and Harley 2011). The suspension was maintained at 4°C during mixing to prevent collagen denaturation. Suspensions of three different collagen concentrations were made:

0.5 w/v% (1x), 1.0 w/v% (2x), and 1.5 w/v% (3x). The ratio of collagen to GAG (11.25:1) was kept constant for all three suspension variants.

2.3.1.2 Anisotropic CG scaffold fabrication via freeze-drying

Scaffolds were fabricated via directional solidification as previously described (Caliari and Harley 2011). Briefly, CG suspension was pipetted into individual wells (6-12 mm diameter, 15-30 mm deep) in a 5 in x 5 in poly(tetrafluoroethylene) (PTFE)-copper mold and placed on a precooled (-10°C) freeze-dryer shelf (VirTis, Gardiner, NY). The mismatch in thermal conductivity between the PTFE mold body and the copper bottom (k_{Cu}/k_{PTFE} ~ 1600) promoted unidirectional heat transfer through the more conductive copper (Caliari and Harley 2011). The CG suspension was frozen at -10°C for 2 h and then sublimated at 0°C and 200 mTorr to remove ice crystals, resulting in dry, porous CG material.

2.3.1.3 Anisotropic CG scaffold crosslinking

Following lyophilization, all scaffolds were dehydrothermally crosslinked at 105°C for 24 h under vacuum (< 25 Torr) in a vacuum oven (Welch, Niles, IL). Scaffolds were hydrated via immersion in 100% ethanol for 2-3 h followed by sequential phosphate-buffered saline (PBS) washes over the next 24 h. Scaffolds were crosslinked further using carbodiimide chemistry in a solution of 1-ethyl-3-[3-dimethylaminopropyl] carbodiimide hydrochloride (EDAC, Sigma-Aldrich, St. Louis, MO) and *N*-hydroxysulfosuccinimide (NHS, Sigma-Aldrich, St. Louis, MO) at a molar ratio of 5:2:1 EDAC:NHS:COOH (Olde Damink, Dijkstra et al. 1996; Harley, Leung et al. 2007) for 1 h at 37°C. Scaffolds were then rinsed in PBS under shaking and stored in fresh PBS until use.

2.3.2 SEM analysis

Scaffold microstructural architecture was analyzed using scanning electron microscopy (SEM). SEM was performed using a JEOL JSM-6060LV Low Vacuum Scanning Electron Microscope (JEOL USA, Peabody, MA). The SEM was equipped with both a secondary electron (SE) detector and a backscatter electron (BSE) detector, allowing scaffolds to be visualized under low vacuum without a conductive coating (Harley, Lynn et al. 2010).

2.3.3 Determination of scaffold relative density

Scaffold relative density (ρ^*/ρ_s) was calculated by dividing the dry scaffold density (ρ^*) by the known density of collagen (ρ_s, 1.3 g cm^{-3}) (Yannas and Tobolsky 1967; Harley, Leung et al. 2007). Dry scaffold density was determined by weighing individual dry scaffolds (12 mm diameter, 15 mm height) and dividing by the scaffold volume.

2.3.4 Quantitative microstructural analysis

Microstructural features of the series of aligned CG scaffolds were quantitatively assessed using previously described stereology methods (O'Brien, Harley et al. 2004; Caliari and Harley 2011). Cylindrical CG scaffolds (8 mm diameter by 15 mm length) were cut into three 5 mm sections: *bottom* (closest to freeze-dryer shelf), *middle*, and *top*. Both longitudinally and transversely oriented scaffold sections were embedded in glycolmethacrylate (Polysciences, Warrington, PA) and serially sectioned (5 μm) on a microtome (Leica Microsystems, Germany). Scaffold sections were mounted on slides and stained with aniline blue (Fisher, Pittsburgh, PA) to enable visualization of CG solid content (O'Brien, Harley et al. 2004; Caliari and Harley 2011). A total

of 36 sections (18 longitudinal, 18 transverse) were analyzed for each relative density. Stained sections were visualized on an optical microscope (Leica Microsystems, Germany) and analyzed using a linear intercept macro in Scion Image. The macro outputs fitting parameters were used to calculate pore diameter and aspect ratio (AR) (O'Brien, Harley et al. 2004; Caliari and Harley 2011).

2.3.5 Permeability analysis

Scaffold permeability (12 mm diameter, 10 mm height) under compression was measured by using a two-piece polycarbonate rig with interchangeable gaskets and spacers (O'Brien, Harley et al. 2007). Polycarbonate spacers having a height of 10.5 mm, 3.5 mm, and 2.2 mm were used to compress the scaffolds to 0%, 65%, and 78% strain, respectively. A hydraulic pressure head of 1.2 in was applied to each scaffold to measure the resulting permeability. Fluid flow rate was measured three times for each scaffold at each strain level. The cross-sectional area of flow was determined by dying the scaffold and monitoring the resulting decrease in dye intensity due to flow through. Permeability was calculated for each scaffold using Darcy's Law (O'Brien, Harley et al. 2007):

$$K = \frac{Ql\mu}{\Delta PA} = \frac{Vl\mu}{t\Delta PA}$$

where K is the permeability, Q is the flow rate, V is the volume of water measured over a period of time t, l is the height of the scaffold under compression, μ is the viscosity of water, ΔP is the applied pressure, and A is the cross-sectional area of flow.

2.3.6 Mechanical testing

Compression tests were performed on CG scaffolds (12 mm diameter, 15 mm height) while tensile tests used scaffolds 6 mm diameter and 30 mm length (Caliari, Ramirez et al. 2011). Choice of sample geometry was dictated by the size of the scaffolds that will be deployed in future *in vivo* models. Compressive and tensile tests were performed in a manner consistent with previous mechanical analysis of CG scaffolds (Freyman, Yannas et al. 2001; Harley, Leung et al. 2007). All specimens tested were dry unless otherwise stated. Scaffolds were loaded to failure at a rate of 1 mm/min using an MTS Instron 2 (Eden Prairie, MN). Elastic modulus was calculated from the slope of the stress-strain curve over a strain range of 5-10% (Harley, Leung et al. 2007; Gibson, Ashby et al. 2010; Caliari, Ramirez et al. 2011). Ultimate tensile strength was determined from the peak stress value on the stress-strain curve while elastic compressive strength was calculated from the stress value where the linear elastic region ended.

2.3.7 Cell culture

2.3.7.1 Tenocyte isolation and culture

Equine tenocytes were isolated from horses aged 2-3 years euthanized for reasons not related to tendinopathy in a manner consistent with protocols approved by the University of Illinois IACUC (Caliari and Harley 2011). Digital flexor tendons were extracted, diced, and incubated in a collagenase solution at 37°C under constant shaking. Digest solution was filtered (40 μm pore size) to isolate tenocytes (Kapoor, Caporali et al. 2010). Tenocytes were plated at a density of 1 x 10^4 cells per cm^2 and cultured in standard culture flasks in high glucose Dulbecco's modified Eagle's medium (DMEM, Fisher, Pittsburgh, PA) supplemented with 10% fetal bovine serum (FBS, Invitrogen, Carlsbad, CA), 1% L-glutamine (Invitrogen, Carlsbad, CA), 1% penicillin/streptomycin (Invitrogen, Carlsbad, CA), 1% amphotericin-B (MP Biomedical, Solon,

OH), and 25 µg/mL ascorbic acid (Wako, Richmond, VA) (Kapoor, Caporali et al. 2010). Cells were fed every 3 days and cultured to confluence at 37°C and 5% CO_2. Cells were used at passage 3.

2.3.7.2 Scaffold culture conditions

Cylindrical CG scaffold plugs (8 mm diameter, ~5 mm thickness) were cut from the middle section of full length 15 mm scaffolds and were placed in ultra-low attachment 6-well plates (Corning Life Sciences, Lowell, MA). Confluent tenocytes were trypsinized and resuspended at a concentration of 5 x 10^5 cells per 20 µL media. Scaffolds were seeded with tenocytes using a previously validated method (Freyman, Yannas et al. 2001; O'Brien, Harley et al. 2005). 10 µL of cell suspension (2.5 x 10^5 cells) was added to each scaffold. The scaffolds were then incubated at 37°C for 15 min, turned over, and seeded with an additional 10 µL of cell suspension for a total of 5 x 10^5 cells seeded per scaffold. Scaffolds were incubated at 37°C and 5% CO_2 and fed with complete DMEM every 3 days for the duration of all experiments as previously described (Caliari and Harley 2011).

2.3.8 Quantification of cell number

Cell attachment at each time point was assayed via DNA quantification. Scaffolds were washed in PBS to remove unattached and dead cells and then placed in a papain solution at 60°C for 24 h to both digest the scaffold and lyse the cells to expose their DNA. Hoechst 33258 dye (Invitrogen, Carlsbad, CA) was used to fluorescently label double-stranded DNA (Kim, Sah et al. 1988). Fluorescence was read (excitation: 360 nm, emission: 465 nm) via a fluorescent spectrophotometer (Tecan, Switzerland). Experimental readings were compared to a standard

curve created by measuring the fluorescence levels for a range of known cell numbers to calculate cell attachment as a percentage of the total number of seeded cells (Kim, Sah et al. 1988).

2.3.9 Quantification of cell metabolic activity

Tenocyte mitochondrial metabolic activity within each scaffold was determined through a non-destructive alamarBlue® assay. Healthy, viable cells continuously convert the active ingredient in alamarBlue® (resazurin) to a fluorescent byproduct (resorufin), allowing comparison of the gross metabolic activity of each cell-seeded construct. Cell-seeded scaffolds were incubated at 37°C in 1x alamarBlue (Invitrogen, Carlsbad, CA) solution with gentle shaking for 2 h (Tierney, Jaasma et al. 2009). Resorufin fluorescence was measured (excitation: 540 nm, emission: 590 nm) via a fluorescent spectrophotometer (Tecan, Switzerland). Relative cell metabolic activity was determined and reported as a percentage of the total number of seeded cells by interpolating scaffold fluorescence readings within a standard curve (Tierney, Jaasma et al. 2009).

2.3.10 Measurement of cell-mediated scaffold contraction

The diameter of each scaffold disk was measured at days 1, 4, 7, and 14 using standard drafting templates and normalized against scaffold diameter at time 0 to determine cell-mediated scaffold contraction (Spilker, Asano et al. 2001; Caliari and Harley 2011).

2.3.11 Measurement of soluble collagen synthesis

Total soluble collagen synthesized from tenocyte-seeded scaffolds and released into the culture media was measured using a Sircol soluble collagen kit (Biocolor Ltd, UK) (Sahoo, Toh et al.

2010). Total soluble collagen synthesis from days 1-7 and days 8-14 was quantified by pooling media samples from each feeding time point. Media samples were concentrated overnight in polyethylene glycol to isolate collagen. Serum components of the media were separated from the soluble collagen using a 48 h pepsin/acetic acid digest followed by centrifugal filtration (filter size: 100 kDa) (Lareu, Zeugolis et al. 2010). The retentate was recovered and incubated with Sirius Red dye for 30 min under shaking. The dyed collagen pellet was recovered, washed, and resuspended in an alkali solution provided with the kit. Sample absorbance was measured at 555 nm; results were interpolated on standard curve created using bovine collagen stock solution (0.5 mg/mL).

2.3.12 RNA isolation and real-time PCR

RNA was extracted from scaffolds via an RNeasy Plant Mini kit (Qiagen, Valencia, CA) as previously described (Duffy, McFadden et al. 2011). Scaffolds were immersed in lysis solution supplemented with 10 μM β-mercaptoethanol for 5 min on ice. The lysates were processed following the kit instructions to isolate RNA. RNA was reverse transcribed to cDNA in a Bio-Rad S1000 thermal cycler using the QuantiTect Reverse Transcription kit (Qiagen, Valencia, CA). Real-time PCR reactions were performed in triplicate using the QuantiTect SYBR Green PCR (Qiagen, Valencia, CA) kit and 10 ng of cDNA per reaction in an Applied Biosystems 7900HT Fast Real-Time PCR System (Carlsbad, CA). All primer sequences were derived from literature and gene specificity was confirmed using BLAST searches (Garvican, Vaughan-Thomas et al. 2008; Taylor, Vaughan-Thomas et al. 2009). Primers were synthesized by Integrated DNA Technologies (Coralville, IA). Expression of the following markers was quantified: collagen type I alpha 2 (COL1A2), collagen type III alpha I (COL3A1), cartilage

oligomeric matrix protein (COMP), decorin (DCN), scleraxis (SCX), tenascin-C (TNC), and matrix metalloproteinases 1, 3, and 13 (MMP1, MMP3, MMP13). Glyceraldehyde 3-phosphate dehydrogenase (GAPDH) was used as a housekeeping gene. Data was analyzed using Sequence Detection Systems software v2.4 (Applied Biosystems, Carlsbad, CA) Results were generated using the delta-delta Ct method and all results were expressed as fold changes normalized to the expression levels of tenocytes at day 0 in 2D culture prior to seeding on scaffolds.

2.3.13 Histology and immunohistochemistry

Scaffold specimens were retrieved at days 7 and 14 of culture and then fixed in 10% neutral buffered formalin for histological analysis. Two scaffolds per experimental group were embedded in paraffin and sequentially sliced (one through the longitudinal plane, one through the transverse plane per group) into 5 μm thick sections. Sections were stained with hematoxylin and eosin (H&E) to allow visualization of cells (purple) and scaffold struts (pink).

2.3.14 Quantitative assessment of scaffold strut and cell alignment

Scaffold pore alignment as well as alignment of tenocytes within scaffolds was determined with the OrientationJ plugin for Image J using previously described methods (Fonck, Feigl et al. 2009; Caliari and Harley 2011). Scaffold strut alignment was measured from SEM images using the Distribution function within OrientationJ; 30x images taken in the longitudinal and transverse planes of bottom, middle, and top regions of the scaffold were analyzed for each relative density (three scaffolds, nine total images for each plane). Cell alignment within the scaffolds after 7 and 14 days in culture was measured from 10x images of H&E stained histology sections (Caliari and Harley 2011). The orientation angles of 450 cells from nine distinct scaffold regions per

scaffold variant were quantified for each sample using the Measure function. Strut and cell alignment at each time point was reported as a histogram of orientation angles (-90° – +90°) with bin intervals of 10° for specimens taken from the longitudinal planes (with 0° corresponding to the direction of alignment in longitudinal sections).

2.3.15 Statistical analysis

One-way analysis of variance (ANOVA) was performed on pore size and shape data while two-way ANOVAs were applied to cell metabolic activity, cell number, scaffold diameter, soluble collagen, and gene expression data sets followed by Tukey-HSD post-hoc tests. Significance was set at $p < 0.05$. At least n = 11 scaffolds were analyzed at each time point for cell metabolic activity and scaffold diameter while n = 6 scaffolds were digested and assayed at each time point for cell number. Pore size and shape analysis was performed on transverse (n = 3) and longitudinal (n = 3) scaffold sections. Gene expression was analyzed for n = 3 scaffolds at each time point. Error was reported in figures as the standard error of the mean unless otherwise noted.

2.4 Results

2.4.1 Pore size and shape analysis

Qualitative SEM and quantitative analysis of pore anisotropy showed that scaffolds with aligned, ellipsoidal pores could be fabricated for all three scaffold relative densities. Together, these results show that overall pore alignment was not influenced by relative density (**Figure 2.1**). Mean transverse pore sizes as well as longitudinal and transverse pore aspect ratios were

calculated for each scaffold variant (**Table 2.1**). The 1x scaffold showed a significantly larger pore size compared to the 2x and 3x scaffolds ($p < 0.01$). However, each scaffold variant exhibited significant anisotropy, with significantly greater pore aspect ratio in the longitudinal plane compared to the transverse plane ($p < 0.002$). Furthermore, there were no significant differences in pore size or aspect ratio along the length of the scaffold (top, middle, bottom sections) for any of the scaffold variants ($p > 0.05$).

2.4.2 Permeability of anisotropic CG scaffolds

Scaffold permeability was analyzed under three degrees of compressive strain levels (0%, 65%, and 78%), revealing a significant influence ($p < 0.0001$) of scaffold relative density and applied strain on permeability (**Figure 2.2**). While all three scaffold variants showed similar permeability at 0% applied strain, the scaffold permeability at each relative density was significantly lower under 65% and 78% strain ($p < 0.008$) with permeability trending downwards as relative density increased.

2.4.3 Mechanical characterization of anisotropic CG scaffolds

Characterization of scaffold mechanical properties in tension (elastic modulus, ultimate tensile strength) and compression (elastic modulus, yield strength) revealed a significant influence ($p < 0.0001$) of scaffold relative density on compressive and tensile mechanical behavior (**Figure 2.3**). In all cases mechanical metrics increased significantly ($p < 0.009$) with relative density with the exception of the increase in elastic compressive strength between 1x and 2x scaffold groups, where the difference was not quite significant ($p = 0.14$).

2.4.4 Tenocyte viability and collagen synthesis in anisotropic CG scaffolds

Tenocyte culture revealed a significant influence ($p < 0.0003$) of scaffold relative density on functional metrics of tenocyte bioactivity: proliferation, metabolic activity, contractile capacity, and soluble collagen synthesis (**Figure 2.4**). For all time points the 2x and 3x scaffolds groups supported a significantly increased number of tenocytes ($p < 0.002$) (**Figure 2.4(a)**) and higher tenocyte metabolic activity ($p < 0.002$) (**Figure 2.4(b)**) compared to the 1x scaffold group. Tenocyte number significantly increased for all groups from day 1 to 4 ($p < 0.002$). However, tenocyte number plateaued for the 1x group between days 4 and 7 ($p = 0.93$) and significantly decreased from day 7 to day 14 ($p = 0.001$). Tenocyte number for the 2x and 3x groups significantly increased between days 4 and 7 ($p < 0.002$). While tenocyte number plateaued for the 2x group between days 7 and 14 ($p = 0.90$), the 3x group showed a significant increase ($p < 0.003$). The 2x and 3x groups showed statistically significant differences in tenocyte number at days 4 and 14 ($p < 0.05$). Additionally, the 2x group displayed significantly higher tenocyte metabolic activity than the 3x group at early time points (days 1 and 4, $p < 0.001$), but there were no significant differences between the groups at day 7 or 14.

Soluble collagen production over the first week was significantly higher in the 2x group than the other two experimental groups ($p < 0.002$) (**Figure 2.4(c)**). However, the 3x group synthesized a significantly greater amount of soluble collagen over the second week of the experiment compared to the 1x group ($p = 0.02$). Fibroblasts are known to have the potential to induce significant contraction of CG scaffolds (Freyman 2001; Harley, Freyman et al. 2007). Scaffold contraction results show that the 1x group had significant contraction as early as day 4 with a significantly lower normalized scaffold diameter than both the 2x and 3x groups at day 4, 7, and

14 ($p < 0.0001$) (**Figure 2.4(d)**). Additionally, the 2x group contracted moderately over the course of the experiment with significant differences between the 3x group at days 4, 7, and 14 ($p < 0.002$).

2.4.5 Tenocyte gene expression within anisotropic CG scaffolds

As tenocytes are known to de-differentiate with 2D culture (Zhu, Li et al. 2010), expression of COL1A2, COL3A1, COMP, DCN, SCX, TNC, MMP1, MMP3, and MMP13 genes was evaluated after 1, 4, 7 and 14 days in culture (**Figures 2.5-2.7**). Results were expressed as fold changes relative to the expression levels of the tenocytes cultured in standard 2D flasks at day 0 prior to scaffold seeding (dashed lines). Significantly increased expression of COL3A1, SCX, TNC, MMP1, MMP3, and MMP13 was observed in 3D scaffolds at day 1 compared to the 2D day 0 results.

2.4.5.1. Structural protein gene expression

COL1A2, COL3A1, COMP, and DCN were expressed at similar levels ($p > 0.05$) for all three scaffold variants at day 1 (**Figure 2.5**). Expression levels generally increased from day 1 to day 4 with the 1x scaffolds showing significantly higher expression of COL3A1 and DCN compared to the other two groups ($p < 0.04$). After day 7 the 1x group had significantly higher COL3A1 expression than the 3x group ($p = 0.04$). By day 14 the 1x and 2x groups showed significant down-regulation from day 7 of COL1A2 and COMP ($p < 0.04$) while there were no significant changes in the 3x group ($p > 0.05$). Overall, while significant increases in structural gene expression was almost ubiquitously observed in the anisotropic scaffolds relative to 2D culture during the first week, and significant differences in gene expression were observed between

several scaffold groups and times, no significant across-the board trends in structural protein gene expression were observed with scaffold relative density with the exception of COMP.

2.4.5.2. Tendon phenotype gene expression

Significant differences ($p < 0.02$) and trends in tendon phenotype gene expression profiles were found with culture time, both relative to 2D culture controls and between scaffold relative densities. Scleraxis (SCX), a transcription factor expressed by healthy tenocytes (Kuo and Tuan 2008; Taylor, Vaughan-Thomas et al. 2009), expression was already significantly elevated at day 1 in all anisotropic scaffolds relative to 2D control cultures ($p < 0.0003$), suggesting a return to tenocyte-specific gene expression after 2D culture (**Figure 2.6(a)**). Over the course of the two week culture period the 1x and 2x groups displayed significant ($p < 0.03$) down-regulation of SCX to the level of 2D control cultures while expression levels in the 3x group remained significantly elevated. Further, loss of SCX expression appeared to be temporally modulated, with increases in scaffold relative density significantly ($p < 0.05$) slowing the loss of SCX expression. Similarly, tenascin-C (TNC), an extracellular matrix glycoprotein associated with bioactive tenocytes (Jarvinen, Jozsa et al. 2003; Doroski, Levenston et al. 2010), expression was significantly influenced by scaffold relative density and culture time ($p < 0.02$) (**Figure 2.6(b)**). After day 1, TNC gene expression increased significantly ($p = 0.007$) in the 3x scaffolds relative to the 1x scaffolds which showed no significant increase in gene expression with culture time, although TNC expression remained significantly elevated compared to the 2D control for all time points. By day 14 there was a direct relation between relative density and expression levels of both SCX and TNC, with significantly increases in expression of both transcripts in the 3x group compared to the 1x and 2x groups ($p < 0.05$).

2.4.5.3. MMP gene expression

Significant differences ($p < 0.003$) and suggestive trends were observed for MMP1, MMP3, MMP13 gene expression with anisotropic scaffold culture, both relative to 2D culture controls and between scaffold relative densities. Healthy tendons typically express lower levels of MMP1 and MMP13 as well as higher levels of MMP3 compared to diseased and/or injured tendons (Gotoh, Hamada et al. 1997; Lo, Marchuk et al. 2004; Jones, Corps et al. 2006; Clegg, Strassburg et al. 2007). There were no significant differences between the groups in MMP1 levels at day 1 ($p > 0.05$) (**Figure 2.7(a)**), but MMP1 expression steadily increased in the 1x and 2x groups over the course of the experiment and by day 14 there was an inverse relationship between relative density and MMP1 expression level with the 3x group significantly down-regulated compared to the 1x/2x groups ($p < 0.0001$). MMP3 levels were initially higher in the 2x/3x groups compared to the 1x group at day 1 ($p < 0.03$) (**Figure 2.7(b)**). This trend was also observed at day 14. While there were no significant differences in MMP13 expression between the groups on day 1 ($p > 0.05$), by day 4 and continuing through the remainder of the culture period MMP13 expression was inversely correlated with scaffold relative density, with the highest relative density (2x and 3x) anisotropic scaffolds showing significantly reduced MMP13 gene expression compared to the 1x group at days 7 and 14 ($p < 0.03$) (**Figure 2.7(c)**).

2.4.6 Tenocyte distribution within scaffolds

Day 14 histology sections from the transverse sections of the scaffolds demonstrated differences in cell infiltration and the maintenance of an open pore structure. Pores in the 1x scaffold appeared significantly smaller and the scaffold appeared significantly denser overall than the 2x

and 3x samples (**Figure 2.8(a-c)**), likely a consequence of the significantly increased scaffold contraction in the initially lower density scaffolds. Additionally, the 1x group showed aggregations of tenocytes on the scaffold outer edge while cells were more equally distributed in the higher density scaffolds (**Figure 2.8(a-c)**).

2.4.7 Tenocyte alignment within anisotropic CG scaffolds

Longitudinal H&E sections from days 7 and 14 were analyzed to determine tenocyte orientation within the scaffolds. At day 7, tenocytes in all three groups trended towards alignment in the direction of heat transfer and pore anisotropy (0°) (**Figure 2.8(d)**). While all groups showed longitudinally aligned cells, tenocytes in the 3x scaffold were significantly more likely to be aligned (between -10° and +10°) compared to the 1x and 2x groups at day 7 ($p < 0.02$). By day 14 of culture tenocytes in the 2x and 3x groups remained preferentially aligned while the tenocytes in the 1x scaffold displayed no alignment preference (random distribution of cell orientation angles) (**Figure 2.8(e)**). Here, tenocytes in the 2x and 3x groups were significantly more longitudinally aligned than the 1x group at day 14 ($p < 0.02$).

2.5 Discussion

This chapter describes the fabrication and functional analysis of a homologous series of anisotropic CG scaffolds with three different relative densities (1x: $\rho^*/\rho_s = 0.0051$, 2x: $\rho^*/\rho_s = 0.0109$, 3x: $\rho^*/\rho_s = 0.0156$). Differential effects of relative density on scaffold microstructure (pore size and shape), permeability, and mechanics were observed that trended with cellular solids theory. Comparing the expression of tendon ECM proteins, transcription factors, and

MMPs reveals direct relationships between CG scaffold relative density, mechanical and microstructural integrity during long-term culture (*i.e.*, preservation of an aligned scaffold microstructure), and subsequent maintenance of a healthy tendon-like cell phenotype.

Scaffold microstructure was evaluated qualitatively via SEM and quantitatively using OrientationJ (Image J) to measure pore alignment as well as via standard stereology approaches to quantify scaffold mean pore size and pore aspect ratio. SEM and OrientationJ analyses indicated that all three scaffold variants showed significant pore anisotropy with no effect of relative density on the degree of anisotropy (**Figure 2.1**). The 1x scaffold did have significantly larger pores than the 2x/3x scaffolds, a trend seen previously in other types of CG scaffolds (Kanungo and Gibson 2010) (**Table 2.1**), but all scaffolds had pore sizes approximately double that of primary equine tenocytes (order 100 – 125 μm) (Caliari and Harley 2011). Additionally, while all scaffold variants showed ellipsoidal pores, the 3x scaffold had a smaller pore aspect ratio in the longitudinal plane (1.55:1 vs. 1.72:1, 1.76:1) compared to the 1x/2x scaffolds. Smaller pore sizes and pore aspect ratios for the more dense scaffolds may be due to the increased viscosity of the denser suspension, resulting in reduced ice crystal aggregation and elongation during the freezing process. However all variants showed highly aligned contact guidance cues, as quantified via strut orientation angles (**Figure 2.1(b)**).

Scaffold permeability and mechanics were also evaluated as a function of relative density, with significant decreases in scaffold permeability observed with degree of compressive loading and relative density. Cellular solids modeling approaches provide a theoretical framework to consider the observed changes in mechanical and microstructural properties of CG scaffolds by describing

them as low-density open-cell foams (O'Brien, Harley et al. 2005; Harley, Freyman et al. 2007; Harley, Leung et al. 2007; O'Brien, Harley et al. 2007; Harley, Kim et al. 2008; Murphy, Haugh et al. 2010). Scaffold permeability is a critical scaffold parameter that dictates the diffusion and exchange of soluble factors, nutrients, and waste throughout the scaffold (Prendergast, Huiskes et al. 1997; Agrawal, McKinney et al. 2000). CG scaffold permeability has previously been shown experimentally to change significantly as a function of scaffold pore size (d), applied strain (ε), and relative density (ρ^*/ρ_s) (O'Brien, Harley et al. 2007). Further, a cellular solids model has been validated to describe the magnitude of these effects, showing that CG scaffold permeability increases proportionally with d^2 but decreases with $(1-\varepsilon)^2$ and $(1-\rho^*/\rho_s)^{3/2}$ (O'Brien, Harley et al. 2007). Although the permeabilities of the three constructs tested were found to be similar at 0% strain, the combined effects of pore size, relative density, and applied strain are evident at higher strain levels where there is a clear inverse relationship between scaffold relative density and permeability that closely matches predictions of the previously described cellular solids model (**Figure 2.2**). It is likely that the lack of observed differences in scaffold permeability at 0% applied strain was primarily influenced by the relatively small difference in the pore size term (d^2, where d = 230 – 290 μm) and relatively small difference in the scaffold porosity $(1-\rho^*/\rho_s)^{3/2}$ term (0.984 – 0.995). At significantly higher applied strains (0.65, 0.78), all scaffolds are a majority of the way through the collapse plateau region of the stress-strain curve (Harley, Leung et al. 2007); here scaffold densification is significant, making it possible to resolve differences in scaffold permeability.

Scaffold mechanical properties at the macro- and microscales have been shown to significantly influence key cell behaviors including adhesion, migration, proliferation, and differentiation as

well as overall construct bioactivity and integrity (Pelham and Wang 1997; Freyman, Yannas et al. 2001; Grinnell, Ho et al. 2003; Engler, Bacakova et al. 2004; Peyton and Putnam 2005; Yeung, Georges et al. 2005; Zaman, Trapani et al. 2006). Mechanical tests were performed on dry, as opposed to hydrated, scaffolds to facilitate sample handling and mounting on the mechanical tester. We have previously shown that hydration and subsequent EDAC crosslinking results in an elastic modulus decrease of approximately an order of magnitude for both isotropic (Harley, Leung et al. 2007) and anisotropic (Caliari, Ramirez et al. 2011) CG scaffolds. For CG scaffolds, modulus and yield strength have previously been shown to increase proportionally with $(\rho^*/\rho_s)^2$ (Harley, Leung et al. 2007; Kanungo and Gibson 2010). Experimentally determined mechanical results, both in tension and compression, follow these trends with observed increases in modulus and yield strength approximately a factor of 4 greater for 2x vs. 1x scaffolds, and over an order of magnitude for 3x vs. 1x scaffolds (**Figure 2.3**). The increase in scaffold modulus at the macroscale (i.e. that measured via compression and tensile tests) is due to an increase in the size, hence flexural rigidity, of the individual struts that make up the scaffold network, not in the modulus of the CG content within each strut (Harley, Freyman et al. 2007; Harley, Leung et al. 2007; Harley, Kim et al. 2008). Previous studies have showed that individual (dermal) fibroblasts could generate sufficient force to buckle single CG scaffold struts and deform the local strut microarchitecture (Freyman 2001; Freyman, Yannas et al. 2001); additionally, careful micromechanical analysis suggested that these fibroblasts could individually generate a mean contractile force of order 20 nN, but that scaffold struts of increased size were able to present sufficient mechanical resistance to prevent cell-mediated contraction and strut buckling (Harley, Freyman et al. 2007). Such results suggested that scaffold relative density may

significantly impact tenocyte contraction and resultant long-term bioactivity and gene expression.

Therefore, to gauge the effect of scaffold relative density on tenocyte bioactivity and specifically contractile capacity, we next examined the behavior of tenocytes in the series of anisotropic CG scaffolds over a 14 day *in vitro* culture period. Critically, significant differences in scaffold contraction were observed, with lower density scaffolds exhibiting significantly greater decreases in scaffold diameter (**Figure 2.4(d)**), correlating to significantly increased cell-mediated contraction. This was not surprising, as it was hypothesized that the higher density scaffolds would present the struts with the largest flexural rigidity ($E_s \cdot I$), hence greatest resistance to cell-mediated contraction. However, with cell-mediated contraction comes significant loss of local microstructural cues (i.e. aligned contact guidance cues from the anisotropic pore microstructure), as was observed in the significant densification of scaffold content seen in histology specimens for the 1x scaffold (**Figure 2.8(a)**). It is interesting to consider the tenocyte bioactivity and gene expression data in the light of not only the initial scaffold microstructure, but also in the context of increased maintenance of anisotropic scaffold microstructural cues with increasing scaffold relative density during long-term culture, and the impact that may have on the kinetics of tenocyte bioactivity and transcriptomic stability. To do this, tenocyte number, metabolic activity, soluble collagen synthesis, and gene expression were all quantified. Initial cell attachment at day 1 was significantly higher in the 2x and 3x groups than the 1x group (**Figure 2.4(a)**); this is consistent with cellular solids predictions stating the increased scaffold specific surface area (proportional to $(\rho^*/\rho_s)^{1/2}$) leads to increased early cell attachment (O'Brien, Harley et al. 2005; Kanungo and Gibson 2010). The 2x and 3x groups had

similar cell numbers through the first week of culture although the 2x group had significantly higher metabolic activity at days 1 and 4 (**Figure 2.4(a-b)**). This may explain why the 2x group produced a significantly higher amount of soluble collagen through the first week of the experiment compared to the other two groups (**Figure 2.4(c)**). During the second week of the experiment the 1x scaffold (and to some extent the 2x scaffold) began to significantly shrink due to contractile forces exerted by attached tenocytes (**Figure 2.4(d)**). This led to significant reductions in cell number for the 1x scaffold and a plateauing of the cell number in the 2x scaffold from day 7 to day 14. In contrast, the mechanically superior 3x scaffold displayed minimal contraction and continual tenocyte proliferation through day 14, resulting in a significantly higher cell number and greater soluble collagen synthesis. Preferential tenocyte cell alignment was lost with scaffold contraction and loss of strut-based aligned contact guidance cues (**Figure 2.8(d-e)**); these results are not surprising given the significant scaffold contraction seen in lower density scaffolds, but presents future avenues for investigation. Notably, it would be interesting to consider whether loss of scaffold anisotropy impacts changes in cell alignment and individual cell aspect ratio (rounded vs. elongated), and whether both or either would be the predominant predictor in loss of tenocyte phenotype within a 3D biomaterial. Such information would have far-reaching significance in the design of future bioactive templates to regenerate tendon injuries.

Transcript levels of the genes COL1A2, COL3A1, COMP, DCN, SCX, TNC, MMP1, MMP3, and MMP13 were evaluated after 1, 4, 7 and 14 days in culture (**Figures 2.5-2.7**). Type I collagen is the primary protein constituent of tendon while type III collagen is highly expressed in immature tendon. COMP and decorin both modulate collagen fibrillogenesis and play key

roles in the fibrocartilagenous region of the tendon-bone interface (Waggett, Ralphs et al. 1998; Yoon and Halper 2005; Halasz, Kassner et al. 2007; Liu, Aschbacher-Smith et al. 2011). Scleraxis is a basic-helix-loop-helix transcription factor that is highly expressed in developing and mature tendon (Kuo and Tuan 2008; Taylor, Vaughan-Thomas et al. 2009). Tenascin-C is a matricellular protein that is associated with normal collagen fibril organization and is up-regulated during mechanical loading (Riley, Harrall et al. 1996; Jarvinen, Jozsa et al. 2003; Doroski, Levenston et al. 2010). Matrix metalloproteinases are critical factors involved in cell migration, wound healing, and remodeling. Recent studies have elucidated that reduced expression of MMP-1 and MMP-13 coupled with elevated expression of MMP-3 is suggestive of a healthy tendon phenotype (Gotoh, Hamada et al. 1997; Lo, Marchuk et al. 2004; Jones, Corps et al. 2006; Clegg, Strassburg et al. 2007).

In our experiments, transcript levels at each time point were normalized against expression levels of tenocytes cultured in standard 2D flasks to determine the influence of an engineered 3D anisotropic microenvironment on the transcriptomic stability of tenocytes. COL1A2, COL3A1, COMP, and DCN were initially expressed at similar levels for all three scaffold types (**Figure 2.5**), although COL3A1 was significantly up-regulated compared to the 2D control. However, from day 7 to day 14 COL1A2 and COMP were down-regulated in the 1x and 2x groups, but not the 3x group. At day 14 although there were no significant differences in COL1A2 or COL3A1 expression, the 3x group had significantly higher COMP expression (4-fold) but significantly lower DCN expression. The expression of critical healthy tenocyte markers SCX and TNC was significantly up-regulated at day 1 compared to the 2D control, possibly due to the anisotropic contact guidance cues provided by all 3D scaffold variants (**Figure 2.6**), though ongoing

experiments are more specifically exploring this behavior. Similarly to the structural protein gene expression data, expression of SCX was about the same for all three experimental groups at day 1. However, there was a steady decrease in SCX expression for the less dense scaffolds over the course of the two week experiment that correlated to increasing scaffold contraction and loss of anisotropic microstructural cues that resulted in reduced cell anisotropy (**Figure 2.8(d-e)**). SCX levels remained relatively constant throughout the two week culture period for the 3x scaffold group and by day 14 SCX was up-regulated 15-fold in the 3x scaffold compared to the 1x scaffold. TNC expression levels, like with SCX, showed a direct relationship with relative density by day 14. Finally, the expression of MMP1, MMP3, and MMP13 was measured (**Figure 2.7**). All three transcripts were initially up-regulated compared to the 2D control. At day 4, the 1x scaffold had higher expression of all three genes compared to the other groups, although by day 14 it had lower MMP3 expression than the 2x/3x groups. The higher levels of MMP1 and MMP13 for the 1x group were maintained through the end of the experiment. Together, these results suggest that scaffold relative density not only had significant importance in regulating traditional measures of tenocyte bioactivity (attachment, proliferation, metabolic activity, collagen synthesis), but that the degree of anisotropy within a 3D biomaterial microenvironment plays a significant role in regulating the transcriptomic stability of tenocytes. Scaffold anisotropy may in fact play a significant role in a variety of other tissue engineering applications where the native tissue exhibits a significant degree of microstructural alignment; additionally, the orientation dependent microstructural and mechanical cues available to individual cells within an anisotropic scaffold structure may also have significant importance in regulating stem cell differentiation processes for those same tissues.

2.6 Conclusions

This work describes the evaluation of scaffold microstructure and mechanics as well as tenocyte viability and gene expression profiles for a homologous series of anisotropic CG scaffolds with variable relative density. SEM and stereology showed that aligned scaffolds with elongated pores and a consistent degree of anisotropy could be fabricated independent of relative density. Scaffold permeability and mechanics, both in tension and compression, demonstrated dependence on relative density with 3x scaffold mechanical properties increasing by over an order of magnitude compared to 1x scaffolds, consistent with predictions made via cellular solids modeling. Equine tenocytes showed increased proliferation, metabolic activity, soluble collagen synthesis, and alignment as well as less cell-mediated scaffold contraction when cultured in higher density scaffolds. The low density 1x scaffolds demonstrated significant contraction that resulted in reduced cell number, loss of microstructural integrity and cell alignment, and loss of tenocyte-specific gene expression profiles over the 14 day culture period. Functional and gene expression analyses also suggested that the highest density anisotropic scaffold maintained a more tendon-like microenvironment that preserves tenocyte transcriptomic stability. Notably, tenocytes in the highest density scaffold displayed marked, significant increases in COMP, TNC, and SCX expression as well as significant decreases in MMP1 and MMP13 expression. This work suggests that scaffold relative density is a critical design parameter, not only for insuring mechanical competence and providing microstructural and mechanical cues at the experiment outset, but also for maintaining essential microstructural cues to direct cell behavior and gene expression over the course of long-term culture.

2.7 Tables

Scaffold	Relative density	Transverse pore size	Pore aspect ratio
1x	0.0051 ± 0.0002	293.1 ± 20.0 μm	Transverse: 1.14± 0.07 Longitudinal: 1.76 ± 0.25
2x	0.0109 ± 0.0003	232.0 ± 14.8 μm	Transverse: 1.16 ± 0.06 Longitudinal: 1.72 ± 0.14
3x	0.0156 ± 0.0009	230.4 ± 36.7 μm	Transverse: 1.15 ± 0.10 Longitudinal: 1.55 ± 0.25

Table 2.1. Mean pore size in the transverse plane as well as pore aspect ratios in the transverse and longitudinal planes for the three anisotropic CG scaffolds (1x, 2x, 3x). Pore aspect ratios in the longitudinal plane were significantly greater ($p < 0.002$) than in the transverse plane for each relative density, indicating that pores are elongated in the direction of the scaffold longitudinal axis. Data expressed as mean ± standard deviation, n = 3.

2.8 Figures

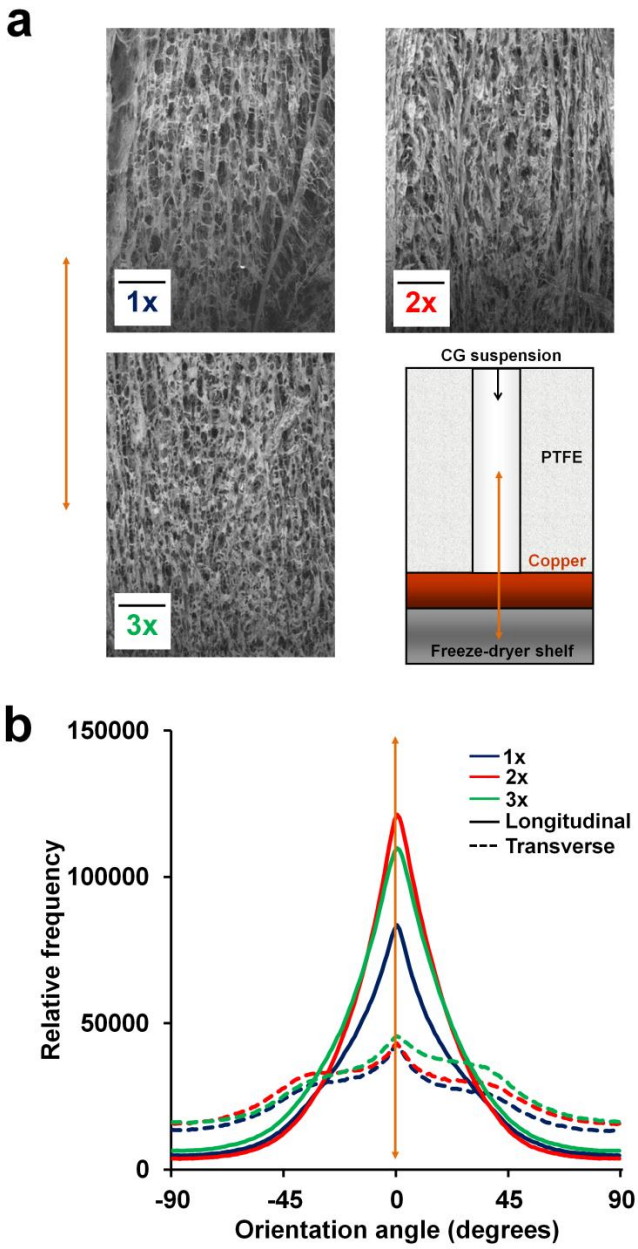

Figure 2.1. Fabrication of anisotropic CG scaffolds via directional solidification. A) SEM images of scaffold microstructure in longitudinal plane. *Top left*: 1x, *Top right*: 2x, and *Bottom left*: 3x scaffold variants. *Bottom right*: schematic of PTFE-copper freeze-drying mold (Caliari and Harley 2011). *Orange arrow:* direction of heat transfer and pore alignment. Scale bars: 500 μm. B) Histogram of scaffold pore alignment angles for the transverse (dotted lines) and longitudinal (solid lines) planes of the anisotropic scaffolds.

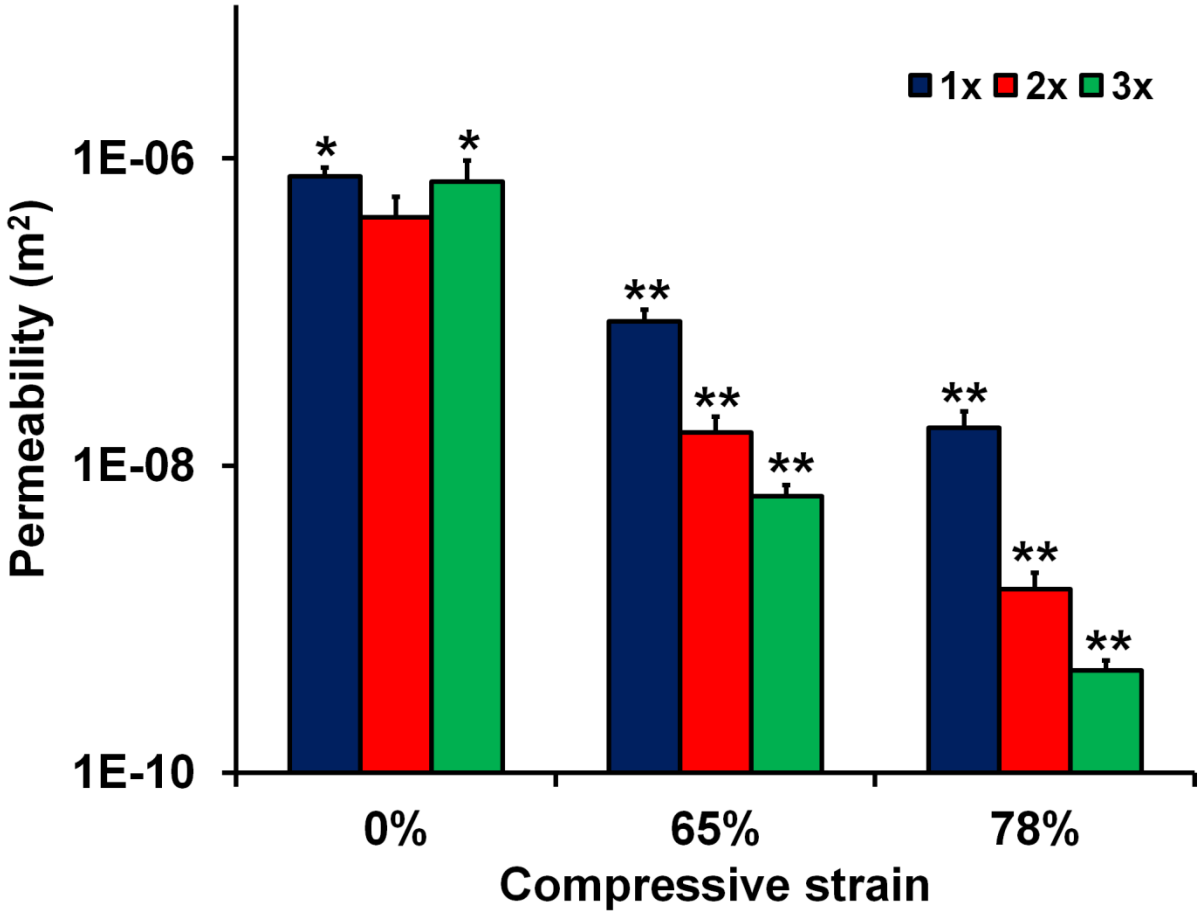

Figure 2.2. Scaffold permeability as a function of relative density and compression. (*) significantly greater than 0% 2x group value, (**) significantly less than the 0% value for given relative density.

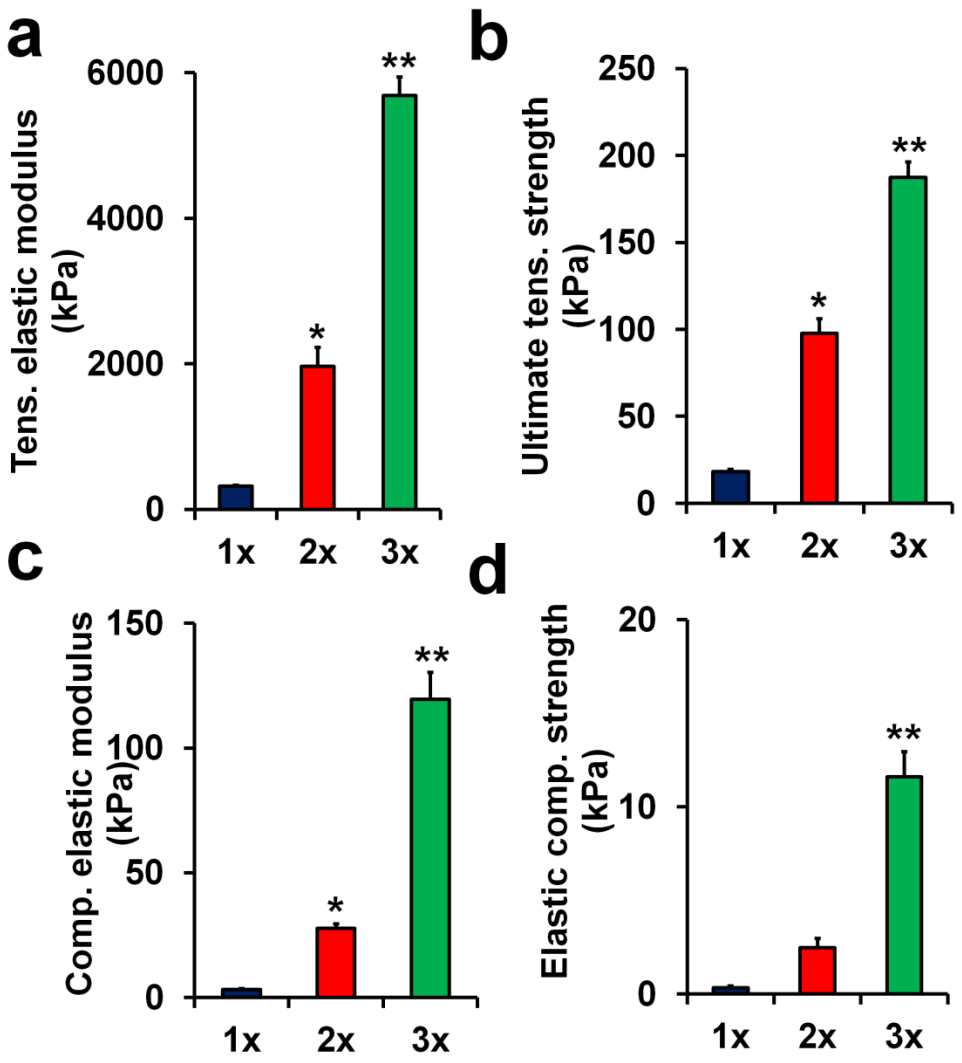

Figure 2.3. Mechanical properties of anisotropic CG scaffolds. A) Tensile elastic modulus, B) ultimate tensile strength, C) compressive elastic modulus, and D) elastic compressive strength in 1x, 2x, and 3x scaffolds. (*) significantly greater than 1x group, (**) significantly greater than 1x and 2x groups. Data expressed as mean ± SEM, n = 6.

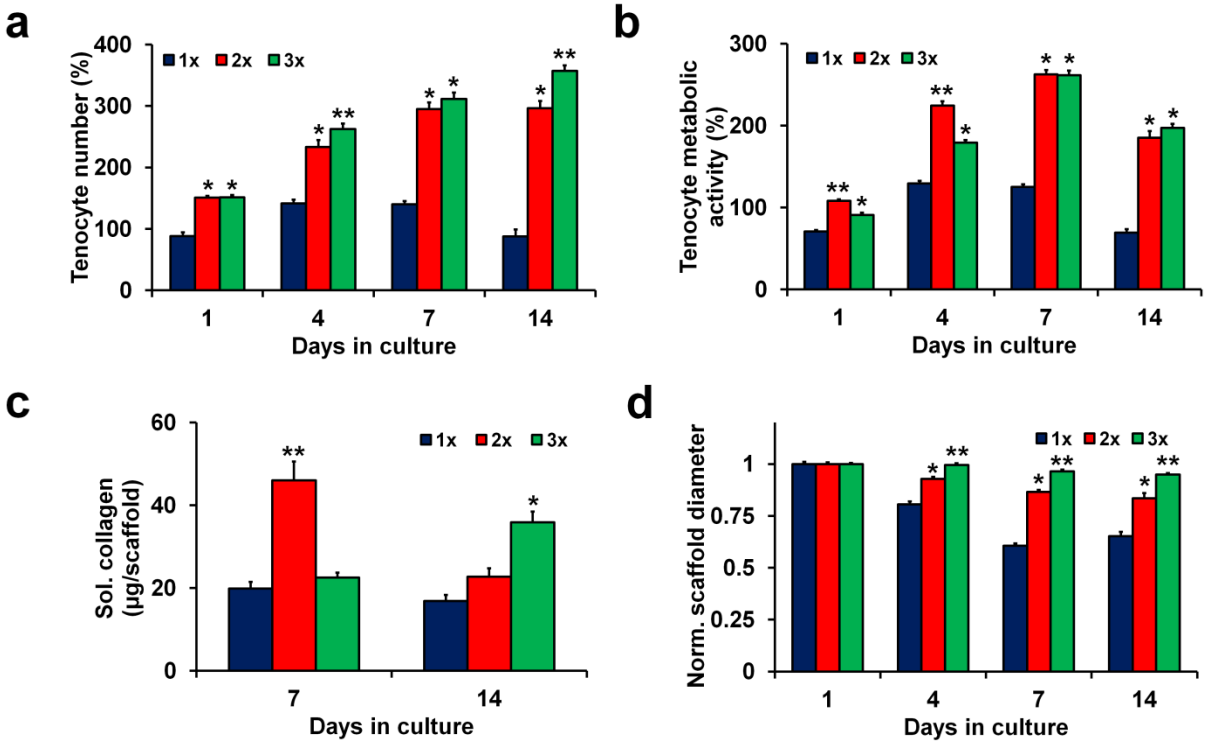

Figure 2.4. Viability, soluble collagen synthesis, and contraction in anisotropic CG scaffolds. A) Tenocyte number, B) tenocyte metabolic activity at 1, 4, 7, and 14 days in 1x, 2x, and 3x scaffold variants. C) Cumulative soluble collagen synthesis through days 1-7 and 8-14 of culture in 1x, 2x, and 3x scaffold variants. D) Scaffold contraction at 1, 4, 7, and 14 days in 1x, 2x, and 3x scaffold groups. (*) significantly greater than 1x group, (**) significantly greater than other two experimental groups. Data expressed as mean ± SEM, n > 3.

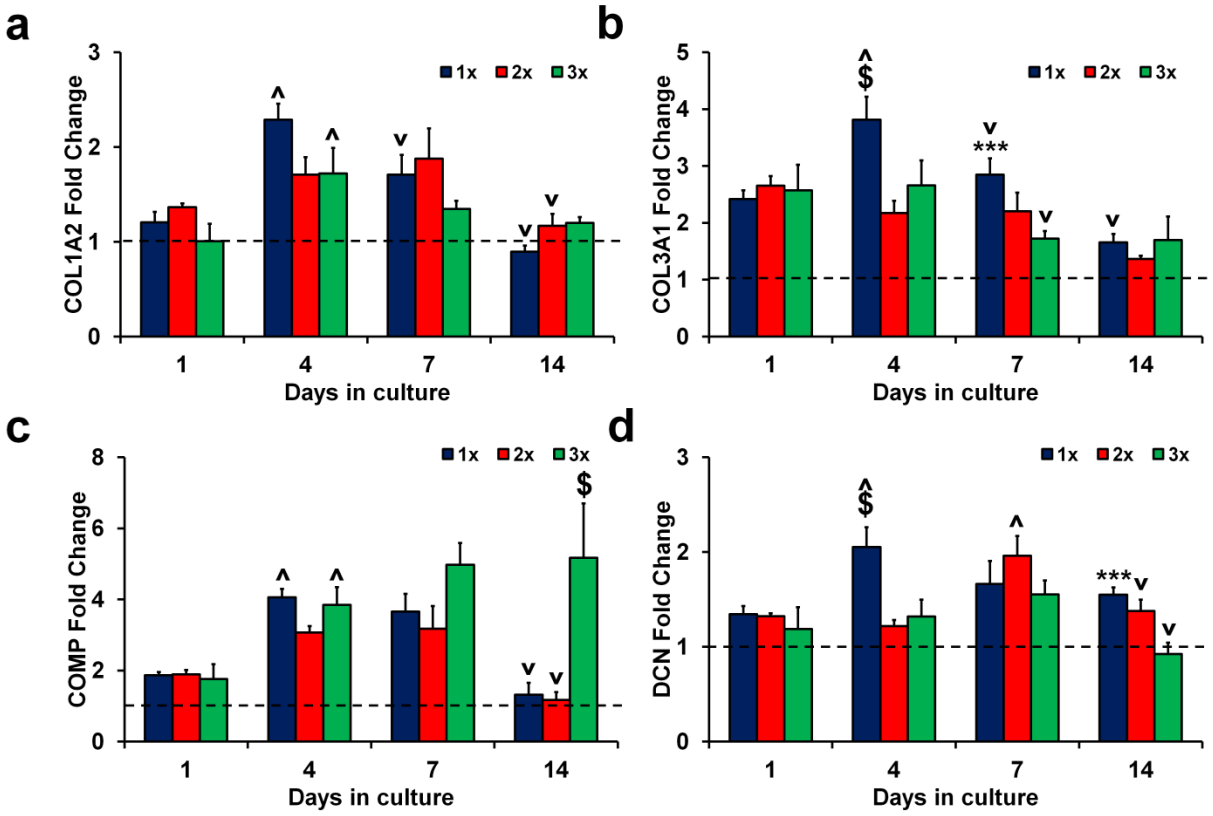

Figure 2.5. Structural protein gene expression in anisotropic CG scaffolds. A) COL1A2, B) COL3A1, C) COMP, and D) DCN expression levels after 1, 4, 7, and 14 days in culture for 1x, 2x, and 3x scaffold variants. Fold changes normalized to transcript levels of tenocytes in 2D culture at day 0 prior to seeding on scaffolds (*dashed line*). (***) significantly greater than 3x group, ($) significantly greater than other two experimental groups, (∧) significantly up-regulated from previous time point, (∨) significantly down-regulated from previous time point. Data expressed as mean ± SEM, n = 3.

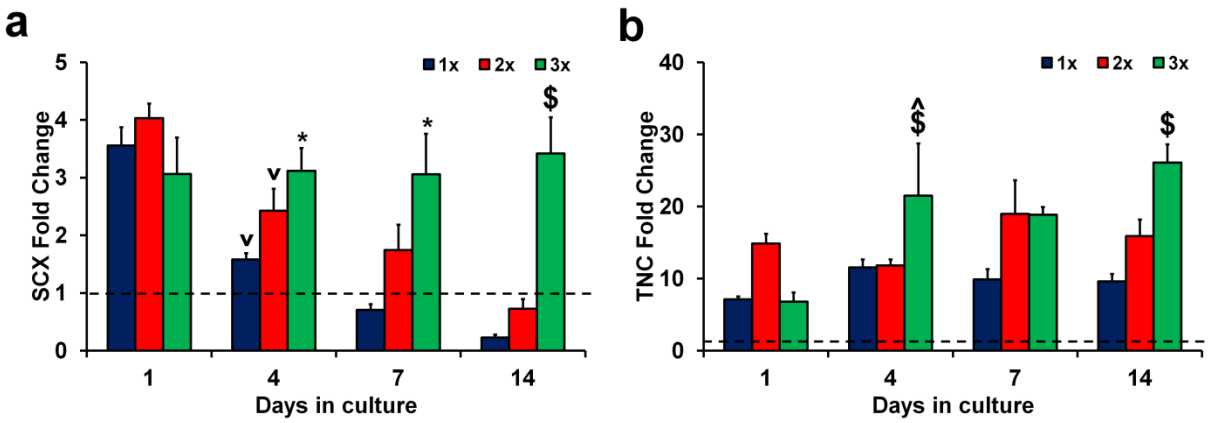

Figure 2.6. Tendon phenotype gene expression in anisotropic CG scaffolds. A) SCX and B) TNC expression levels after 1, 4, 7, and 14 days in culture for 1x, 2x, and 3x scaffold variants. Fold changes normalized to transcript levels of tenocytes in 2D culture at day 0 prior to seeding on scaffolds (*dashed line*). (*) significantly greater than 1x group, ($) significantly greater than other two experimental groups, (∧) significantly up-regulated from previous time point, (∨) significantly down-regulated from previous time point. Data expressed as mean ± SEM, n = 3.

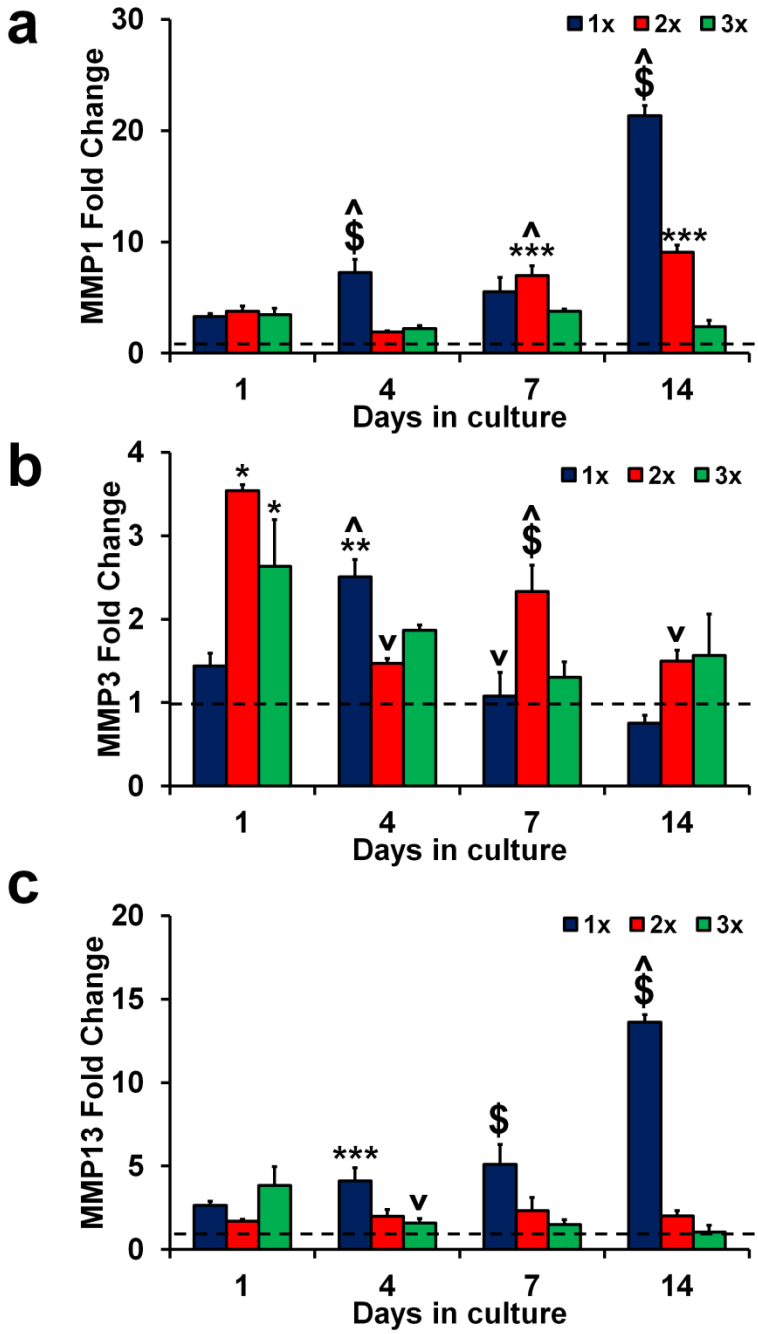

Figure 2.7. MMP gene expression in anisotropic CG scaffolds. A) MMP1, B) MMP3, and C) MMP13 expression levels after 1, 4, 7, and 14 days in culture for 1x, 2x, and 3x scaffold variants. Fold changes normalized to transcript levels of tenocytes in 2D culture at day 0 prior to seeding on scaffolds (*dashed line*). (*) significantly greater than 1x group, (**) significantly greater than 2x group, (***) significantly greater than 3x group, ($) significantly greater than other two experimental groups, (∧) significantly up-regulated from previous time point, (∨) significantly down-regulated from previous time point. Data expressed as mean ± SEM, n = 3.

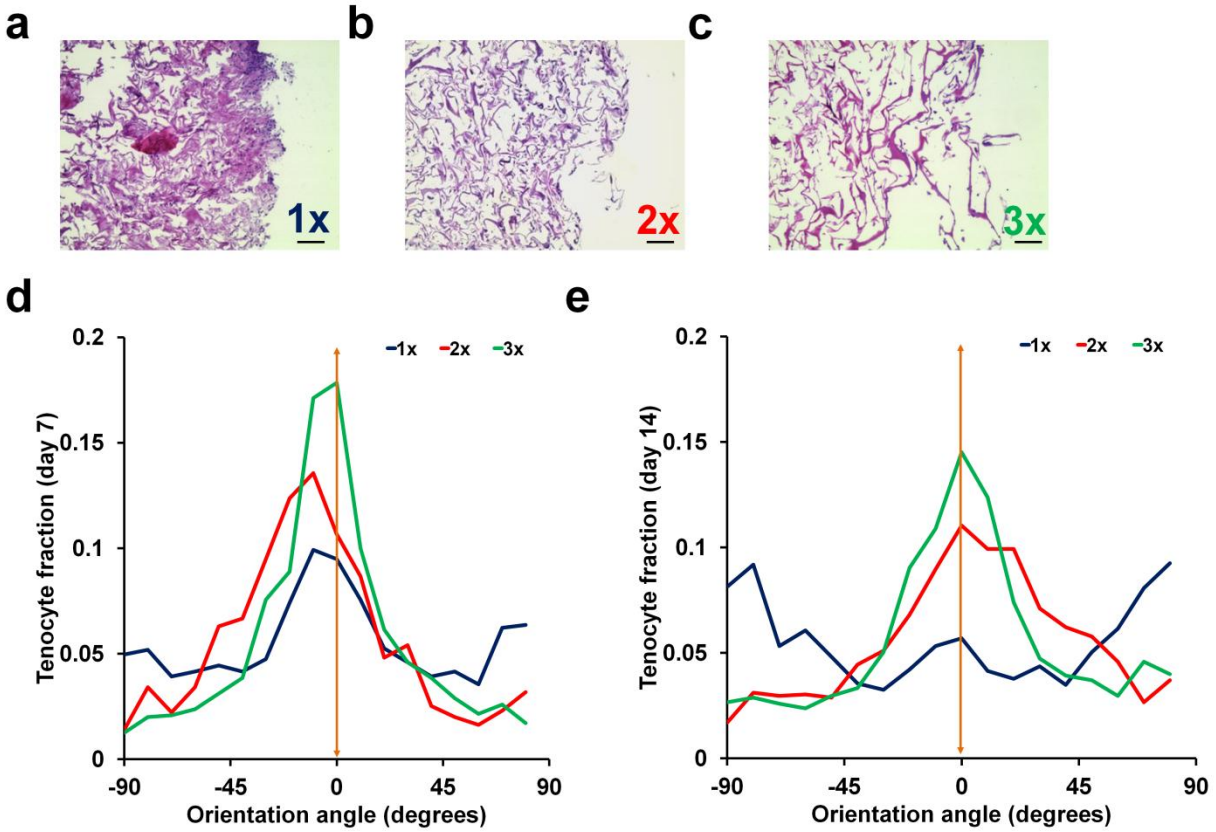

Figure 2.8. Histology and tenocyte alignment. A-C) Day 14 histology sections (transverse plane) for A) 1x, B) 2x, and C) 3x scaffolds. Higher density scaffolds show fewer cell aggregations and better maintenance of an open pore structure. Scale bars: 100 µm. D-E) Frequency plots of tenocyte orientation angles: D) day 7 (longitudinal), E) day 14 (longitudinal). *Orange arrow*: direction of pore alignment.

CHAPTER 3: COMPOSITE GROWTH FACTOR SUPPLEMENTATION STRATEGIES TO ENHANCE TENOCYTE BIOACTIVITY IN ALIGNED COLLAGEN-GAG SCAFFOLDS[3]

3.1 Chapter overview

Biomolecular environments encountered *in vivo* are complex and dynamic, with combinations of biomolecules presented in both freely diffusible (liquid-phase) and sequestered (bound to the extracellular matrix) states. Strategies for integrating multiple biomolecular signals into a biomimetic scaffold provide a platform to simultaneously control multiple cell activities such as motility, proliferation, phenotype, and regenerative potential. Here we describe an investigation elucidating the influence of the dose and mode of presentation (soluble, sequestered) of five biomolecules (SDF-1α, PDGF-BB, IGF-1, bFGF, and GDF-5) on the recruitment, proliferation, collagen synthesis, and genomic stability of equine tenocytes within an anisotropic collagen-GAG scaffold for tendon regeneration applications. Critically, we found single factors led to a dose-dependent trade-off between driving tenocyte proliferation (PDGF-BB, IGF-1) versus maintenance of tenocyte phenotype (GDF-5, bFGF). We identified supplementation schemes using factor pairs (IGF-1, GDF-5) to rescue tenocyte phenotype and gene expression profiles while simultaneously driving proliferation. These results suggest coincident application of multi-biomolecule cocktails has significant value in regenerative medicine applications where control of cell proliferation and phenotype are required. Finally, we demonstrated an immobilization strategy that allows efficient sequestration of bioactive levels of these factors within the scaffold network. We showed sequestration can lead to greater sustained bioactivity than soluble

[3] This chapter has been adapted from the following publication:
Caliari, S. R. and B. A. Harley (2013). "Composite growth factor supplementation strategies to enhance tenocyte bioactivity in aligned collagen-GAG scaffolds." Tissue Eng Part A **19**(9-10): 1100-1112.

supplementation, making this approach particularly amenable to *in vivo* translation where diffusive loss is a concern and continuous biomolecule supplementation is not feasible.

3.2 Introduction

Tendons are highly organized connective tissues composed of a hierarchy of collagen fiber bundles that join muscle to bone. Tendons can be injured through a variety of acute and chronic modes (Butler, Juncosa-Melvin et al. 2008; James, Kesturu et al. 2008; Liu, Ramanath et al. 2008; Xu and Murrell 2008) with some 35 million injuries occurring annually in the United States (Schoen 2005). Of these injuries, severe tendon traumas account for more than 1 million physician visits and 250,000 surgical procedures annually in the United States (Vitale, Vitale et al. 2007). While tendon homeostasis is maintained by fibroblast-like cells called tenocytes interspersed within collagen fibrils, these cells have limited intrinsic regenerative capacity. As a result, tendon defects undergo a repair-mediated wound healing process that results in the formation of a mechanically and histomorphologically inferior extracellular matrix (ECM) (James, Kesturu et al. 2008; Liu, Ramanath et al. 2008; Xu and Murrell 2008). The current clinical gold standard for many types of ligament and tendon repair is an autograft, often taken from the middle section of the patellar ligament or a piece of hamstring tendon. Like all autograft procedures, this approach is not ideal due to the creation of a secondary injury site (Cole, Ginn et al. 2005), necessitating the development of novel treatments to drive functional regeneration.

Biomaterials such as tissue engineering scaffolds may offer a pathway to functional regeneration of tendon injuries including rotator cuff lesions (Gulotta and Rodeo 2011) as well as quadriceps,

patellar, and Achilles tendon ruptures. Collagen-glycosaminoglycan (CG) scaffolds are regulatory compliant ECM analogs that have been applied to a wide range of regenerative medicine applications, both *in vivo* for soft tissue applications such as dermis, peripheral nerves, conjunctiva, brain, and cartilage (Yannas, Lee et al. 1989; Yannas 2001; Harley, Spilker et al. 2004; Huang, Hsu et al. 2012) as well as *in vitro* as 3D templates to probe various cellular activities including adhesion, proliferation, migration, and differentiation (O'Brien, Harley et al. 2005; Farrell, O'Brien et al. 2006; Harley and Gibson 2008; Harley, Kim et al. 2008; Duffy, McFadden et al. 2011). CG scaffolds have also been adapted for a variety of orthopedic applications covering osteochondral, bone, and tendon tissue engineering (Harley, Lynn et al. 2010; Harley, Lynn et al. 2010; Caliari and Harley 2011; Caliari, Ramirez et al. 2011). We have recently demonstrated a directional freeze-drying method to create geometrically anisotropic CG scaffolds with aligned tracks of ellipsoidal pores that mimic elements of native tendon anisotropy (Caliari and Harley 2011). While we showed that platelet-derived growth factor BB (PDGF-BB) and insulin-like growth factor 1 (IGF-1) promoted increased tenocyte proliferation and migration within these anisotropic scaffolds (Caliari and Harley 2011), a major concern remains the trade-off between increased proliferation and retention of tenocyte-associated phenotype (Thomopoulos, Harwood et al. 2005).

Soluble factor supplementation is a widely applied scaffold enhancement strategy and has shown considerable functional value for tendon tissue engineering (Molloy, Wang et al. 2003; Gulotta and Rodeo 2009). PDGF-BB and IGF-1 have previously been shown to promote dose-dependent increases in tenocyte proliferation and collagen synthesis, both individually and in concert (Abrahamsson, Lundborg et al. 1991; Yoshikawa and Abrahamsson 2001; Thomopoulos,

Harwood et al. 2005; Costa, Wu et al. 2006; Caliari and Harley 2011). Additionally, both factors have been noted as chemoattractants of tenocytes (Caliari and Harley 2011) as well as mesenchymal stem cells (MSCs) (Li, Yu et al. 2007; Ozaki, Nishimura et al. 2007; Ponte, Marais et al. 2007). This study aimed to assess the individual and combined effects of a wider range of soluble factors on cell viability, protein synthesis, and gene expression in the context of tendon tissue engineering. While largely unexplored, optimal supplementation strategies should not only support increased cell migration and proliferation, but also matrix protein synthesis and up-regulation of tenocyte phenotypic markers. Along with PDGF-BB and IGF-1 we investigated three additional factors: basic fibroblast growth factor (bFGF), stromal cell-derived factor 1α (SDF-1α), and growth/differentiation factor 5 (GDF-5). The growth factor bFGF has shown the capacity to improve tenocyte proliferation and collagen synthesis (Thomopoulos, Harwood et al. 2005), MSC chemotaxis (Schmidt, Ladage et al. 2006), and the tenogenic differentiation of MSCs both in 2D (Ker, Chu et al. 2011) and 3D (Sahoo, Toh et al. 2010) culture systems. SDF-1α has been implicated as a potent chemoattractant of MSCs during wound healing (Son, Marquez-Curtis et al. 2006; Ponte, Marais et al. 2007), but recently has shown the ability to improve ligament stem cell proliferation and migration (Du, Yang et al. 2012) as well as functional tendon regeneration in a rat Achilles model (Shen, Chen et al. 2010). GDF-5 has been shown to increase both tenocyte and adipose-derived stem cell proliferation and expression of tendon markers (Park, Hogan et al. 2010; James, Kumbar et al. 2011; Keller, Hogan et al. 2011) as well as formation of neo-tendinous tissue in a rat ectopic model (Wolfman, Hattersley et al. 1997). Together these factors have been implicated in tenocyte recruitment, proliferation, and functional action, though their individual (dose-dependent) and combinatorial effects on tenocyte genomic stability and phenotype within an engineered scaffold remain largely unexplored.

Additionally, many growth factors are sequestered, as opposed to freely soluble, in the native ECM (Liu, Chen et al. 2006). Therefore, while important to probe dose effects of soluble factors on cell activity, it is important to consider strategies to immobilize and pattern proteins such as growth factors and other cytokines in order to develop long-term tissue engineering solutions (Shen, Shoichet et al. 2008; Anderson, Chen et al. 2009; Ker, Chu et al. 2011; Martin, Caliari et al. 2011; Oh, Kim et al. 2011). Factor immobilization may offer numerous advantages including improved protein stability and reduced diffusion, increasing localization of the therapeutic effects within the material (Shen, Shoichet et al. 2008).

This chapter describes the evaluation of the effects of five biomolecules (PDGF-BB, IGF-1, bFGF, SDF-1α, GDF-5) on tenocyte chemotaxis, proliferation, soluble collagen synthesis, and gene expression within anisotropic CG scaffolds. While previous studies have evaluated the roles of one or several of these factors, often in 2D culture settings, the comprehensive evaluation of the dose-dependent, combinatorial, and matrix-bound versus soluble effects of these factors on tenocyte phenotype and proliferative potential within a 3D anisotropic scaffold has not been undertaken.

3.3 Materials and methods

3.3.1 CG suspension preparation

A 1.5 w/v% CG suspension was prepared by homogenizing type I microfibrillar collagen from bovine tendon (Sigma-Aldrich, St. Louis, MO) and chondroitin sulfate from shark cartilage

(Sigma-Aldrich, St. Louis, MO) in 0.05 M acetic acid (Yannas, Lee et al. 1989; O'Brien, Harley et al. 2004; Caliari and Harley 2011).

3.3.2 Anisotropic CG scaffold fabrication via freeze-drying

Scaffolds were fabricated via directional solidification as previously described (Caliari and Harley 2011). Briefly, degassed CG suspension was added to a poly(tetrafluoroethylene) (PTFE)-copper mold and placed on a precooled (-10°C) freeze-dryer shelf (VirTis, Gardiner, NY). The CG suspension was frozen at -10°C for 2 h and then sublimated at 0°C and 200 mTorr to remove ice crystals. The thermal conductivity mismatch between copper and PTFE promoted unidirectional heat transfer, resulting in a dry, highly porous CG scaffold with aligned tracks of ellipsoidal pores (Caliari and Harley 2011). The anisotropic scaffold variant used throughout these studies was previously shown to support high tenocyte bioactivity while resisting tenocyte-mediated contraction (Caliari and Harley 2011; Caliari, Weisgerber et al. 2012).

3.3.3 Scaffold crosslinking

Dry scaffolds were dehydrothermally crosslinked at 105°C for 24 h under vacuum (< 25 torr) in a vacuum oven (Welch, Niles, IL) following lyophilization. Chemical crosslinking of scaffolds was achieved using carbodiimide chemistry with a solution of 1-ethyl-3-[3-dimethylaminopropyl] carbodiimide hydrochloride (EDC, Sigma-Aldrich, St. Louis, MO) and *N*-hydroxysulfosuccinimide (NHS, Sigma-Aldrich, St. Louis, MO) at a molar ratio of 5:2:1 EDC:NHS:COOH (Olde Damink, Dijkstra et al. 1996; Harley, Leung et al. 2007) for 1 h at 37°C.

3.3.4 Tenocyte isolation and culture

Equine tenocytes were isolated via collagenase II digestion of superficial digital flexor tendons from horses aged 2-3 years euthanized for reasons not related to tendon injury using a method approved by the University of Illinois IACUC and previously described in significant detail (Kapoor, Caporali et al. 2010). Tenocytes were cultured in high glucose Dulbecco's modified Eagle's medium (DMEM, Fisher, Pittsburgh, PA) as previously described (Kapoor, Caporali et al. 2010). Cells were fed every 3 days and cultured to confluence at 37°C and 5 % CO_2. Cells were used at passage 4.

3.3.5 Tenocyte chemotaxis assay

Tenocyte chemotaxis into anisotropic CG scaffolds was analyzed with a modified Transwell membrane experiment (Caliari and Harley 2011). Unseeded scaffolds were placed in 24-well plates underneath polycarbonate Transwell membrane inserts (8 μm pore size, 6.5 mm diameter; Fisher Scientific, Pittsburgh, PA). Scaffolds were cut so that they were in direct contact with the membrane above without being compressed. Serum-free media supplemented with an individual dose of one of the five soluble factors assayed (**Table 3.1**) was placed in the lower chamber with the CG scaffold. 5×10^5 tenocytes were then added to the top side of the Transwell membrane in serum-free, non-supplemented DMEM. Directed tenocyte migration through the membrane and into the scaffold was assayed after 24 h by removing the scaffolds and quantifying the amount of DNA to determine the total number of tenocytes in the scaffold (Caliari and Harley 2011).

3.3.6 Scaffold culture conditions

Geometrically anisotropic CG scaffold cylinders (6.5 mm diameter, ~5 mm thickness) were set in ultra-low attachment 6-well plates (Corning Life Sciences, Lowell, MA) (Caliari and Harley 2011). Confluent tenocytes were trypsinized and resuspended at a concentration of 5 x 10^5 cells per 20 μL media. 10 μL of cell suspension (2.5 x 10^5 cells) was added to each side of the scaffold (5 x 10^5 cells/scaffold) using a previously described static seeding method (Freyman, Yannas et al. 2001). Scaffolds were cultured in serum-free media to eliminate the influence of exogenous serum components with the exception of the positive control (10% FBS). Rat recombinant PDGF-BB and human recombinant SDF-1α were purchased from R&D Systems (Minneapolis, MN). Human recombinant IGF-1, bFGF, and GDF-5 were acquired from ProSpec (Israel). All soluble factors were reconstituted in the manufacturer's recommended solutions then diluted to experimental concentrations (**Table 3.1**) in serum-free media. Soluble factor doses were selected based on the literature (Abrahamsson, Lundborg et al. 1991; Yoshikawa and Abrahamsson 2001; Thomopoulos, Harwood et al. 2005; Costa, Wu et al. 2006; Park, Hogan et al. 2010; James, Kumbar et al. 2011; Keller, Hogan et al. 2011; Du, Yang et al. 2012) and on preliminary screening experiments that assayed at least six dose levels per factor (data not shown). Immobilization experiments were carried out in serum-free, non-supplemented media. Scaffolds were incubated at 37°C and 5% CO_2 and fed every 3 days.

3.3.7 Protein immobilization

Scaffolds used for immobilization studies were crosslinked using the same 5:1 EDC:COOH ratio as before but with the NHS amount increased to a mass ratio of 1:2.5 EDC:NHS to promote more efficient immobilization (Shen, Shoichet et al. 2008). Following 30 min incubation in the crosslinking solution, 10 μL of protein solution was added directly to the top of the scaffold (6.5

mm diameter, ~ 5 mm thickness). Scaffolds were then incubated at 37°C for 15 min and turned over. An additional 10 µL of protein solution was added to the scaffold followed by a 45 min incubation period. All scaffolds were then rinsed twice in PBS under shaking for 1.5 h and stored in fresh PBS at 4°C until use.

Protein immobilization efficiency studies were first performed with a bovine serum albumin Alexa Fluor® 594 conjugate (BSA594, Invitrogen, Carlsbad, CA) and PDGF-BB (R&D Systems, Minneapolis, MN). Scaffolds were digested in papain buffer at 60°C for 2 h to enable direct measurement of protein immobilization levels from scaffold digest solutions. BSA594 immobilization was determined by reading scaffold digest fluorescence (excitation: 560 nm, emission: 635 nm) on a fluorescent spectrophotometer (Tecan, Switzerland) and interpolating the results on a standard curve created with BSA594 that underwent identical thermal and enzymatic treatments (Odedra, Chiu et al. 2011). Additionally, PDGF-BB immobilization was subsequently quantified with an ELISA kit (R&D Systems, Minneapolis, MN).

3.3.8 Mechanical testing

Tensile testing was performed on scaffolds (6 mm diameter, 20 mm gauge length) crosslinked with two different EDC:NHS:COOH ratios (standard 5:2:1 and increased NHS content for protein immobilization) (Caliari, Ramirez et al. 2011). Scaffolds were pulled to failure at a rate of 1 mm min^{-1} using an MTS Insight electromechanical load frame (Eden Prairie, MN). Elastic modulus was calculated from the slope of the stress-strain curve over a strain range of 5-10% (Gibson, Ashby et al. 2010; Caliari, Ramirez et al. 2011). Ultimate tensile strength was determined from the peak stress value on the stress-strain curve.

3.3.9 Tenocyte number quantification

The number of tenocytes in each scaffold specimen was determined using a DNA quantification assay (Caliari and Harley 2011). Scaffolds were rinsed in PBS to remove any dead or unattached cells and then digested in papain buffer solution at 60°C for 24 h. DNA was fluorescently labeled with Hoechst 33258 dye (Invitrogen, Carlsbad, CA) (Kim, Sah et al. 1988). Fluorescence was read (excitation: 360 nm, emission: 465 nm) on a fluorescent spectrophotometer (Tecan, Switzerland).

3.3.10 Tenocyte metabolic activity quantification

The mitochondrial metabolic activity of tenocytes seeded within scaffolds was evaluated via the alamarBlue® assay (Caliari and Harley 2011). Scaffolds were incubated in alamarBlue® solution (Invitrogen, Carlsbad, CA) with gentle shaking for 2 h (Tierney, Jaasma et al. 2009). Viable cells reduce resazurin in the alamarBlue® solution to the fluorescent byproduct resorufin. Resorufin fluorescence was measured (excitation: 540 nm, emission: 580 nm) on a fluorescent spectrophotometer (Tecan, Switzerland).

3.3.11 Tenocyte soluble collagen synthesis quantification

The total amount of soluble collagen synthesized by tenocytes within scaffolds and released into culture media was quantified using the Sircol soluble collagen kit (Biocolor Ltd, UK) (Sahoo, Toh et al. 2010). Total soluble collagen synthesis over the 7 day duration of the culture experiments was measured by pooling media samples from each feeding time point. Collagen was labeled with Sirius Red dye for 30 min under shaking. Solution absorbance was measured at

555 nm; results were interpolated on standard curve created using a 0.5 mg/mL bovine collagen solution.

3.3.12 RNA isolation

Scaffolds were rinsed in PBS to remove dead/unattached cells and then immersed in lysis buffer supplemented with 10 μM β-mercaptoethanol (Sigma-Aldrich, St. Louis, MO) for 5 min on ice. Following lysis, RNA was extracted from scaffolds with an RNeasy Plant Mini kit (Qiagen, Valencia, CA) (Duffy, McFadden et al. 2011). RNA was quantified via spectrophotometry.

3.3.13 Reverse transcription and real-time PCR

Reverse transcription and real-time PCR were performed on tenocytes post-culture using the QuantiTect Reverse Transcription and SYBR Green PCR kits respectively (Qiagen, Valencia, CA) as previously described (Caliari, Weisgerber et al. 2012). RNA was reverse transcribed to cDNA using a Bio-Rad S1000 thermal cycler. Real-time PCR reactions were performed in triplicate with 10 ng of cDNA per reaction in an Applied Biosystems 7900HT Fast Real-Time PCR System (Carlsbad, CA). Expression profiles of the following genes were evaluated: collagen type I alpha 2 (COL1A2), collagen type III alpha I (COL3A1), cartilage oligomeric matrix protein (COMP), decorin (DCN), scleraxis (SCX), and tenascin-C (TNC). Glyceraldehyde 3-phosphate dehydrogenase (GAPDH) was used as a housekeeping gene. Primer sequences were taken from literature (Taylor, Vaughan-Thomas et al. 2009) and synthesized by Integrated DNA Technologies (Coralville, IA). Data was analyzed using Sequence Detection Systems software v2.4 (Applied Biosystems, Carlsbad, CA). Results were generated using the

delta-delta Ct method and all results were expressed as fold changes normalized to the expression levels of tenocytes cultured in non-supplemented control scaffolds.

3.3.14 Statistical analysis

One-way analysis of variance (ANOVA) was performed on tenocyte number, metabolic activity, soluble collagen, and gene expression data sets followed by Tukey-HSD post-hoc tests. Significance was set at $p < 0.05$. Chemotaxis experiments used $n = 6$ scaffolds per group while the 7 day culture experiments used $n = 9$ scaffolds per group. Tenocyte metabolic activity was evaluated for all 9 scaffolds at days 1, 4, and 7. At day 7, $n = 6$ scaffolds were used to evaluate tenocyte number while $n = 3$ scaffolds were applied to gene expression analyses. Soluble collagen synthesis was quantified for $n = 3$ media samples per experimental group. Error is reported in figures as the standard error of the mean unless otherwise noted.

3.4 Results

3.4.1 Tenocyte chemotaxis

Tenocyte chemotaxis towards soluble factor gradients into anisotropic CG scaffolds was evaluated after a 24 h migration period (**Figure 3.1**). PDGF-BB and IGF-1 induced significant increases in tenocyte migration compared to the non-supplemented, serum-free media control for all dose levels ($p < 0.002$). Dose-dependent trends were observed with the higher PDGF-BB doses as well as the highest IGF-1 dose ($p < 0.0007$). While the low dose of bFGF induced a significant increase in tenocyte chemotaxis ($p < 0.0001$), chemotaxis for the higher doses decreased significantly in a dose-dependent manner ($p < 0.001$). No significant differences were

observed between the control group and the SDF-1α/GDF-5 groups except for the medium dose of SDF-1α ($p < 0.05$).

3.4.2 Tenocyte proliferation, metabolic activity, and soluble collagen synthesis

Tenocyte number, metabolic activity, and soluble collagen synthesis were evaluated following a 7 day *in vitro* culture period in media containing the same soluble factors doses as the chemotaxis experiment (**Figure 3.2**). We chose to assess both number and metabolic activity to ensure that tenocytes were proliferating while remaining healthy and active. Tenocyte number and metabolic activity results largely followed the trends established in the chemotaxis results with the PDGF-BB and IGF-1 groups eliciting the greatest response. The PDGF-BB and IGF-1 groups showed dose-dependent significant increases in tenocyte number ($p < 0.0001$) and metabolic activity ($p < 0.0001$) (**Figure 3.2(a-b)**). There were no significant differences in tenocyte number between the negative control and the bFGF, SDF-1α, and GDF-5 groups (**Figure 3.2(a)**). However, the GDF-5 experimental groups showed significantly greater metabolic activity than the negative control ($p < 0.04$) with the high dose group having significantly higher metabolic activity than the other two doses ($p < 0.02$) (**Figure 3.2(b)**).

Cumulative soluble collagen synthesis results over the 7 day culture period showed that PDGF-BB and IGF-1 supplemented groups exhibited the greatest total soluble collagen synthesis (**Figure 3.2(c)**). However these increases were not as pronounced as those observed for the cell number and metabolic activity results, suggesting significantly decreased collagen synthesis on a per cell basis. PDGF-BB and IGF-1 supported significant increases over the control for all dose levels ($p < 0.003$). There was no dose-dependence observed for the PDGF-BB groups, however

the low dose of IGF-1 supported significantly lower collagen synthesis than the medium and high doses ($p < 0.0003$). No significant differences were observed between the control and the bFGF, SDF-1α, and GDF-5 groups.

3.4.3 Structural protein gene expression

The expression levels of tendon associated structural protein genes COL1A2, COL3A1, COMP, and DCN were evaluated at the end of the 7 day culture time (**Figure 3.3**). COL1A2 expression was significantly decreased in a dose-dependent manner with PDGF-BB supplementation ($p < 0.03$) while expression in the IGF-1 groups was significantly up-regulated ($p < 0.0001$) (**Figure 3.3(a)**). Expression in the higher doses of bFGF were significantly down-regulated ($p < 0.006$) while the high dose for both the SDF-1α and GDF-5 groups was significantly higher than their respective lower doses ($p < 0.03$).

COL3A1 expression profiles followed similar trends to COL1A2 (**Figure 3.3(b)**). PDGF-BB exhibited dose-dependent down-regulation ($p < 0.0001$) while the low and medium IGF-1 groups were significantly up-regulated ($p < 0.02$) with peak levels at the medium dose. Down-regulation was observed for all three bFGF groups ($p < 0.05$) with the medium and high doses displaying significantly lower expression than the low dose ($p < 0.002$). As with COL1A2, the highest expression levels for the SDF-1α and GDF-5 groups were achieved for the high dose.

COMP expression decreased in a dose-dependent fashion for all soluble factors tested except GDF-5 (**Figure 3.3(c)**). In the case of PDGF-BB, COMP was drastically down-regulated (~10,

100, and 250-fold for the low, medium, and high doses respectively). Conversely, COMP expression in the GDF-5 groups increased significantly with dose ($p < 0.05$).

The PDGF-BB supplemented groups again showed dose-dependent down-regulation of the DCN gene ($p < 0.002$). DCN was also down-regulated for all bFGF groups ($p < 0.02$). DCN expression remained relatively unchanged for the IGF-1, SDF-1α, and GDF-5 groups with only the high SDF-1α and low GDF-5 doses showing significant differences compared to the non-supplemented control ($p < 0.02$).

3.4.4 Tendon phenotype gene expression

As with the structural protein genes, PDGF-BB induced dose-dependent down-regulation of SCX ($p < 0.004$) (**Figure 3.4(a)**). SCX expression was up-regulated for all three doses of bFGF ($p < 0.02$) as well as the high dose of GDF-5 ($p < 0.0001$). There were no significant differences between the non-supplemented control and the IGF-1/SDF-1α experimental groups.

TNC expression stayed near the baseline for the PDGF-BB, IGF-1, and SDF-1α groups (**Figure 3.4(b)**). TNC was up-regulated for the bFGF (medium and high doses, $p < 0.0001$) and the GDF-5 (low and high doses, $p < 0.04$) groups. High doses for both bFGF and GDF-5 elicited significantly higher expression of TNC compared to their respective low doses ($p < 0.0001$).

3.4.5 Soluble factor pairs: Tenocyte proliferation, metabolic activity, and soluble collagen synthesis

The synergistic effects of pairing PDGF-BB or IGF-1 with bFGF or GDF-5 were then evaluated over a 7 day culture period in an attempt to simultaneously drive proliferation and phenotypic stability. The medium dose level for all factors was used (PDGF-BB: 50 ng/mL, IGF-1: 50 ng/mL, bFGF: 5 ng/mL) except for GDF-5 (high dose, 500 ng/mL). Tenocyte number after 7 days was significantly greater for all four pairings tested compared to the non-supplemented control ($p < 0.0001$) (**Figure 3.5(a)**). Additionally, the pairings with PDGF-BB had significantly higher cell number than the IGF-1 pairings ($p < 0.004$) with the PDGF-BB/GDF-5 pair showing the greatest tenocyte proliferation of all the groups ($p < 0.0001$). Tenocyte metabolic activity showed similar trends to the cell number results (**Figure 3.5(b)**). All four soluble factor pairings demonstrated significantly greater metabolic activity than the control at all time points (days 1, 4, and 7; $p < 0.0001$). As with cell number, the PDGF-BB groups showed significantly higher metabolic activity than the IGF-1 groups at all points ($p < 0.02$). By day 7, the pairings with GDF-5 had higher metabolic activity than their bFGF counterparts ($p < 0.006$) with the PDGF-BB/GDF-5 pairing eliciting the greatest overall response ($p < 0.0001$).

Soluble collagen synthesis over the course of the 7 day experiment was significantly increased for all four soluble factor pairings compared to the control ($p < 0.003$) (**Figure 3.5(c)**). Despite supporting less proliferation than the PDGF-BB pairings, the IGF-1/GDF-5 pairing induced a significantly greater amount of soluble collagen synthesis than all of the other experimental groups ($p < 0.03$).

3.4.6 Soluble factor pairs: Tenocyte gene expression

Neither bFGF nor GDF-5 was able to rescue tenocyte phenotype when paired with PDGF-BB as expression of COL1A2, COL3A1, COMP, DCN, and TNC was significantly down-regulated ($p < 0.05$) (**Figure 3.6**). Both IGF-1 supplemented groups showed no significant differences with the non-supplemented control for expression of COL1A2, COL3A1, DCN, and TNC. However, the IGF-1/GDF-5 pairing elicited a non-significant increase in COL1A2 expression as well as significant increases in COMP and SCX expression ($p < 0.04$).

3.4.7 Soluble factor immobilization validation

Efficient protein immobilization in the range of ~ 50% was achieved for both BSA594 and PDGF-BB (**Figure 3.7(a-b)**). Consistent immobilization efficiency over the range of tested protein loadings was shown for both proteins ($R^2 > 0.95$). As much as 1 µg of BSA594 could be immobilized per scaffold without any observed detrimental effects on tenocyte proliferation after 7 days in culture ($p > 0.05$). The increased NHS content used during crosslinking for immobilization had minimal effects on scaffold mechanical properties, eliciting a slightly significant decrease in tensile elastic modulus (520.9 ± 106.6 kPa vs. 414.0 ± 66.2 kPa, $p = 0.047$) but a non-significant increase in ultimate tensile strength (52.8 ± 16.4 kPa vs. 55.4 ± 10.2 kPa, $p = 0.588$).

3.4.8 Immobilized factor tenocyte gene expression

The effect of covalently sequestering PDGF-BB, IGF-1, bFGF, or GDF-5 within scaffolds on the expression of tenocyte associated markers COL1A2, COMP, SCX, and TNC was measured after 7 days of culture (**Figure 3.7(c)**). Candidate factors were immobilized at equivalent levels (estimated based on 50% immobilization efficiency as seen with BSA594 and PDGF-BB) to the

medium soluble dose for each factor with the exception of GDF-5 (high dose). The PDGF-BB group showed a significant increase in COL1A2 expression compared to the other experimental groups ($p < 0.02$) while the bFGF elicited significant up-regulation of TNC over all other groups ($p < 0.02$).

We also compared the expression levels of COL1A2, COMP, SCX, and TNC transcripts for immobilized factor pairs (PDGF-BB/bFGF, PDGF-BB/GDF-5, IGF-1/bFGF, IGF-1/GDF-5) following 7 days of culture (**Figure 3.7(d)**). All groups showed significantly down-regulated levels of COMP ($p < 0.02$) and SCX ($p < 0.008$) compared to the control except for IGF-1/GDF-5 SCX expression. However, the IGF-1/GDF-5 group had significantly higher levels of both COMP ($p < 0.03$) and SCX ($p < 0.02$) expression compared to the other immobilized factor pair groups. Groups with bFGF trended towards elevated TNC expression as seen with both soluble and immobilized bFGF alone.

3.4.9 Comparison of equivalent soluble and immobilized PDGF-BB doses

We then evaluated the effect of a single equivalent soluble vs. immobilized PDGF-BB dose (100 ng/mL) on tenocyte metabolic activity (**Figure 3.8**). The soluble group was fed a single dose of PDGF-BB at the beginning of the experiment (replaced with non-supplemented media at day 2) while the immobilized group was fed with non-supplemented media throughout (same total PDGF-BB dose presented over the life of the experiment). Both PDGF-BB groups had significantly higher metabolic activity than the control at all time points ($p < 0.01$). While the soluble group initially had higher metabolic activity at days 1 and 4 (although these differences

were non-significant), by day 7 the immobilized group showed significantly higher metabolic activity than the soluble group ($p = 0.036$).

3.5 Discussion

This work establishes relationships between biomolecule supplementation and functional tenocyte behaviors including proliferation, migration, protein synthesis, and transcript expression in a model anisotropic CG scaffold system for tendon tissue engineering. We hypothesized that the five soluble factors tested would differentially affect metrics of tenocyte bioactivity. Additionally, we hypothesized that combinations of the factors would lead to more optimal tenocyte proliferation, matrix synthesis, and transcriptomic stability, and that insoluble factor presentation would enable a pathway to more efficient *in vivo* translation of these scaffold systems. As others have suggested that tenocyte isolation method may impact proliferation and phenotypic behavior (Wagenhauser, Pietschmann et al. 2012), we used a single isolation method previously established to support retrieval of tenocytes capable of alignment and functional matrix biosynthesis (Kapoor, Caporali et al. 2010).

CG scaffolds have previously been deployed as acellular constructs *in vivo*, offering the potential for accelerated regulatory approval and clinical translation (Yannas, Lee et al. 1989; Harley, Spilker et al. 2004). Therefore, one of our initial design goals was to identify soluble factor agonists of tenocyte chemotaxis in order to increase the speed of cell recruitment into the scaffold. We measured the capacity of each biomolecule (in freely soluble form) to recruit tenocytes to the anisotropic CG scaffolds using a modified Transwell membrane assay (Wynn,

Hart et al. 2004; Ponte, Marais et al. 2007). We had previously shown that PDGF-BB and IGF-1 promoted dose-dependent increases in tenocyte chemotaxis into anisotropic CG scaffolds (Caliari and Harley 2011). For the studies described here we tested a wider range of PDGF-BB and IGF-1 doses in addition to bFGF, SDF-1α, and GDF-5. For this work we used a new anisotropic scaffold variant with a higher relative density (1.5%) than those used earlier with PDGF-BB and IGF-1 (0.5%). This variant was chosen for its ability to prevent significant tenocyte-mediated contraction, along with the resultant loss of tenocyte alignment and down-regulation of tenocyte-specific gene profiles, during long-term culture (Caliari, Weisgerber et al. 2012). However, as they are three times denser than previous scaffolds it is critical to examine strategies to improve tenocyte recruitment as well as subsequent proliferation and metabolic activity and compare the effectiveness of diffusion-mediated biomolecule transport versus sequestered biomolecules for enhancing tenocyte response.

As expected based on our previous results (Caliari and Harley 2011), PDGF-BB and IGF-1 both induced dose-dependent significant increases in tenocyte chemotaxis (**Figure 3.1**) and proliferation (**Figure 3.2(a-b)**). Although some significant differences were observed between certain bFGF, SDF-1α, and GDF-5 groups and the non-supplemented control for these metrics, no overall trends were found. In addition to measures of cell motility and viability it was critical to evaluate functional outputs as they related to soluble factor supplementation. To this end, we evaluated the amount of collagen synthesized by tenocytes and secreted into the culture media over the course of the 7 day experiment (**Figure 3.2(c)**). We assessed soluble collagen synthesis instead of total collagen content in the scaffold in order to more precisely resolve differences between groups (tenocytes produced only μg quantities of collagen over the 7 day culture while

each scaffold specimen had a dry weight of about 3 mg prior to cell seeding). While some of the collagen measured is likely degraded from the original scaffold, all scaffolds were identical with slow degradation kinetics based on the crosslinking density used (Pek, Spector et al. 2004). Additionally, since soluble factor treatment can affect matrix metalloproteinase activity (McCarrel and Fortier 2009) it is possible that this also contributed to the soluble collagen readout, although this needs to be investigated further. Again, the PDGF-BB and IGF-1 groups supported significantly increased collagen synthesis compared to the negative control while the other three groups promoted minimal changes from the baseline. Closer examination of these results revealed some intriguing trends relating tenocyte proliferation and functional phenotype (using collagen synthesis as a proxy). For example, the highest PDGF-BB doses significantly stimulated proliferation, resulting in approximately 15 times the number of cells as the non-supplemented control but only ~2.5 times the amount of soluble collagen synthesized. A similar trend was previously observed for PDGF-BB supplementation of tenocytes in 2D culture, but these results were not investigated further (Thomopoulos, Harwood et al. 2005). We hypothesized that the observed trade-off between tenocyte proliferation and collagen synthesis on a per cell basis may be indicative of greater changes in tenocyte phenotype and pursued in depth analysis of resultant gene expression profiles.

We first looked at the transcript levels of tenocyte-associated structural protein genes for type I collagen (COL1A2), type III collagen (COL3A1), cartilage oligomeric matrix protein (COMP), and decorin (DCN) after 7 days (**Figure 3.3**). While type I collagen constitutes the majority of the protein content of many tissues in the body, including tendon, type III collagen, COMP, and decorin play important roles in maintaining mechanical integrity and directing collagen

fibrillogenesis (Yoon and Halper 2005; Halasz, Kassner et al. 2007; Liu, Aschbacher-Smith et al. 2012). We observed dose-dependent down-regulation of COL1A2, COL3A1, COMP, and DCN for the PDGF-BB groups, supporting the hypothesis that increased tenocyte proliferation leads to a decrease in collagen synthesis on a per cell basis. In contrast, IGF-1 promoted up-regulation of COL1A2 and COL3A1. GDF-5 also up-regulated COMP for all three doses. We next investigated the expression profiles of two phenotypic markers of tenocytes: scleraxis (SCX), a basic-helix-loop-helix transcription factor found both in immature and adult tendon (Kuo and Tuan 2008; Taylor, Vaughan-Thomas et al. 2009), and tenascin-C (TNC), a protein associated with normal collagen fibril organization and expressed in mechanically dynamic regions of tendon (Riley, Harrall et al. 1996; Doroski, Levenston et al. 2010) (**Figure 3.4**). We again found dose-dependent down-regulation with PDGF-BB supplementation. However, we also observed significant up-regulation of both SCX and TNC for the bFGF and GDF-5 groups.

Together, the outcomes of the proliferation, collagen synthesis, and gene expression analyses demonstrate the capacity of soluble factor supplementation to elicit complex phenotypic changes for tenocytes within an anisotropic biomaterial. While PDGF-BB and IGF-1 supported a pro-proliferation phenotype with significantly increased tenocyte chemotaxis, metabolic activity, and number, they also synthesized less collagen on a per cell basis. Critically, PDGF-BB supplementation induced significant and dose-dependent down-regulation of several key tenogenic genes. In contrast, bFGF and GDF-5 had little impact on tenocyte chemotaxis, proliferation, or collagen synthesis but up-regulated tenocyte markers SCX and TNC, indicating a pro-tenocyte phenotype. These results suggested a trade-off between increased proliferation and maintenance of a healthy tenocyte phenotype, so we performed a series of “rescue”

experiments. We hypothesized that pairing either bFGF or GDF-5 with PDGF-BB or IGF-1 would have synergistic effects on measures of tenocyte viability, soluble collagen synthesis, and transcriptomic stability. We chose bioactive levels of all groups (PDGF-BB: 50 ng/mL, IGF-1: 50 ng/mL, bFGF: 5 ng/mL, GDF-5: 500 ng/mL) and examined tenocyte bioactivity after 7 days in culture. For all four pairings tested, tenocyte proliferation, metabolic activity, and soluble collagen synthesis were significantly increased over the non-supplemented control (**Figure 3.5**). Gene expression results revealed that pairing either bFGF or GDF-5 with PDGF-BB was unable to rescue tendon phenotype (**Figure 3.6**). In contrast, the IGF-1/GDF-5 pairing promoted increased expression of COL1A2, COMP, and SCX while also inducing significantly more collagen synthesis than the other groups. These results suggest that it is possible to design supplementation schemes to both drive tenocyte proliferation while maintaining transcriptomic stability.

While soluble supplementation allows us to screen biomolecule dosages, this strategy will likely be less impactful for clinical translation due to short biomolecule half-life *in vivo*, rapid loss of factor via diffusion or internalization, and inability to easily provide additional doses. Inspired by the sequestration of biomolecules within the native ECM (Liu, Chen et al. 2006), we explored immobilizing these factors within the anisotropic CG scaffold to evaluate relative biomolecule bioactivity as a function of presentation modality. Using a carbodiimide crosslinking approach previously described for ubiquitous attachment of multiple biomolecules within biomaterials (Shen, Shoichet et al. 2008; Odedra, Chiu et al. 2011), we showed that efficient factor immobilization could be achieved within the CG scaffold. We determined immobilization efficiency with both a model protein (BSA594) as well as one of our factors of interest (PDGF-

BB), and demonstrated both were immobilized within CG scaffolds with efficiencies of ~ 50% (**Figure 3.7(a-b)**). By increasing the amount of the NHS stabilization agent used during carbodiimide crosslinking we improved the efficiency of immobilization (data not shown) and observed little effect on overall scaffold mechanics.

We explored the ability for scaffold-immobilized factors to drive tenocyte bioactivity in a manner similar to that observed for soluble media supplementation. While there are likely some minor variations in immobilization efficiency based on protein size, conformation, and amine/carboxyl content, based on our results with PDGF-BB and BSA594 (**Figure 3.7(a-b)**) we assumed an immobilization efficiency of 50% for subsequent immobilization experiments using PDGF-BB, IGF-1, bFGF, and GDF-5. Gene expression trends for these immobilized factors largely mirrored the results from the soluble experiments (**Figure 3.7(c-d)**), including increased expression of COMP, SCX, and TNC for GDF-5, decreased expression of COMP and SCX for PDGF-BB, and significant up-regulation of TNC for bFGF. Interestingly, we also observed a significant up-regulation of COL1A2 for the PDGF-BB group. While soluble PDGF-BB did not have as significant an inhibitory effect on COL1A2 expression as on other markers, down-regulation was observed for higher doses. The differences found here may be due to reduced levels of tenocyte proliferation induced by a single, immobilized dose of PDGF-BB compared to repeated soluble doses over the course of a long-term experiment. While we were able to confirm that repeated soluble supplementation of PDGF-BB resulted in increased tenocyte proliferation and metabolic activity compared to a single immobilized dose (data not shown), we used a slightly modified approach to compare the metabolic activity of tenocytes grown on scaffolds supplemented with a single, equivalent dose of PDGF-BB (either soluble or immobilized) over

the course of 7 days (**Figure 3.8**). We immobilized PDGF-BB such that the total amount immobilized on the scaffold was equivalent to the total soluble biomolecule content in the soluble experimental group. This experiment revealed that as expected, the freely soluble group initially induced higher levels of metabolic activity. However, by day 7 the sustained, localized effect of the immobilized PDGF-BB allowed that group to surpass the soluble group, leading to a significant increase in tenocyte metabolic activity.

3.6 Conclusions

We have demonstrated the dose-dependent effects of soluble factors PDGF-BB, IGF-1, bFGF, SDF-1α, and GDF-5 on tenocyte migration, viability, collagen synthesis, and gene expression within anisotropic CG scaffolds as a model system for tendon repair. Taken together, our work suggests a critical trade-off between induction of rapid cell migration/proliferation and the expression of normal tenocyte phenotypic markers. Pairing proliferative (IGF-1) and phenotypic (GDF-5) factors can support significantly increased tenocyte proliferation and soluble collagen synthesis in addition to up-regulation of key genetic markers (COL1A2, COMP, and SCX), indicating that combining factor pairs with an engineered CG scaffold may be an approach towards optimizing a construct for tendon tissue engineering. Facile immobilization of these factors within scaffolds was accomplished using carbodiimide chemistry and induced similar effects as soluble supplementation but in a manner more amenable to *in vivo* translation. Improved understanding of the individual and combined effects of the soluble factors investigated here is motivating ongoing work in our lab integrating immobilized and patterned

factor presentation within scaffolds for functional musculoskeletal tissue engineering applications.

3.7 Tables

Soluble Factor	Soluble Factor Dose (ng/mL)			
	Low	Medium	High	References
PDGF-BB	10	50	100	(Yoshikawa and Abrahamsson 2001; Thomopoulos, Harwood et al. 2005; Costa, Wu et al. 2006)
IGF-1	10	50	200	(Abrahamsson, Lundborg et al. 1991; Costa, Wu et al. 2006)
bFGF	0.1	5	10	(Thomopoulos, Harwood et al. 2005; Costa, Wu et al. 2006)
SDF-1α	10	50	200	(Du, Yang et al. 2012)
GDF-5	10	100	500	(Park, Hogan et al. 2010; James, Kumbar et al. 2011; Keller, Hogan et al. 2011)

Table 3.1. Soluble factor doses (ng/mL) used for tenocyte chemotaxis, proliferation, soluble collagen synthesis, and gene expression experiments. Soluble factor doses were informed by the literature and selected based on preliminary screening experiments that assayed at least six dose levels per factor.

3.8 Figures

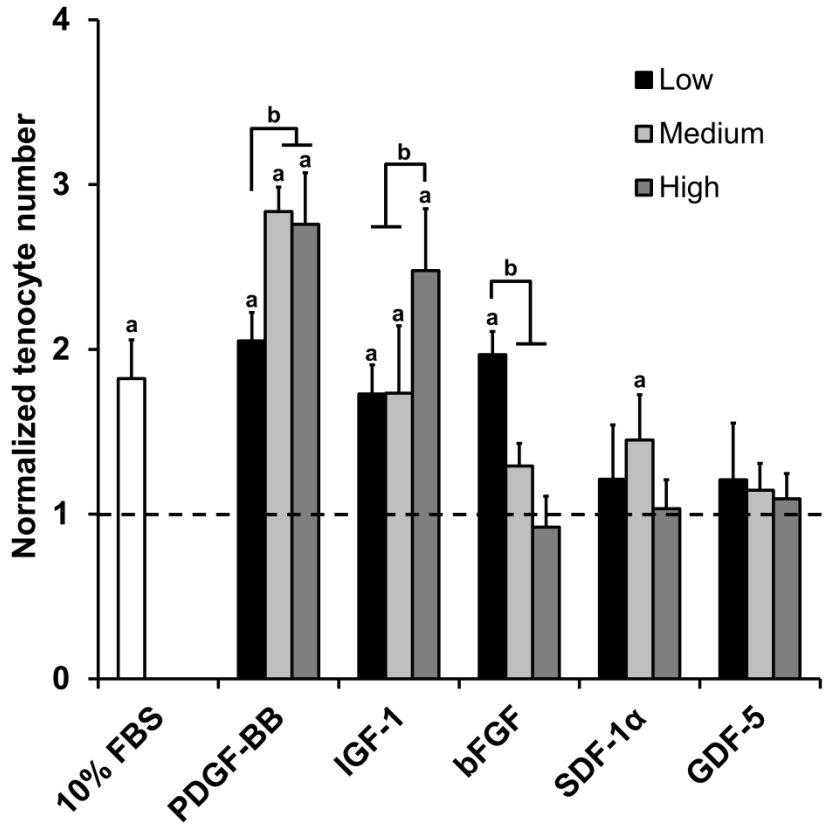

Figure 3.1. Tenocyte migration into anisotropic CG scaffolds in response to soluble factor gradients. Tenocyte chemotaxis over 24 h was measured for three different doses of PDGF-BB, IGF-1, SDF-1α, bFGF, and GDF-5 (n = 6). *Black dashed line:* level of tenocyte chemotaxis for non-supplemented media control. *a*: significant increase compared to non-supplemented media control. *b:* dose-dependent increase.

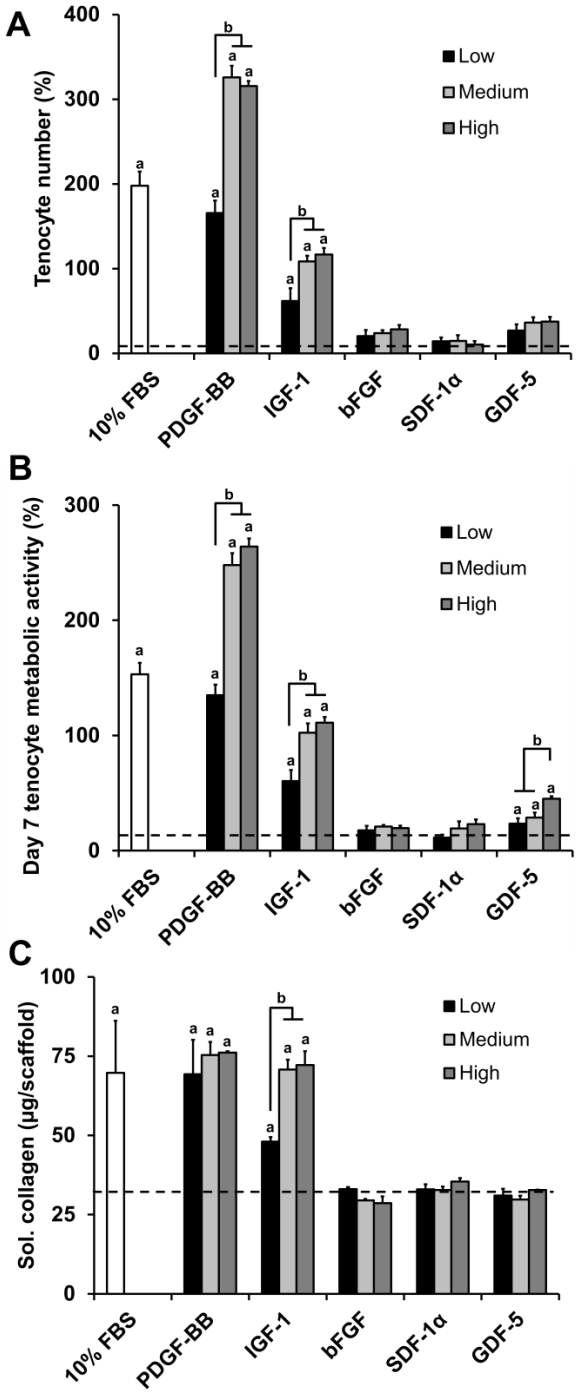

Figure 3.2. Tenocyte viability and collagen synthesis in anisotropic CG scaffolds in response to soluble factor supplementation. Tenocyte A) number (n = 6), B) metabolic activity (n = 9), and C) soluble collagen synthesis (n = 3) after 7 days culture in anisotropic CG scaffolds was measured for three different doses of PDGF-BB, IGF-1, SDF-1α, bFGF, and GDF-5. *Black dashed line:* level of non-supplemented media control. *a*: significant increase compared to non-supplemented media control. *b:* dose-dependent increase.

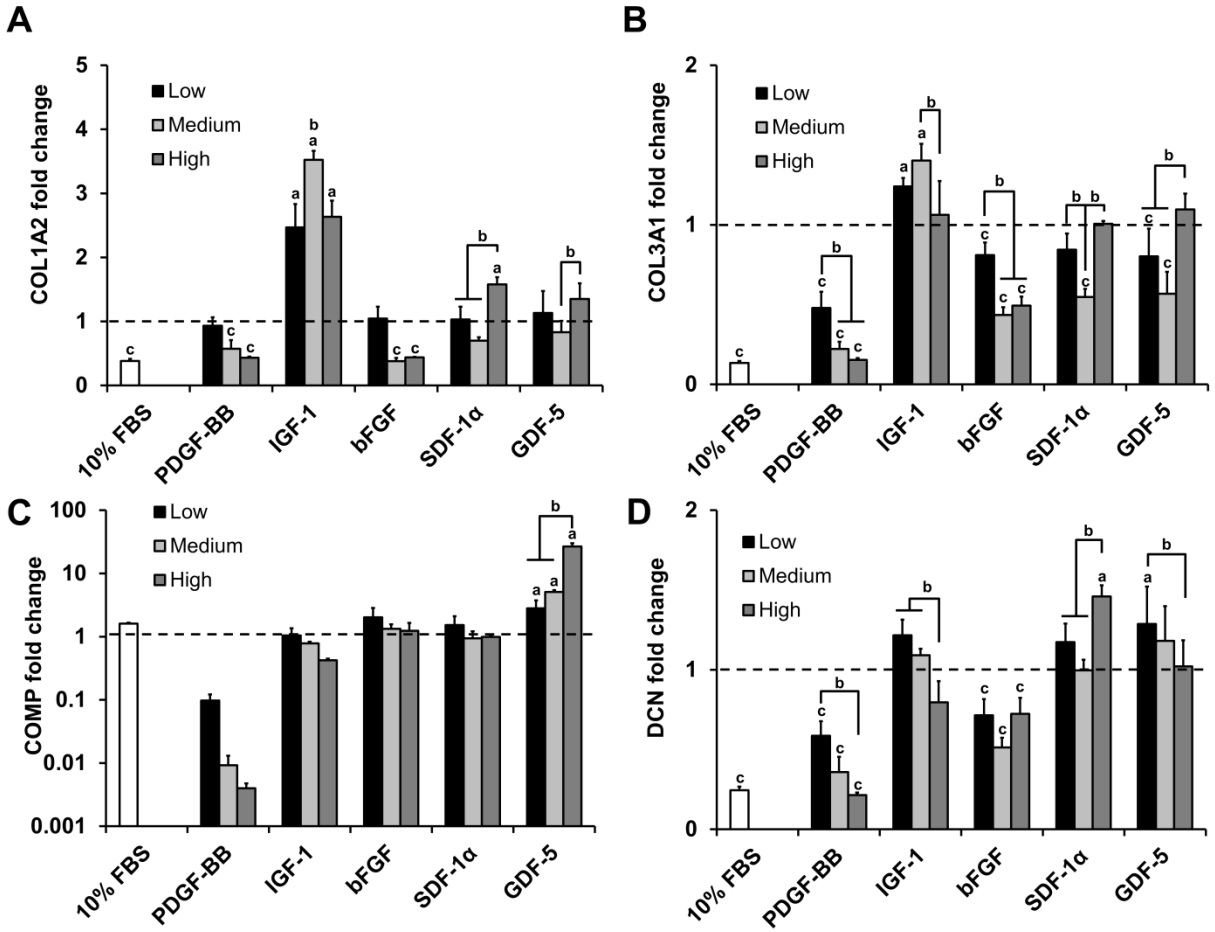

Figure 3.3. Expression levels for tenocyte structural protein genes within anisotropic CG scaffolds. Expression of A) COL1A2, B) COL3A1, C) COMP, and D) DCN after 7 days culture in anisotropic CG scaffolds was measured for three different doses of PDGF-BB, IGF-1, SDF-1α, bFGF, and GDF-5 (n = 3). *Black dashed line:* expression level of non-supplemented media control. *a*: significant up-regulation compared to non-supplemented media control. *b:* dose-dependent increase. *c*: significant down-regulation compared to non-supplemented media control.

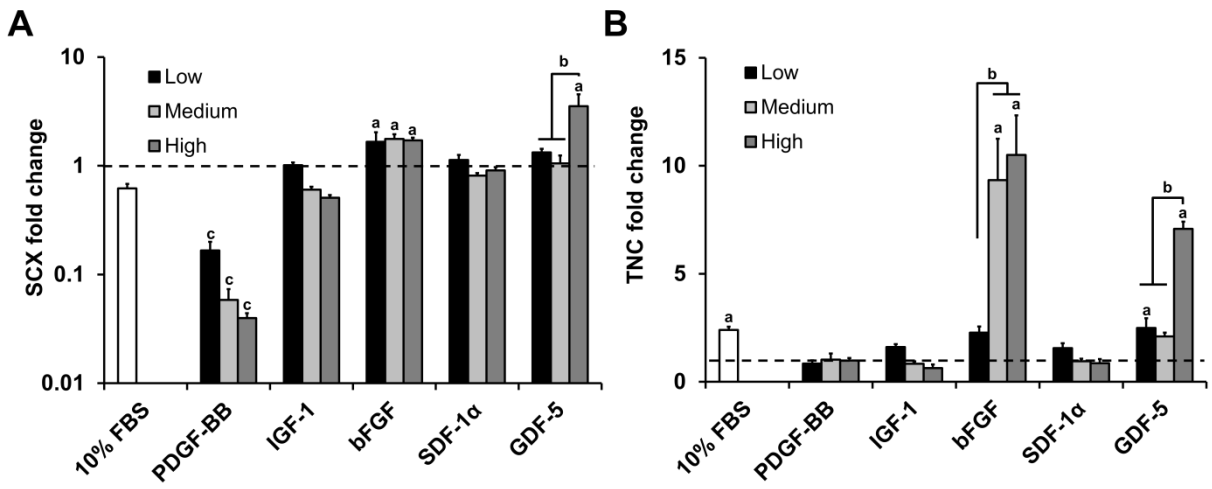

Figure 3.4. Expression levels for tenocyte phenotype genes within anisotropic CG scaffolds. Expression of A) SCX and B) TNC after 7 days culture in anisotropic CG scaffolds was measured for three different doses of PDGF-BB, IGF-1, SDF-1α, bFGF, and GDF-5 (n = 3). *Black dashed line:* expression level of non-supplemented media control. *a*: significant up-regulation compared to non-supplemented media control. *b:* dose-dependent increase. *c*: significant down-regulation compared to non-supplemented media control.

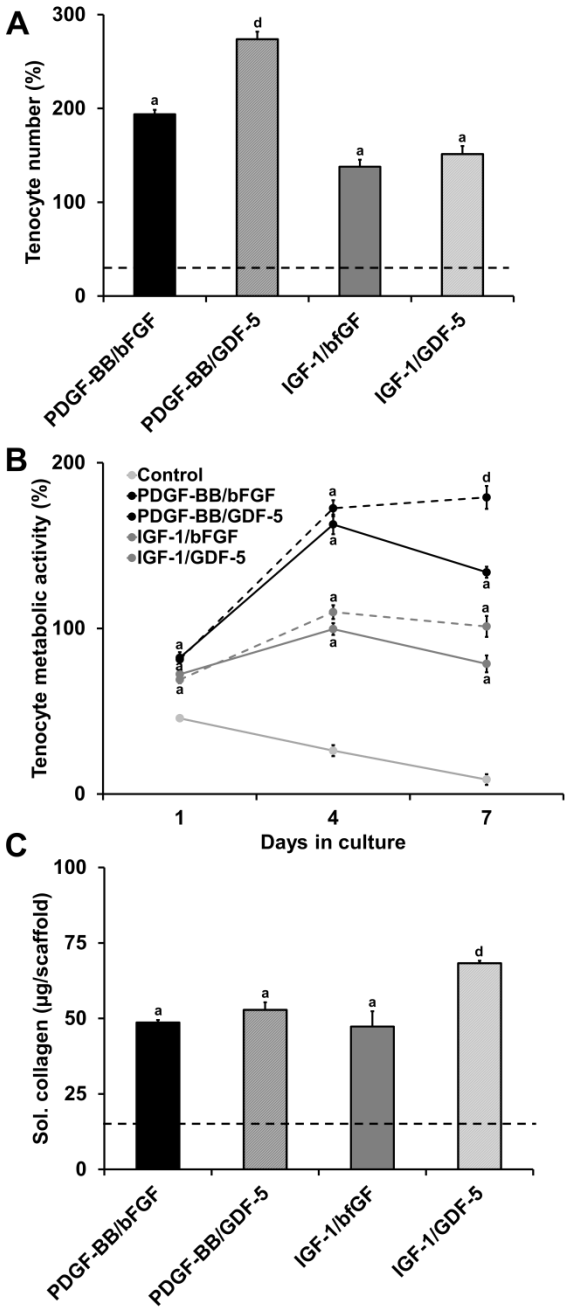

Figure 3.5. Influence of soluble factor combinations on tenocyte viability and collagen synthesis. Tenocyte A) number (n = 6), B) metabolic activity (n = 9), and C) soluble collagen synthesis (n = 3) after 7 days culture in anisotropic CG scaffolds was measured for four different soluble factor pairs: PDGF-BB/bFGF, PDGF-BB/GDF-5, IGF-1/bFGF, and IGF-1/GDF-5. *Black dashed line:* level of non-supplemented media control. *a*: significant increase compared to non-supplemented media control. *d:* significantly greater than all other experimental groups.

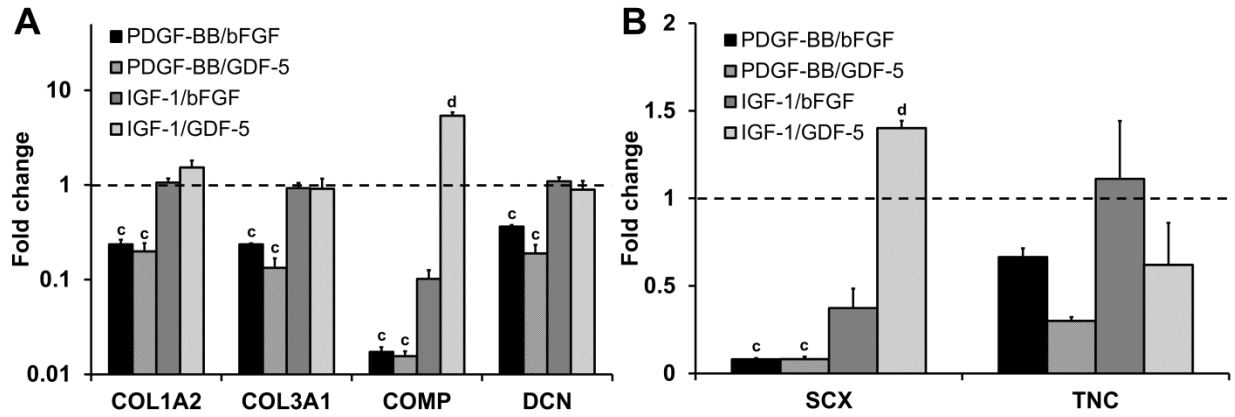

Figure 3.6. Influence of soluble factor combinations on tenocyte gene expression. Tenocyte expression of A) structural protein genes (COL1A2, COL3A1, COMP, DCN) and B) phenotype genes (SCX, TNC) was measured for four different soluble factor pairs: PDGF-BB/bFGF, PDGF-BB/GDF-5, IGF-1/bFGF, and IGF-1/GDF-5 after 7 days culture in anisotropic CG scaffolds (n = 3). *Black dashed line:* expression level of non-supplemented media control. *a*: significant increase compared to non-supplemented media control. *c*: significant down-regulation compared to non-supplemented media control.

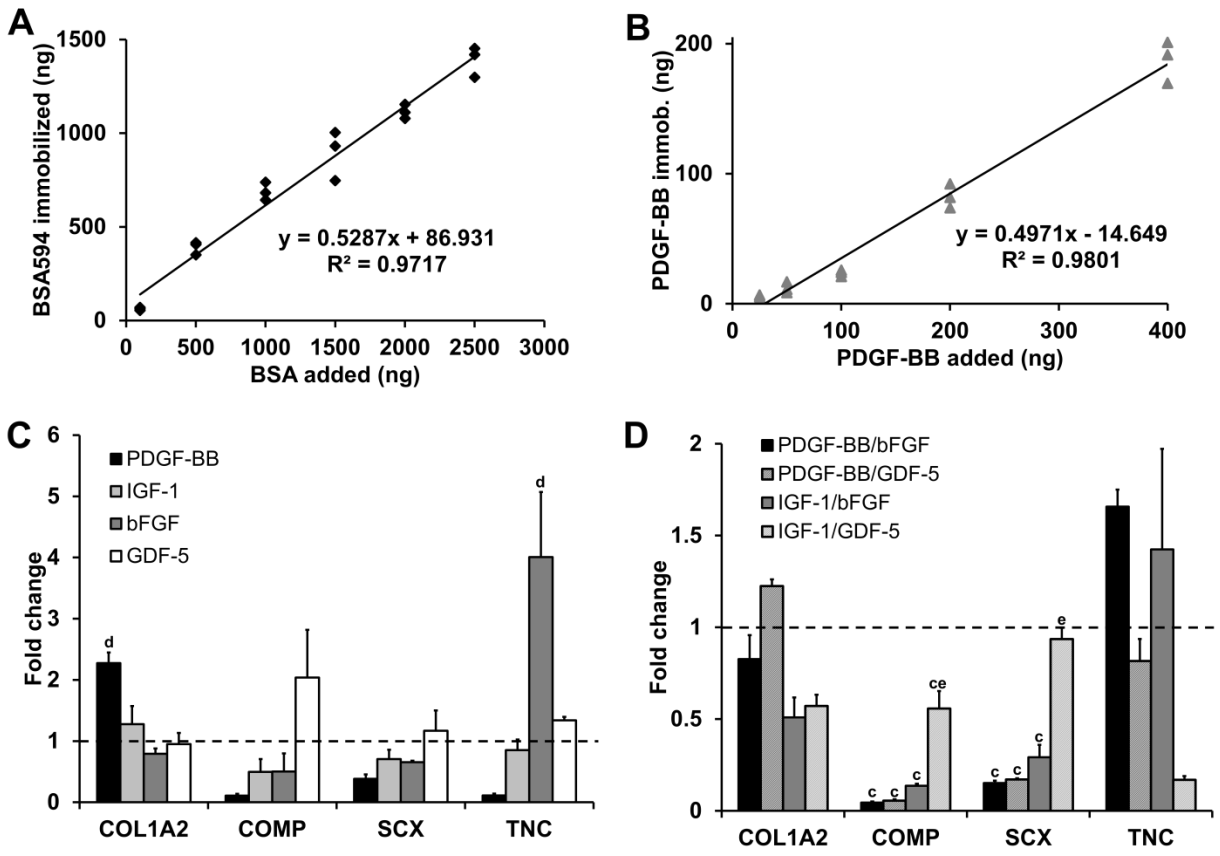

Figure 3.7. Immobilization of biomolecules to the CG scaffold via carbodiimide chemistry. Characteristic calibration curves for immobilization of A) bovine serum albumin labeled with Alexa Fluor® 594 (BSA594) and B) PDGF-BB. C) Expression of COL1A2, COMP, SCX, and TNC for tenocytes seeded in scaffolds in response to immobilized PDGF-BB, IGF-1, bFGF, and GDF-5 (n = 3). D) Expression of COL1A2, COMP, SCX, and TNC for tenocytes seeded in scaffolds in response to immobilized factor pairs PDGF-BB/bFGF, PDGF-BB/GDF-5, IGF-1/bFGF, and IGF-1/GDF-5 (n = 3). *Black dashed line:* expression level of non-supplemented media control. *c*: significant down-regulation compared to non-supplemented media control. *d:* significantly greater than all other experimental groups. *e:* significantly greater than other factor pair groups.

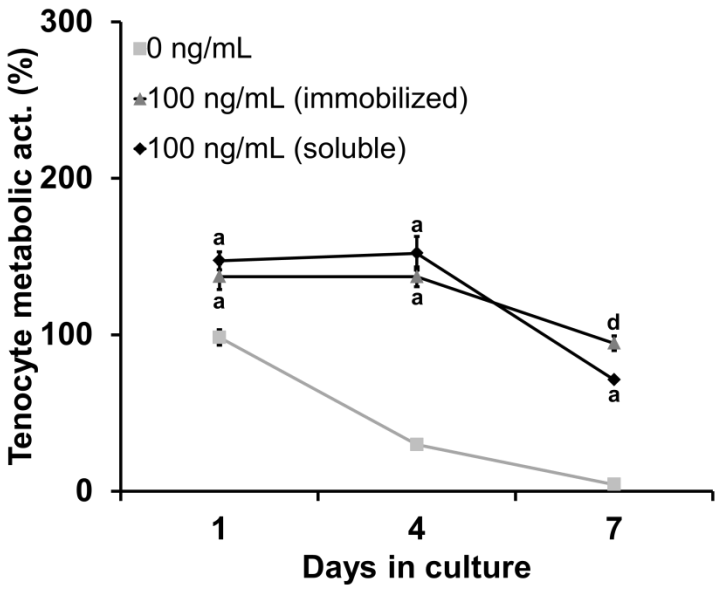

Figure 3.8. Comparison of equivalent soluble and immobilized doses of PDGF-BB on tenocyte metabolic activity. Tenocyte metabolic activity over 7 days of culture was compared for an equivalent single dose of soluble or immobilized PDGF-BB (n = 3). By day 7 the immobilized PDGF-BB group had significantly higher metabolic activity than both the soluble PDGF-BB and control groups. *a*: significant increase compared to non-supplemented media control. *d:* significant influence of soluble vs. immobilized dose at given time point.

CHAPTER 4: SELECTIVE MODIFICATION OF COLLAGEN-GAG STRUCTURAL AND BIOCHEMICAL PROPERTIES TO ENHANCE TENOGENIC, CHONDROGENIC, AND OSTEOGENIC MSC DIFFERENTIATION[4]

4.1 Chapter overview

Current biomaterial approaches for engineering orthopedic interfaces such as the tendon-bone junction (TBJ) are limited by a lack of understanding of how insoluble (microstructure, composition) and soluble regulators of stem cell fate work in concert to promote differentiation, especially in the context of tendon tissue engineering. This work uses selective modification of a well-characterized 3D collagen-glycosaminoglycan (CG) scaffold system to probe the combined influences of structural and biochemical instructive cues to drive human bone marrow-derived mesenchymal stem cell (MSC) differentiation down tenogenic, osteogenic, and chondrogenic lineages respectively. Tenogenic differentiation is enhanced in geometrically anisotropic scaffolds as demonstrated by significant increases in scleraxis (SCXB) expression and Rho-associated protein kinase 1 (ROCK1) activity compared to isotropic controls. Blebbistatin treatment results in abrogation of these microstructurally-driven effects. Osteogenic differentiation is achieved by coupling a biomimetic CG-calcium phosphate scaffold with osteogenic induction media, with significantly higher expression of osteogenic genes alkaline phosphatase (ALP) and runt-related transcription factor 2 (RUNX2) as well as higher levels of mineralization observed. Finally, chondrogenic differentiation is optimally driven by combining chondrogenic induction media with a lower density scaffold that promotes increased cellular condensation and significantly higher expression of chondrogenic genes type II collagen (COL2A1) and aggrecan (ACAN) as well as increased GAG deposition. Together these data provide critical insight regarding design rules for orthopedic tissue engineering scaffolds.

[4] This chapter has been adapted from the following publications:
Caliari, S. R. and B. A. C. Harley (in preparation). "Selective modification of collagen-GAG scaffold structural and biochemical properties to enhance tenogenic, chondrogenic, and osteogenic MSC differentiation."

4.2 Introduction

Orthopedic junctions connect soft tissue and bone to promote joint stability and locomotion. However, these interfaces are mechanically heterogeneous and therefore common injury sites due to the presence of stress concentrations.(Thomopoulos, Marquez et al. 2006) One important class of orthopedic interface is the tendon-bone junction (TBJ). Tendons are non-mineralized tissues composed of highly aligned, anisotropic type I collagen fiber bundles that transfer muscle-generated force to the skeletal system to enable normal movement. Comparatively, bone is mineralized and more isotropic in its structural organization. Importantly, tendon and bone are connected by a narrow (100-1000 μm (Moffat, Sun et al. 2008)) fibrocartilagenous interface rich in type II collagen and proteoglycans such as aggrecan that helps dissipate stress concentrations during mechanical loading (Galatz, Rothermich et al. 2007). The osteotendinous interfacial milieu contains elegant gradations of extracellular matrix (ECM) proteins, ECM alignment, mineral content, and growth factors to maintain joint patency (Wopenka, Kent et al. 2008; Genin, Kent et al. 2009). Unfortunately, TBJs such as the supraspinatus-humerus junction in the rotator cuff are still common injury sites with current repair strategies poorly recapitulating the tendinous, cartilaginous, and osseous regions found in the native TBJ, resulting in suboptimal patient outcomes (Boileau, Brassart et al. 2005; Millar, Wu et al. 2009).

An alternative repair strategy to guide regeneration of a spatially-graded osteotendinous junction could apply a biomaterial seeded with a progenitor cell type (*e.g.*, mesenchymal stem cells (MSCs)). Here, instructive cues engineered into the biomaterial design could promote spatially-

graded stem cell lineage specification down tenogenic, chondrogenic, and osteogenic lineages respectively. Towards the design of such an instructive biomaterial, a wide range of studies have investigated the use of material biophysical properties to induce divergent MSC bioactivity and lineage specification. Seminal work from Engler *et al.* defined the role of substrate elasticity, without biomolecular perturbation, in driving MSCs down neurogenic, myogenic, and osteogenic lineages with increasing substrate stiffness (Engler, Sen et al. 2006). More recent work has demonstrated that substrate geometry (Kilian, Bugarija et al. 2010) and tethering (Trappmann, Gautrot et al. 2012) can have a profound influence on stem cell fate. While these studies were performed on planar substrates, it has been more difficult to translate these findings into design rules for 3D biomaterials. However, recent progress has been made in this arena towards understanding the roles of crosslinking, rigidity (Huebsch, Arany et al. 2010), and degradation properties (Khetan, Guvendiren et al. 2013) in directing stem cell lineage. In parallel, many approaches have used soluble cues in the form of induction media (Gao, Dennis et al. 2001; Sheehy, Vinardell et al. 2013) or growth factor supplementation (Yilgor, Tuzlakoglu et al. 2009) to aid differentiation and regeneration. However, few approaches have considered the combined influence of both insoluble (mechanics, structural organization, composition) and soluble (growth factor, cytokine) cues on guiding MSC fate. The lack of understanding of how insoluble and soluble regulators of stem cell fate work in concert to promote differentiation, especially in the context of tendon tissue engineering, is a critical limiting factor to the development of improved TBJ repair strategies.

In this study we have evaluated the potential for integrated biophysical and biochemical signals within an instructive biomaterial environment to guide separate tenogenic, osteogenic, and

chondrogenic MSC differentiation (**Figure 4.1)**. Such an effort precedes development of integrated biomaterials to repair multi-tissue junctions such as the TBJ. This study used selective modifications to a well-characterized collagen-glycosaminoglycan (CG) scaffold system. CG scaffolds possess many advantageous properties for tissue engineering, including high porosity, natural ligands to support cell adhesion and bioactivity, and approval for use by various regulatory agencies (Harley and Gibson 2008). As analogs of the native ECM, these materials can serve as platforms to quantitatively study cell adhesion (O'Brien, Harley et al. 2005), migration (Harley, Kim et al. 2008), and regenerative potential (Yannas, Lee et al. 1989; Harley, Spilker et al. 2004). While previous efforts to drive MSC differentiation within CG scaffolds have focused on single osteogenic or chondrogenic differentiation (Farrell, O'Brien et al. 2006; Curtin, Cunniffe et al. 2012; Murphy, Matsiko et al. 2012), this study addresses the suitability of CG scaffolds to guide MSC differentiation towards an osteotendinous junction phenotype, in particular focusing on tenogenic differentiation. Unlike osteogenic or chondrogenic differentiation, there is no well-established induction media to guide tenogenic MSC differentiation. Several methods to induce tenogenesis include co-culture with primary fibroblasts (Canseco, Kojima et al. 2012; Lovati, Corradetti et al. 2012), cell stretching through mechanical stimulation (Juncosa-Melvin, Shearn et al. 2006; Subramony, Dargis et al. 2012), and inducing cell alignment/elongation through the use of contact guidance cues (Cheng, Gurkan et al. 2008; Kapoor, Caporali et al. 2010). In this study we have made selective structural modifications to our standard CG scaffold in order to bias MSC differentiation potential. In conjunction with biomolecule stimulation we explored the potential of these modified CG scaffolds to support separate tenogenic, chondrogenic, and osteogenic lineage specification. Due to the facile nature of these scaffold modifications and previous studies integrating disparate CG

scaffold compartments to fabricate continuous constructs (Harley, Lynn et al. 2010), we believe this work will eventually inform the design of CG scaffolds for numerous musculoskeletal tissue engineering applications, specifically the repair of orthopedic interfaces.

4.3 Materials and methods

*All reagents purchased from Sigma-Aldrich (St Louis, MO) unless otherwise specified.

4.3.1. Precursor suspension preparation

Low and high density CG suspensions (0.5 and 1.5 collagen w/v% respectively) were prepared by homogenizing type I microfibrillar collagen and chondroitin sulfate in 0.05 M acetic acid as previously described (O'Brien, Harley et al. 2004). Collagen-GAG-calcium phosphate (CGCaP) suspension was prepared via triple co-precipitation of type I collagen (1.9 w/v%) and chondroitin sulfate as before with the addition of calcium salts (calcium hydroxide, calcium nitrate tetrahydrate) in phosphoric acid to create 40 wt% mineralized scaffolds (Harley, Lynn et al. 2010).

4.3.2 Scaffold fabrication via freeze-drying

Four scaffold types were used in this study, including three different non-mineralized CG scaffolds and a mineralized CGCaP scaffold (**Table 4.1**). All scaffolds were fabricated using a VirTis freeze-dryer (Gardiner, NY). All studies used an isotropic CG scaffold as a control. Tenogenic differentiation studies used geometrically-anisotropic high density (1.5 w/v%) CG scaffolds fabricated via directional solidification at a freezing temperature of -10°C in a

thermally-mismatched mold (Caliari and Harley 2011; Caliari, Weisgerber et al. 2012). This scaffold variant was previously identified to support tenocyte proliferation and phenotypic stability while resisting cellular contraction (Caliari and Harley 2011; Caliari, Weisgerber et al. 2012). Isotropic low density CG scaffolds were used in chondrogenesis experiments while mineralized CGCaP scaffolds were examined in osteogenesis studies. Isotropic low density and high density CG scaffolds as well as mineralized CGCaP scaffolds were fabricated using a constant cooling method at a final freezing temperature of -10°C (O'Brien, Harley et al. 2004). The freeze-drying process resulted in dry, macroporous scaffolds (O'Brien, Harley et al. 2004; Harley, Lynn et al. 2010; Caliari and Harley 2011).

4.3.3 Scaffold hydration and crosslinking

Dry CG scaffolds underwent dehydrothermal crosslinking in a vacuum oven (Welch, Niles, IL) at 105°C for 24 h. All scaffolds were then sterilized in ethanol for 1 h, hydrated in PBS overnight, and crosslinked for 1.5 h in a solution of 1-ethyl-3-[3-dimethylaminopropyl] carbodiimide hydrochloride (EDC) and N-hydroxysulfosuccinimide (NHS) at a molar ratio of 5:2:1 EDC:NHS:COOH where COOH represents the amount of collagen in the scaffold (Olde Damink, Dijkstra et al. 1996; Harley, Leung et al. 2007).

4.3.4 MSC culture in scaffolds

Human bone marrow-derived mesenchymal stem cells (MSCs) were purchased from Lonza (Walkersville, MD) and cultured in complete growth media as supplied by the manufacturer. Cells were used at passage 6 for all experiments. 7.5×10^4 MSCs were seeded onto scaffold discs (6 mm diameter, 3 mm thickness) using a previously validated static seeding method (O'Brien,

Harley et al. 2005). All groups were cultured in complete growth media (Lonza) except as noted in **Table 4.1**. All soluble factors were human recombinant proteins from ProSpec (Israel). Proteins were diluted to experimental concentrations (**Table 4.1**) in complete media at doses selected based on the literature (Thomopoulos, Harwood et al. 2005; Costa, Wu et al. 2006; Park, Hogan et al. 2010; Caliari and Harley 2013). Blebbistatin (concentration: 50 μM) was used for experiments examining the linkage between scaffold anisotropy and MSC tenogenesis (Engler, Sen et al. 2006). Scaffolds were cultured at 37°C and 5% CO_2 and fed twice a week for all experiments.

4.3.5 Quantification of MSC metabolic activity

MSC mitochondrial metabolic activity on scaffolds was quantified using an alamarBlue® fluorescent assay (Invitrogen) previously used to determine the metabolic health of cells grown on CG scaffolds (Tierney, Jaasma et al. 2009). Briefly, MSC-seeded scaffolds were incubated in alamarBlue® solution for 2.5 h, where viable cells continuously reduce the alamarBlue® dye to a fluorescent byproduct (resorufin). Fluorescence was measured (excitation: 540 nm, emission: 580 nm) on a fluorescent spectrophotometer (Tecan, Switzerland).

4.3.6 Confocal microscopy

MSC-seeded scaffolds were fixed in 10% neutral buffered formalin and stored at 4°C until staining. Following permeabilization in 0.1 % Triton X100 in PBS for 10 min, MSC were stained with Alexa Fluor® 488 phalloidin (F-actin, Invitrogen, Carlsbad, CA) for 20 min and DAPI (nuclei, Invitrogen) for 5 min. Scaffolds were imaged with a Zeiss 710 multiphoton confocal microscope (10x objective) equipped with a Spectraphysics Mai-Tai Ti-Sapphire laser. Cell

shape index (CSI) was quantified for at least 50 cells per experimental group using ImageJ (Choi and Harley 2012).

4.3.7 RNA isolation, reverse transcription, and real-time PCR

Total RNA was isolated from cell-seeded scaffolds using an RNeasy Plant Mini kit (Qiagen, Valencia, CA) (Duffy, McFadden et al. 2011; Caliari, Weisgerber et al. 2012). RNA was reverse transcribed to cDNA using the QuantiTect Reverse Transcription kit (Qiagen) in a Bio-Rad S1000 thermal cycler. Primer sets for PCR reactions were mined from the literature (Pauly, Klatte et al. 2010; Zhou, Xu et al. 2011) (**Table 4.2**) and synthesized by Integrated DNA Technologies (Coralville, IA) with the exception of the scleraxis (SCXB) primer set, which was purchased from Qiagen. Real-time PCR reactions were executed in triplicate using SYBR green chemistry (QuantiTect SYBR Green PCR kit, Qiagen) in an Applied Biosystems 7900HT Fast Real-Time PCR system (Applied Biosystems, Carlsbad, CA). Data were analyzed using Sequence Detection Systems software v2.4 (Applied Biosystems) via the delta-delta Ct method with GAPDH serving as a housekeeping gene. Results were expressed as fold changes normalized to the expression levels of MSCs cultured in isotropic scaffolds at day 7.

4.3.8 Protein isolation and Western blotting

Protein lysates were obtained by immersing scaffolds in RIPA buffer supplemented with protease and phosphatase inhibitors for 30 min on ice. Lysates were separated on 10% polyacrylamide gels via electrophoresis and transferred to nitrocellulose membranes (Fisher Scientific, Pittsburgh, PA) using standard techniques. Antibodies for Rho-associated protein kinase 1 (ROCK1), β-catenin, double phosphorylated extracellular signal-regulated protein

kinase 1/2 (pERK-1/2), and β-actin were purchased from Cell Signaling Technology (Beverly, MA) and used at 1:2000 dilution in 5% non-fat milk. Horseradish peroxide (HRP)-conjugated secondary antibodies (Cell Signaling) were added following primary antibody incubation. Signal was developed using SuperSignal West Pico Chemiluminescent Substrate solutions (Thermo Scientific, Rockford, IL) and visualized on an Image Quant LAS 4010 (GE Healthcare, Pittsburgh, PA). Band intensities were quantified using ImageJ and expression levels were normalized to β-actin expression.

4.3.9 SMAD8 siRNA transfection

Smad8 silencing experiments were performed using a commercially available siRNA kit (Santa Cruz Biotechnology, Dallas, TX). Transfection was performed by following kit instructions and using siRNA targeting either SMAD8 or a scrambled control. Transfected MSCs were then seeded on anisotropic scaffolds for further analysis.

4.3.10 Histology

Scaffolds from the osteogenic and chondrogenic experimental sets were fixed in 10% neutral buffered formalin for histological analysis after 21 days in culture. Scaffold discs were embedded in paraffin wax, serially cut into 5 μm sections, and mounted on microscope slides. Slides were deparaffinized and stained with either hematoxylin and eosin (H&E) to assess cellular distribution, Alizarin red to evaluate mineralization, or Alcian blue to visualize GAG content.

4.3.11 Statistical analysis

Two-way analysis of variance (ANOVA, independent variables time and scaffold/biomolecule treatment) was performed on metabolic activity and gene expression data sets followed by Tukey-HSD post-hoc tests. Significance was set at $p < 0.05$. Metabolic activity and gene expression experiments used at least $n = 3$ scaffolds per group while Western blotting and histological analyses used $n = 2$ scaffold per group. Error is reported in figures as the standard error of the mean.

4.4 Results

4.4.1 MSC metabolic activity in CG scaffolds

Two-way ANOVA analyses revealed a significant effect of both culture time ($p < 0.0001$) and scaffold treatment ($p < 0.0001$) on MSC metabolic activity in the tenogenic, osteogenic, and chondrogenic differentiation experimental sets (**Figure 4.2, 4.11**).

4.4.1.1 Tenogenic cultures

Isotropic and anisotropic scaffolds both supported steadily increasing, but similar, levels of metabolic activity throughout the experiment (**Figure 4.2(a)**). All tenogenic groups showed significant increases in metabolic activity from day 7 to day 14 ($p < 0.002$) with the anisotropic as well as IGF-1, GDF-5, and GDF-7-supplemented anisotropic scaffolds having significantly higher activity than the isotropic control ($p < 0.007$) (**Figure 4.11(a)**). However, by day 21 these differences between groups had been eliminated while the bFGF-supplemented anisotropic group displayed significantly lower metabolic activity than the isotropic control group ($p < 0.0001$) (**Figure 4.11(a)**).

4.4.1.2 Osteogenic cultures

Isotropic scaffolds consistently had significantly higher metabolic activity compared to mineralized scaffold groups (**Figure 4.2(b), 4.11(b)**). Osteogenic induction media led to significantly increased metabolic activity in mineralized scaffolds compared to non-supplemented mineralized scaffolds at all three time points ($p < 0.0001$). While only the two non-mineralized groups showed significant increases in metabolic activity from day 7 to day 14 ($p < 0.04$), all experimental groups displayed significantly increased metabolic activity on day 21 compared to day 14 ($p < 0.03$) (**Figure 4.11(b)**).

4.4.1.3 Chondrogenic cultures

The chondrogenic media supplemented groups showed significantly higher metabolic activity than the isotropic control at day 7 ($p < 0.04$) (**Figure 4.2(c)**). However, on day 14 the low density chondrogenic as well as the low density TGF-β1 and TGF-β3-supplemented groups displayed significantly lowered metabolic activity compared to day 7 ($p < 0.04$) (**Figure 4.11(c)**). By day 21, all groups had significantly lower metabolic activity than the isotropic group ($p < 0.003$).

4.4.2 Tenogenic gene expression

The expression of the tenogenic genes scleraxis (SCXB) and tenascin-C (TNC) was quantified at days 7, 14, and 21 of culture (**Figure 4.3**). There was a significant effect of both culture time ($p < 0.0001$) and scaffold treatment ($p = 0.01$) on SCXB expression. While no statistically significant differences in SCXB expression were observed at day 7, anisotropic scaffolds showed elevated expression at days 14 and 21 compared to the isotropic group ($p < 0.03$) (**Figure**

4.3(a)). Although the bFGF and GDF-7-supplemented anisotropic scaffolds also significantly up-regulated SCXB at days 14 and 21 ($p < 0.03$) (**Figure 4.3(a), 4.12(a)**), there was no apparent synergistic effect of both anisotropy and growth factor supplementation on SCXB expression. While there was no significant effect of scaffold treatment on TNC expression ($p = 0.52$), culture time did have a significant effect ($p < 0.0001$) with the GDF-5 and GDF-7-supplemented anisotropic scaffolds showing late up-regulation of TNC between days 14 and 21 ($p < 0.04$) (**Figure 4.3(b)**).

Type I collagen (COL1A1) expression was also quantified (**Figure 4.12(c)**). Two-way ANOVA showed a significant effect of both culture time and scaffold treatment on COL1A1 expression ($p < 0.0001$). COL1A1 expression was initially up-regulated in the IGF-1, GDF-5, and GDF-7-supplemented anisotropic groups at day 7 ($p < 0.002$), but down-regulated in the bFGF supplemented anisotropic group ($p = 0.01$) compared to the isotropic control. However, following down-regulation in the IGF-1, GDF-5, and GDF-7 groups at day 14 ($p < 0.005$) there were no significant differences between any experimental groups on either day 14 or 21.

4.4.3 MSC morphology and expression of tenogenic genes and proteins in response to blebbistatin

Based on previous work in our lab that suggested the importance of scaffold structural anisotropy for supporting tenocyte alignment and phenotypic maintenance (Caliari and Harley 2011; Caliari, Weisgerber et al. 2012) as well as the SCXB expression results shown here, we were curious how scaffold anisotropy may impact MSC cytoskeletal organization. We examined MSC response to scaffold anisotropy and resultant tenogenic specification in the presence of

blebbistatin, a myosin II inhibitor, for 7 days. Confocal microscopy revealed a drastic reduction in MSC elongation and spreading within CG scaffolds when treated with blebbistatin (**Figure 4.4(a,b)**). Blebbistatin-treated MSC-seeded anisotropic scaffolds also showed a significant increase in cell shape index (increased cell roundness) compared to non-treated anisotropic scaffolds ($p < 0.0001$) (**Figure 4.4(c)**). Subsequent gene expression analyses showed trends towards down-regulation of COL1A1, SCXB, and TNC expression in anisotropic scaffolds in response to blebbistatin treatment (**Figure 4.4(d)**).

We also examined activation of the RhoA/ROCK, mitogen-activated protein kinase (MAPK), and canonical Wnt signaling pathways in response to scaffold anisotropy and blebbistatin treatment by measuring protein levels of ROCK1, pERK1/2, and β-catenin respectively (**Figure 4.5**). Anisotropic scaffolds displayed significantly higher levels of ROCK1 compared to isotropic scaffolds with blebbistatin treatment abrogating this effect ($p < 0.05$). Blebbistatin treatment also led to downward trends of pERK1/2 expression with significant differences observed ($p = 0.03$).

4.4.4 Effect of Smad8 silencing on MSC elongation and tenogenic gene expression

Since GDF supplementation resulted in late up-regulation of TNC we explored Smad8 silencing via siRNA transfection to determine the role that Smad8 plays in mediating tenogenic phenotype. MSCs were transfected for 24 h and then seeded onto anisotropic scaffolds for 24 h. Smad8-silenced MSCs showed reduced elongation and increased spreading compared to MSCs treated with control siRNA (**Figure 4.6(a)**). This effect was quantified by measuring MSC coherency, a metric of elongation (measured on a scale of 0 to 1) where higher values indicate increased feature elongation. A significant decrease in MSC elongation was observed in the Smad8

siRNA-treated group (p = 0.04) (**Figure 4.6(b)**). Additionally, the expression of a panel of tenogenic genes related to ECM production (COL1A1, COMP) and phenotype (SCXB, SIX1, TNC) was measured for the two groups (**Figure 4.6(c)**). Expression generally trended towards down-regulation in the Smad8-treated group with significant down-regulation of COMP observed (p = 0.009).

4.4.5 Osteogenic gene expression and histology

Significant effects of both culture time and scaffold mineral content/biomolecule treatment were found for the expression of all three osteogenic genes examined (ALP, RUNX2, OCN, $p < 0.05$) (**Figure 4.7, 4.13**). Notably, ALP expression was significantly up-regulated at all time points for both the isotropic and mineralized scaffolds groups cultured in osteogenic induction media ($p <$ 0.02) (**Figure 4.7(a), 4.13(a)**). Although the isotropic osteogenic group showed higher ALP expression than the mineralized osteogenic group at day 7 by about a factor of 3, the mineralized osteogenic group displayed significant ALP up-regulation from day 7 to day 14 and day 14 to day 21 ($p < 0.05$), finishing with an ALP expression level about twice that of the isotropic osteogenic group.

Similarly, expression levels of RUNX2 were significantly elevated in both of the osteogenic induction groups at day 21 ($p < 0.003$) (**Figure 4.7(b)**). Although the isotropic osteogenic media group had higher expression than its mineralized counterpart at day 7 (**Figure 4.13(b)**), this trend was reversed by day 21. OCN expression was initially up-regulated in the non-supplemented and BMP-2-supplemented mineralized groups compared to the isotropic control at day 7 ($p < 0.009$) (**Figure 4.13(c)**). BMP-2 and BMP-7 supplementation elicited a significant up-regulation of

OCN compared to the isotropic control at day 14 ($p < 0.0003$), although this trend had disappeared by day 21 ($p > 0.05$). However, by the final time point the isotropic osteogenic group displayed significant OCN up-regulation compared to the isotropic control ($p = 0.02$) (**Figure 4.7(c)**).

Histological sections were taken after day 21 to evaluate MSC distribution and mineralization via H&E and Alizarin red staining respectively (**Figure 4.8, 4.15(a)**). While there did not appear to be major differences in MSC infiltration based on H&E sections, Alizarin red staining revealed notable differences between groups. Significant mineralization was observed in all groups with the combination of osteogenic media and a mineralized scaffold leading to the greatest level of mineralization (**Figure 4.8(d)**). BMP-2 supplementation did not appear to improve mineral deposition over the non-supplemented mineralized group (**Figure 4.8(c), 4.15(a)**).

4.4.6 Chondrogenic gene expression and histology

COL2A1 expression levels were found to be significantly elevated at day 21 by the combination of a low density scaffold and chondrogenic induction media ($p < 0.0001$) (**Figure 4.9(a)**). While the effect of scaffold treatment on SOX9 was non-significant ($p = 0.41$), SOX9 expression was up-regulated in the isotropic chondrogenic group at the intermediate time point (day 14, $p = 0.004$) while significant up-regulation occurred in the low density chondrogenic group at the final time point (day 21, $p = 0.02$) (**Figure 4.9(b), 4.14(b)**). ACAN was significantly down-regulated in the low density TGF-β-supplemented groups at day 7 ($p < 0.03$) (**Figure 4.14(c)**). The chondrogenic induction groups saw significant up-regulation from day 7 to day 14 ($p < 0.02$)

which led to significantly higher transcript levels than the isotropic control at this time point ($p < 0.03$). However, from day 14 to day 21 ACAN was significantly down-regulated in the isotropic chondrogenic group ($p < 0.0001$) while the low density chondrogenic group maintained its significantly higher expression level compared to the isotropic control ($p = 0.02$) (**Figure 4.9(c)**).

Chondrogenic phenotype was further evaluated by staining histology sections with H&E and Alcian blue to assess MSC distribution and GAG deposition respectively (**Figure 4.10, 4.15(b)**). The low density chondrogenic and TGF-β3 groups showed significant scaffold contraction and cellular condensation as demonstrated by H&E staining (**Figure 4.10(d), 4.15(b)**). Alcian blue staining appeared to be strongest in the low density chondrogenic group (**Figure 4.10(d)**) while no major differences in GAG content were apparent in the other experimental groups.

4.5 Discussion

This study aimed to identify whether select alterations of biomaterial structural properties in conjunction with biomolecule supplementation could impact multi-lineage MSC differentiation in a model 3D CG scaffold under development for osteotendinous repair (**Figure 4.1**). Here we have used minimalist approaches to screen a large experimental space.

While tendon injuries represent an important class of orthopedic trauma, comprehensive evaluation of strategies to drive MSC tenogenic differentiation have not been explored in the context of a 3D biomaterial. We first hypothesized that a combination of geometric anisotropy and tenogenic growth factor supplementation would improve tenogenic MSC differentiation.

Previous work in our lab has identified scaffold pore anisotropy as a key regulator of tenocyte alignment (Caliari and Harley 2011) and resultant maintenance of tenogenic phenotypic stability (Caliari, Weisgerber et al. 2012). Other investigations have shown that inducing cell alignment and elongation via substrate contact guidance cues can affect tenocyte phenotype (Kapoor, Caporali et al. 2010) and drive MSC fibroblastic differentiation (Yin, Chen et al. 2010; Subramony, Dargis et al. 2012). Growth factors can also influence the tenogenic response (Molloy, Wang et al. 2003; Gulotta and Rodeo 2009). The growth factor bFGF was reported to improve tenocyte and MSC proliferation, collagen synthesis, chemotaxis, and tenogenic differentiation (Thomopoulos, Harwood et al. 2005; Schmidt, Ladage et al. 2006; Ker, Chu et al. 2011). Similarly, IGF-1 has been suggested to promote tenocyte and MSC proliferation, migration, tenogenic gene expression, and ECM biosynthesis (Costa, Wu et al. 2006; Ozaki, Nishimura et al. 2007; Caliari and Harley 2011; Caliari and Harley 2013). Separately, GDF-5 and GDF-7 have implicated in promoting tenogenic gene expression, collagen production, cell migration, and tendinous tissue formation *in vivo* (Wolfman, Hattersley et al. 1997; Date, Furumatsu et al. 2010; Park, Hogan et al. 2010; Hagerty, Lee et al. 2012). Therefore, our aim was to evaluate whether 3D scaffold anisotropy increased MSC tenogenic specification, and further whether selective addition of bFGF, IGF-1, GDF-5, or GDF-7 improved this response. We chose factor dosages based on previous work in our lab with tenocytes (Caliari and Harley 2011; Caliari and Harley 2013) as well as from the literature (Thomopoulos, Harwood et al. 2005; Costa, Wu et al. 2006; Park, Hogan et al. 2010), although we acknowledge subsequent studies may optimize factor dosing.

Scaffold anisotropy and growth factor (IGF-1, GDF-5, GDF-7) supplementation improved MSC metabolic activity compared to the isotropic control out to 14 days in culture, but by 21 days these differences had been eliminated with the exception of the bFGF group, which showed lower activity (**Figure 4.2(a), 4.11(a)**). The expression of tenogenic genes COL1A1, SCXB, and TNC was also measured to assess the combined effects of soluble factor supplementation and scaffold anisotropy on tenogenic phenotype. Type I collagen is the predominant ECM protein in tendon while scleraxis and tenascin-C are markers of tenogenic phenotype (Riley, Harrall et al. 1996; Schweitzer, Chyung et al. 2001). While growth factors IGF-1, GDF-5, and GDF-7 initially promoted COL1A1 up-regulation, this effect was not sustained over the course of the 21 day experiment (**Figure 4.12(c)**), suggesting a need to explore additional factor combinations or different doses in future studies. In contrast, growth factors did not seem to affect TNC expression until day 21 where expression in the GDF-5 and GDF-7 groups was up-regulated (**Figure 4.3(b)**). Finally, pore anisotropy promoted steady increases in SCXB expression over the course of the experiment compared to the isotropic control (**Figure 4.3(a), 4.12(a)**). While SCXB was also up-regulated in the anisotropic groups supplemented with bFGF and GDF-7, there did not appear to be a synergistic effect of anisotropy and growth factor supplementation on SCXB expression. These results indicate that for some tendon markers (SCXB) cell alignment/anisotropy may be more important while for others (TNC) growth factor cues may be the overriding factor.

While our gene expression results indicated the scaffold anisotropy plays a role in early tenogenic differentiation, it remained unclear what pathways MSCs might utilize to sense scaffold anisotropy given that scaffold pores were larger (> 150 μm) than the MSCs. We

hypothesized that canonical mechanotransduction pathways may play a role, so we designed a series of experiments where MSC-seeded anisotropic scaffolds were exposed to the myosin II inhibitor blebbistatin to remove the capability of MSCs to stretch out and "feel" the microstructure of their environment. Confocal microscopy and cell shape index analyses revealed that blebbistatin treatment had a significant effect on actin organization, resulting in rounded MSCs as opposed to MSCs stretching and spreading within anisotropic CG scaffolds in the non-treated group (**Figure 4.4(a-c)**). Further, after blebbistatin treatment MSCs showed trends towards down-regulation of COL1A1, SCXB, and TNC (**Figure 4.4(d)**).

The activation of signaling pathways associated with RhoA/ROCK, MAPK, and canonical Wnt signaling was also investigated as a function of pore anisotropy and blebbistatin treatment. Notably, RhoA/ROCK has been shown to be integral for stretch-induced fibroblastic MSC differentiation (Xu, Song et al. 2012), and increased ROCK activation was observed for cells on aligned versus non-aligned 2D electrospun substrates (Andalib, Lee et al.). Further, ERK1/2 activation was previously shown to be critical for stretch-induced collagen synthesis in tendon fibroblasts (Paxton, Hagerty et al. 2012). Finally, while differential Wnt signaling has been suggested to be prominently involved in osteogenic/chondrogenic development (Day, Guo et al. 2005), it has also been shown to be involved in tendon morphogenesis (Hartmann and Tabin 2001; Guo, Day et al. 2004) with tendon ECM components such as biglycan modulating canonical Wnt activity (Berendsen, Fisher et al. 2011). In this study, while there was no apparent effect of substrate anisotropy on ERK1/2 or canonical Wnt signaling, ROCK1 expression was significantly higher in the anisotropic scaffold group compared to the isotropic control, replicating the trend previously observed on the 2D electrospun mat (Andalib, Lee et al.) in our

3D scaffold (**Figure 4.5**). Blebbistatin treatment led to abrogation of ROCK1 up-regulation in the anisotropic group as well as downward trends in activation of ERK1/2. Taken together our results, in the context of the known role RhoA/ROCK signaling plays in mechanotransduction, suggest that microstructural contact guidance cues presented by anisotropic versus isotropic CG scaffolds can alter intracellular signaling in a similar manner to mechanical stimuli. Future studies will integrate bioreactor mechanical stimulation to possibly improve the effects observed here.

Since GDF supplementation was observed to elicit late up-regulation of TNC we wanted to further understand the mechanism behind this behavior. GDF-5 and 7 act through the canonical BMP signaling pathway, which is known to play an integral role in tendon development (Liu, Aschbacher-Smith et al. 2012). Smads are intracellular proteins that transmit cell surface receptor signals to the nucleus to enable transcription and subsequent protein synthesis. In particular, Smads 1/5/8 are known to play an important role in canonical BMP signaling (ten Dijke and Arthur 2007). While these three Smads are often grouped together, recent work has demonstrated that Smad 1 and 5, but not 8, are necessary for normal skeletal (bone and cartilage) development (Retting, Song et al. 2009) while Smad8 may be more critical for tendon morphogenesis (Hoffmann, Pelled et al. 2006). Using a commercially available siRNA against Smad8, we attempted to tease out its role in MSC tenogenic differentiation. Smad8 silencing resulted in increased spreading (reduced elongation) of MSCs (**Figure 4.6(a,b)**). Since cell elongation/stretching is known to be an important hallmark of tenogenic phenotype (Moffat, Kwei et al. 2009; Kapoor, Caporali et al. 2010), this result is indicative of reduced tenogenic phenotype. PCR analysis of characteristic tenogenic gene expression generally showed down-

regulation in response to Smad8 silencing (**Figure 4.6(c)**), further demonstrating the importance of Smad8 to tenogenesis.

While primarily focused on examining pathways to increase CG scaffold-mediated tenogenic MSC differentiation, we also examined modifications to our standard CG scaffold to enhance osteogenic and chondrogenic MSC differentiation. While differentiation down these lineages is far better characterized than tenogenic differentiation, we were interested in exploring the combined influence of scaffold structural properties and biomolecule supplementation on MSC fate. We hypothesized that osteogenic differentiation would be enhanced by the combination of a scaffold incorporating a biomimetic calcium phosphate (CaP) phase and further supplementation with factors in the BMP family (BMP-2 and 7) or with standard osteogenic induction media. Mineralized CG scaffolds used in this study, in addition to providing a more mechanically robust microenvironment (Weisgerber, Kelkhoff et al. in review) that may drive osteogenic differentiation itself (Engler, Sen et al. 2006), also display a biomimetic calcium phosphate phase that has been shown in a range of previous studies to improve osteogenic outcomes in terms of new matrix deposition (Kang, Kim et al. 2011; Curtin, Cunniffe et al. 2012) and osteogenic gene expression (Beck, Zerler et al. 2000; Muller, Bulnheim et al. 2008).

Osteogenic differentiation was tracked by measuring the expression of the osteogenic genes ALP, RUNX2, and OCN and through subsequent histological analysis. Osteogenic induction media had a greater effect on osteogenic gene expression than select BMP-2/7 supplementation, leading to significant up-regulation of all three genes by day 21 (**Figure 4.7**). While BMP supplementation led to ALP and OCN up-regulation at the intermediate time point, the positive

effects of supplementation did not reach that of the osteogenic induction media (**Figure 4.13**). Incorporation of a mineral phase improved ALP and RUNX2 expression by day 21. Although ALP expression in the mineralized osteogenic group initially lagged behind that of its non-mineralized counterpart, likely due to reduced MSC metabolic activity in the more dense and less permeable (Weisgerber, Kelkhoff et al. in review) mineralized scaffold (**Figure 4.2(b)**), the mineralized osteogenic scaffold showed the highest degree of osteogenesis. By day 21 ALP expression was twice as high in the mineralized osteogenic group. Histological analysis confirmed that the combination of osteogenic induction media and the mineralized scaffold promoted osteogenesis as evidenced by increased staining for mineral via Alizarin red compared to other groups (**Figure 4.8**).

Finally, we hypothesized that chondrogenic MSC differentiation would be ideally achieved in CG scaffolds by lowering scaffold relative density in conjunction with soluble supplementation of TGF-β (with or without chondrogenic induction media). Scaffold relative density and crosslinking density have been shown to be important factors towards resisting cell-mediated contraction (Torres, Freyman et al. 2000; Vickers, Gotterbarm et al. 2010; Caliari, Weisgerber et al. 2012; Rowland, Lennon et al. 2013). In particular, lowering the degree of CG scaffold crosslinking led to increased contraction, cellular condensation, and MSC chondrogenesis as measured by type II collagen and GAG synthesis (Vickers, Gotterbarm et al. 2010). Here we aimed to replicate this effect in a lower density scaffold, and possibly enhance it through the use of soluble biomolecular supplementation. This effort was also motivated by features of the native osteotendinous junction where there is reduced stiffness in a small part of the fibrocartilagenous transition between tendon and bone. This dip in stiffness has been hypothesized to be critical for

alleviating stress concentrations and maintaining joint patency (Thomopoulos, Williams et al. 2003; Genin, Kent et al. 2009).

Lower density scaffolds consistently displayed lower metabolic activity than the isotropic scaffold group after day 7 (**Figure 4.2(c)**), most likely due to a combination of extensive MSC-mediated contraction, reduced metabolite diffusion, and differentiation into less metabolically-active cells (**Figure 4.10**). Chondrogenic phenotype was initially tracked through the expression of chondrogenic genes COL2A1, SOX9, and ACAN (**Figure 4.9, 4.14**). As with osteogenic differentiation, the chondrogenic induction media had the most profound effect on lineage specification while soluble TGF-β1 or 3 alone had little effect. However, the combination of the low density scaffold with chondrogenic induction media clearly led to the most chondrogenic transcriptomic profile with significantly increased expression of all three markers tested after day 21. Histology also revealed strong staining for GAG deposition in the low density chondrogenic group compared to other experimental groups (**Figure 4.10**). Additionally, H&E-stained sections showed extensive pore contraction and cellular condensation in the lower density groups, which likely promoted chondrogenesis (**Figure 4.10**).

4.6 Conclusions

This work used simple modifications to a standard CG scaffold to investigate the roles of scaffold structure (geometric anisotropy, mineral content, relative density) in combination with biomolecule supplementation on driving tenogenic, osteogenic, and chondrogenic MSC differentiation respectively. The importance of scaffold microstructural anisotropy for enhancing

tenogenic differentiation was shown by increased expression of the phenotype marker SCXB as well as increased ROCK1 levels in anisotropic compared to isotropic scaffolds. Notably, small molecule cytoskeletal or Smad8 inhibition abrogated these effects. MSC osteogenic differentiation was enhanced by osteogenic induction media, although the inclusion of a mineral phase in the scaffold led to elevated ALP and RUNX2 expression as well as increased mineralization after 21 days. Chondrogenic differentiation was enhanced by combining classic chondrogenic induction media with a low density scaffold that enhanced cellular condensation and led to significant up-regulation of COL2A1 and ACAN as well as increased GAG production. Together, these data provide insight into critical scaffold instructive cues that should inform the development of CG scaffolds for a variety of single and multi-tissue musculoskeletal tissue engineering applications. In particular, these data suggest a scaffold with an anisotropic tendon region and a mineralized bone region, joined with lower density interface and coupled with spatially-graded biomolecular cues, may be optimal for osteotendinous repair.

4.7 Tables

Tenogenic	**Scaffold type, biomolecule dose**	
Biomolecule treatment	**CG (isotropic, high density)**	**CG (anisotropic, high density)**
None	N/A	N/A
bFGF		5 ng/mL
IGF-1		100 ng/mL
GDF-5		100 ng/mL
GDF-7		100 ng/mL
Chondrogenic	**Scaffold type, biomolecule dose**	
Biomolecule treatment	**CG (isotropic, high density)**	**CG (isotropic, low density)**
None	N/A	N/A
Chondrogenic	N/A	N/A
TGF-β1		5 ng/mL
TGF-β3		5 ng/mL
Osteogenic	**Scaffold type, biomolecule dose**	
Biomolecule treatment	**CG (isotropic, high density)**	**CGCaP (40 wt% mineral)**
None	N/A	N/A
Osteogenic	N/A	N/A
BMP-2		50 ng/mL
BMP-7		50 ng/mL

Table 4.1. Study design with scaffold type and biomolecule supplementation combinations specified for each desired lineage. Two scaffold types (six experimental groups total) were assayed for each lineage. CG and CGCaP scaffolds are sometimes referred to in the text as "non-mineralized" and "mineralized" respectively.

Transcript	Sequence	Reference
ACAN	Forward: 5'-TGCATTCCACGAAGCTAACCTT-3' Reverse: 5'-GACGCCTCGCCTTCTTGAA-3'	(Zhou, Xu et al. 2011)
ALP	Forward: 5'-AGCACTCCCACTTCATCTGGAA-3' Reverse: 5'-GAGACCCAATAGGTAGTCCACATTG-3'	(Zhou, Xu et al. 2011)
COL1A1	Forward: 5'-CAGCCGCTTCACCTACAGC-3' Reverse: 5'-TTTTGTATTCAATCACTGTCTTGCC-3'	(Zhou, Xu et al. 2011)
COL2A1	Forward: 5'-GGCAATAGCAGGTTCACGTACA-3' Reverse: 5'-CGATAACAGTCTTGCCCCACTT-3'	(Zhou, Xu et al. 2011)
GAPDH	Forward: 5'-AGAAAAACCTGCCAAATATGATGAC-3' Reverse: 5'-TGGGTGTCGCTGTTGAAGTC-3'	(Zhou, Xu et al. 2011)
OCN	Forward: 5'-CAGCGAGGTAGTGAAGAGA-3' Reverse: 5'-GAAAGCCGATGTGGTCAG-3'	(Zhou, Xu et al. 2011)
RUNX2	Forward: 5'-AGAAGGCACAGACAGAAGCTTGA-3' Reverse: 5'-AGGAATGCGCCCTAAATCACT-3'	(Zhou, Xu et al. 2011)
SCXB	Purchased from Qiagen	N/A
SOX9	Forward: 5'-AGCGAACGCACATCAAGAC-3' Reverse: 5'-GCTGTAGTGTGGGAGGTTGAA-3'	(Zhou, Xu et al. 2011)
TNC	Forward: 5'-TTCACTGGAGCTGACTGTGG-3' Reverse: 5'-TAGGGCAGCTCATGTCACTG-3'	(Pauly, Klatte et al. 2010)

Table 4.2. Primer sequences used for PCR.

4.8 Figures

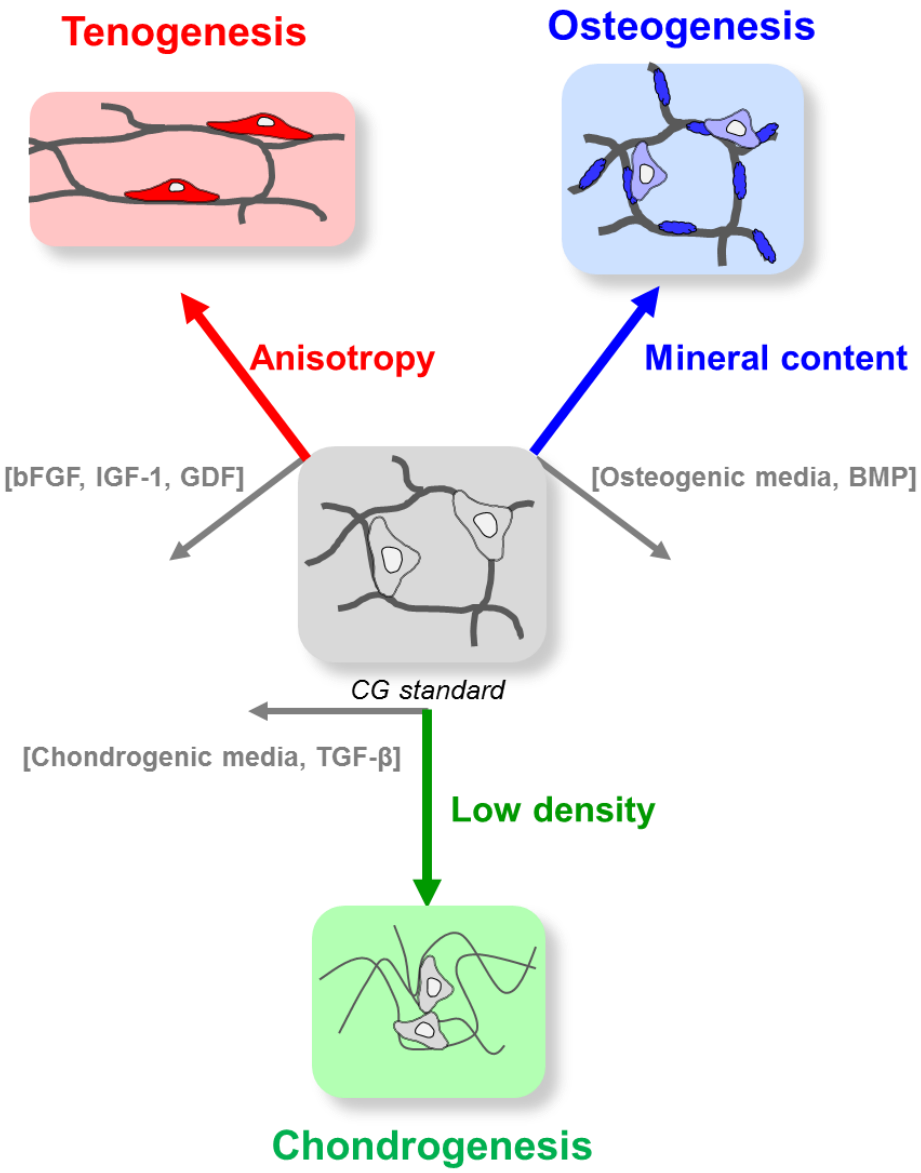

Figure 4.1. Schematic of study paradigm. Biomaterial-mediated repair of orthopedic interfaces requires spatially-graded presentation of instructive cues to promote lineage specification. This study used selective modification of a 3D CG scaffold to assess combinations of structural and biochemical instructive cues for driving MSC differentiation down tenogenic, chondrogenic, and osteogenic lineages respectively towards the development of integrated biomaterials for orthopedic interfacial engineering.

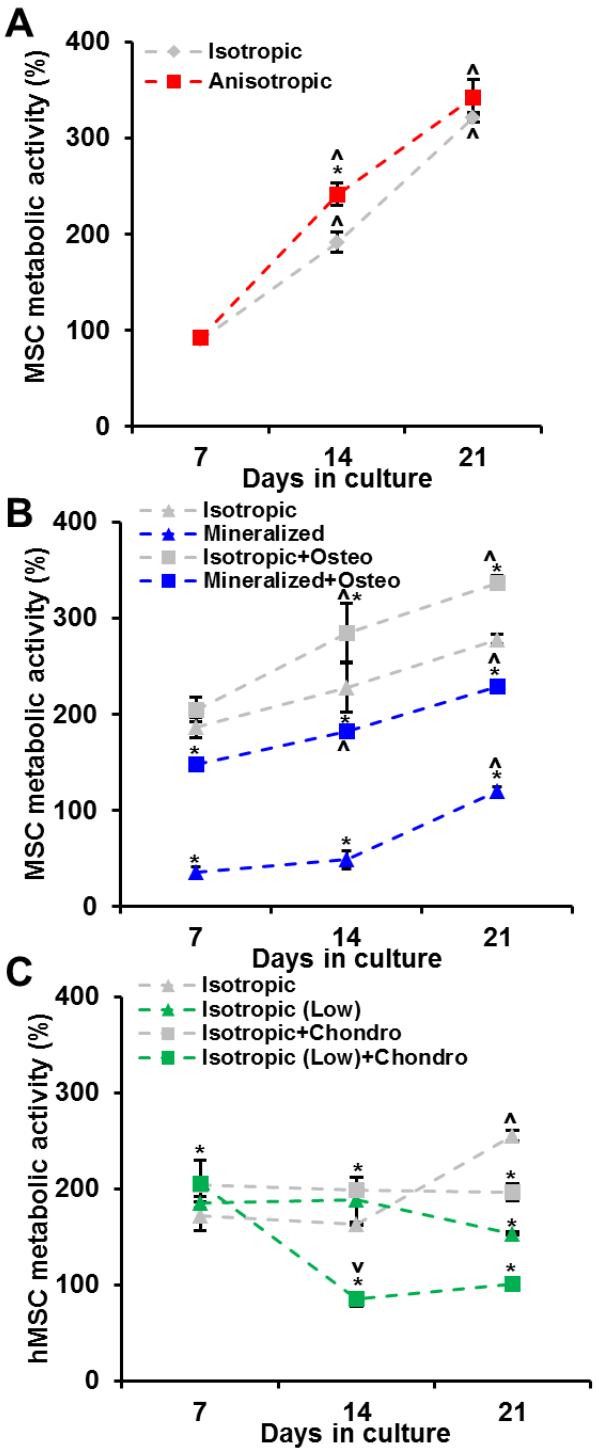

Figure 4.2. MSC metabolic activity in CG scaffolds. Metabolic activity was measured at days 7, 14, and 21 using alamarBlue® incubation on MSC-seeded scaffolds to drive A) tenogenic, B) osteogenic, and C) chondrogenic differentiation (n = 3). *: significant difference at that time point compared to isotropic group. ∧: significant increase compared to previous time point. ∨: significant decrease compared to previous time point.

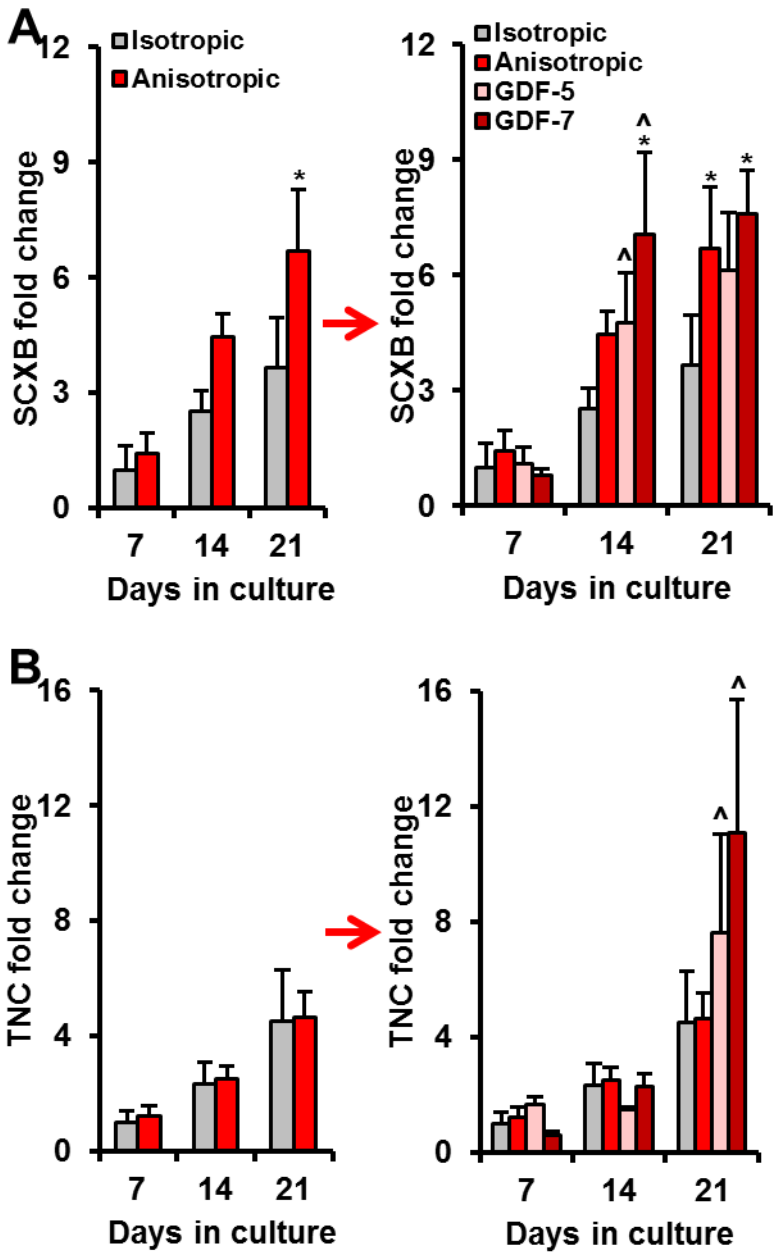

Figure 4.3. MSC tenogenic gene expression in response to different pore anisotropy and soluble factor supplementation conditions. Expression of tenogenic genes A) SCXB and B) TNC was measured at days 7, 14, and 21 (n = 3). While GDF supplementation did not improve SCXB expression, it is elicited significant up-regulation of TNC at day 21.*: significant difference at that time point compared to isotropic group. ^: significant up-regulation compared to previous time point.

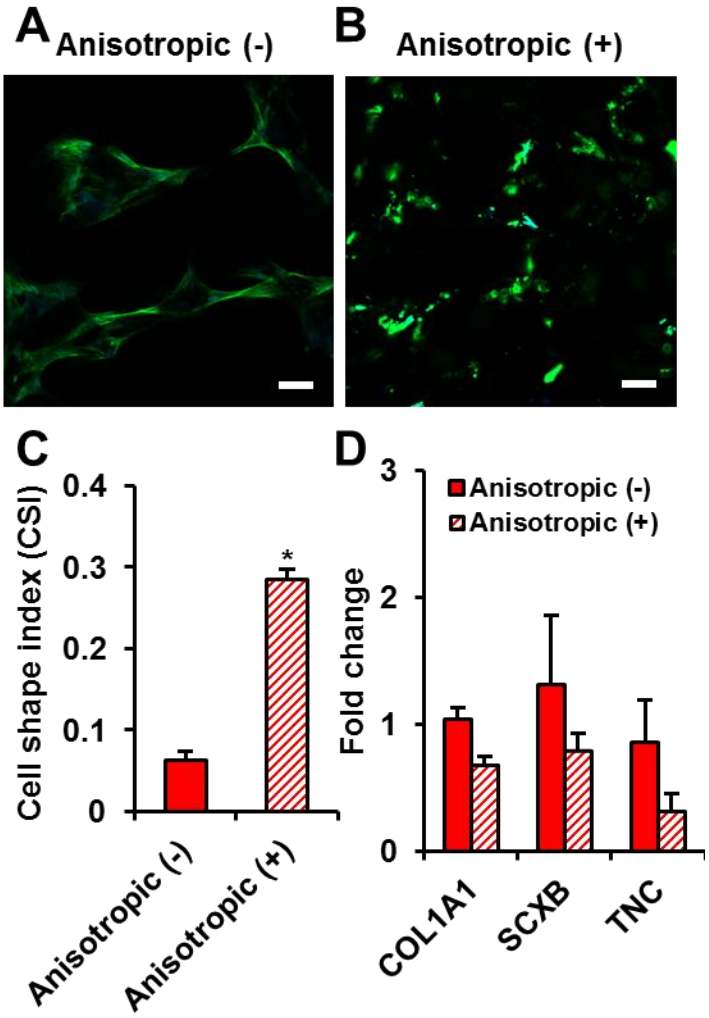

Figure 4.4. MSC cytoskeletal organization and gene expression within CG scaffolds in response to blebbistatin. Confocal micrographs of MSC-seeded scaffolds reveal the influence of blebbistatin treatment (50 µM) on actin organization. MSCs stretch and elongate when cultured without blebbistatin (-) in A) anisotropic scaffolds, while they become less spread and more rounded in response to B) blebbistatin (+). *Green channel*: actin (Alexa Fluor® 488 phalloidin). *Blue channel*: nuclei (DAPI). *Scale bar*: 50 µm. C) Cell shape index results show significantly higher (*) circularity in MSCs treated with blebbistatin compared to non-treated groups. D) Expression of tenogenic genes COL1A1, SCXB, and TNC was measured at day 7 (n = 3).

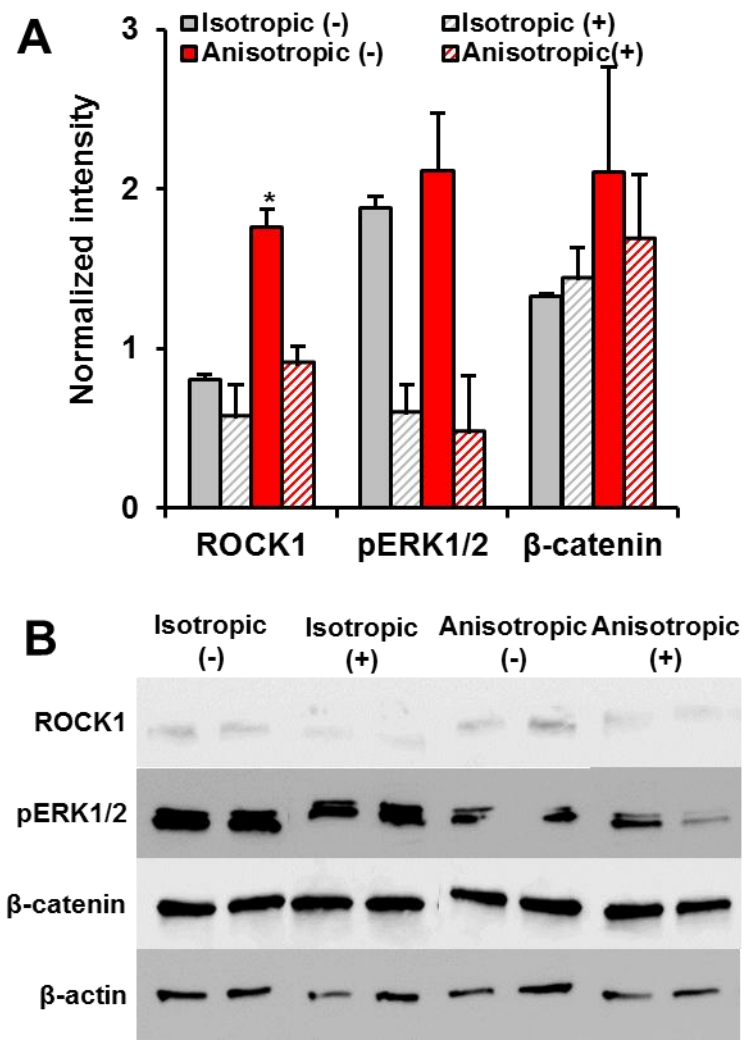

Figure 4.5. Protein expression in isotropic versus anisotropic scaffolds with and without blebbistatin treatment. A) Quantified protein levels of ROCK1, pERK1/2, and β-catenin. ROCK1 levels are significantly higher in anisotropic scaffolds compared to other groups. B) Western blots of ROCK1, pERK1/2, β-catenin, and β-actin (loading control) proteins. *: significantly higher than all other experimental groups.

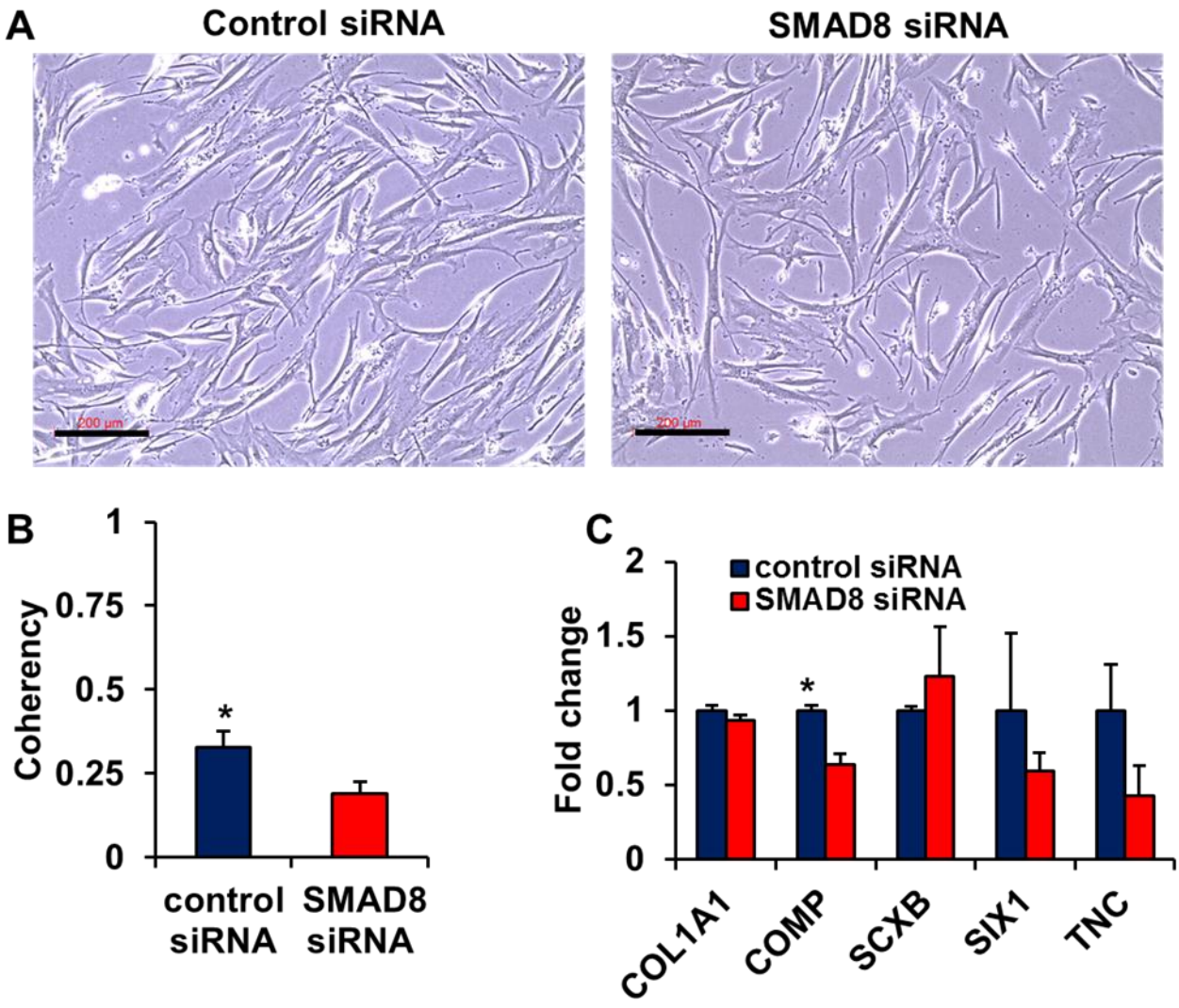

Figure 4.6. Silencing SMAD8 to influence tenogenic differentiation. A) Optical micrographs of MSCs in 2D culture following treatment with control siRNA (*left*) or siRNA targeting SMAD8 (*right*). Scale *bar*: 200 µm. B) MSC coherency, a measure of cell elongation, was significantly lower in the SMAD8 siRNA treated group. C) Expression of tenogenic genes in response to siRNA treatment. *: significantly higher expression.

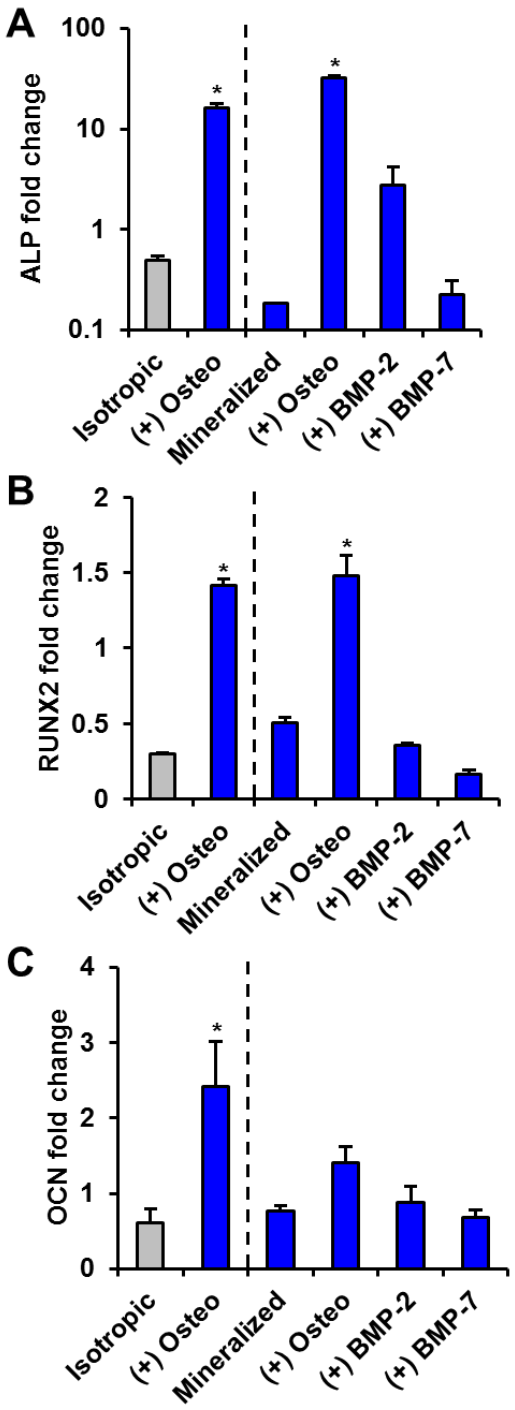

Figure 4.7. MSC osteogenic gene expression in response to scaffold mineralization and soluble factor supplementation. Day 21 expression of osteogenic genes A) ALP, B) RUNX2, and C) OCN was measured (n = 3) with osteogenic induction media promoting significantly elevated expression levels. *: significant difference compared to isotropic control.

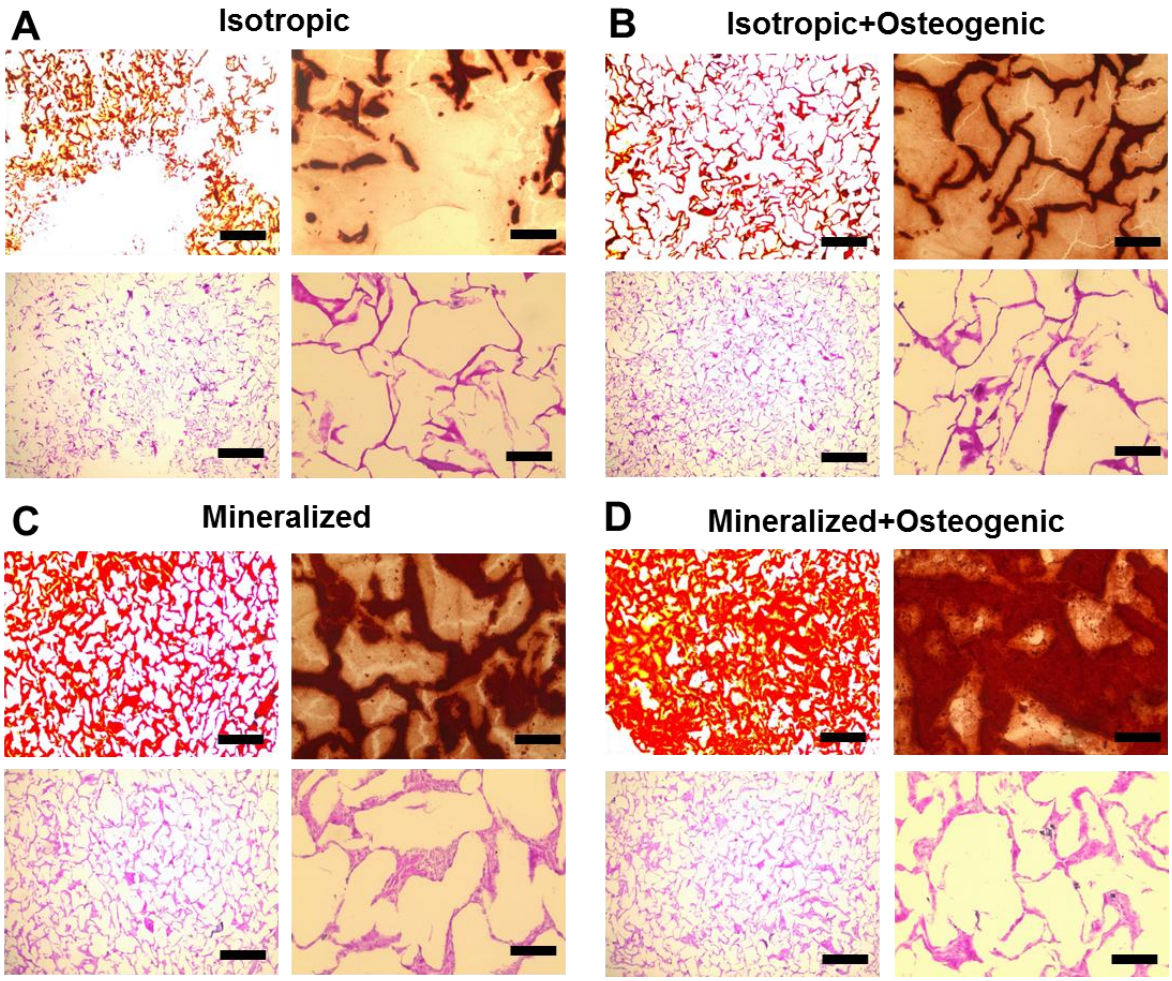

Figure 4.8. Alizarin red and H&E staining from osteogenesis studies. Representative histology sections from day 21 time point reveal the highest mineral content in the Mineralized+Osteogenic group with similar cellular distribution observed in all groups. A) Isotropic, B) Isotropic+Osteogenic, C) Mineralized, D) Mineralized+Osteogenic. *Scale bars*: 500 µm (4x objective images on left), 100 µm (20x objective images on right).

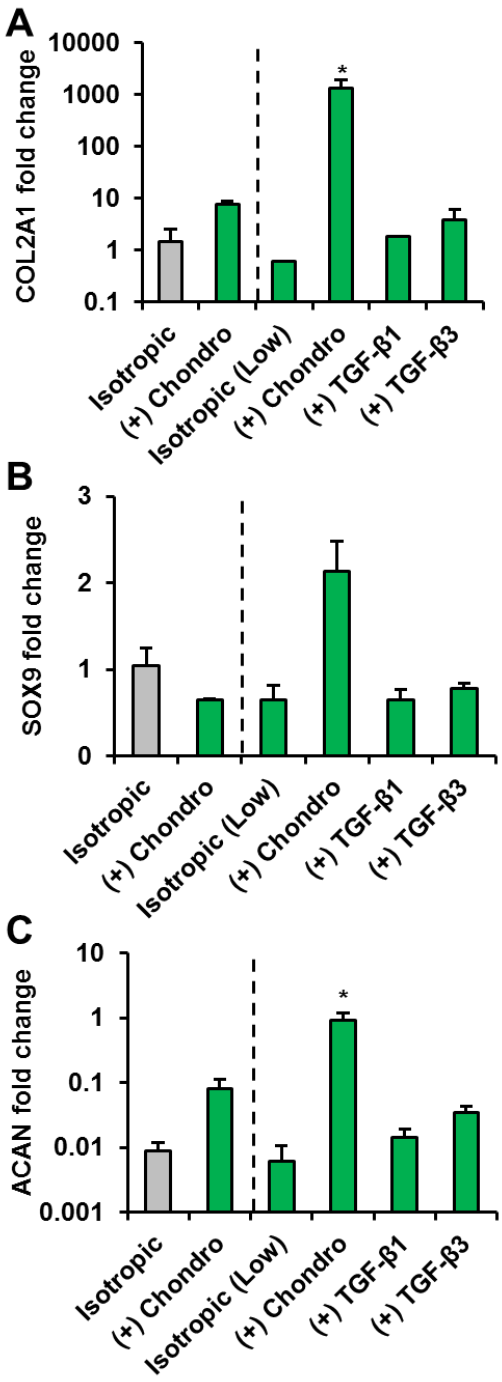

Figure 4.9. MSC chondrogenic gene expression in response to varying scaffold relative density and soluble factor supplementation. Day 21 expression of chondrogenic genes A) COL2A1, B) SOX9, and C) ACAN was measured (n = 3) with the combination of a low density scaffold with chondrogenic induction media promoting significant up-regulation of COL2A1 and ACAN. *: significant difference compared to isotropic control.

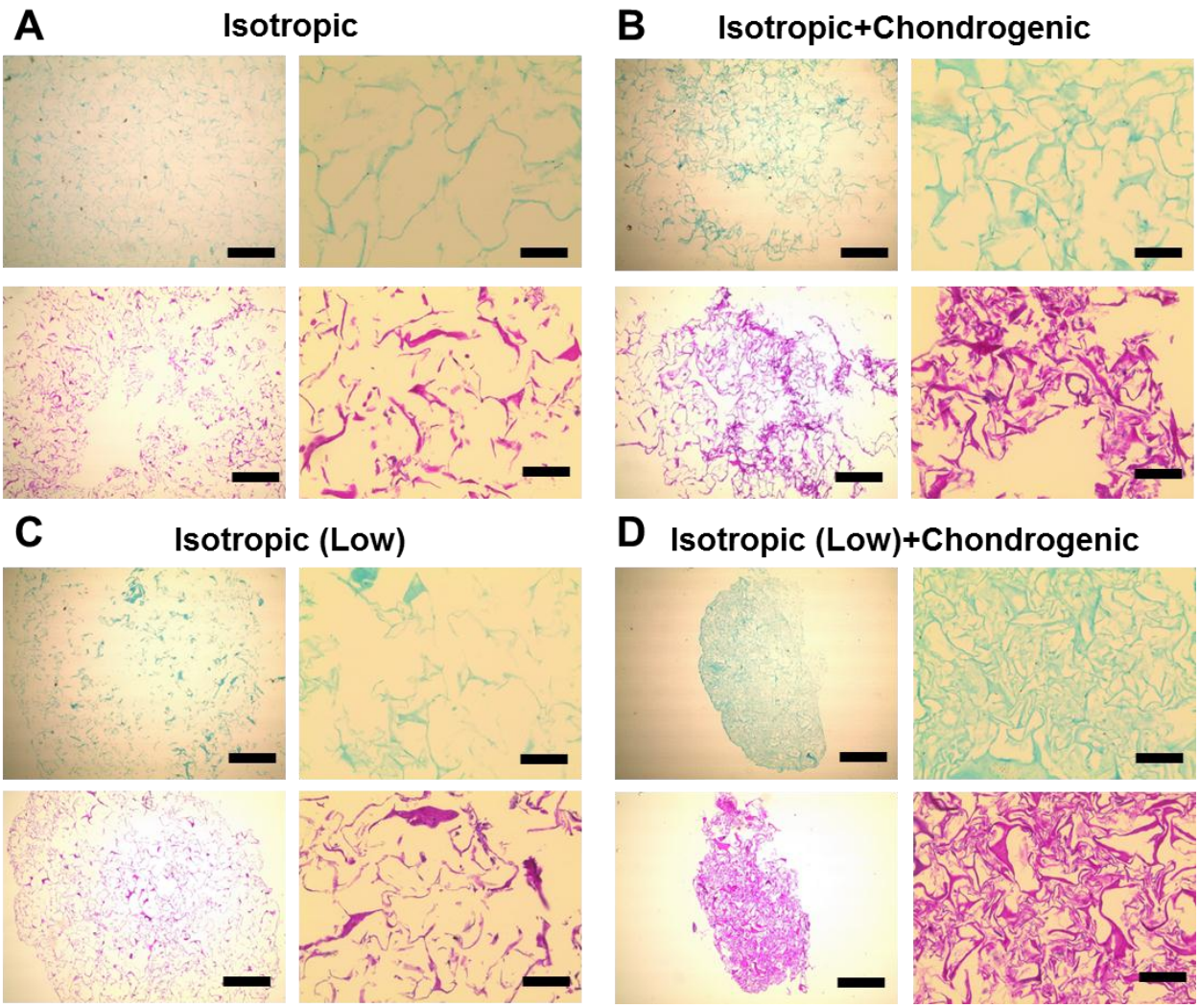

Figure 4.10. Alcian blue and H&E staining from chondrogenesis studies. Representative histology sections from day 21 time point reveal higher GAG content and cellular condensation in the Isotropic (Low)+Chondrogenic group. A) Isotropic, B) Isotropic+Chondrogenic, C) Isotropic (Low), D) Isotropic (Low)+Chondrogenic. *Scale bars*: 500 µm (4x objective images on left), 100 µm (20x objective images on right).

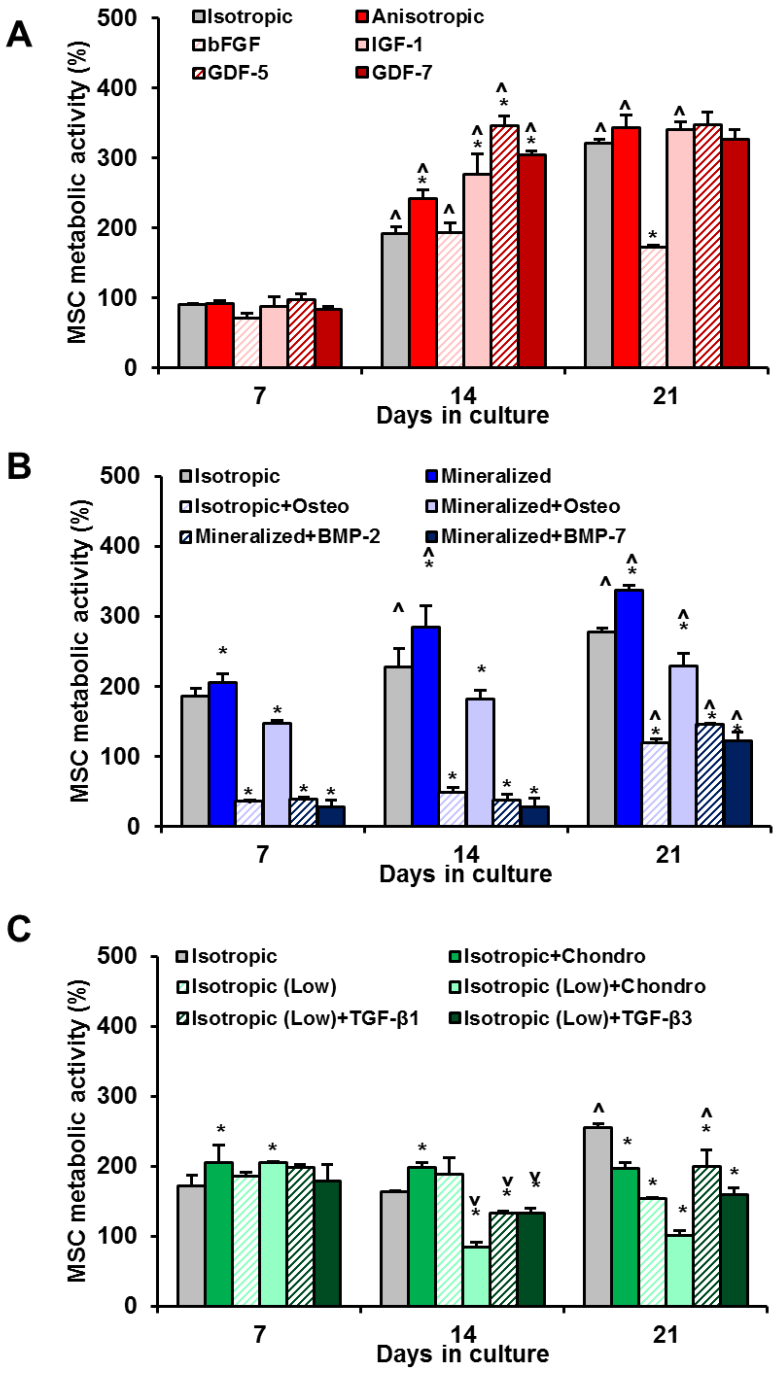

Figure 4.11. Complete MSC metabolic activity in CG scaffolds. Metabolic activity was measured at days 7, 14, and 21 using alamarBlue® incubation on MSC-seeded scaffolds to drive A) tenogenic, B) osteogenic, and C) chondrogenic differentiation (n = 3). *: significant difference at that time point compared to isotropic group. ∧: significant increase compared to previous time point. ∨: significant decrease compared to previous time point.

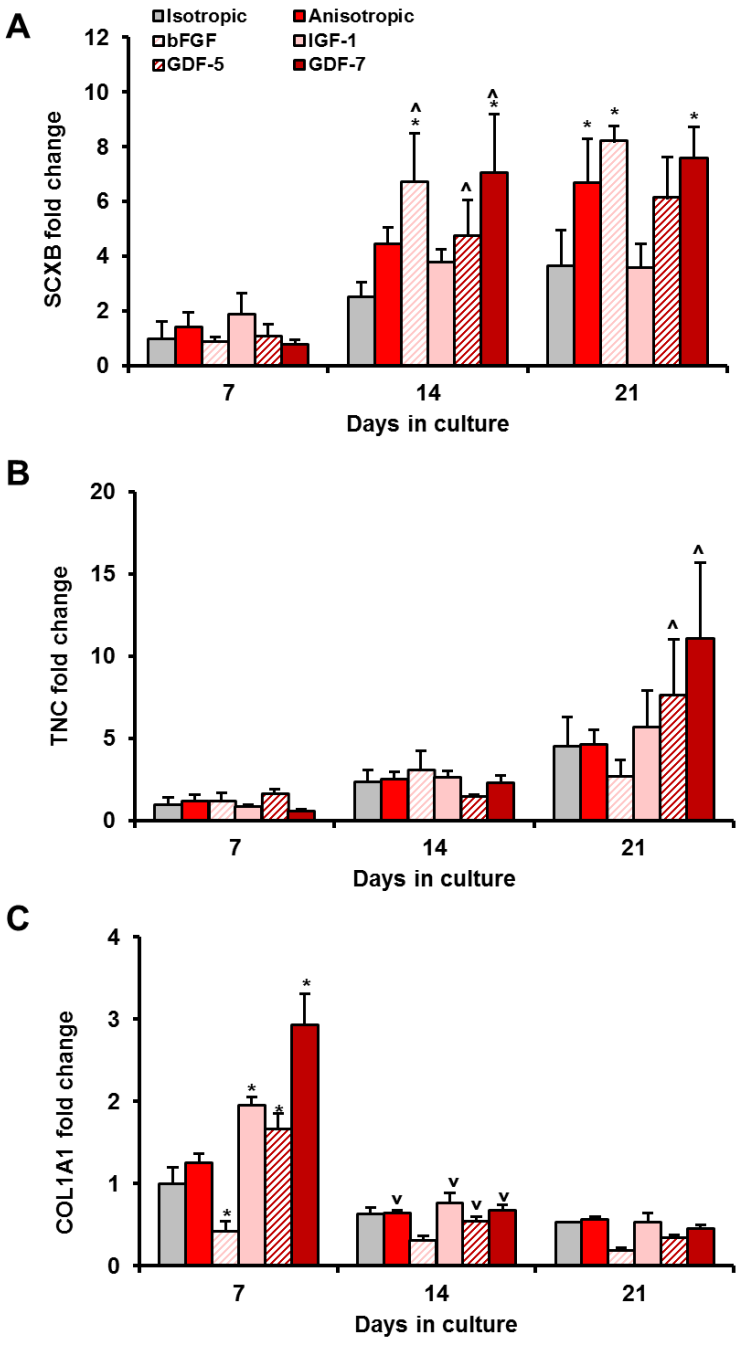

Figure 4.12. Complete MSC tenogenic gene expression in response to different pore anisotropy and soluble factor supplementation conditions. Expression of tenogenic genes A) SCXB, B) TNC, and C) COL1A1 was measured at days 7, 14, and 21 (n = 3). *: significant difference at that time point compared to isotropic group. ∧: significant up-regulation compared to previous time point. ∨: significant down-regulation compared to previous time point.

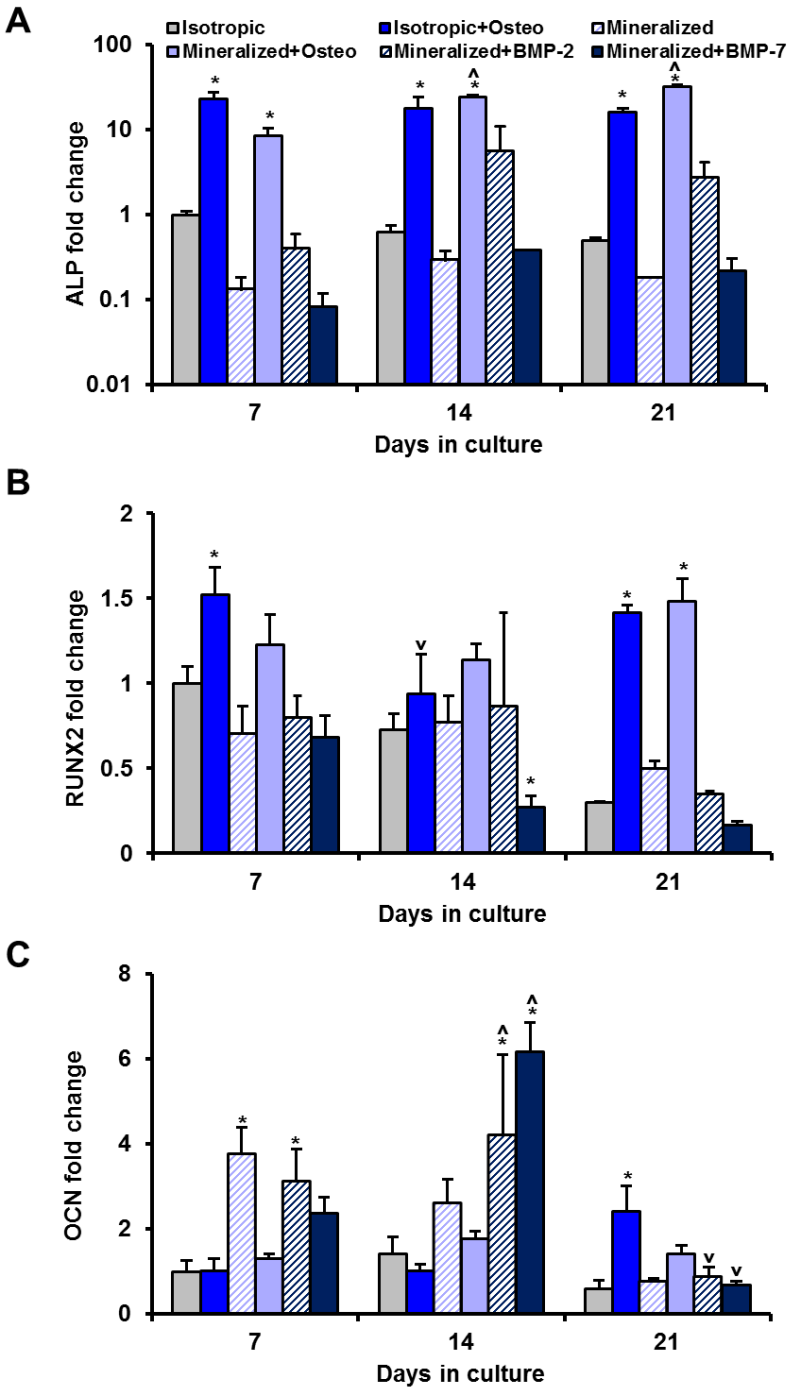

Figure 4.13. Complete MSC osteogenic gene expression in response to scaffold mineralization and soluble factor supplementation. Expression of osteogenic genes A) ALP, B) RUNX2, and C) OCN was measured at days 7, 14, and 21 (n = 3). *: significant difference at that time point compared to isotropic group. ∧: significant up-regulation compared to previous time point. ∨: significant down-regulation compared to previous time point.

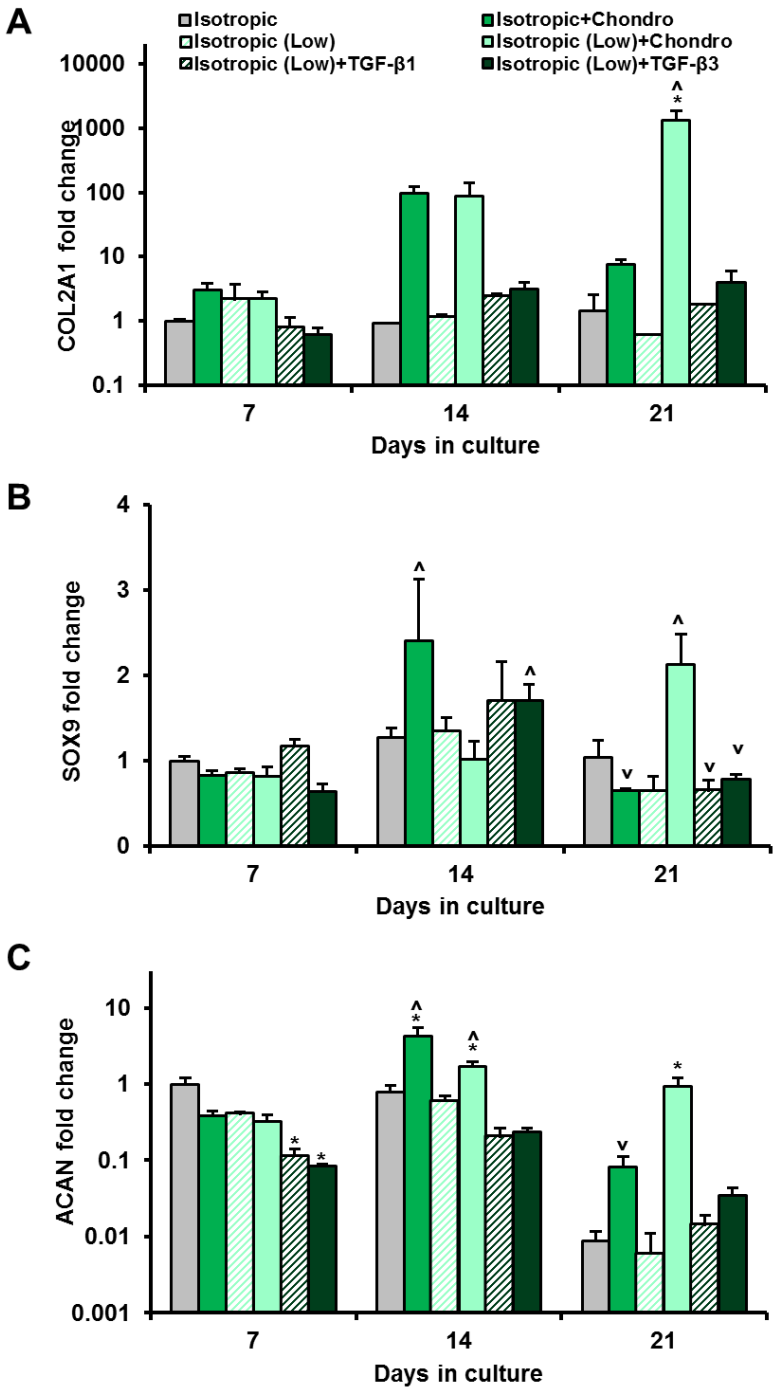

Figure 4.14. Complete MSC chondrogenic gene expression in response to varying scaffold relative density and soluble factor supplementation. Expression of chondrogenic genes A) COL2A1, B) SOX9, and C) ACAN was measured at days 7, 14, and 21 (n = 3). *: significant difference at that time point compared to isotropic control. ∧: significant up-regulation compared to previous time point. ∨: significant down-regulation compared to previous time point.

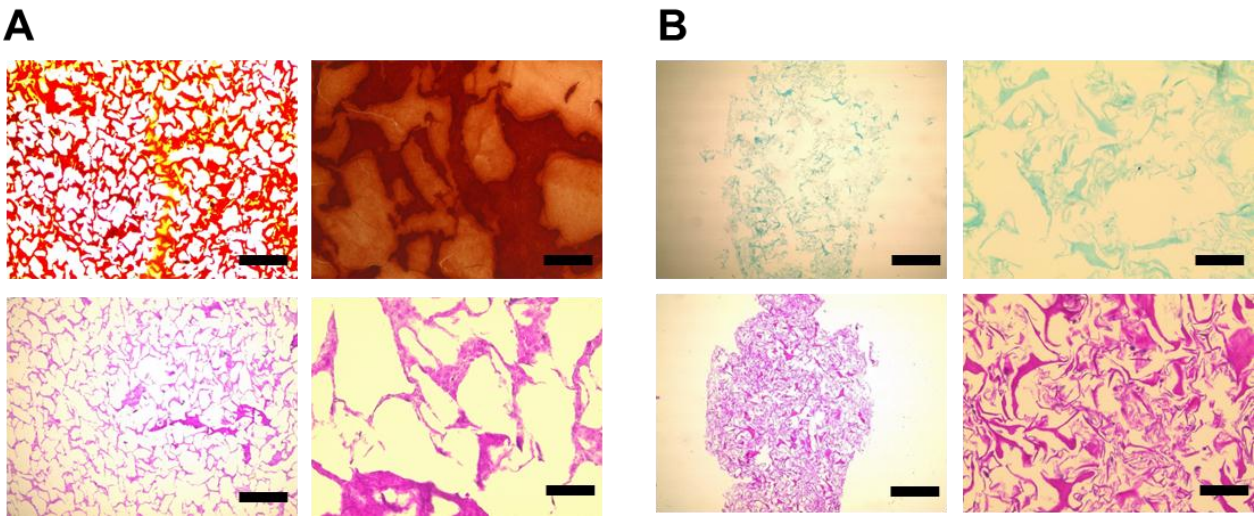

Figure 4.15. Histology from growth factor-supplemented groups. Representative histology sections from day 21 time point for growth factor-treated groups. A) Mineralized+BMP-2, B) Low Density+TGF-β3. *Scale bars*: 500 μm (4x objective images on left), 100 μm (20x objective images on right).

CHAPTER 5: COLLAGEN-GAG SCAFFOLD BIOPHYSICAL PROPERTIES BIAS MSC LINEAGE SELECTION IN THE PRESENCE OF MIXED SOLUBLE SIGNALS[5]

5.1 Chapter overview

Biomaterial strategies for regenerating multi-tissue structures require unique approaches. One strategy is to design scaffolds so that their local biophysical properties can enhance site-specific effects of an otherwise heterogeneous biomolecular environment. This investigation examined the role of biomaterial physical properties (relative density, mineral content) on human mesenchymal stem cell (MSC) phenotype in the presence of mixed soluble signals to drive osteogenesis or chondrogenesis. We tested a series of 3D collagen-glycosaminoglycan (CG) scaffolds with properties inspired by extracellular matrix (ECM) characteristics across the osteotendinous interface (tendon, cartilage, and bone). We found selective scaffold mineralization induced a depressed chondrogenic response compared to non-mineralized groups as demonstrated by gene expression and histological analyses. Interestingly, the greatest chondrogenic response was found in a higher density, non-mineralized scaffold variant despite increased contraction and cellular condensation in lower density non-mineralized scaffolds. In fact, the lower density scaffolds demonstrated significantly higher expression of osteogenic transcripts as well as ample mineralization after 21 days of culture. This effect may be due to local stiffening of the scaffold microenvironment as the scaffold contracts, leading to increased cell density, accelerated differentiation, and possible endochondral ossification as evidenced by a transition from a GAG-rich milieu to higher mineralization at later culture times. These findings will help shape the design rules for graded biomaterials to regenerate distinct fibrillar, fibrocartilagenous, and mineralized regions of orthopedic interfaces.

[5] This chapter has been adapted from the following publication:
Caliari, S. R. and B. A.C. Harley (submitted). "Collagen-GAG scaffold biophysical properties bias MSC lineage selection in the presence of mixed soluble signals."

5.2 Introduction

Orthopedic interfaces such as osteochondral and osteotendinous junctions contain gradations of extracellular matrix (ECM) components, both organic (*e.g.*, collagens, proteoglycans) and inorganic (*e.g.*, hydroxyapatite mineral) (Galatz, Sandell et al. 2006; Galatz, Rothermich et al. 2007; Genin, Kent et al. 2009). Additionally, a mixed set of soluble regulators of cell behavior such as growth factors and cytokines reside within these graded interfaces (Kuo, Petersen et al. 2008). Tissue engineering strategies for spatially-graded, multi-tissue structures therefore require a nuanced understanding of both soluble and insoluble (microstructural, mechanical, and compositional) regulators of cell behavior.

An emerging paradigm for scaffold design in orthopedic interface engineering is the creation of biomaterials containing spatially-ordered biophysical and/or biochemical properties. Such multi-compartment biomaterials may be used to drive spatially-defined mesenchymal stem cell (MSC) differentiation or alternatively support the activity of multiple compartment-specific differentiated cell types (*e.g.*, fibroblasts, chondrocytes, and osteoblasts) (Xu and Murrell 2008; Fox, Bedi et al. 2011; Ker, Chu et al. 2011). While directing MSC differentiation in a spatially-selective manner may become a more efficient and clinically viable approach, it is difficult to selectively regulate differentiation through material properties alone.

The most common approach for driving MSC differentiation *in vitro* is the application of lineage-specific media cocktails containing various soluble factors (*e.g.*, small molecules, amino

acids, cytokines, and/or steroids). Although these differentiation media have been used extensively to drive osteogenic, chondrogenic, and adipogenic MSC differentiation (Pittenger, Mackay et al. 1999), their usefulness is limited when trying to recapitulate the dynamic microenvironments of multi-tissue structures where graded, and sometimes competing, soluble and insoluble signals influence the phenotype of multiple classes of differentiated cell types.

As a first order solution, mixed media formulations using combinations of osteogenic, chondrogenic, and/or adipogenic media may be applied to cell-biomaterial constructs. Here, biomaterial characteristics may bias cell response to a cocktail of signals containing multiple, disparate differentiation cues. To better design such systems, it is important to unravel the role material properties play on MSC differentiation potential in the presence of multiple competing soluble cues. This approach has been extensively applied in combined osteogenic-adipogenic (Khetan and Burdick 2010; Kilian, Bugarija et al. 2010) as well as osteogenic-chondrogenic environments (Wagner, Lindsey et al. 2008). These studies revealed the influence of properties such as elastic modulus, pore size, ligand density, and chemical composition on MSC lineage specification and signal transduction. Critically, these studies represent a paradigm shift away from designing biomaterials that simply enhance the effects of soluble factors. Instead, they suggest that through improved understanding of the role material properties play in differentiation potential, stem cell fate can be biased towards specific lineages in the presence of heterogeneous biomolecular environments more analogous to those encountered *in vivo*.

This study explores the potential for systematic alteration of a collagen-glycosaminoglycan (CG) scaffold platform to bias osteogenic versus chondrogenic MSC differentiation. CG biomaterials

have been used in diverse regenerative medicine applications ranging from clinical treatment of skin (Yannas, Lee et al. 1989) and peripheral nerve (Chamberlain, Yannas et al. 1998) defects to use as model systems to address fundamental questions about cellular processes such as adhesion (O'Brien, Harley et al. 2005), motility (Harley, Kim et al. 2008), and differentiation (Farrell, O'Brien et al. 2006). This chapter describes the influence of CG scaffold relative density and mineral content on the differentiation potential of MSCs in the presence of mixed osteogenic and chondrogenic signals. We investigated three scaffold groups: a low density, non-mineralized scaffold that we hypothesized to be amenable to chondrogenesis (Farrell, O'Brien et al. 2006; Vickers, Squitieri et al. 2006), a higher density variant with superior mechanical competence more suitable for tendon/ligament tissue engineering (Caliari, Weisgerber et al. 2012), and a mineralized CG scaffold previously developed for bone tissue engineering applications (Harley, Lynn et al. 2010). While variants of these scaffolds have previously been shown to support separate osteogenic and chondrogenic MSC differentiation in the presence of differentiation media (Farrell, O'Brien et al. 2006), the impact of CG scaffold physical properties, such as relative density and mineral content, on biasing MSC differentiation in the presence of competing soluble signals has not been evaluated. Further, elucidating the influence of scaffold physical properties on MSC lineage specification would inform the design of materials to regenerate multi-tissue structures such as osteochondral and osteotendinous interfaces.

5.3 Materials and methods

*All reagents were purchased from Sigma-Aldrich (St Louis, MO) unless otherwise specified

5.3.1 Precursor suspension preparation

Three different collagen-GAG suspensions were prepared to make low density, high density, and mineralized CG scaffold variants. Low density and high density non-mineralized CG suspensions consisted of type I collagen from bovine Achilles tendon and chondroitin sulfate in 0.05 M acetic acid (Yannas, Burke et al. 1980). Suspensions were prepared at 0.5% w/v or 1.5% w/v collagen (collagen:GAG ratio of 11.25:1) for the low versus high density variants respectively. Calcium phosphate-mineralized collagen-GAG (CGCaP) suspension was produced from collagen (1.9 w/v%) and GAG (0.84 w/v%) as before along with calcium salts ($Ca(OH)_2$, $Ca(NO_3)_2 \cdot 4H_2O$) in phosphoric acid. A titrant-free concurrent mapping method was used to generate CGCaP suspension that yielded scaffolds with 40 wt% mineral content (Lynn, Best et al. 2010).

5.3.2 Scaffold fabrication via freeze-drying

Scaffolds were fabricated via lyophilization in a Genesis freeze-dryer (VirTis, Gardiner, NY) using a constant cooling rate method as previously described (O'Brien, Harley et al. 2004). Briefly, CG or CGCaP suspensions were degassed and added to 3" x 3" polysulfone freeze-drying molds, then cooled at a constant rate of 1°C/min to a final freezing temperature of -10°C. The suspensions were maintained at this temperature for 2 h to completely freeze the suspension followed by sublimation of the ice crystals at 0°C and 200 mTorr to produce dry scaffolds with pores > 150 μm (Caliari, Weisgerber et al. 2012; Weisgerber, Kelkhoff et al. in review).

5.3.3 Scaffold crosslinking

CG scaffolds were dehydrothermally crosslinked at 105°C for 24 h under vacuum (< 25 torr) in a vacuum oven (Welch, Niles, IL) following lyophilization. Additional chemical crosslinking for all CG and CGCaP scaffolds was performed using a mixture of 1-ethyl-3-[3-dimethylaminopropyl] carbodiimide hydrochloride (EDC) and *N*-hydroxysulfosuccinimide (NHS) at a molar ratio of 5:2:1 EDC:NHS:COOH, where COOH represents the scaffold carboxyl (collagen) content (Olde Damink, Dijkstra et al. 1996; Harley, Leung et al. 2007), in PBS for 1.5 h at 25°C.

5.3.4 Cell culture

Human bone marrow-derived mesenchymal stem cells (MSCs) were purchased from Lonza (Walkersville, MD). The MSCs were cultured in complete mesenchymal stem cell growth medium purchased from the manufacturer (Lonza) at 37°C and 5% CO_2, fed twice a week, and used at passage 6 for all experiments.

5.3.5 Cell-seeded scaffold culture conditions

CG and CGCaP scaffold pieces (6 mm diameter, 3 mm thickness) were seeded with MSCs using a previously validated static seeding method (O'Brien, Harley et al. 2005). Briefly, scaffolds were seeded with 7.5 x 10^4 MSCs per 20 µL media (10 µL on each side of scaffold) in ultra-low attachment 6-well plates (Corning Life Sciences, Lowell, MA). Cells were allowed to attach for 2.5 h before adding media to well plates. Cell-seeded scaffolds were cultured at 37°C and 5% CO_2 and fed twice a week with a 1:1 mix of osteogenic and chondrogenic differentiation media as supplied by Lonza. For histology studies, control scaffolds were cultured in standard growth media (Lonza).

5.3.6 MSC metabolic activity quantification

The mitochondrial metabolic activity of MSCs seeded within scaffold pieces was quantified using the alamarBlue® assay (Tierney, Jaasma et al. 2009). Cell-seeded scaffolds were incubated in alamarBlue® solution (Invitrogen, Carlsbad, CA) with gentle shaking for 2 h. The reduction of resazurin in the solution by metabolically active cells to the fluorescent byproduct resorufin was measured on a fluorescent spectrophotometer (Tecan, Switzerland).

5.3.7 Quantification of scaffold contraction

The diameter of each scaffold piece was measured at the 1, 7, 14, and 21 day time points using standard drafting templates and normalized against starting scaffold diameter at day 0 to determine scaffold contraction as previously described (Spilker, Asano et al. 2001). Cellular solids modeling was used to predict changes in scaffold elastic modulus (E^*) as a function of scaffold contracted diameter (d) where E^* is proportional to d^{-6} (Gibson, Ashby et al. 2010).

5.3.8 RNA isolation, reverse transcription, and real-time PCR

Isolation of RNA from MSC-seeded scaffolds was performed at day 7, 14, and 21 time points using an RNeasy Plant Mini kit (Qiagen, Valencia, CA) (Duffy, McFadden et al. 2011; Caliari, Weisgerber et al. 2012). Scaffold were rinsed with PBS and then added to RLT lysis buffer (supplied with the kit) supplemented with β-mercaptoethanol for 5 min on ice. The lysates were processed following the kit instructions to isolate RNA that was then reverse transcribed to cDNA in a Bio-Rad S1000 thermal cycler using the QuantiTect Reverse Transcription kit (Qiagen). Real-time PCR reactions were performed in triplicate using the QuantiTect SYBR

Green PCR (Qiagen) kit in an Applied Biosystems 7900HT Fast Real-Time PCR System (Applied Biosystems, Carlsbad, CA). All primer sequences used were taken from the literature (Frank, Heim et al. 2002; Zhou, Xu et al. 2011) (**Table 5.1**) and were synthesized by Integrated DNA Technologies (Coralville, IA). Expression levels of the chondrogenic markers collagen type II alpha 1 (*COL2A1*), aggrecan (*ACAN*), and sex determining region Y box 9 (*SOX9*) as well as osteogenic markers runt-related transcription factor 2 (*RUNX2*), bone sialoprotein (*BSP*), alkaline phosphatase (*ALP*), and osteocalcin (*OCN*) were quantified with glyceraldehyde 3-phosphate dehydrogenase (*GAPDH*) used as a housekeeping gene. Data were analyzed using Sequence Detection Systems software v2.4 (Applied Biosystems) using the delta-delta Ct method and all results were expressed as fold changes normalized to the expression levels of MSCs cultured in the high density CG scaffolds at day 7.

5.3.9 Histology

Cell-seeded scaffolds at days 7, 14, and 21 were fixed in 10% neutral buffered formalin for histological analyses. Fixed scaffold pieces were embedded in paraffin and sequentially sliced into 5 μm thick sections. Sections were deparaffinized and stained with hematoxylin and eosin (H&E) to visualize cellular organization within scaffolds, Alizarin red to assess mineral content, and Alcian blue to determine GAG content.

5.3.10 Statistical analysis

Two-way analysis of variance (ANOVA) was performed on metabolic activity, scaffold diameter, and gene expression data sets (independent variables time and scaffold type) followed by Tukey-HSD post-hoc tests. Significance was set at $p < 0.05$. At least $n = 3$ scaffolds were

analyzed at each time point for all metrics. Error was reported in figures as the standard error of the mean unless otherwise noted.

5.4 Results

5.4.1 Scaffold contraction and metabolic activity

Scaffold contraction was measured at time points of days 1, 7, 14, and 21 (**Figure 5.1(a)**). High density non-mineralized scaffolds showed minor contraction while mineralized scaffolds did not contract over the entire course of the experiment. However, low density non-mineralized scaffolds showed an early loss of structural integrity that was maintained throughout the experiment.

All experimental groups demonstrated sustained metabolic activity over the course of the 21 day experiment (**Figure 5.1(b)**). Metabolic activity was initially significantly higher in the high density non-mineralized group at day 7 ($p < 0.03$). On day 14 activity significantly decreased in the low density group ($p = 0.01$), held steady in the high density group, and significantly increased in the mineralized group ($p = 0.009$) with the low density group having significantly lower metabolic activity than the other two experimental groups ($p < 0.0009$). Metabolic activity for the low and high density non-mineralized groups remained relatively constant from day 14 to day 21 while the mineralized group showed a significant increase ($p = 0.0003$). The mineralized and high density non-mineralized scaffold groups maintained significantly higher metabolic activity than the lower density non-mineralized group ($p < 0.0003$) at the completion of the experiment.

5.4.2 Trends in chondrogenic gene expression

The expression of chondrogenic genes *COL2A1*, *ACAN*, and *SOX9* was measured after 7, 14, and 21 days in culture (**Figure 5.2**). Statistical analyses revealed a significant influence of both culture time and scaffold type on expression of *COL2A1* and *ACAN* ($p < 0.05$). Elevated levels of *COL2A1* were observed in the non-mineralized scaffold groups with significantly higher expression in the higher density non-mineralized group compared to the other groups at day 21 ($p < 0.02$) (**Figure 5.2(a)**). These results were largely mirrored in the *ACAN* expression profile with significantly higher expression at day 21 in the high density non-mineralized group ($p < 0.002$) as well as significantly higher expression at day 21 in the lower density group compared to the mineralized scaffolds ($p = 0.03$) (**Figure 5.2(b)**). *SOX9* expression was also elevated in the non-mineralized groups compared to the mineralized group at day 21 with significantly higher expression in the low density non-mineralized group compared to the mineralized group ($p = 0.01$) (**Figure 5.2(c)**).

5.4.3 Trends in osteogenic gene expression

The expression of osteogenic genes *RUNX2*, *BSP*, *ALP*, and *OCN* was measured after 7, 14, and 21 days in culture (**Figure 5.3**). Statistical analyses revealed a significant influence of both culture time and scaffold type on expression of *BSP*, *ALP*, and *OCN* ($p < 0.008$). *RUNX2* expression in the mineralized scaffolds showed non-significant increases over the non-mineralized groups at days 7 and 14, peaking at day 14 before decreasing in day 21 (**Figure 5.3(a)**). Meanwhile, the non-mineralized groups showed steady increases in *RUNX2* expression with significant increases between days 7 and 14 for the low density group ($p = 0.04$) and

between days 14 and 21 for the high density group ($p = 0.005$). No significant differences were found between the groups for *BSP* expression at days 7 and 14 (**Figure 5.3(b)**). However, *BSP* expression in the low density non-mineralized group was significantly up-regulated from day 14 to day 21 and was significantly higher than the other groups at the day 21 time point ($p < 0.005$). There were no differences in *ALP* expression between the groups at day 7, but there was significantly up-regulated expression in the low density non-mineralized group at each successive time point with significantly higher overall expression than the other experimental groups at days 14 ($p < 0.03$) and 21 ($p < 0.0002$) (**Figure 5.3(c)**). No significant differences in *OCN* expression between the groups were observed at days 7 and 14, but at day 21 there was a significant up-regulation in low density non-mineralized group expression, resulting in significantly higher expression levels than the other two experimental groups ($p < 0.02$) (**Figure 5.3(d)**).

5.4.4 Histology: H&E, Alizarin red, Alcian blue

Histological staining for cellular distribution, mineralization, and GAG content was undertaken using H&E, Alizarin red, and Alcian blue stains respectively. We first assessed MSC/scaffold organization through H&E staining (**Figure 5.4**). Although MSC infiltration appeared similar in all experimental groups, staining clearly shows evidence of increased pore contraction and cellular condensation in the non-mineralized mixed media groups (**Figure 5.4(b,d)**) compared to the corresponding growth media samples (**Figure 5.4(a,c)**). While the non-mineralized scaffold variants displayed little to no mineralization when cultured in growth media after 21 days (**Figure 5.5(a,c)**), their counterparts cultured in mixed induction media showed significant mineralization by day 21 (**Figure 5.5(b,d)**). There did not appear to be significant differences in

mineralization between the mineralized (growth) (**Figure 5.5(e)**) and mineralized (mixed) (**Figure 5.5(f)**) media groups. Finally, we evaluated GAG distribution as a proxy for chondrogenesis via Alcian blue staining (**Figure 5.6**). The biggest difference between the growth and mixed media pairs after 21 days appears to be in the high density, non-mineralized variant where mixed media supported increased GAG staining (**Figure 5.6(d)**). There appeared to be more GAG in the low density mixed media groups compared to their growth media counterparts at days 7 and 14, although this difference was eliminated by day 21 (**Figure 5.6(b)**).

5.5 Discussion

This study examined the effects of scaffold relative density and mineral content on MSC viability, phenotype, and ECM distribution over the course of three weeks in the presence of competing osteogenic and chondrogenic media supplements. Previous work with CG scaffolds and other materials had shown that lower elastic modulus led to increased contraction, cellular condensation, and chondrogenic response (Vickers, Squitieri et al. 2006; Tang and Spector 2007; Vickers, Gotterbarm et al. 2010; Caliari and Harley in preparation) while increased elastic modulus and mineral content promoted a more osteogenic phenotype (Curtin, Cunniffe et al. 2012; Murphy, Matsiko et al. 2012; Caliari and Harley in preparation). However, these efforts focused on generating biomaterials for monolithic tissue applications using single media (osteogenic, chondrogenic) formulations. For this study we hypothesized that the lower density non-mineralized scaffolds would promote more of a chondrogenic phenotype mediated by contraction-induced cellular condensation while the mineralized scaffolds would facilitate osteogenesis in the presence of joint chondrogenic-osteogenic signals.

We first tracked MSC metabolic activity and scaffold contraction over the course of a three week *in vitro* culture period (**Figure 5.1**). Cells were metabolically active in all scaffolds types, although there was a dip in metabolic activity in the low density non-mineralized group from day 7 to day 14, consistent with previous results in contracting scaffolds (Torres, Freyman et al. 2000; Caliari, Weisgerber et al. 2012; Caliari and Harley in preparation). There are several possible explanations for this observation, including cell death due to reduced permeability following cell-mediated contraction as well as differentiation to a less metabolically active cell type (*e.g.*, MSC to chondrocyte or osteoblast). In order to further investigate our hypotheses about the influence of scaffold physical properties in the presence of competing signals, we next examined the expression of a battery of osteogenic and chondrogenic markers.

We assessed the expression of chondrogenic genes *COL2A1*, *ACAN*, and *SOX9* as well as osteogenic genes *RUNX2*, *BSP*, *ALP*, and *OCN* over three weeks culture. Not surprisingly, the expression levels of all three chondrogenic markers were depressed for the mineralized scaffolds at day 21 (**Figure 5.2**). Interestingly, the higher density non-mineralized scaffolds surpassed the low density non-mineralized scaffolds in expression of *COL2A1* and *ACAN* by day 21 despite reduced scaffold contraction. These results differ markedly from previously observed trends with these scaffolds when cultured in pure chondrogenic differentiation media (Caliari and Harley in preparation). This shows that in the presence of multiple differentiation signals scaffold contraction and cellular condensation may not be beneficial for driving chondrogenesis. Likewise, in the presence of mixed media supplements, the mineralized scaffold did not appear to drive the most substantial osteogenic response despite previous reports showing that

mineralized CG scaffolds in combination with pure osteogenic media promote optimal osteogenesis (Caliari and Harley in preparation). In fact, the low density scaffold group displayed significantly higher expression of the osteogenic markers *BSP*, *ALP*, and *OCN* at day 21 compared to the other two experimental groups (**Figure 5.3**). These results suggest a scaffold identified to improve chondrogenesis in chondrogenic media may be best suited for osteogenesis in mixed osteogenic-chondrogenic media conditions. Notably, these results also suggest that separate optimization may be necessary to identify media cocktails to support divergent chondrogenesis and osteogenesis in close spatial order.

In order to more closely examine the spatial and temporal variations in cellular organization and ECM synthesis within these scaffolds we performed histological analyses. We looked at H&E (**Figure 5.4**), Alizarin red (**Figure 5.5**), and Alcian blue (**Figure 5.6**) staining to assess cellular infiltration/organization, mineral production, and GAG synthesis respectively. Here, we compared each scaffold type in growth and mixed media to better visualize the influence of media supplementation on the responses we observed. Results typically correlated well with the observed gene expression profiles. H&E staining clearly revealed increased contraction and cellular condensation in the low density mixed media group (**Figure 5.4**). While there was little mineral deposition in the non-mineralized scaffold groups at days 7 or 14, by day 21 Alizarin red staining revealed robust mineralization in the low density mixed media group compared to the growth media control (**Figure 5.5**), corroborating the osteogenic gene expression results. Similarly, although Alcian blue staining was initially stronger in the lower density groups, by day 21 the strongest staining appeared to be in the high density, mixed media group (**Figure 5.6**), which mirrored the results of the chondrogenic gene expression analyses.

The discrepancy between previously reported single media results and these mixed media results was initially confounding. However, the kinetics of MSC-mediated scaffold contraction may offer a compelling case to resolve these findings. One possible explanation for the phenotypic switch in the lower density non-mineralized scaffolds between day 14 (higher GAG content) and day 21 (robust mineralization, up-regulation of osteogenic genes) is the occurrence of endochondral ossification. Keogh *et al.* previously observed accelerated osteogenic maturation of MC3T3-seeded CG scaffolds with lower crosslinking density (increased contraction) (Keogh, O'Brien et al. 2010). Our noted differences in contraction may suggest that a similar mechanism could be driving the response observed here.

Another possible driver of osteogenesis in the low density scaffold group could be local stiffening of the extracellular environment following contraction. We explored this possibility using cellular solids theory to predict changes in elastic modulus for contracted versus non-contracted scaffolds. Considering that the low density non-mineralized scaffold contracted to about half of its original length in each dimension, this represents a reduction in volume by about a factor of 8 and therefore an increase in relative density by the same factor. Cellular solids modeling predicts that elastic modulus is proportional to the square of relative density (Gibson, Ashby et al. 2010), so the significant contraction observed in lower density non-mineralized scaffolds could result in an increase of elastic modulus by a factor of ~60. This indicates that although the low density non-mineralized scaffolds were initially ~20-fold softer than the mineralized scaffolds (Kanungo and Gibson 2009; Kanungo and Gibson 2010), contraction-

induced remodeling could result in the low density non-mineralized scaffold being ~ 3-fold stiffer than the mineralized scaffold variant.

The results of this study suggest a disconnect between conventional single media strategies for driving stem cell lineage specification *in vitro* and the multi-modal approaches needed for multi-tissue interface engineering where many signals work in concert *in vivo*. Notably, results from *in vitro* mixed media supplementation suggested unexpected roles of scaffold relative density and mineralization in biasing MSC differentiation towards fibrocartilage and bone. Importantly, these results suggest that non-obvious modifications to biomaterial biophysical properties and soluble factor supplementation may be necessary to selectively enhance or repress disparate differentiation events. Given that we and others have recently begun to demonstrate approaches to generate biomaterials containing spatially-graded biophysical properties (Erisken, Kalyon et al. 2008; Li, Xie et al. 2009; Harley, Lynn et al. 2010; Xie, Li et al. 2010), future studies developing combined biomaterial-growth factor approaches will be critical for repairing complex orthopedic interfaces.

5.6 Conclusions

Biomaterials for complex tissue engineering applications must be able to instruct cell behavior in the presence of the multivariate environments encountered *in vivo*. Using a series of CG scaffolds with physical properties optimized to specific components of orthopedic interfaces, we investigated the impact of scaffold relative density and mineral content on MSC lineage specification in the presence of mixed osteogenic and chondrogenic signals. We found that

mineralized scaffolds were able to suppress chondrogenic outcomes compared to the two non-mineralized variants investigated as evidenced by gene expression and histological analyses. While the higher density non-mineralized scaffold elicited a greater chondrogenic response than the mineralized scaffold, the more surprising result was the heightened osteogenic response observed in the lower density, non-mineralized scaffold group with heightened chondrogenesis occurring in the higher density, non-mineralized group. This unexpected response may be due to local stiffening of the extracellular environment due to cell-mediated scaffold contraction. The increased cell density as a result of contraction may have also accelerated the kinetics of MSC differentiation and maturation, leading to a response similar to endochondral ossification. These results will inform ongoing work in our lab designing multi-compartment scaffolds for graded tissue regeneration.

5.7 Tables

Transcript	Sequence	Reference
ACAN	Forward: 5'-TGCATTCCACGAAGCTAACCTT-3' Reverse: 5'-GACGCCTCGCCTTCTTGAA-3'	(Zhou, Xu et al. 2011)
ALP	Forward: 5'-AGCACTCCCACTTCATCTGGAA-3' Reverse: 5'-GAGACCCAATAGGTAGTCCACATTG-3'	(Zhou, Xu et al. 2011)
BSP	Forward: 5'-TGCCTTGAGCCTGCTTCC-3' Reverse: 5'-GCAAAATTAAAGCAGTCTTCATTTTG-3'	(Frank, Heim et al. 2002)
COL2A1	Forward: 5'-GGCAATAGCAGGTTCACGTACA-3' Reverse: 5'-CGATAACAGTCTTGCCCCACTT-3'	(Zhou, Xu et al. 2011)
GAPDH	Forward: 5'-AGAAAAACCTGCCAAATATGATGAC-3' Reverse: 5'-TGGGTGTCGCTGTTGAAGTC-3'	(Zhou, Xu et al. 2011)
OCN	Forward: 5'-CAGCGAGGTAGTGAAGAGA-3' Reverse: 5'-GAAAGCCGATGTGGTCAG-3'	(Zhou, Xu et al. 2011)
RUNX2	Forward: 5'-AGAAGGCACAGACAGAAGCTTGA-3' Reverse: 5'-AGGAATGCGCCCTAAATCACT-3'	(Zhou, Xu et al. 2011)
SOX9	Forward: 5'-AGCGAACGCACATCAAGAC-3' Reverse: 5'-GCTGTAGTGTGGGAGGTTGAA-3'	(Zhou, Xu et al. 2011)

Table 5.1. Primer sequences from literature used for PCR.

5.8 Figures

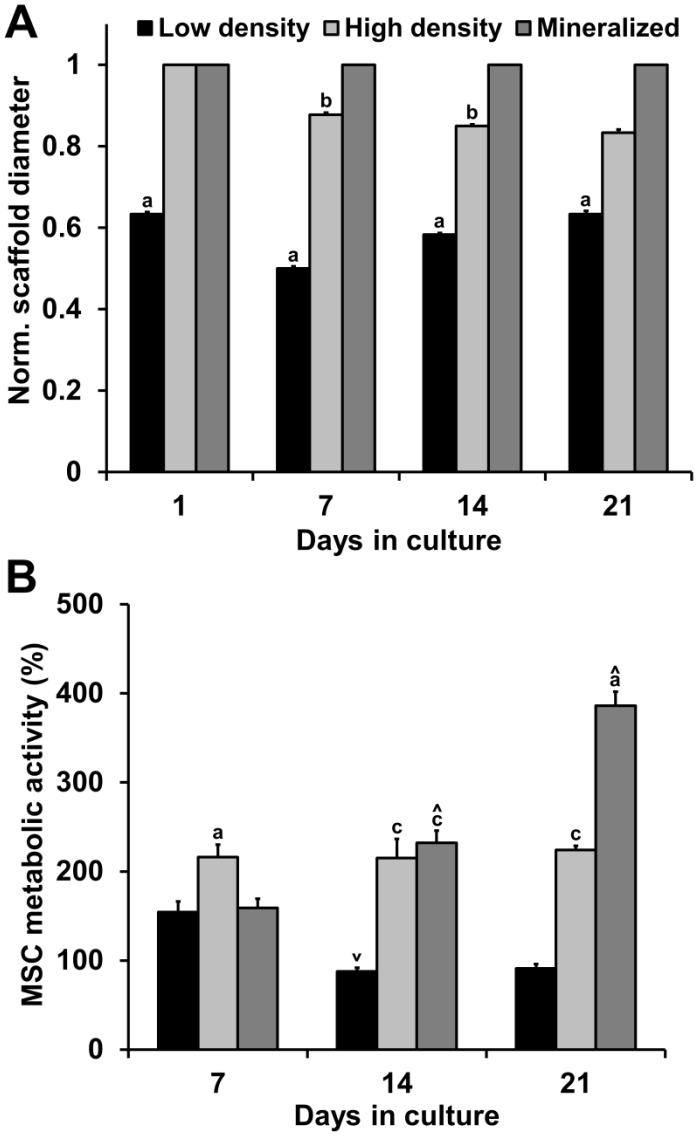

Figure 5.1. MSC contraction and metabolic activity as a function of time and scaffold type. A) Pronounced cell-mediated contraction was observed for the low density group with minor contraction in the high density group and negligible contraction in the mineralized scaffold group. B) Human mesenchymal stem cells remained metabolically active over extended culture times. *a:* significantly different from other two experimental groups, *b:* significantly different from mineralized group, *c*: significantly different from low density group, ∧*:* significantly increased from previous time point, ∨*:* significantly decreased from previous time point.

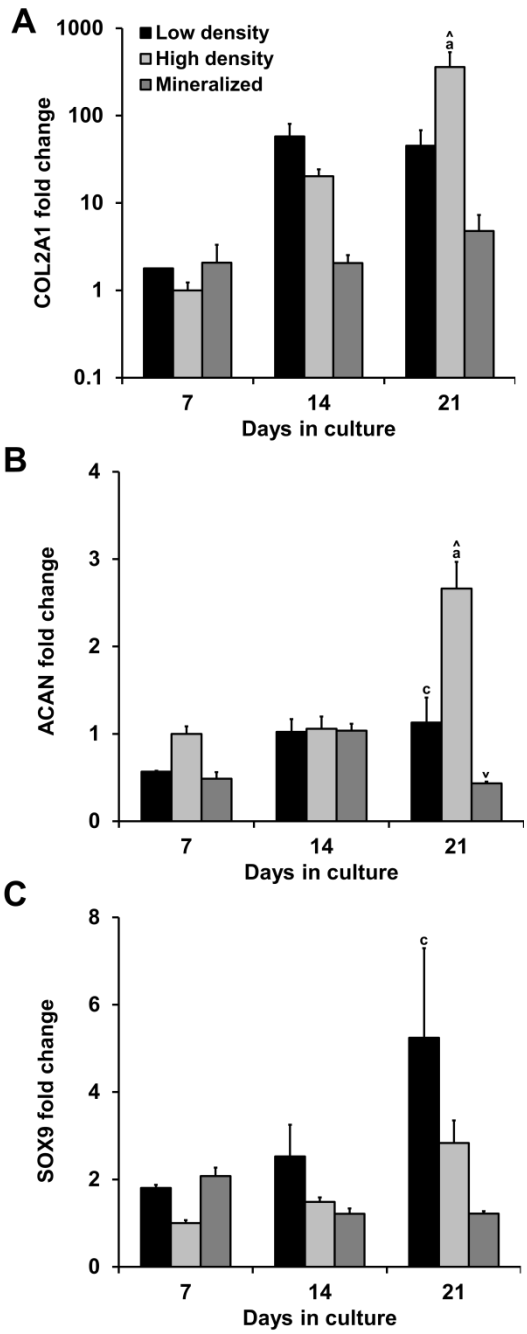

Figure 5.2. Trends in chondrogenic gene expression. Expression profiles of chondrogenic genes A) collagen type II alpha 1 (*COL2A1*), B) aggrecan (*ACAN*), and C) sex determining region Y box 9 (*SOX9*) were tracked for 21 days. After 21 days expression levels of all three transcripts were depressed in the mineralized group with significantly higher expression of *COL2A1* and *ACAN* observed in the high density group. *a:* significantly different from other two experimental groups, *c:* significantly different from mineralized group, ∧*:* significantly increased from previous time point, ∨*:* significantly decreased from previous time point.

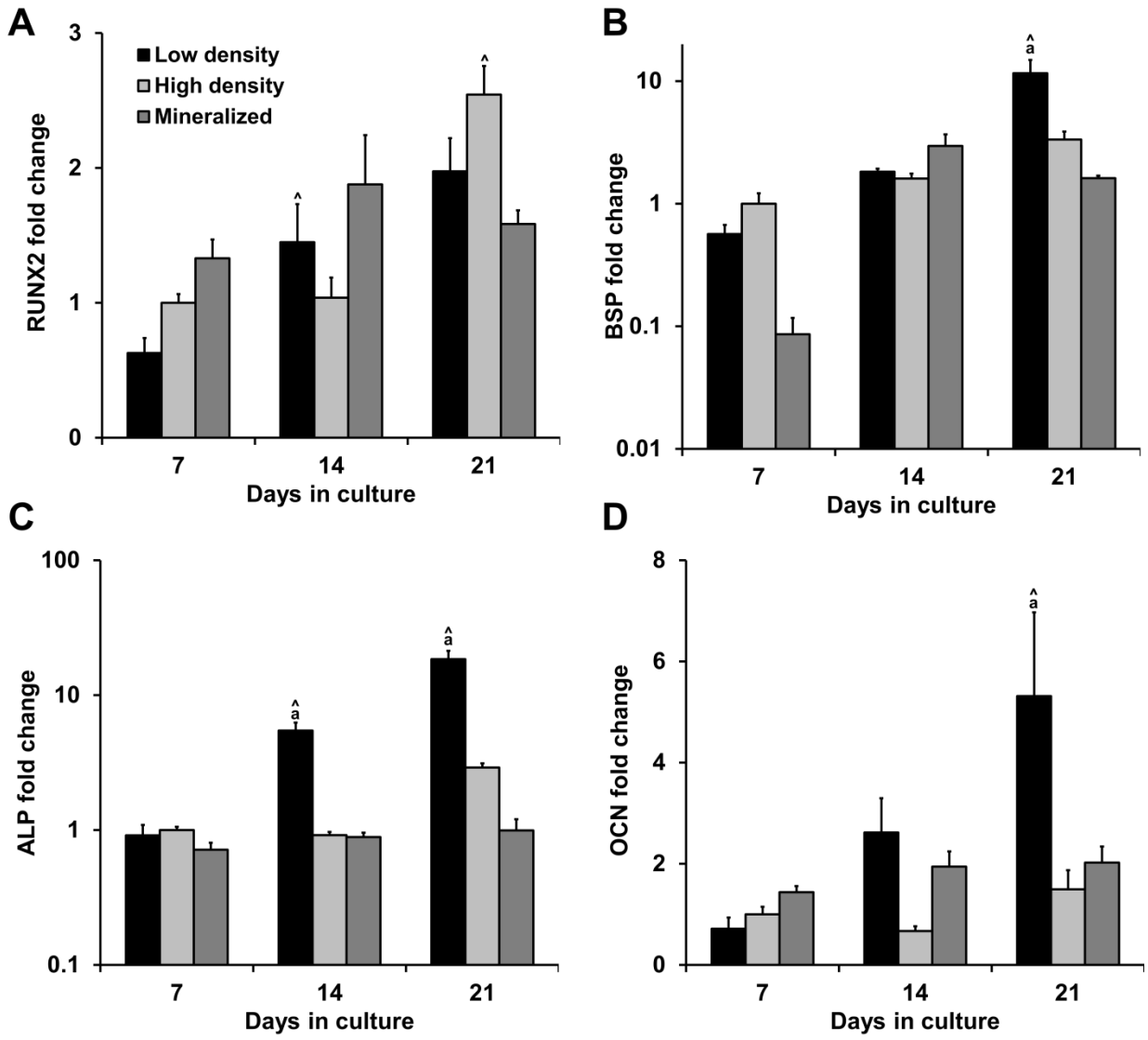

Figure 5.3. Trends in osteogenic gene expression. Expression profiles of osteogenic genes A) runt-related transcription factor 2 (*RUNX2*), B) bone sialoprotein (*BSP*), C) alkaline phosphatase (*ALP*), and D) osteocalcin (*OCN*) were tracked for 21 days. After 21 days *BSP*, *ALP*, and *OCN* were all significantly up-regulated in the low density non-mineralized group. *a:* significantly different from other two experimental groups, ^*:* significantly increased from previous time point.

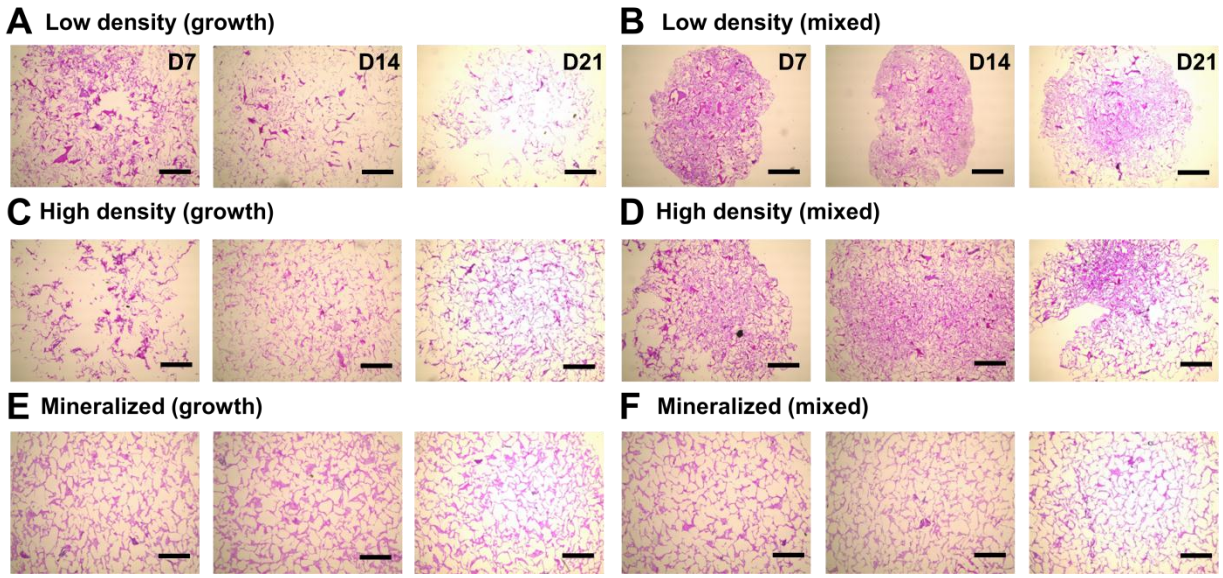

Figure 5.4. Hematoxylin & Eosin (H&E) staining of scaffold sections. Histology sections show differences in MSC distribution and scaffold contraction. A) Low density (growth), B) Low density (mixed), C) High density (growth), D) High density (mixed), E) Mineralized (growth), F) Mineralized (mixed). *Scale bars*: 500 µm.

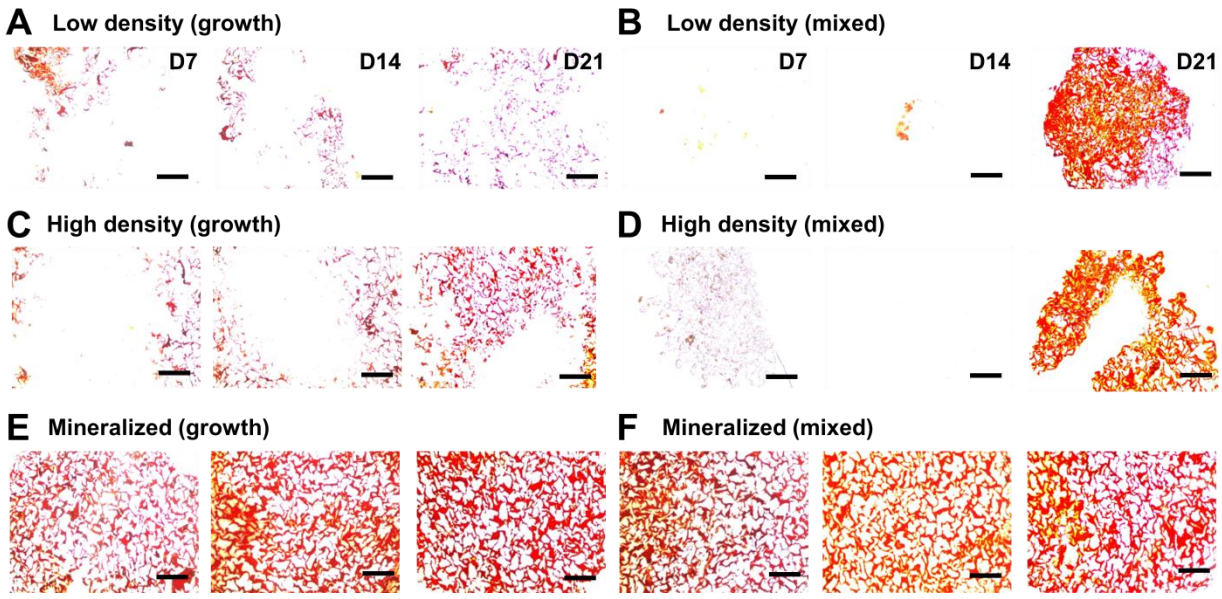

Figure 5.5. Alizarin red staining of scaffold sections. Histology sections reveal differential mineral content as a function of scaffold type and media treatment with the non-mineralized scaffold groups showing little mineralization at days 7 or 14, but robust mineralization in the mixed media groups at day 21. A) Low density (growth), B) Low density (mixed), C) High density (growth), D) High density (mixed), E) Mineralized (growth), F) Mineralized (mixed). *Scale bars*: 500 µm.

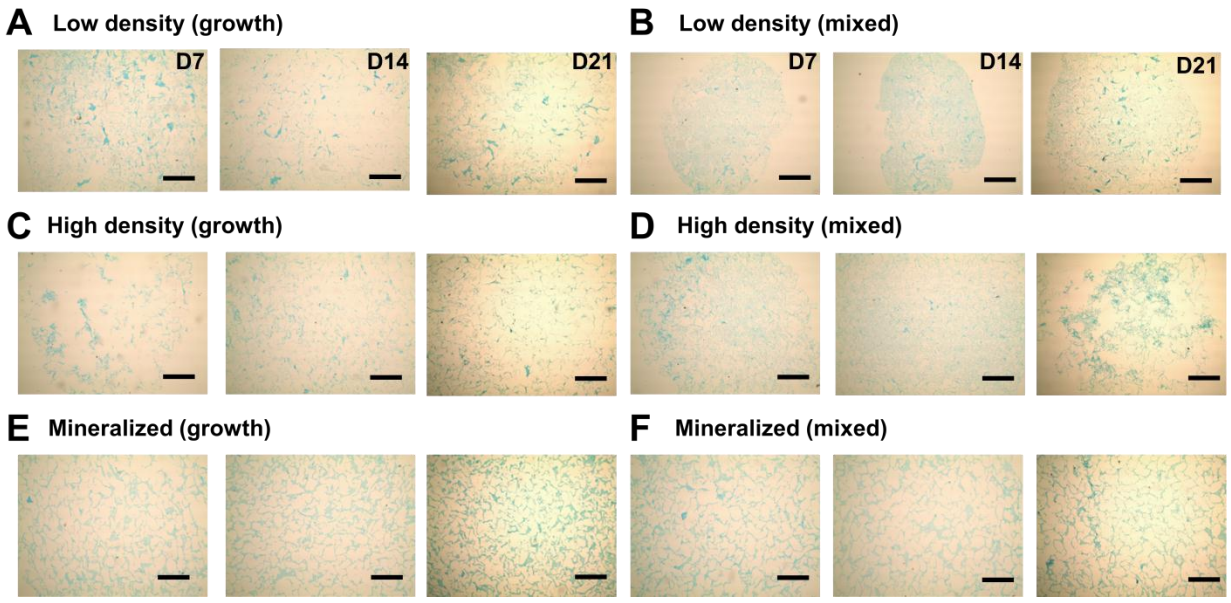

Figure 5.6. Alcian blue staining of scaffold sections. Histology sections reveal differential GAG content as a function of scaffold type and media treatment with higher GAG levels initially in the lower density mixed groups but higher levels in the high density mixed group by day 21. A) Low density (growth), B) Low density (mixed), C) High density (growth), D) High density (mixed), E) Mineralized (growth), F) Mineralized (mixed). *Scale bars*: 500 µm.

CHAPTER 6: SPATIALLY-GRADED COLLAGEN SCAFFOLDS TO ENGINEER THE TENDON-BONE JUNCTION[6]

6.1 Chapter overview

Biomaterial strategies are needed that can capture the spatially-graded, heterogeneous microstructural, mechanical, and biochemical properties of tissues. In particular, orthopedic interfaces like the tendon-bone junction (TBJ) contain gradations of extracellular matrix (ECM) proteins, growth factors, and mineral content that provide an elegant solution to the problem of joining two mechanically dissimilar tissues. This work aims to adapt a regulatory compliant collagen-glycosaminoglycan (CG) system to provide a framework to engineer the TBJ. Multi-compartment CG scaffolds were fabricated with distinct regions of pore anisotropy and mineral content that mimicked the native TBJ. Qualitative SEM and quantitative pore alignment analyses demonstrated aligned pores in the tendon (CG) compartment with more amorphous pores in the bone (CGCaP) compartment, with the two compartments joined at a continuous interface. MicroCT and EDX analyses showed distinct regions of calcium phosphate content. Additionally, biomolecules were directly incorporated into the separate compartments during the fabrication process while maintaining activity. Scaffolds were then seeded with human bone marrow-derived mesenchymal stem cells (MSCs) and grown in a Flexcell® bioreactor system. MSC-seeded scaffolds showed compartment and stretch-dependent integrin engagement profiles with higher levels of fibronectin-related integrins expressed in the tendon compartment and in both compartments in response to stretch. Long-term culture led to compartment-specific genomic and proteomic profiles with significant up-regulation of osteogenic genes bone sialoprotein (BSP) and osteocalcin (OC) in the bone compartment as well as significant up-regulation of type

[6] This chapter has been adapted from the following publication:
Caliari, S. R. D.W. Weisgerber, et al. (in preparation). "Spatially-graded collagen scaffolds to engineer the tendon-bone junction."

I collagen (COL1A1) in the tendon compartment in response to stretch. Second harmonic generation imaging revealed more organized (aligned) collagen in the tendon compartment compared to the bone. Histological analyses showed MSC infiltration in both compartments as well as localization of mineral content to the bone compartment. Together, these data show that a multi-compartment CG scaffold with distinct regions of pore anisotropy, mineral content, and biomolecule incorporation can be successfully fabricated. MSC-seeded TBJ scaffolds can also support spatially-graded differentiation events, suggesting that these scaffolds may be suitable for *in vivo* regeneration of the TBJ.

6.2 Introduction

There is a critical need for new biomaterial strategies that can recapitulate elements of the heterogeneous microstructural and compositional properties of tissues to enable repair and regeneration. While most tissue engineering approaches focus on the repair of single tissues, orthopedic tissue injuries often occur at the interface between soft tissue and bone, referred to in this chapter as multi-tissue junctions. Common classes of multi-tissue junctions include cartilage-bone (osteochondral), meniscus-bone, ligament-bone, and the tendon-bone junction (TBJ). A classic example of a commonly injured TBJ is the supraspinatus-humerus junction in the rotator cuff. The supraspinatus tendon connects the supraspinatus muscle, one of four muscles in the rotator cuff, to the humerus and is the most commonly injured TBJ in the rotator cuff. This TBJ contains elegant patterns of extracellular matrix (ECM) proteins, growth factors, and a linear gradient of mineral content that serve to minimize stress concentrations between the geometrically anisotropic, compliant tendon and the more amorphous, stiffer bone (E_{bone} ~

10^2*E_{tendon}) (Galatz, Sandell et al. 2006; Thomopoulos, Marquez et al. 2006; Galatz, Rothermich et al. 2007; Wopenka, Kent et al. 2008; Genin, Kent et al. 2009; Thomopoulos, Genin et al. 2010). Despite the presence of this highly organized milieu, the junction remains a common injury site (Woo, Debski et al. 2000; Wopenka, Kent et al. 2008) with rotator cuff injuries resulting in over 4 million physician visits and 75000 surgical procedures per year in the US alone (Vitale, Vitale et al. 2007; Butler, Juncosa-Melvin et al. 2008). Current clinical approaches often forsake biological reintegration for direct mechanical fixation of the tendon to the bone. These approaches fail to recapitulate the graded structure of the interface, resulting in high stress concentrations and failure rates following repair as high as 94% in some demographics (Klepps, Bishop et al. 2004; Boileau, Brassart et al. 2005; Galatz, Rothermich et al. 2007; Millar, Wu et al. 2009), highlighting the necessity for improved repair strategies.

Recent advances in the regenerative medicine field have considered strategies to present spatially-graded instructive cues towards the repair of multi-tissue junctions such as the TBJ. Engineered materials with gradients of mineral content have been used to promote spatially-stratified osteogenic responses. Mutsuzaki *et al.* used a soaking process to hybridize calcium phosphate to the end of a tendon graft as a means to improve osteotendinous integration (Mutsuzaki, Sakane et al. 2011). Samavedi *et al.* used a co-electrospun system incorporating a nano-hydroxyapatite-doped polymer solution to produce a graded material that supported spatially-defined areas of osteogenic differentiation (Samavedi, Guelcher et al. 2012). Li *et al.* created nanofiber PCL mats with a gradation of hydroxyapatite mineral to influence MC3T3 preosteoblast activity (Li, Xie et al. 2009). Other approaches have focused on the combination of scaffold anisotropy and/or mechanical stimulation as a pathway towards eliciting tenogenic

outcomes. Moffat *et al.* showed that rotator cuff fibroblasts cultured on aligned nanofiber mats conformed to the substrate via contact guidance cues, resulting in increased cell and ECM alignment as well as superior mechanics compared to isotropic mats (Moffat, Kwei et al. 2009). Subramony *et al.* showed that the combination of matrix alignment and mechanical stretching was necessary for the induction of fibroblastic MSC differentiation on nanofiber PLGA mats (Subramony, Dargis et al. 2012). Paxton *et al.* used extracellular-signal related protein kinase (ERK) 1/2 phosphorylation for optimizing a stretch protocol for engineered ligaments that suggested short, infrequent bouts of stretch were favorable for maximizing collagen synthesis and overall mechanical properties (Paxton, Hagerty et al. 2012). Together, these data suggest that a biomaterial with spatially-graded presentation of tenogenic (geometric anisotropy) and osteogenic (calcium phosphate mineral) cues, in conjunction with mechanical stimulation, may be optimal for the repair of the TBJ.

One class of materials that has found substantial success in the clinic is the collagen-glycosaminoglycan (CG) scaffold system. CG scaffolds have been applied clinically for the regeneration of numerous soft tissues, including dermis (Yannas, Lee et al. 1989) and peripheral nerves (Harley, Spilker et al. 2004). These scaffolds have also been considered for the repair of other non-mineralized tissues including cartilage (Capito and Spector 2007; Vickers, Gotterbarm et al. 2010), tendon (Caliari and Harley 2011; Caliari, Ramirez et al. 2011), and cardiac muscle (Gonnerman, Kelkhoff et al. 2012). Additionally, mineralized variants of the CG scaffold (CGCaP) have recently been developed for bone tissue engineering applications (Al-Munajjed and O'Brien 2009; Harley, Lynn et al. 2010; Lynn, Best et al. 2010). Together these scaffolds have been applied to not only understand microenvironmental regulators of tissue-specific cells,

but also to explore cell behaviors including adhesion (O'Brien, Harley et al. 2005; Murphy, Haugh et al. 2010), motility (Harley, Kim et al. 2008), and differentiation (Farrell, O'Brien et al. 2006).

Recent work has enabled the fabrication of CG scaffolds with aligned tracks of ellipsoidal pores in order to mimic the native anisotropy of tendon and other tissues (Caliari and Harley 2011). Pore alignment was shown to encourage tenocyte alignment (Caliari and Harley 2011; Caliari, Weisgerber et al. 2012), phenotypic stability (Caliari, Weisgerber et al. 2012), and improved scaffold mechanical competence (Caliari, Ramirez et al. 2011). Combined with a previous study which showed that CG and CGCaP scaffolds could be integrated in a continuous manner to form layered, multi-compartment scaffolds for osteochondral applications (Harley, Lynn et al. 2010), this chapter aims to create, for the first time, a biomaterial with spatially-graded regions of both geometric anisotropy and mineral content to mimic the native TBJ. This material, in conjunction with mechanical stimulation, would be hypothesized to drive spatially-graded tenogenic and osteogenic MSC differentiation.

6.3 Materials and methods

*All reagents purchased from Sigma Aldrich (St Louis, MO) unless otherwise specified.

6.3.1 Preparation of collagen suspensions

Two versions of collagen suspension were made. The first was a high density CG suspension composed of 1 w/v% purified fibrillar collagen derived from bovine dermis (Collagen Matrix, Franklin Lakes, NJ) and chondroitin sulfate from shark cartilage in 0.05 M acetic acid.

Additionally, a collagen-glycosaminoglycan-calcium phosphate (CGCaP) suspension was made by adding calcium salts ($Ca(OH)_2$, $Ca(NO_3)_2{\cdot}4H_2O$) to the collagen and chondroitin sulfate and by substituting phosphoric acid as the solvent (Harley, Lynn et al. 2010; Lynn, Best et al. 2010). A titrant-free concurrent mapping method was used to produce suspension that led to CGCaP scaffolds that were 40 wt% mineral (Lynn, Best et al. 2010). Suspensions were homogenized at 15000 rpm and 4°C to prevent collagen denaturation as previously described (Yannas, Lee et al. 1989; O'Brien, Harley et al. 2004). Following homogenization suspensions were stored overnight at 4°C and degassed prior to use.

6.3.2 Scaffold fabrication via freeze-drying

Multi-compartment TBJ scaffolds were fabricated by combining directional solidification (Caliari and Harley 2011) with a liquid-phase co-synthesis method (Harley, Lynn et al. 2010) (**Figure 6.1**). A thermally-mismatched mold composed of a Teflon body joined to a 1/16" thick copper base was used for the freeze-drying process to induce directional solidification. First, degassed CG suspension was pipetted into cylindrical holes in the Teflon-copper mold (6 mm diameter, 15 mm deep). Then, CGCaP suspension was carefully layered on top of the CG suspension (CG:CGCaP suspension volume ratio 2:1). The suspensions were allowed to interdiffuse at 4°C for 20 min prior to freeze-drying. For biomolecule incorporation studies, AlexaFluor® 488-streptavidin conjugate (Invitrogen, Carlsbad, CA) and AlexaFluor® 594-BSA conjugate (Invitrogen) were directly added to the degassed CGCaP and CG suspensions respectively at a final concentration of 1 µg/mL immediately prior to loading in the freeze-drying mold. The suspension-loaded mold was placed on a freeze-dryer shelf (VirTis, Gardiner, NY) precooled to -10°C and maintained at this temperature for 2 h to complete freezing. Following

freezing, the shelf temperature was ramped up to 0°C at a rate of 1°C/min while pulling a vacuum of 200 mTorr to remove ice crystals via sublimation. Freeze-drying results in the formation of dry, macroporous scaffolds that are amenable to post-fabrication hydration, crosslinking, and cell seeding (O'Brien, Harley et al. 2004; Harley, Lynn et al. 2010; Caliari and Harley 2011).

6.3.3 SEM and EDX analyses

Scanning electron microscopy (SEM) and energy dispersive X-ray spectroscopy (EDX) were used to qualitatively assess scaffold microarchitecture and elemental composition respectively. SEM/EDX analyses were executed on a JEOL JSM-6060LV Low Vacuum Scanning Electron Microscope (JEOL USA, Peabody, MA) using a combination of secondary and backscatter electron detection under low vacuum to enable scaffold visualization without a conductive coating (Harley, Lynn et al. 2010). EDX was used to acquire compositional mapping data of calcium (Ca) and phosphorus (P) content within longitudinal interfacial sections of the multi-compartment scaffolds.

6.3.4 MicroCT analysis

Micro-computed tomography (MicroCT) analysis was performed with Xradia MicroXCT-400 (Xradia, Pleasanton, CA) at 25 kEv and 5 W. Total scaffold scans were performed with a voxel size of 15 µm while scans to determine the width of the interface between the CG and CGCaP compartments used a voxel size of 4 µm. Interface width was determined by projecting a 4x4 grid of squares (individual square size: 670 µm x 670 µm) through the height of the scaffold. The average pixel intensity of each data point (square) in the Z-stack was then calculated. Z-slices

possessing an average intensity between the mean ± 3 StDev of the first image slice (taken to be pure CGCaP compartment) and the last image slice (taken to be pure CG compartment) were considered part of the interfacial region.

6.3.5 Scaffold placement in Flexcell® plates

Cell-free, dry scaffolds (6 mm diameter, 10 mm length) were immobilized onto non-treated Flexcell® 6-well plates (Flexcell, Hillsborough, NC) using poly(dimethylsiloxane) (PDMS, MG Chemicals, Canada) (Boerboom, Rubbens et al. 2008). A thin strip of PDMS (monomer: curing agent ratio 10:1) was added to the center of each well using a pipet tip. Control scaffolds that were not stretched were similarly immobilized in standard 6-well plates. PDMS-treated plates were exposed to UV for 30 min, followed by placement of the scaffolds (two per well) in the partially-cured PDMS strips. Plates were then stored at 37°C for at least 2 h to complete curing prior to subsequent scaffold sterilization, hydration, and crosslinking steps.

6.3.6 Scaffold hydration and crosslinking

Scaffolds were sterilized in ethanol for 1 h and then rinsed several times in phosphate-buffered saline (PBS) overnight. Carbodiimide crosslinking of scaffolds was performed in a solution of 1-ethyl-3-[3-dimethylaminopropyl] carbodiimide hydrochloride (EDC) and *N*-hydroxysulfosuccinimide (NHS) in PBS under shaking for 1.5 h at room temperature. The molar ratio of reaction components was 5:2:1 EDC:NHS:COOH where COOH represents the scaffold carboxyl (collagen) content (Olde Damink, Dijkstra et al. 1996; Harley, Leung et al. 2007). For incorporation of biomolecules (BSA, BMP, PDGF) post-fabrication these proteins were directly

added to scaffolds during the carbodiimide crosslinking process as previously described (Caliari and Harley 2013).

6.3.7 MSC culture in scaffolds

Human bone marrow-derived mesenchymal stem cells from healthy donors were bought from Lonza (Walkersville, Maryland) and cultured in low glucose DMEM supplemented with 10% MSC-validated FBS (Invitrogen) and antibiotics (Invitrogen) at 37°C and 5% CO_2. MSCs were fed twice per week and used at passage 6 for all experiments.

Confluent MSCs were trypsinized and re-suspended to a concentration of 3 x 10^5 cells per 60 µL media. 20 µL of cell suspension were added to the middle and the ends of each scaffold for a total of 3 x 10^5 MSCs seeded per scaffold (O'Brien, Harley et al. 2005). MSC-seeded scaffolds were incubated at 37°C and 5% CO_2 for 2.5 h to allow cells to attach, and then 6 mL complete DMEM was added to each well. MSC-scaffold constructs were cultured at 37°C and 5% CO_2 with media changes occurring twice per week. Flexcell experiments were performed using an intermittent stretch paradigm inspired by Paxton *et al.* which was shown to encourage tenogenesis (Paxton, Hagerty et al. 2012). MSC-seeded scaffolds were stretched uniaxially (longitudinal scaffold plane) for a total of 4 h/day (8 separate 30 min bouts of stretch) at 10% max strain and a frequency of 0.5 Hz.

6.3.8 Quantification of MSC metabolic activity

The metabolic activity of MSCs in TBJ scaffolds was assessed using the alamarBlue® assay (Invitrogen) (Tierney, Jaasma et al. 2009). AlamarBlue® measures mitochondrial metabolic

activity through the continuous reduction of the alamarBlue® dye (resazurin) to the fluorescent byproduct resorufin by healthy, active cells. Fluorescence was measured (excitation: 540 nm, emission: 580 nm) on a fluorescent spectrophotometer (Tecan, Switzerland).

6.3.9 Multiphoton microscopy

MSC cytoskeletal organization within scaffolds was assessed using confocal microscopy. MSC-seeded scaffolds were rinsed in PBS and fixed in 10% neutral buffered formalin at 4°C until analysis. Cell-scaffold constructs were permeabilized in 0.1% Triton X100 in PBS (Fisher Scientific, Pittsburgh, PA) for 10 min followed by incubation in Image-iT® FX signal enhancer (Invitrogen) for 20 min. Constructs were then stained with Alexa Fluor® 488 phalloidin for 20 min and then counterstained with DAPI to label cell nuclei for 5 min. Stained constructs were stored in PBS in the dark at 4°C until imaging. Confocal micrographs were acquired with a Zeiss 710 multiphoton confocal microscope (10x objective) equipped with a Spectraphysics Mai-Tai Ti-Sapphire laser. In addition to cytoskeletal imaging, collagenous organization was measured using second harmonic generation (SHG) imaging.

6.3.10 Quantitative assessment of scaffold strut and collagen fiber alignment

Scaffold strut alignment was quantified using the OrientationJ plugin within ImageJ (Fonck, Feigl et al. 2009). SEM images (30x magnification) of both the transverse and longitudinal planes in the CG and CGCaP compartments were used for the analysis. Scaffold strut alignment was quantified using OrientationJ's 'Distribution' function. Alignment of collagen fibers was quantified from confocal images acquired through SHG imaging. Orientation angles of individual collagen fibers (100 per group) were measured using the 'Measure' function.

Alignment data were reported in terms of orientation angle (-90° – +90°) where 0° corresponds to direction of heat transfer during freezing in the longitudinal plane.

6.3.11 RNA isolation, reverse transcription, and real-time PCR

Expression of tenogenic (COL1A1, SCXB, TNC) and osteogenic (ALP, BSP, OC) transcripts by MSCs seeded within TBJ scaffolds was evaluated via real-time PCR. RNA was isolated from MSC-scaffold constructs using an RNeasy Plant Mini kit as previously described (Qiagen, Valencia, CA) (Duffy, McFadden et al. 2011; Caliari, Weisgerber et al. 2012). Following a PBS wash to remove dead and unattached cells, constructs were immersed in lysis buffer (supplied with kit) on ice for 5 min. Lysates were processed by following the kit instructions to yield high-purity RNA. RNA was then quantified using spectrophotometry. 120 ng of RNA for each sample was reverse transcribed to cDNA using random primers and following kit instructions (QuantiTect Reverse Transcription kit, Qiagen). PCR primers (sequences acquired from the literature (Frank, Heim et al. 2002; Pauly, Klatte et al. 2010; Zhou, Xu et al. 2011) with the exception of the scleraxis (SCXB) primer set, which was purchased from Qiagen) were purchased from Integrated DNA Technologies (Coralville, IA). PCR reactions (10 µL) were performed in triplicate using a QuantiTect SYBR green PCR kit (Qiagen) in conjunction with an Applied Biosystems 7900HT Fast Real-Time PCR system (Applied Biosystems, Carlsbad, CA). Data analysis was performed with Sequence Detection Systems software v2.4 (Applied Biosystems) and fold changes were calculated using the delta-delta Ct method with GAPDH as the housekeeping gene.

6.3.12 Protein isolation and western blotting

MSC-scaffold constructs were immersed in RIPA lysis buffer for 30 min on ice. Lysates were mixed with 4x Laemlii buffer and loaded (50 µL/lane) onto 10% polyacrylamide gels. Gel electrophoresis was performed at 100 V. Separated gels were then transferred to nitrocellulose membranes (Fisher Scientific) at 300 mA for 2 h at 4°C. Membranes were then blocked in 5 w/v% non-fat milk for 30 min at room temperature and then incubated overnight with primary antibodies at 4°C. Antibodies for integrin subunits α4, α5, αV, β1, and β3 were purchased as part of an integrin sampler kit from Cell Signaling Technology (Beverly, MA). β-actin was used as the loading control (Cell Signaling). All primary antibodies were used at a 1:2000 dilution. Following thorough rinsing, rabbit horseradish peroxide (HRP)-conjugated secondary antibody (Cell Signaling, 1:2500 dilution) was added for 1 h at room temperature. Signal was developed using SuperSignal West Pico Chemiluminescent Substrate solutions (Thermo Scientific, Rockford, IL) and visualized on an Image Quant LAS 4010 (GE Healthcare, Pittsburgh, PA). Band intensities were quantified using ImageJ and expression levels were normalized to β-actin expression.

6.3.13 Histology and immunohistochemistry

Evidence of MSC infiltration and mineralization was assessed through hematoxylin and eosin (H&E) and alizarin red staining respectively. MSC-seeded scaffolds were fixed in 10% neutral buffered formalin, embedded in paraffin wax, serially sectioned (7 µm thick sections), and mounted on microscope slides. Following drying, slides were deparaffinized and then stained with the appropriate reagent. Stained sections were visualized on a Leica optical microscope (10x objective).

6.3.14 Statistical analysis

One-way analysis of variance (ANOVA) was performed on metabolic activity, loading efficiency, gene expression, and protein expression data sets followed by Tukey-HSD post-hoc tests. Significance was set at $p < 0.05$. Analysis of microstructure via SEM used $n = 3$ scaffolds. Metabolic activity, gene expression experiments, and Western blotting used $n = 3$ scaffolds per group while histological analyses used $n = 2$ scaffold per group. Error is reported in figures as the standard error of the mean unless otherwise noted.

6.4 Results

6.4.1 Analysis of TBJ scaffold microstructure

Four sets of SEM images were acquired to assess TBJ scaffold microstructure: i) CG compartment (transverse plane), ii) CG compartment (longitudinal plane), iii) CGCaP compartment (transverse plane), and iv) CGCaP compartment (longitudinal plane). Longitudinal SEM micrographs suggested that the CG compartment had highly aligned, geometrically anisotropic pores (**Figure 6.2(a)**) while the CGCaP compartment had a more amorphous pore structure (**Figure 6.2(b)**). Importantly, continuity of the collagen strut network was demonstrated at the CG-CGCaP interface (**Figure 6.2(c)**). Quantification of strut alignment in ImageJ demonstrated a strong peak around 0° in the CG longitudinal plane, confirming that the pores in the CG compartment were preferentially aligned in the direction of heat transfer during the freeze-drying process (**Figure 6.2(d)**).

6.4.2 Analysis of TBJ scaffold mineral content

Mineral distribution within the TBJ scaffold was assessed using microCT and EDX. Whole scaffold microCT scans demonstrated two distinct regions of pixel intensity corresponding to the CG and CGCaP compartments (**Figure 6.3(a)**). Using the difference in pixel intensity between the two compartments, the interface width was calculated to be 247 ± 101 μm (**Figure 6.3(b)**). Compositional maps of the elements calcium (**Figure 6.3(c)**) and phosphorus (**Figure 6.3(d)**) were obtained using EDX to confirm that the CaP content was indeed localized to the CGCaP compartment.

6.4.3 Direct incorporation of biomolecules into TBJ scaffolds during fabrication

The ability to directly incorporate biomolecules into distinct compartments in TBJ scaffolds during the freeze-drying process was assessed using several model proteins. Fluorescently-labeled streptavidin and BSA showed localization to the CGCaP and CG compartments respectively (**Figure 6.4(a)**). Addition of equivalent amounts of fluorescently labeled BSA or BMP pre-fabrication (added directly to suspension immediately before freeze-drying) or post-fabrication (incorporated via carbodiimide crosslinking) showed no significant differences in loading efficiency between the groups ($p = 0.42$) (**Figure 6.4(b)**). Finally, the maintenance of biomolecule activity through the freeze-drying process was demonstrated through the incorporation of the mitogenic factor PDGF-BB. Equivalent amounts (400 ng per scaffold) of PDGF-BB added pre- and post-fabrication both led to significantly increased MSC metabolic activity after 7 days culture compared to a non-supplemented control ($p < 0.02$) while there was no difference between the two PDGF-BB groups ($p = 0.89$) (**Figure 6.4(c)**). We also have begun to incorporate Cy-labeled proteins into the CG and CGCaP suspension to enable FRET analysis

of the CG-CGCaP compartment interface. Preliminary experiments demonstrate the feasibility of this approach (**Figure 6.5**).

6.4.4 Effects of bioreactor stretch on tenocyte organization and tenogenic gene expression

Tenocyte-seeded single compartment CG scaffolds were intermittently stretched for 7 days to confirm that stretch promoted a tenogenic phenotype in our scaffolds without any adverse side effects (**Figure 6.6(a)**). Confocal micrographs demonstrated that cells within scaffolds were more elongated in response to stretch (**Figure 6.6(b)**). The expression of a panel of tenogenic genes related to ECM synthesis (COL1A2, COL3A1, COMP, DCN), tenogenic phenotype (SCX, TNC), and ECM metabolism (MMP1, 3, and 13) was assessed in response to stretch (**Figure 6.6(c)**). Stretch induced significant up-regulation of the phenotype marker TNC ($p = 0.02$) and down-regulation of MMP-1 and 3 ($p < 0.04$).

6.4.5 Compartment and stretch-dependent integrin engagement in MSC-seeded TBJ scaffolds

A 24 h stretch experiment was conducted in the TBJ scaffolds to assess differential MSC integrin engagement in the CG and CGCaP compartments, both in static and dynamic culture (**Figure 6.7(a)**). Western blots of fibronectin-related integrin subunits α4, α5, αV, β1,and β3 revealed higher expression across the board in the CG compartment compared to the CGCaP compartment (**Figure 6.7(b)**). Additionally, intermittent stretch over the 24 h culture time consistently led to higher integrin expression in both compartments. In particular, expression of the β1 subunit was significantly higher in the CG compartment compared to the CGCaP region ($p = 0.04$) (**Figure 6.7(c)**).

6.4.6 Long term culture of MSC-seeded TBJ scaffolds: metabolic activity and gene expression

A 6 week long-term culture study was undertaken to see if the combination of intermittent stretch with the MSC-seeded TBJ scaffold could lead to spatially-graded differentiation. Metabolic activity of MSCs within TBJ scaffold was maintained and increased over the 6 week culture period (**Figure 6.8(a)**). Although there was a significant difference between the groups at 4 weeks ($p = 0.02$), the stretch group had a significant increase in metabolic activity from week 4 to 6 ($p = 0.002$) so that by the conclusion of the study there were no significant differences between the two groups ($p = 0.23$).

Expression of osteogenic genes ALP, BSP, and OC was measured after 6 weeks culture in the separate CG (tendon) and CGCaP (bone compartments) (**Figure 6.8(b)**). BSP and OC were both up-regulated in the CGCaP compartment compared to the CG compartment ($p < 0.05$). Additionally, the expression of tenogenic genes COL1A1, SCXB, and TNC were assessed (**Figure 6.8(c)**). Focusing on the CG compartment, stretch induced a significant up-regulation of the COL1A1 gene ($p = 0.04$).

6.4.7 Confocal microscopy: second harmonic generation imaging

SHG imaging was utilized to assess the organization of collagen within the MSC-scaffold constructs. Images show more aligned collagen fibrils in the CG compartment (**Figure 6.9(a)**) compared to the more diffuse fibers in the CGCaP compartment (**Figure 6.9(b)**). OrientationJ quantification of collagen fiber alignment demonstrates that while stretch does not seem to effect collagen alignment there is an overall trend towards increased alignment and organization in the CG compartment (**Figure 6.9(c)**).

6.4.8 Histology

Histological analysis of TBJ scaffolds was undertaken after 6 weeks in culture, focusing on determination of MSC infiltration into the scaffold and mineralization through the use of H&E and Alizarin red stains respectively. Representative H&E micrographs of the CG (**Figure 6.10(a)**) and the CGCaP (**Figure 6.10(b)**) compartments revealed adequate MSC distribution throughout the scaffold with no discernible effect of stretch observed. Alizarin red staining revealed significant mineral content in the CGCaP compartment after 6 weeks of culture (**Figure 6.10(c)**) with clear separation of mineral content at the CG/CGCaP interface maintained after the long-term culture period (**Figure 6.10(d)**).

6.5 Discussion

This study introduced a new potential biomaterial for TBJ repair composed of a multi-compartment CG-CGCaP scaffold that enabled spatially-graded presentation of microstructural, mechanical, and compositional cues. We have shown that MSCs seeded onto TBJ scaffolds fundamentally interact with the engineered ECM environment in a compartment and stretch-dependent manner. Long-term stretch induces spatially-graded tenogenic and osteogenic differentiation events as evidenced by compartment-specific genomic and proteomic profiles observed.

We first sought to validate the approach of combining directional solidification (Caliari and Harley 2011) with layering (Harley, Lynn et al. 2010) to create multi-compartment TBJ scaffolds

(**Figure 6.1**). Qualitative SEM and quantitative OrientationJ analyses demonstrated that TBJ scaffolds had more aligned pores in the CG compartment longitudinal plane while pores were more isotropic in the CGCaP compartment (**Figure 6.2**), mimicking the native TBJ microstructure. Interdiffusion between the two suspension layers was adequate to promote integration and continuity at the interface as evidenced by collagen fiber organization (**Figure 6.2(c)**). The creation of a smooth, continuous interface was an essential goal of the fabrication process and should improve the ability of the TBJ scaffold to withstand loading without delamination. There are several possible explanations as to why directional solidification induced alignment in the CG but not CGCaP compartments. Changes in suspension viscosity have previously been shown to affect mass transfer processes involved in ice crystal coarsening during the freezing process (Haugh, Murphy et al. 2010; Caliari and Harley 2011), so the increased viscosity of the CGCaP suspension may have slowed down this process, preventing ice crystal aggregation and elongation. Also, the increased salt content in the CGCaP suspension may have altered the coarsening kinetics of that compartment.

After demonstrating distinct regions of pore anisotropy within the TBJ scaffold, we next validated the compartmentalization of calcium phosphate mineral content. MicroCT scans show distinct regions of pixel intensity, indicating the presence of two compositionally-distinct compartments (**Figure 6.3(a)**). This disparity in pixel intensity was taken advantage of to determine the width of the interdiffusion zone between the two compartments (**Figure 6.3(b)**). The calculated interface width of 247 μm is similar to the width of the native TBJ interfacial zone (~100-1000 μm depending on species) (Moffat, Sun et al. 2008; Wopenka, Kent et al. 2008). Finally, to confirm the presence of calcium phosphate mineral we performed EDX

analysis to obtain elemental maps of calcium and phosphorus content (**Figure 6.3(c-d)**). Compositional maps taken at the CG-CGCaP interface were superimposed on SEM images that show the aligned pores of the CG compartment merging into the isotropic pores of the CGCaP compartment. These maps confirm the localization of calcium and phosphorus content to the CGCaP side of the scaffold. While the CaP phase was not investigated in this study, previous work with CGCaP materials has characterized the initial phase as brushite, which can be hydrolytically converted to the more biologically-relevant hydroxyapatite (Harley, Lynn et al. 2010).

In addition to spatial organization of mineral content and ECM organization, the native TBJ also contains distinct profiles of biomolecules such as growth factors. Growth factors and cytokines have been shown to have considerable beneficial effects for driving tenogenic (Thomopoulos, Harwood et al. 2005; Park, Hogan et al. 2010; Manning, Kim et al. 2011) and osteogenic (Yilgor, Tuzlakoglu et al. 2009; Lan Levengood, Polak et al. 2010) phenotype. While we have previously demonstrated methods for immobilizing biomolecules within CG scaffolds in a spatially-patterned (Martin, Caliari et al. 2011) or ubiquitous (Caliari and Harley 2013) manner, these methods involved adding factors post-fabrication. In order to enhance the "off-the-shelf" potential of this material, we were interested in directly incorporating biomolecules into the distinct compartments of the TBJ scaffold during the freeze-drying process in an efficient manner that would maintain bioactivity. As a proof of concept, we added different fluorescently-labeled proteins into the separate CG and CGCaP precursor suspensions immediately prior to layering and freeze-drying. Confocal imaging revealed incorporation and compartmentalization of the labeled proteins (**Figure 6.4(a)**). Loading efficiency for incorporating proteins pre-

fabrication or post-fabrication (via carbodiimide crosslinking) showed no differences for two model proteins (**Figure 6.4(b)**). Critically, the maintenance of bioactivity through the freeze-drying process was demonstrated for PDGF-BB, a mitogenic factor that produced equivalent increases in MSC metabolic activity when added in equivalent doses pre- or post-fabrication (**Figure 6.4(c)**).

Once we had characterized the microstructural and compositional properties of the TBJ scaffold we were interested in exploring the effect of bioreactor stimulation in the form of uniaxial tension on cell phenotype. Before working with TBJ scaffolds, we validated our bioreactor scheme in a single compartment CG scaffold. Numerous studies have shown the benefit of mechanical stimulation for tenogenesis (Juncosa-Melvin, Shearn et al. 2006; Paxton, Hagerty et al. 2012; Subramony, Dargis et al. 2012). For this work, we adapted a stretch paradigm based on Paxton *et al.* which optimized stretch conditions to maximize collagen synthesis and mechanical integrity in an engineered fibrin gel system for ligament tissue engineering (Paxton, Hagerty et al. 2012). The bioreactor used was a commercially available Flexcell® system that has been applied to numerous tissue engineering applications (Ahearne, Bagnaninchi et al. 2008; Boerboom, Rubbens et al. 2008). Confocal imaging of tenocytes within mechanically-stimulated scaffolds demonstrates the influence of stretch (**Figure 6.6(b)**). Stretching generally led to up-regulation of tenogenic genes as well as down-regulation of MMPs (**Figure 6.6(c)**).

After validating the Flexcell® bioreactor setup in a single compartment scaffold we quickly moved to the multi-compartment TBJ scaffold system. We were interested in understanding at a fundamental level how MSCs were sensing their microenvironment; in particular we wanted to

tease out the influence of compartment and stretch on MSC-microenvironment interactions through the measurement of integrin expression. We chose to look at a set of integrin subunits whose ligand was fibronectin. Fibronectin, in addition to serving as an adhesion ligand for cells, influences other cellular processes including proliferation and differentiation. Fibronectin expression has been shown to be dependent on mechanical stretch for a variety of cell types, including fibroblasts (Steward, Cheng et al. 2011) and MSCs (Kinneberg, Nirmalanandhan et al. 2010). Our results indicate that MSCs in the CG compartment are consistently engaging fibronectin-related integrins at a higher level than in the CGCaP compartment (**Figure 6.7(b-c)**). Both compartments trended towards increased integrin expression in response to stretch (**Figure 6.7(c)**). These trends may be due to the increased elasticity of the CG compartment compared to the CGCaP compartment, allowing MSCs in the softer compartment to grab and pull on the microenvironment more than in the rigid CGCaP compartment.

Following short-term culture experiments, we interrogated the ability of the TBJ scaffold to support long-term MSC viability and guide spatially-graded lineage specification in conjunction with intermittent stretch. Although the stretch group had lower MSC metabolic activity than the static group at all time points, this difference was not significant by the end of the experiment (**Figure 6.8(a)**). Expression of osteogenic and tenogenic genes was also tracked as a proxy for differentiation. Osteogenic genes BSP and OC, a late-stage marker of osteogenesis, were significantly up-regulated after 6 weeks in the CGCaP compartment (**Figure 6.8(b)**). Stretch led to up-regulation of COL1A1 in the CG compartment (**Figure 6.8(c)**). Type I collagen is the primary protein constituent of tendon.

Additionally, collagen organization was measured using SHG imaging. SHG images reveal more organized, aligned collagen fibers in the CG compartment compared to the CGCaP compartment (**Figure 6.9(a-b)**). This was confirmed quantitatively by OrientationJ analysis of collagen fiber alignment angles (**Figure 6.9(c)**). H&E analyses reveal adequate cell infiltration in both the CG and CGCaP compartments (**Figure 6.10(a-b)**). This was expected as the freezing temperature of -10°C was chosen to support the formation of larger pores that facilitate cell migration and support increased cellular metabolic activity as well as greater resistance to cellular contractile forces (Caliari and Harley 2011).

An important limitation of SHG when used in conjunction with collagen-based materials is that there is no way to differentiate between scaffold and MSC-synthesized collagen. Similarly, although mineral content was restricted to the CGCaP compartment as evidenced by Alizarin red staining (**Figure 6.10(c-d)**), it is unclear how much of the mineral is from the original scaffold itself. It is promising, however, that there was no mineral deposition observed in the CG compartment after 6 weeks of culture. Ongoing studies will optimize stretch conditions for our TBJ scaffold system and evaluate activation of salient signaling pathways such as extracellular signal-related protein kinase (ERK) 1/2, Rho-associated protein kinase (RhoA/ROCK), and Wnt/β-catenin that are known to be involved in osteotendinous development. *In vivo* ectopic studies will begin to ascertain the suitability of these materials for TBJ repair in a load-bearing defect.

6.6 Conclusions

There is a critical need for improved biomaterials for engineering orthopedic interfaces. Here we present an approach to fabricate a spatially-graded multi-compartment CG scaffold for engineering the TBJ. We show TBJ scaffolds with graded pore anisotropy and mineral content can be fabricated in a manner that mimics key elements of the native TBJ. Additionally, we demonstrate the capability to incorporate therapeutic biomolecules into separate compartments directly through the freeze-drying fabrication process in an efficient manner while maintaining bioactivity. We then focused on integrating our TBJ scaffold into a Flexcell® bioreactor system as a pathway towards inducing spatially-graded tenogenic and osteogenic MSC differentiation. MSC-seeded TBJ scaffolds demonstrate compartment and stretch-dependent profiles of fibronectin-related integrin engagement with increased utilization in the CG compartment as well as in both compartments in response to stretch. Longer-term stretch studies revealed sustained MSC metabolic activity in both static and dynamic cultures with compartment-specific genomic and proteomic profiles. Osteogenic genes BSP and OC were significantly up-regulated in the CGCaP compartment while COL1A1 was significantly up-regulated in the CG compartment in response to stretch. Further analysis demonstrated greater alignment of collagen fibers in the CG compartment as well as maintained demarcation of mineral content at the interface between the CG and CGCaP compartments. Together these data show that the multi-compartment TBJ scaffold introduced here can mimic key microstructural and compositional characteristics of the native TBJ, and that in conjunction with uniaxial tensile strain this scaffold can guide spatially-graded MSC differentiation. Ongoing work is assessing the suitability of these scaffolds for *in vivo* regeneration of the TBJ.

6.7 Figures

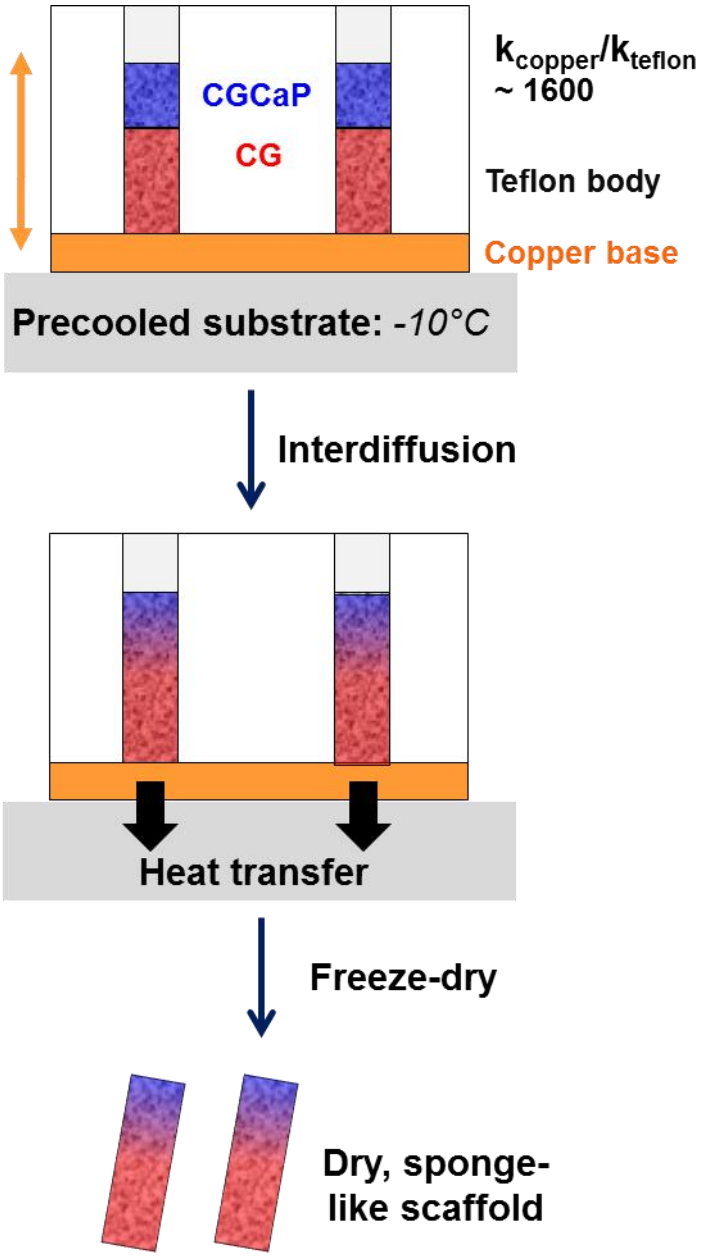

Figure 6.1. Schematic of approach to make multi-compartment TBJ scaffolds with distinct regions of pore anisotropy and mineral content. The approach combined directional solidification to produce aligned pores in the CG (red) region along with liquid phase co-synthesis to integrate the non-mineralized CG (red) and mineralized CGCaP (blue) compartments together via diffusive mixing.

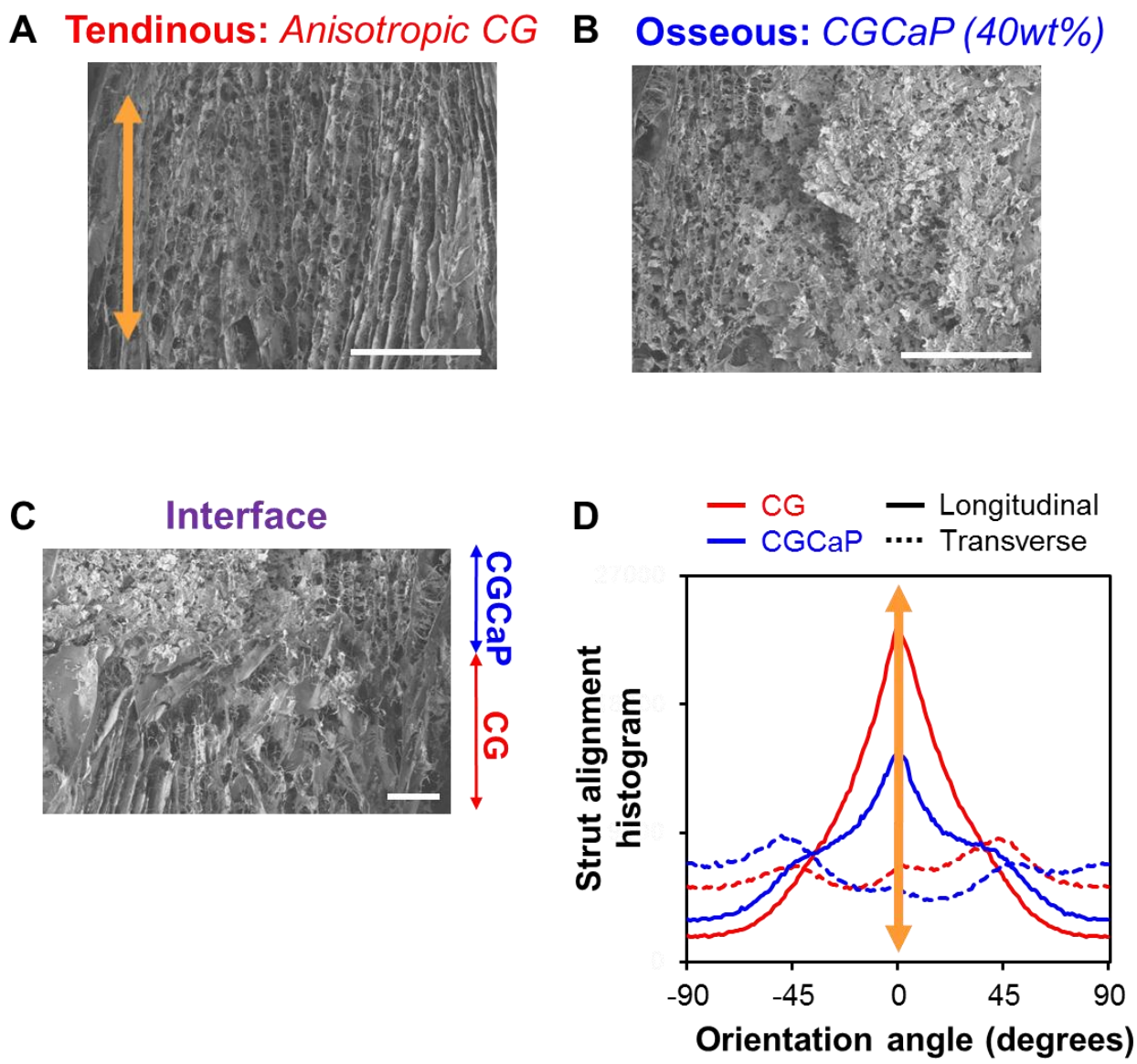

Figure 6.2. Microarchitecture of multi-compartment TBJ scaffolds. Scanning electron micrographs of TBJ scaffold porous architecture showed A) highly aligned pores in the tendinous or CG region, B) amorphous pores in the osseous or CGCaP region, and C) continuity of collagen fibers at the interface between the compartments. D) OrientationJ analysis of pore alignment demonstrated that pores were longitudinally aligned in the CG compartment, but more randomly aligned in the corresponding CGCaP compartment. *Scale bars*: 200 µm.

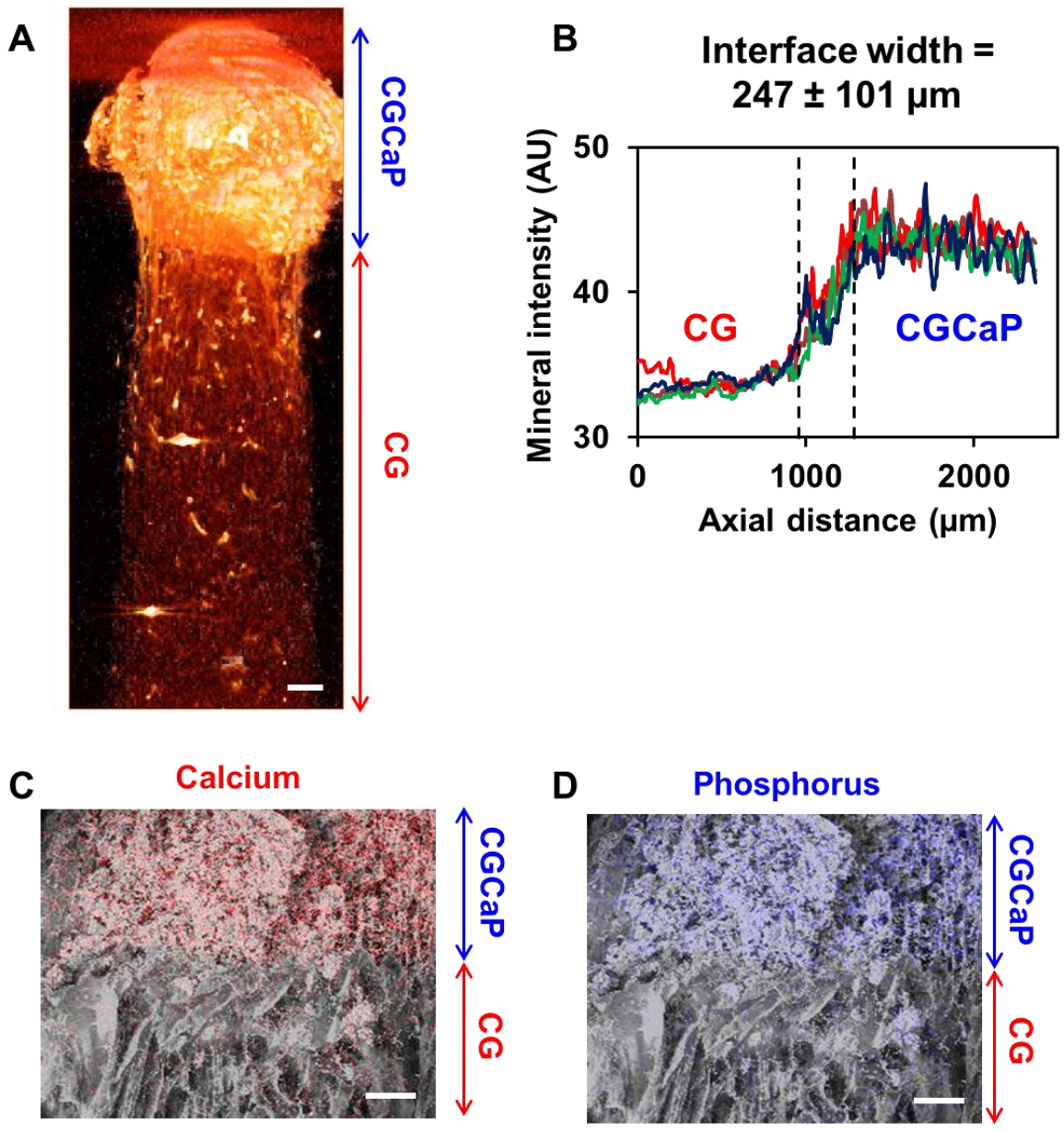

Figure 6.3. Distribution of calcium phosphate (CaP) content within TBJ scaffolds. A) MicroCT image of multi-compartment TBJ scaffold. *Scale bar*: 1 mm. B) Using differences in the intensity of the mineralized versus non-mineralized compartments, the interface width was calculated to be approximately 247 ± 101 µm. C) Energy-dispersive x-ray spectroscopy (EDX) analysis of scaffold elemental composition revealed localization of calcium and D) phosphorus content primarily in the CGCaP (mineralized) region of the scaffold. *Scale bars*: 200 µm. MicroCT analysis courtesy of Daniel Weisgerber.

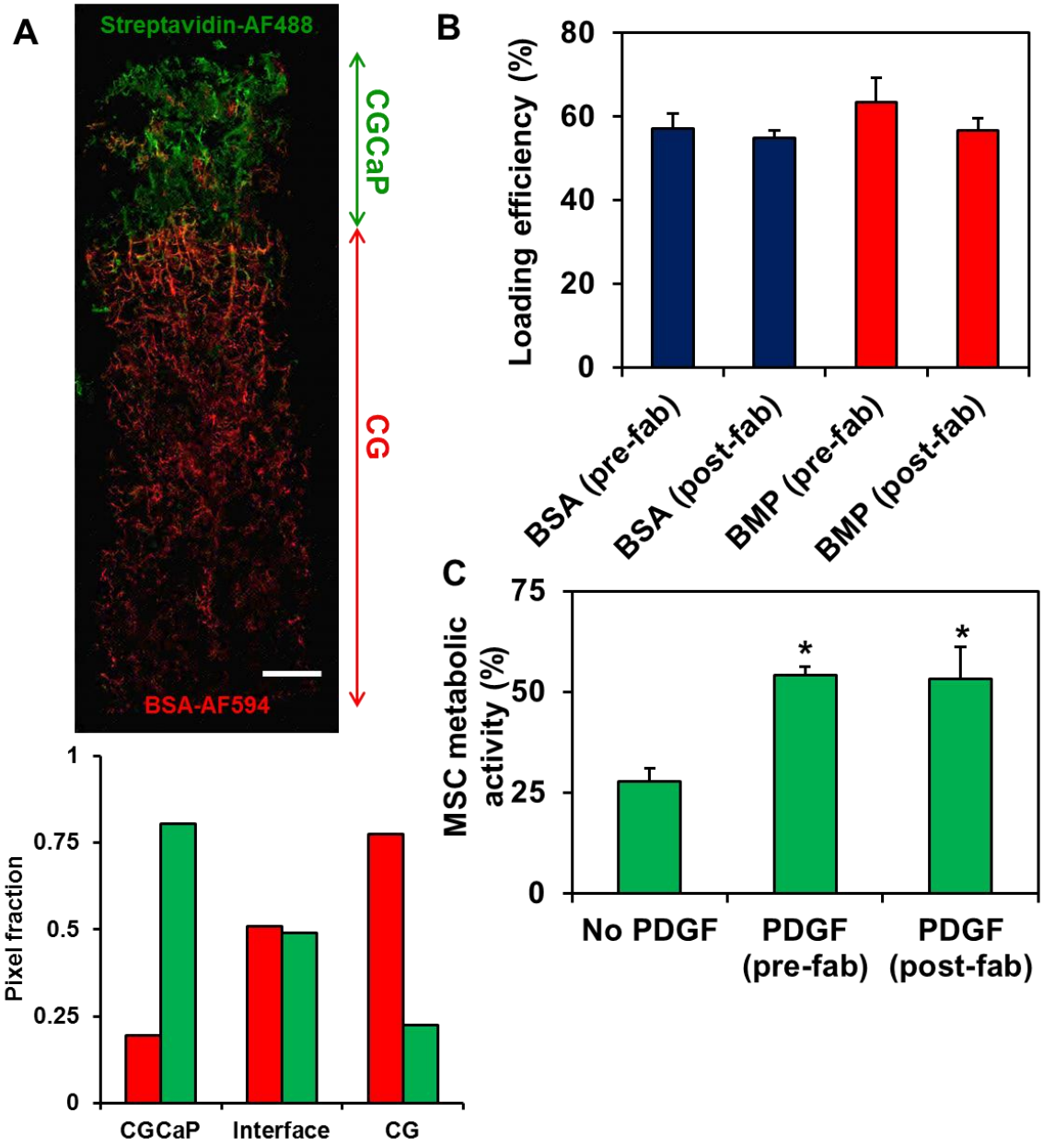

Figure 6.4. Direct incorporation of biomolecules within TBJ scaffolds during lyophilization. A) Confocal micrograph of TBJ scaffold loaded with AlexaFluor 488-streptavidin conjugate in the mineralized (CGCaP) compartment and AlexaFluor 594-BSA conjugate in the non-mineralized (CG) compartment. B) Loading efficiency of fluorescently-labeled BSA and BMP-2 when added in equivalent amount either pre-fabrication (during lyophilization) or post-fabrication (via carbodiimide crosslinking). C) MSC metabolic activity on scaffolds with no PDGF or PDGF incorporated either pre- or post-fabrication. *Scale bar*: 1 mm. *: significantly higher than the no PDGF group.

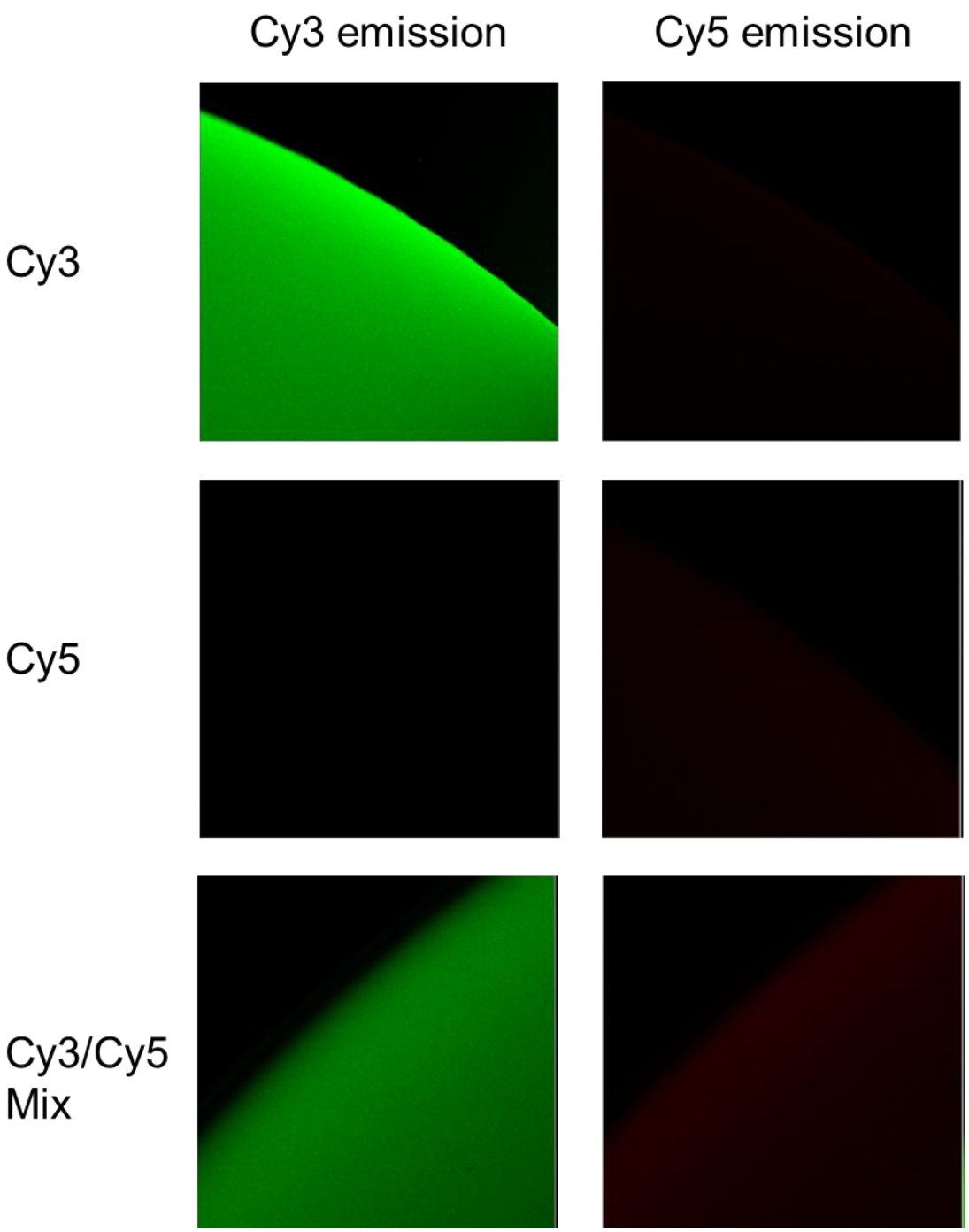

Figure 6.5. FRET analysis of Cy3-Cy5 compounds. As a proof of concept we show here that BSA labeled with Cy3 and Cy5 respectively can interact and be analyzed via FRET when excited at the donor (Cy3) wavelength. Ongoing work is seeking to use FRET to enable analysis of the interfacial region of our multi-compartment scaffolds.

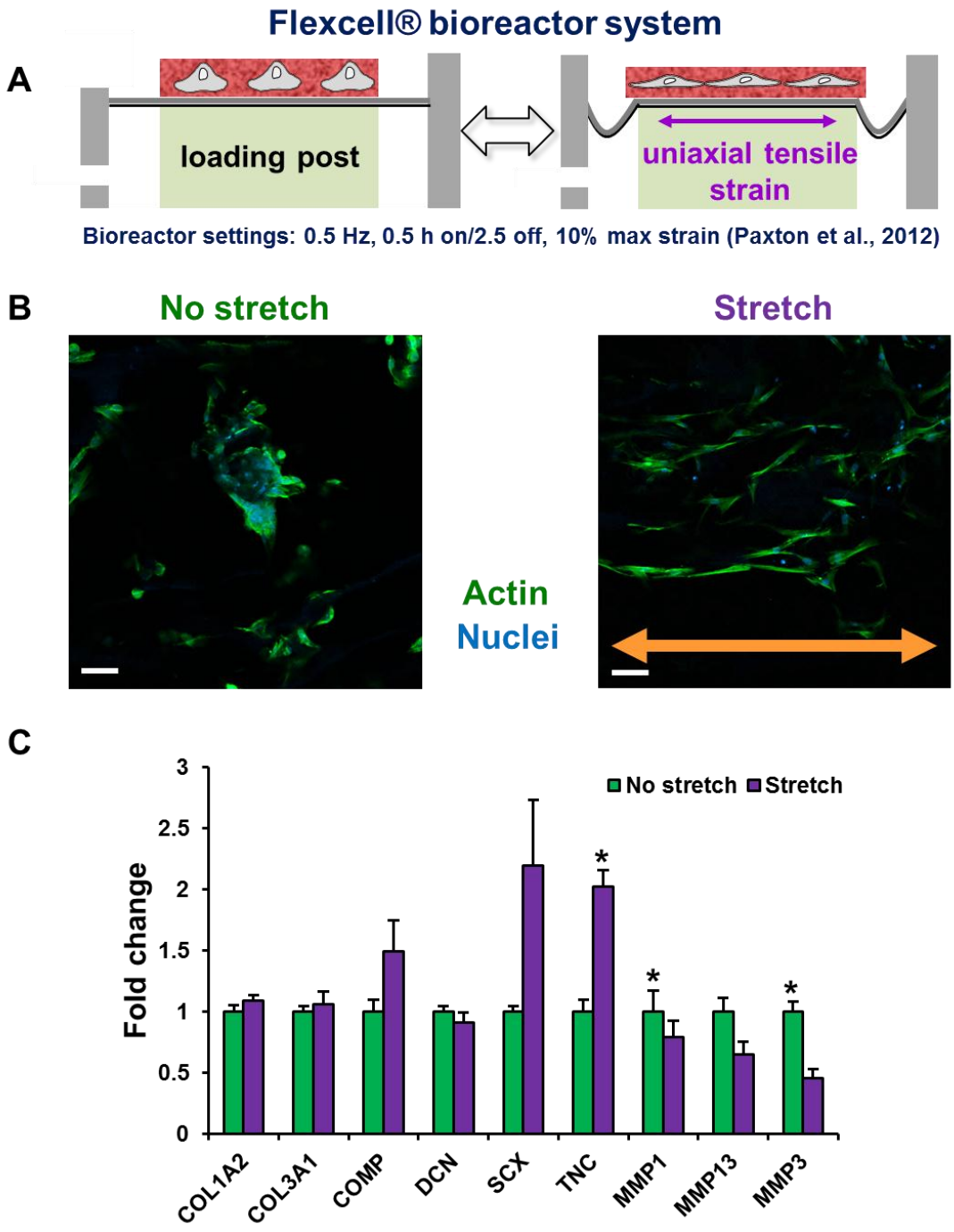

Figure 6.6. Effects of mechanical stretch on tenocyte behavior in aligned CG scaffold. A) Schematic of Flexcell® bioreactor system where uniaxial tensile strain can be imposed on cell-seeded scaffolds adhered to flexible well plate membranes. B) Confocal micrograph of tenocytes in scaffolds with (*right*) or without (*left*) stretch. *Green channel*: actin (Alexa Fluor® 488 phalloidin). *Blue channel*: nuclei (DAPI). *Scale bar*: 50 µm. C) Expression of tenogenic genes in response to intermittent uniaxial stretch. *: significantly higher expression.

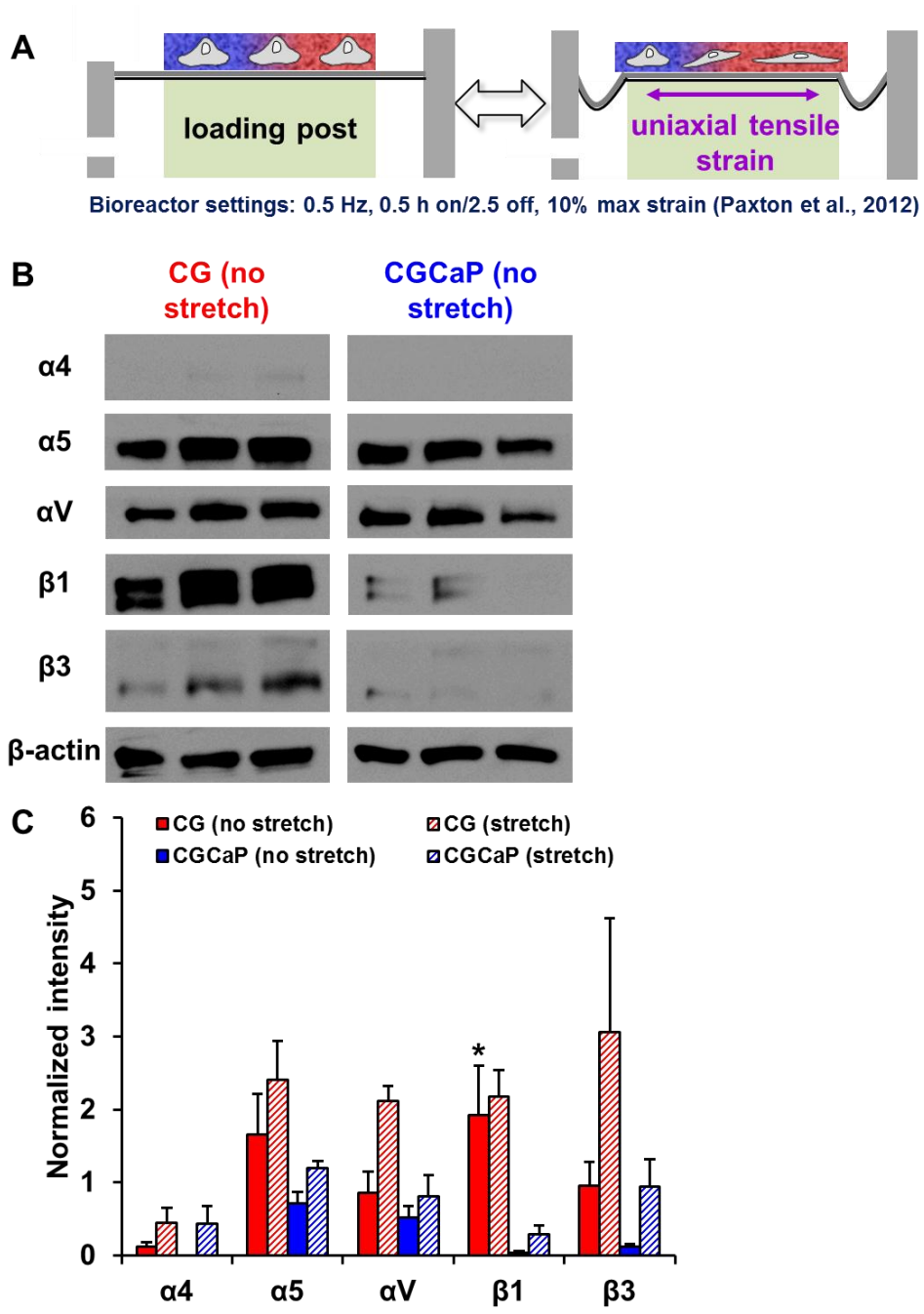

Figure 6.7. Influence of compartment and stretch on integrin engagement. A) Schematic of Flexcell® bioreactor system loaded with MSC-seeded multi-compartment TBJ scaffold. B) Western blots of tendon (CG) and bone (CGCaP) no stretch fibronectin-related integrin subunit engagement showed consistently higher expression in the tendon (CG) compartment. C) Normalized blot intensity quantitatively demonstrated higher levels of expression in the tendon (CG) compartment and in response to stretch for both compartments. *: significantly higher expression.

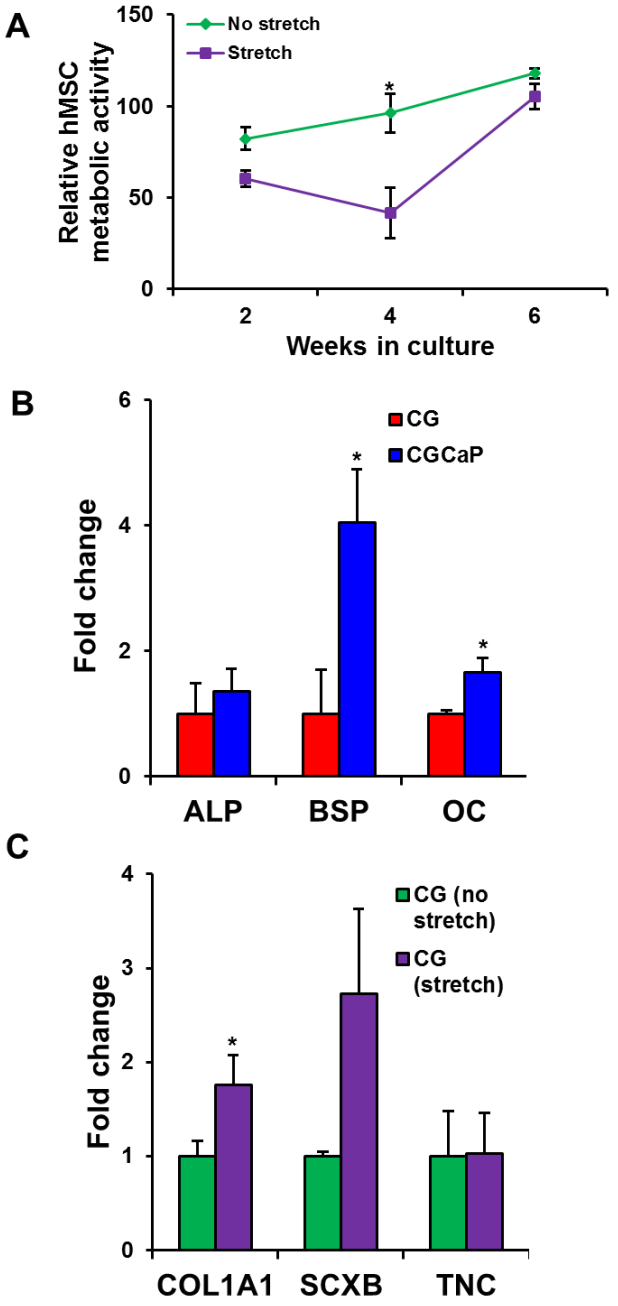

Figure 6.8. MSC proliferative and genomic responses to long-term culture on TBJ scaffolds. A) TBJ scaffolds maintained adequate and sustained MSC metabolic activity over the entire 6 week experiment. B) Expression of osteogenic genes alkaline phosphatase (ALP), bone sialoprotein (BSP), and osteocalcin (OC) was elevated in the bone (CGCaP) compartment. C) In response to stretch, expression of tenogenic markers type I collagen (COL1A1), scleraxis (SCXB), and tenascin-C (TNC) was elevated in the tendon (CG) compartment.*: significantly higher expression.

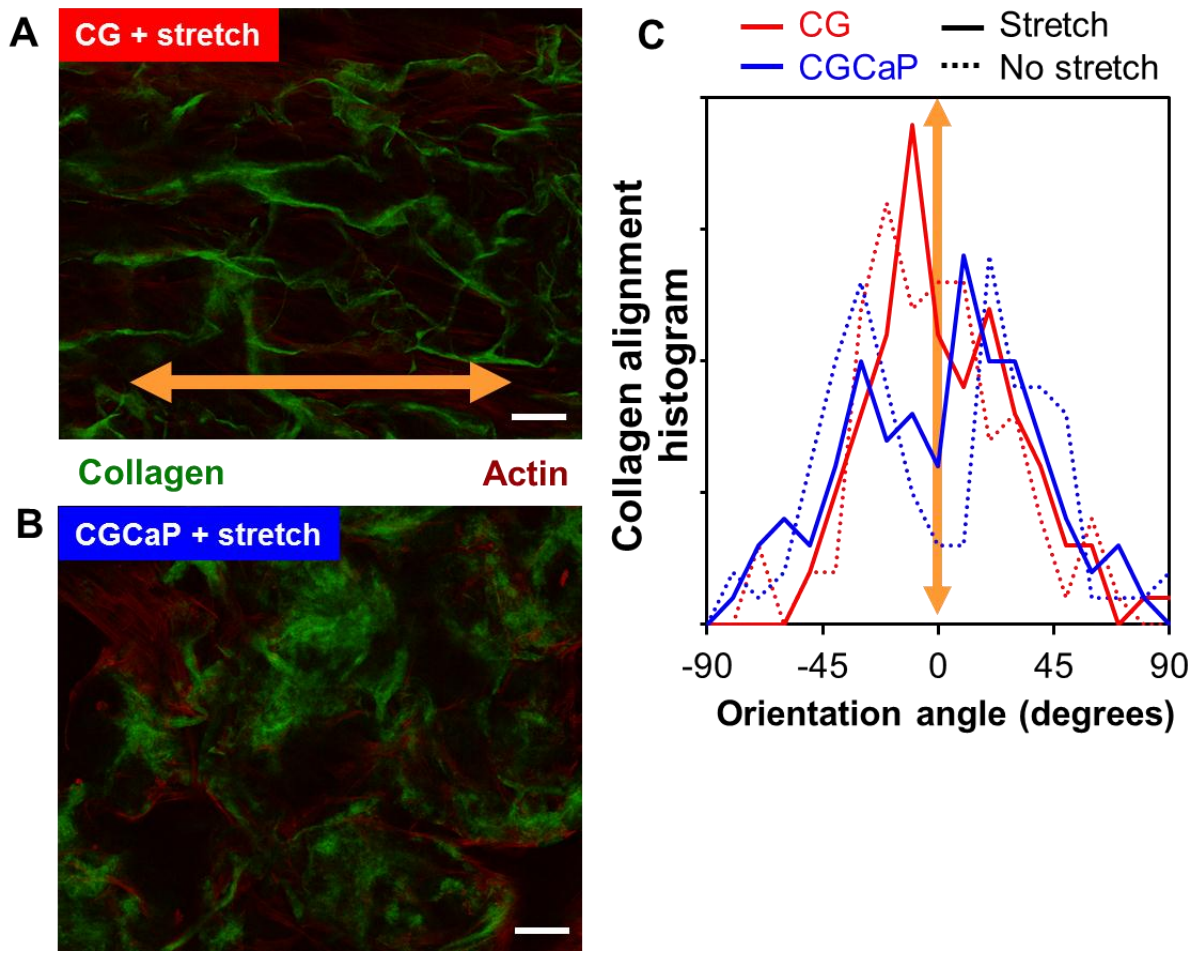

Figure 6.9. Second harmonic generation (SHG) imaging of scaffold collagen organization. A) Collagen organization in response to stretch in the tendon (CG) and B) bone (CGCaP) compartments. *Green channel*: collagen. *Red channel*: actin. *Scale bars*: 50 µm. C) Quantification of collagen alignment in distinct compartments showed trend towards increased alignment and organization in the tendon (CG) compartment.

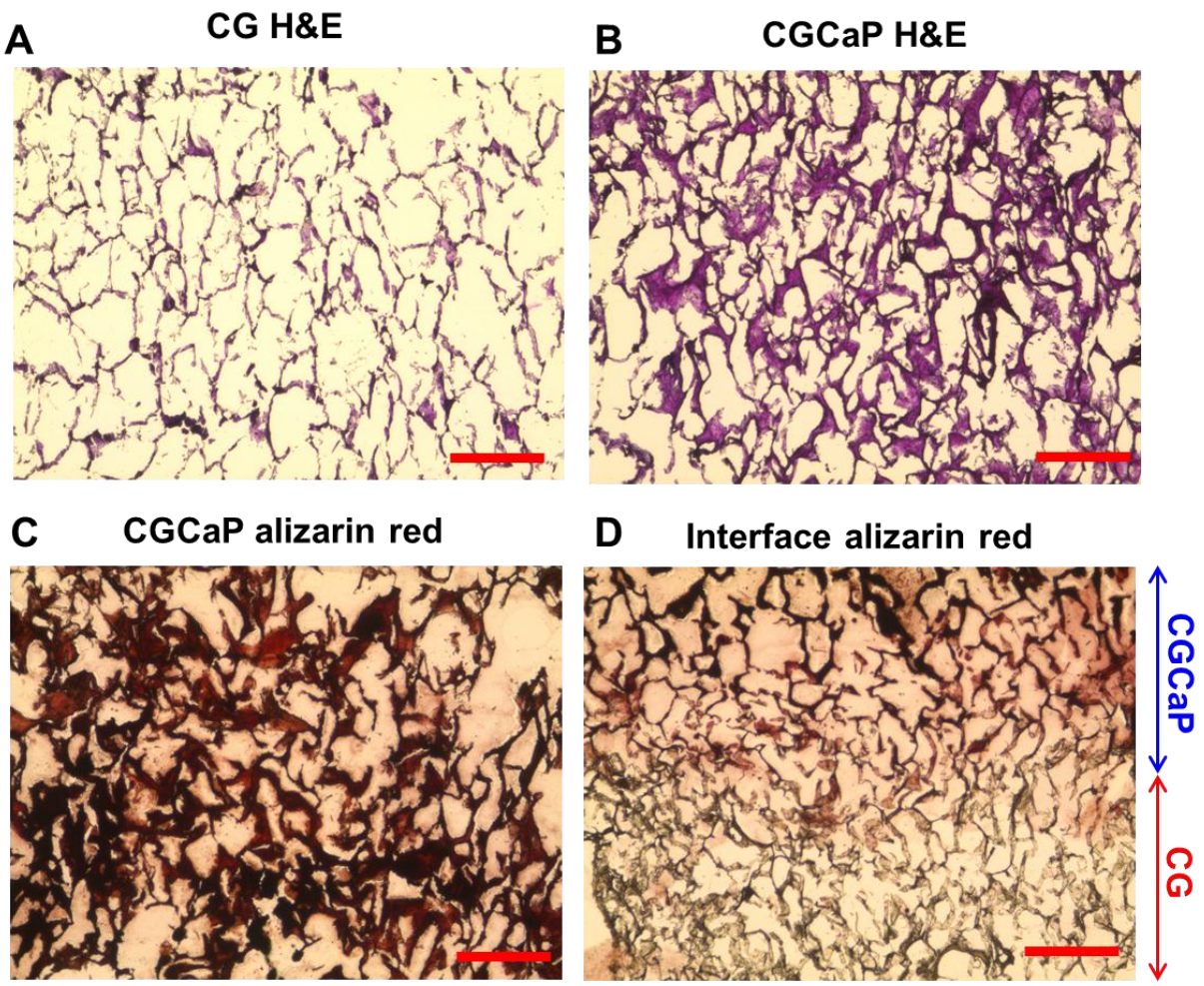

Figure 6.10. Histological analysis of MSC-seeded scaffolds after 6 weeks of culture. A) Hematoxylin and eosin (H&E) staining of the tendon (CG) and B) bone (CGCaP) compartments revealed MSC infiltration to the center of the scaffold. C) Mineral staining via alizarin red showed mineral localized primarily to the bone (CGCaP) compartment and D) not in the tendon (CG) compartment. *Scale bars*: 200 µm.

CHAPTER 7: CONCLUSIONS AND FUTURE WORK

7.1 Conclusions

Chapter 2 describes the evaluation of scaffold microstructure and mechanics as well as tenocyte viability and gene expression profiles for a homologous series of anisotropic CG scaffolds with variable relative density. SEM and stereology showed that aligned scaffolds with elongated pores and a consistent degree of anisotropy could be fabricated independent of relative density. Scaffold permeability and mechanics, both in tension and compression, demonstrated dependence on relative density with 3x scaffold mechanical properties increasing by over an order of magnitude compared to 1x scaffolds, consistent with predictions made via cellular solids modeling. Equine tenocytes showed increased proliferation, metabolic activity, soluble collagen synthesis, and alignment as well as less cell-mediated scaffold contraction when cultured in higher density scaffolds. The low density 1x scaffolds demonstrated significant contraction that resulted in reduced cell number, loss of microstructural integrity and cell alignment, and loss of tenocyte-specific gene expression profiles over the 14 day culture period. Functional and gene expression analyses also suggested that the highest density anisotropic scaffold maintained a more tendon-like microenvironment that preserves tenocyte transcriptomic stability. Notably, tenocytes in the highest density scaffold displayed marked, significant increases in COMP, TNC, and SCX expression as well as significant decreases in MMP1 and MMP13 expression. This work suggests that scaffold relative density is a critical design parameter, not only for insuring mechanical competence and providing microstructural and mechanical cues at the experiment outset, but also for maintaining essential microstructural cues to direct cell behavior and gene expression over the course of long-term culture.

Chapter 3 utilized the optimized high density anisotropic CG scaffold identified in Chapter 2 to evaluate the dose-dependent effects of soluble factors PDGF-BB, IGF-1, bFGF, SDF-1α, and GDF-5 on tenocyte migration, viability, collagen synthesis, and gene expression. Taken together, the data in this chapter suggest a critical trade-off between induction of rapid cell migration/proliferation and the expression of normal tenocyte phenotypic markers. Pairing proliferative (IGF-1) and phenotypic (GDF-5) factors can support significantly increased tenocyte proliferation and soluble collagen synthesis in addition to up-regulation of key genetic markers (COL1A2, COMP, and SCXB), indicating that combining factor pairs with an engineered CG scaffold may be an approach towards optimizing a construct for tendon tissue engineering. Facile immobilization of these factors within scaffolds was accomplished using carbodiimide chemistry and induced similar effects as soluble supplementation but in a manner more amenable to *in vivo* translation. Improved understanding of the individual and combined effects of the soluble factors investigated here is motivating ongoing work in our lab integrating immobilized and patterned factor presentation within scaffolds for functional musculoskeletal tissue engineering applications.

Chapter 4 used simple modifications to a standard CG scaffold to investigate the roles of scaffold structure (geometric anisotropy, mineral content, relative density) in combination with biomolecule supplementation on driving tenogenic, osteogenic, and chondrogenic MSC differentiation respectively. The importance of scaffold microstructural anisotropy for enhancing tenogenic differentiation was shown by increased expression of the phenotype marker SCXB as well as increased ROCK1 levels in anisotropic compared to isotropic scaffolds. Notably, small molecule cytoskeletal or Smad8 inhibition abrogated these effects. MSC osteogenic

differentiation was enhanced by osteogenic induction media, although the inclusion of a mineral phase in the scaffold led to elevated ALP and RUNX2 expression as well as increased mineralization after 21 days. Chondrogenic differentiation was enhanced by combining classic chondrogenic induction media with a low density scaffold that enhanced cellular condensation and led to significant up-regulation of COL2A1 and ACAN as well as increased GAG production. Together, these data provide insight into critical scaffold instructive cues that should inform the development of CG scaffolds for a variety of single and multi-tissue musculoskeletal tissue engineering applications. In particular, these data suggest a scaffold with an anisotropic tendon region and a mineralized bone region, joined with lower density interface and coupled with spatially-graded biomolecular cues, may be optimal for osteotendinous repair.

Biomaterials for complex tissue engineering applications must be able to instruct cell behavior in the presence of the multivariate environments encountered *in vivo*. Using a series of CG scaffolds with physical properties optimized to specific components of orthopedic interfaces, Chapter 5 investigated the impact of scaffold relative density and mineral content on MSC lineage specification in the presence of mixed osteogenic and chondrogenic signals. We found that mineralized scaffolds were able to suppress chondrogenic outcomes compared to the two non-mineralized variants investigated as evidenced by gene expression and histological analyses. While the higher density non-mineralized scaffold elicited a greater chondrogenic response than the mineralized scaffold, the more surprising result was the heightened osteogenic response observed in the lower density, non-mineralized scaffold group with heightened chondrogenesis occurring in the higher density, non-mineralized group. This unexpected response may be due to local stiffening of the extracellular environment due to cell-mediated scaffold contraction. The

increased cell density as a result of contraction may have also accelerated the kinetics of MSC differentiation and maturation, leading to a response similar to endochondral ossification. These results will inform ongoing work in our lab designing multi-compartment scaffolds for graded tissue regeneration.

There is a critical need for improved biomaterials for engineering orthopedic interfaces. Chapter 6 presented an approach to fabricate a spatially-graded multi-compartment CG scaffold for engineering the TBJ. We showed TBJ scaffolds with graded pore anisotropy and mineral content can be fabricated in a manner that mimics key elements of the native TBJ. Additionally, we demonstrated the capability to incorporate therapeutic biomolecules into separate compartments directly through the freeze-drying fabrication process in an efficient manner while maintaining bioactivity. We then focused on integrating our TBJ scaffold into a Flexcell® bioreactor system as a pathway towards inducing spatially-graded tenogenic and osteogenic MSC differentiation. MSC-seeded TBJ scaffolds demonstrate compartment and stretch-dependent profiles of fibronectin-related integrin engagement with increased utilization in the CG compartment as well as in both compartments in response to stretch. Longer-term stretch studies revealed sustained MSC metabolic activity in both static and dynamic cultures with compartment-specific genomic and proteomic profiles. Osteogenic genes BSP and OC were significantly up-regulated in the CGCaP compartment while COL1A1 was significantly up-regulated in the CG compartment in response to stretch. Further analysis demonstrated greater alignment of collagen fibers in the CG compartment as well as maintained demarcation of mineral content at the interface between the CG and CGCaP compartments. Together these data show that the multi-compartment TBJ scaffold introduced here can mimic key microstructural and compositional characteristics of the

native TBJ, and that in conjunction with uniaxial tensile strain this scaffold can guide spatially-graded MSC differentiation. Ongoing work is assessing the suitability of these scaffolds for *in vivo* regeneration of the TBJ.

7.2 Future work

7.2.1 Naturally-inspired design strategies

Tissue engineering strategies are increasingly being informed by natural processes. In my master's thesis, we discussed the development of a mechanically efficient scaffold-membrane composite that mimicked naturally-occurring core-shell composites such as plant stems and porcupine quills (Caliari, Ramirez et al. 2011). This composite will be re-visited in Appendix B. Other innovative biomimetic material systems have recently emerged such as polymer actuators driven by water flow (Ma, Guo et al. 2013) and tissue adhesives based on microstructured barbs on porcupine quills to minimize penetration force (Cho, Ankrum et al. 2012).

Increasingly, the processes of development and morphogenesis are being investigated to inspire regenerative medicine applications. In particular, fetal healing may serve as a model for regeneration strategies. In contrast to adult healing, fetal tendons can heal with little inflammation, no significant changes in cytokine activities, and full restoration of mechanical properties (Favata, Beredjiklian et al. 2006). This suggests that intrinsic cells in fetal tendon may have regenerative capabilities. Notably, fetal platelets at the wound site display reduced expression of TGF-β1, TGF-β2, PDGF, and bFGF as well as increased VEGF and TGF-β3 compared to adult platelets (Yannas, Kwan et al. 2007). Another study tracked the expression

patterns of key genes in tendon development using a chick model. Interestingly, TGF-β1 was not expressed at all during this process while TGF-β2 and TGF-β3 were expressed at differential levels (Kuo, Petersen et al. 2008), suggesting that TGF-β1 antagonists may be relevant candidates for future work.

Emerging theories suggest that tendon development is "passive". Muscle anchors to bone, and tendons form from a population of scleraxis-expressing cells. Tendon development is "passive" and driven by skeletal growth. As the embryo develops, the tendon is stretched and elongated to the proper length. Interestingly, tendons and ligaments are not too long or short in conditions such as dwarfism, perhaps indicative that growth of these connective tissues is driven by the growth of other tissues (muscles, cartilage, and bone). Additionally, mechanical force is known to up-regulate scleraxis and promote the release of various growth factors and other cytokines. As tendons are stretched during development, they likely release a cascade of these chemoattractive molecules to recruit a poorly-defined set of mesenchymal cells to contribute to tendon growth and elongation. Identification of these cytokines, as well as the source of these cells, will be critical for future work in the field of tendon tissue engineering. Much of the work in this thesis has discussed scleraxis, a transcription factor and a specific marker for tendon and ligaments. Recent work has shown that TGF-β activated MSCs promote Smad3 phosphorylation, binding of Smad3 to Scx, translocation to the nucleus, and induction of pro-tenogenic gene expression such as COL1A2 (Berthet, Chen et al. 2013). The release of cytokines following stretch during development likely serves two purposes: *i*) recruit mesenchymal cells to the developing tendon, and *ii*) initiate autocrine activity whereby released cytokines locally activate tendon progenitor cell growth factor pathways which in turn leads to Smads (and possibly other

signaling proteins) binding with transcription factors like Scx (and others like Mohawk) in order to drive gene transcription and synthesis of tenogenic proteins such as type I collagen.

7.2.2 Combinatorial strategies to assess regulators of cell activity

As suggested in Chapter 1, combinatorial strategies for assaying many microenvironmental combinations in parallel are emerging as powerful tools in the field. Driven in part by systems-level analytic tools in the genomics field, approaches to rapidly probe many different biomaterials at once (and efficiently process the accumulation of data) should help towards understanding the complex network of microenvironmental regulators of cellular behaviors. By paring down this network to a minimal constellation of instructive cues, new and improved regenerative template can be designed. To this end, Appendix A discusses the development of a CG scaffold array system towards combinatorial evaluation of multiple biophysical and biochemical cues involved in cell-CG scaffold interactions.

7.2.3 Animal models

One key step forward will be the initialization of animal trials to evaluate the *in vivo* efficacy of these materials. Mouse and pig ectopic models will be used to initially assess graft durability and capacity to support cellular infiltration, growth, and *de novo* ECM synthesis. Eventually, these materials will be implanted into load-bearing defects. Working with Lou Soslowsky at UPenn, we will implant miniaturized versions of our multi-compartment scaffolds into rat rotator cuff defects to assess performance.

7.2.4 Final thoughts

The suite of technologies presented here represents a path towards designing instructive biomaterials to repair orthopedic interfaces and regulate stem cell fate. The material systems applied in this thesis must be vetted through rigorous animal models to ascertain their utility for pre-clinical and clinical applications. In parallel, by quantitatively tuning the biophysical and biochemical properties of CG scaffolds we can start to ask fundamental questions about how the extracellular environment regulates key biological events including cell attachment, proliferation, motility, differentiation, and signal transduction. Such studies will undoubtedly help address fundamental human health challenges including the repair of orthopedic tissues and the design of platforms to more thoroughly understand physiological and pathological tissue states.

APPENDIX A: MACROPOROUS COLLAGEN SCAFFOLD GRADIENT ARRAYS FOR PARALLEL IDENTIFICATION OF BIOPHYSICAL AND BIOCHEMICAL REGULATORS OF CELL ACTIVITY[7]

A.1 Introduction

The native cellular microenvironment is highly complex and dynamic, consisting of soluble (growth factors, cytokines) and insoluble (extracellular matrix (ECM) protein, mechanical) regulatory cues. While it is impossible to completely replicate the complexity of human tissues in engineered biomaterials, there is a specific need for combinatorial systems where biophysical and biochemical regulators of cell behavior can be rapidly screened in order to determine the minimum constellation of cues necessary for inclusion in new biomaterial designs. Advances in systems biology have enabled multi-scale analysis of interconnected signaling networks involved with intrinsic regulation of cell behavior; however similar advances in biomaterials technology have been slower to occur.

The advent of robotic and microfluidic technologies has begun to enable the fabrication of material arrays to probe ECM and biomolecular regulators of embryonic stem cell (ESC) (Anderson, Levenberg et al. 2004; Flaim, Teng et al. 2008; Qi, Du et al. 2010; Cosson, Allazetta et al. 2013) and adult stem cell (Nakajima, Ishimuro et al. 2007; Gobaa, Hoehnel et al. 2011; Woodruff, Fidalgo et al. 2013) differentiation. While these studies provided important insight, they were all performed in 2D hydrogel systems. Recently, some progress has been made in developing combinatorial arrays of 3D scaffolds that can more accurately mimic the architecture of native tissues. A method to fabricate combinatorial arrays of 3D macroporous salt-leached synthetic polymer scaffolds in a 96-well plate using a dual syringe pump system was recently

[7] This chapter has been adapted from the following publication:
Caliari S.R., E.A. Gonnerman, et al. (in preparation). " Macroporous collagen scaffold gradient arrays for parallel identification of biophysical and biochemical regulators of cell activity."

developed to probe the effects of polymer composition on MC3T3 pre-osteoblast adhesion and proliferation (Yang, Bolikal et al. 2008). A similar approach using a gradient maker enabled the creation of a library of 3D PEG-based scaffolds with variable moduli to demonstrate that encapsulated MC3T3 cells underwent osteogenic maturation in gels that were stiffer than 225 kPa (Chatterjee, Lin-Gibson et al. 2010). Despite these advances, no method for producing arrays of 3D, naturally-derived polymeric scaffolds has been developed.

Collagen-glycosaminoglycan scaffolds are naturally-derived polymeric biomaterials that have been used as regenerative templates for the skin, peripheral nerve, conjunctiva and cartilage (Yannas, Lee et al. 1989; Yannas 2001; Harley, Spilker et al. 2004), as well as analogs of the native ECM to assess cell-matrix interactions *in vitr*o (Harley, Freyman et al. 2007; Harley, Kim et al. 2008; Caliari and Harley 2011). These scaffolds are highly porous (> 99%) and bioactive materials possessing natural adhesion sites. In addition, CG scaffolds possess tunable structural and mechanical properties. It has been shown that altering thermal processing during lyophilization can control resultant scaffold pore size (O'Brien, Harley et al. 2004) and anisotropy (Caliari and Harley 2011). In addition to control of the scaffold pore architecture, our group has previously demonstrated methods to immobilize biomolecules on CG scaffolds in a ubiquitous (Caliari and Harley 2013) or spatially-restricted (Martin, Caliari et al. 2011) manner to elicit specific cellular responses. Here we present a novel, systematic, materials-based screening tool, containing both biomolecule and structural cues, for exploring the combined effects of biophysical cues on cell behavior.

A.2 Materials and methods

*All materials purchased from Sigma-Aldrich (St Louis, MO) unless otherwise specified

A.2.1 CG array and sheet scaffold fabrication

CG scaffolds were freeze-dried from a suspension of type I collagen from bovine tendon and chondroitin sulfate from shark cartilage in 0.05 M acetic acid as described extensively (Yannas, Lee et al. 1989; O'Brien, Harley et al. 2004). Scaffold arrays with two distinct microstructural regions were fabricated by controlling local heat transfer during the freeze-dry process. A specialized mold was created for this purpose, consisting of a polysulfone chip (2 mm thick) with circular holes (6.5 mm diameter) drilled all the way through it, mounted on a removable base. The geometry and spacing of the nodes was designed to be identical to the dimensions of a 96-well plate. The removable base contained an aluminum section and a polysulfone section ($k_{aluminum}/k_{polysulfone} \approx 850$); this disparity in thermal conductivity was intended to control local heat transfer, and subsequently ice crystal growth kinetics, during freezing. Some experiments also used an array with 12 nodes on a uniformly aluminum base. This array had the same geometry as the first array, making it amenable to analysis on microplate readers as well.

For the scaffold array, degassed suspension was pipetted directly into the cylindrical nodes of the array. For sheet scaffold controls, degassed suspension was pipetted into a 5”x 5” aluminum tray (O'Brien, Harley et al. 2004; Martin, Caliari et al. 2011). Thermocouples were inserted into representative nodes to obtain freezing profiles for comparison with microstructural analysis. In both cases, the suspension was cooled at a rate of 1ºC/min until reaching a final freezing temperature of -10°C or -40°C to make isotropic scaffolds. The suspension was held at the final

freezing temperature for 1-2 h, resulting in an interpenetrating network of ice crystals surrounded by CG co-precipitate. Scaffolds with aligned pores were fabricated by placing the suspension-loaded array on a pre-cooled (-10°C) freeze-dryer shelf and holding at that temperature for 2 h as previously described (Caliari and Harley 2011). Following solidification, the ice crystals were sublimated under vacuum (0°C, 200 mTorr), leaving behind scaffolds with an interconnected, macroporous microstructure. The base was removed from the scaffold array, and the sheet scaffold was removed from the aluminum mold prior to crosslinking and hydration. Scaffolds were dehydrothermally crosslinked under vacuum (< 25 Torr) at 105ºC for 24 h (Harley, Spilker et al. 2004). Individual scaffolds samples from the sheet scaffold were cut into cylindrical plugs (diameter: 6 mm, height: ~ 2 mm) using a biopsy punch. Scaffold plugs and the scaffold array were then immersed in 100% ethanol for 1 h, rinsed multiple times in phosphate-buffered saline without calcium and magnesium (PBS), and subsequently stored in PBS at 4ºC until use.

A.2.2 Gradient scaffold fabrication

Scaffolds with linear biomolecular gradients were created using a standard gradient maker setup (CBS Scientific, San Diego, CA). Degassed CG suspension was carefully mixed with biomolecules and loaded into gradient maker. Mixed suspension was metered to array using a mini-peristaltic pump (CBS Scientific). Approximately 100 µL of suspension was loaded per node. Gradient scaffolds were then fabricated via freeze-drying as already described.

A.2.3 Scaffold pore size analysis

Scaffolds were removed from the array, hydrated in ethanol, and embedded in glycolmethacrylate. Samples were serially sectioned in the transverse plane (5 µm thick), and

stained with aniline blue in order to visualize the CG struts. Images were captured at 10x magnification using a contrast-phase microscope (Leica Microsystems, Germany) and analyzed using a linear intercept macro in Scion Image. The macro calculated a best-fit ellipse representation of the average pore for each section (O'Brien, Harley et al. 2004).

A.2.4 CG scaffold chemical crosslinking

Scaffolds were crosslinked using carbodiimide chemistry in a solution containing 1-ethyl-3-[3-dimethylaminopropyl] carbodiimide hydrochloride (EDC) and N-hydroxysulfosuccinimide (NHS) at a molar ratio of 5:20.6:1 EDC:NHS:COOH (where COOH represents collagen carboxyl content) and incubated under moderate shaking at room temperature for 1.5 h (Olde Damink, Dijkstra et al. 1996; Harley, Leung et al. 2007; Caliari and Harley 2013). Scaffolds were then rinsed 2x in PBS for 1 h and stored in PBS at 4°C until use.

A.2.5 Protein immobilization within CG scaffolds

Protein immobilization within CG scaffolds was performed in conjunction with the carbodiimide crosslinking process. Proteins were added 30 min into the 1.5 h crosslinking time. For creation of protein gradients within the CG array, 5 μL of biotinylated concanavalin A (Invitrogen, Carlsbad, CA) solution (0, 1.25, 2.5, 3.75, 5 μg/mL) was pipetted directly onto the hydrated scaffolds of a second-generation array chip (MACOR chip, 384-well plate node geometry/spacing) and incubated at room temperature for 30 min. The array was then rinsed 2x in PBS for 1 h, blocked with 1% BSA, then stained overnight at 4ºC with Alexa Fluor® 488 streptavidin (Invitrogen), rinsed 2x in PBS, then imaged using a Typhoon imager (GE

Lifesciences, Pittsburgh, PA). Mean fluorescent intensity was quantified using the histogram feature in ImageJ.

Bulk immobilization of growth factors within array scaffolds was achieved in a similar manner. Human recombinant growth/differentiation factors 5 and 7 (GDF-5/7, ProSpec, Israel) were diluted to a concentration of 400 ng (each) per 10 µL in PBS. 10 µL of protein solution was then added directly onto each scaffold node. Scaffolds were incubated for 1 h at room temperature, rinsed 2x in PBS for 1 h, and then stored in PBS at 4°C until use. Previous work has established the loading efficiency of this method as ~ 50% (Caliari and Harley 2013).

A.2.6 SEM analysis

The microstructure of the CG scaffold array nodes was analyzed using a JEOL JSM-6060LV Low Vacuum Scanning Electron Microscope (JEOL USA, Peabody, MA). By using a combination of secondary and backscatter electron detection under low vacuum, non-conductive CG scaffolds could be visualized without sputter coating (Harley, Lynn et al. 2010).

A.2.7 Tenocyte and MSC culture

Equine tenocytes derived from the superficial digital flexor tendons of horses were isolated using a previously validated method approved by the University of Illinois IACUC (Kapoor, Caporali et al. 2010). Tenocytes were cultured on T75 flasks in high glucose Dulbecco's modified Eagle's medium (DMEM) supplemented with 10% fetal bovine serum (FBS, Invitrogen) and antibiotics (Invitrogen) as previously described (Kapoor, Caporali et al. 2010). Tenocytes were used at passage 4. Human bone marrow-derived mesenchymal stem cells (MSCs) were purchased from

Lonza (Walkersville, Maryland) and cultured in low glucose DMEM with 10% MSC-validated FBS (Invitrogen) and antibiotics (Invitrogen). MSCs were used at passage 6. Both cell types were fed twice a week and cultured at 37°C at 5% CO_2 in normoxic conditions. For some 2D screening studies, tenocytes and MSCs were indirectly co-cultured using a Transwell membrane setup (Fisher Scientific, Pittsburgh, PA).

A.2.8 2D cell culture screening studies

As a precursor to 3D array experiments, the combinatorial effects of various soluble factors on driving tenogenic MSC differentiation was assessed in a 2D 96-well format. 1 x 10^3 MSCs were seeded into each well and cultured for 14 days in the presence of various growth factors and soluble differentiation agents. Each growth factor group was cultured with and without dexamethasone (0.1 μM) and ascorbic acid (50 μM). Growth factors were purchased from ProSpec (Israel) and used at a concentration of either 50 ng/mL (TGF-β1, 3) or 500 ng/mL (GDF-5, 6, 7, BMP-2). Following 14 days of culture, MSC were fixed in formalin, permeabilized in 0.1% Triton X-100 in PBS, blocked in 3% BSA, and incubated with primary antibodies against scleraxis and thrombospondin 4 (1:100 dilution) overnight at 4°C. Following incubation, wells were rinsed and incubated with secondary antibodies conjugated to AlexaFluor® 568 (scleraxis) and AlexaFluor® 488 (thrombospondin 4) respectively at room temperature for 2 h. Finally, wells were rinsed and nuclei were stained with Hoechst 33642. 100 μL of PBS were added to each well, and fluorescent signal was obtained for each of the three fluorophores on a plate reader (Tecan, Switzerland).

A.2.9 Cell culture within CG array

The hydrated scaffold array containing scaffolds with average pore sizes of 88 μm and 157 μm was immersed in complete culture medium (> 1 h), blotted on sterile Kimwipes to remove excess liquid, and placed in a 100 mm diameter culture dish. Cells (tenocytes or MSCs) were re-suspended at a concentration of 1 x 10^5 cells/10 μL media and seeded onto scaffold nodes using a previously validated static seeding method (O'Brien, Harley et al. 2005). 10 μL of cell suspension was pipetted onto the center of the pan side of each scaffold, for a total concentration of 1 x 10^5 cells/scaffold. Cells were allowed to attach for 2.5 h, after which time medium was added to culture dish to completely submerge the array. Experiments involving growth factors were conducted in low serum conditions (2% FBS). Scaffolds were cultured at 37ºC and 5% CO_2, and culture medium was twice a week.

A.2.10 Plate reader fluorescent quantification of cell number

In order to demonstrate the scaffold array's compatibility with existing high-throughput technologies, we devised an experiment to quantify cell number using a plate reader (Tecan, Switzerland). Confluent tenocytes and MSCs were stained with CellTracker™ Green CMFDA (Invitrogen) while in culture, washed in PBS, trypsinized, centrifuged at 500 *g*, and resuspended in complete media at concentrations of 2 x 10^4, 5 x 10^4, and 1 x 10^5 cells/10 μL. 10 μL of cell solution was pipetted directly onto scaffolds within the array, scaffold plugs placed within a 96-well plate, or directly onto a 96-well plate containing 100 μL of PBS to prevent dehydration. Cells were allowed to attach for 2 h prior to analysis. The array was placed on an inverted 96-well plate lid for reading on the plate reader. The average fluorescence for each sample was determined by taking 16 measurements at different locations in each well, to account for heterogeneities in the scaffold groups.

A.2.11 Determination of cell metabolic activity

The metabolic activity of the cells within each scaffold was determined using an alamarBlue® assay (Tierney, Jaasma et al. 2009). AlamarBlue® is a colorimetric non-destructive method of assessing cellular metabolism. Scaffolds were removed from the array with sterile forceps and placed in complete medium containing 10% alamarBlue® (Invitrogen), then incubated under moderate shaking at 37ºC for 3 h. Changes in fluorescent intensity were measured using a fluorometer (Tecan, Switzerland).

A.2.12 RNA isolation

Individual scaffold nodes were cut and separately rinsed in PBS to remove unattached cells followed by immersion in lysis buffer (Qiagen, Valencia, CA) supplemented with 10 μM β-mercaptoethanol for 5 min on ice. Lysates were then processed using the RNeasy Plant Mini kit (Qiagen) (Duffy, McFadden et al. 2011) with RNA quantified via spectrophotometry.

A.2.13 Reverse transcription and real-time PCR

120 ng of RNA was reverse transcribed to cDNA using hexameric primers with the QuantiTect Reverse Transcription kit (Qiagen) in a Bio-Rad S1000 thermal cycler. Real-time PCR reactions were performed in triplicate on an Applied Biosystems 7900HT Fast Real-Time PCR Systems (Carlsbad, CA) using SYBR Green chemistry (Qiagen). Primer sequences were derived from the literature (Frank, Heim et al. 2002; Caceres, Suwyn et al. 2007; Pauly, Klatte et al. 2010; Zhou, Xu et al. 2011) and synthesized by Integrated DNA Technologies (Coralville, IA) with the exception of the scleraxis (SCXB) primer set, which was purchased from Qiagen. Ct data was

analyzed using Sequence Detection Systems software v2.4 (Applied Biosystems, Carlsbad, CA) with transcript fold changes normalized to the expression levels of MSCs cultured in the isotropic, small pore, no growth factor group.

A.2.14 Statistical analysis

One-way analysis of variance (ANOVA) followed by Tukey's HSD post-hoc test was performed on pore size, cell metabolic activity, and gene expression data sets. Statistical significance was set at $p < 0.05$. At minimum of $n = 5$ independent scaffolds per group were used for pore size analysis, and $n = 3$ samples were examined metabolic activity and gene expression analyses. For plate reader quantification of cell number corresponding to CellTracker™ Green CMFDA intensity, at least $n = 3$ samples were analyzed per cell seeding density. Error is reported in figures as the standard error of the mean unless otherwise noted.

A.3 Results and Discussion

A.3.1 Scaffold microstructural analysis

The pore sizes and corresponding aspect ratios for the four freezing parameters examined are reported in **Table A.1**. The aspect ratio for the best fit ellipse was near 1 for all four groups examined, indicating that scaffolds produced in this array mold have an isotropic microstructure. The differences in base thermal conductivity appear to have a greater impact on scaffold pore size than final freezing temperature, but both parameters contribute to significant differences in mean pore size. Significant differences in mean pore size were observed for scaffolds within the aluminum section of the array undergoing different freezing treatments ($p < 0.05$). The mean

pore sizes were 77 ± 16 μm and 88 ± 28 μm, for freezing temperatures of -10ºC and -40ºC, respectively. The mean pore size for scaffolds within the polysulfone section of the array were 126 ± 32 μm and 157 ± 47 μm, for freezing temperatures of -10ºC and -40ºC, respectively. This difference in pore size due to final freezing temperature was also statistically significant ($p < 0.001$). For a single final freezing temperature treatment, the difference in base thermal conductivity significantly impacted pore size ($p < 0.0001$); this was true for both freezing temperatures examined (-10ºC and -40ºC).

These differences can be qualitatively observed by examining the suspension freezing profiles. Directly following ice crystal nucleation, the temperature of the collagen suspension increases during an ice crystal growth phase; the suspension is then sub-cooled to the final freezing temperature. The length of the ice crystal growth phase can be correlated to the average pore size of the scaffold; the longer the growth phase, the larger the average pore size. The solidification profiles shown in **Figure A.2** support the stereological pore analysis results. SEM analysis offers another method to qualitatively assess pore microstructure. SEM micrographs (**Figure A.3**) show a stark influence of both base thermal conductivity and freezing conditions (constant cooling = isotropic, flash cooling = anisotropic) on pore size and shape respectively. SEM of the isotropic scaffolds supports the observations via stereology that the pores are relatively round. Additionally, while anisotropic CG scaffolds have previously been fabricated in thermally-mismatched molds (Caliari and Harley 2011), we were able to replicate this effect in the scaffold arrays by simply placing the array mold on a pre-cooled substrate (e.g. freeze-dryer shelf) prior to lyophilization.

A.3.2 Patterning of biomolecular gradients within CG array

Following the creation of CG arrays with step gradients in pore microstructure, we wanted to assess the ability to create orthogonal gradients of biomolecules within the array set-up. Using carbodiimide-mediated crosslinking chemistry, biotinylated concanavalin A was successfully immobilized in a step-wise gradient fashion onto the scaffolds within the array (**Figure A.4(a-b)**). The resulting protein gradient was near-linear ($R^2 = 0.91$, **Figure A.4(c)**).

A.3.3 Scaffold array integration with well-plate reader technology

We next sought to confirm that the scaffold array could be integrated with standard microplate readers. We specifically designed the array mold dimensions so that readouts of cell behavior could be tracked via fluorescence over time. As a proof of concept, we tracked cell number using CellTracker Green® in three different groups: *i*) cells only, *ii*) cells seeded on scaffold plugs placed in a standard 96-well plate, and *iii*) cells seeded on scaffold array nodes. Increased CellTracker Green® intensity corresponds to a higher number of cells. As expected, the average intensity for the array scaffolds, scaffold plugs, and cell-only controls increased with increased cell seeding density for both tenocytes (**Figure A.5(a)**) and MSCs (**Figure A.5(b)**) in a linear manner (**Figure A.5(c)**). While the fluorescent signal was lower across the board for the tenocyte groups compared to the MSCs, this is likely due to less dye uptake on a per cell basis because the tenocyte flasks contained more cells than the corresponding MSC flasks. However, the calibration curves for both cell types show good linearity with R^2 values greater than 0.93.

A.3.4 Integrating gradient maker technology with scaffold arrays

After confirming that scaffolds could be analyzed using plate reader technology, we used a commercially-available gradient maker to fabricate CG scaffolds with linear biomolecular gradients within our array setup (**Figure A.6**). Scaffolds were initially fabricated with a gradient of fluorescently-labeled biomolecule, BSA-Cy5, to validate our setup. Direct quantification of the fluorescent signal of the scaffold array nodes on a standard microplate reader showed incorporation of a linear gradient (R^2 = 0.97, **Figure A.6(b,c)**). Next, we wanted use a biomolecular gradient to elicit a specific biological response. This was accomplished by incorporating a gradient of a BMP-2 biomimetic modular peptide (Lee, Wagoner-Johnson et al. 2009). MSC-seeded scaffolds were cultured in osteogenic induction media for 7 days and then fixed, permeabilized, and incubated with an antibody against osteocalcin, a marker of osteogenesis. The osteocalcin antibody was then tagged with a fluorescently-labeled secondary antibody with osteocalcin-related fluorescent signal quantified directly within the scaffold nodes via a plate reader. Results demonstrated that increasing amounts of BMP-2 peptide incorporation resulted in trends towards increasing osteocalcin expression (**Figure A.6(d)**). This finding shows that biomolecules incorporated into scaffold arrays via gradient maker technology maintain activity and can elicit a specific biological response.

A.3.5 2D screening of factors to drive tenogenic differentiation

The development of the array system described in this chapter is motivated by the need for platforms that enable efficient combinatorial screening of biophysical and biochemical regulators of cell activity. One application of interest for our group is the decoding of environmental factors that regulate tenogenic MSC differentiation. While differentiation down many mesenchymal lineages, including osteogenesis, chondrogenesis, and adipogenesis, has been well characterized

(Pittenger, Mackay et al. 1999), the same cannot be said for driving tenogenic differentiation. We believe that this array offers a platform to test many combinations of factors in order to solve this and similar challenges.

Before using our 3D scaffold array, we performed a series of 2D experiments to select key soluble signals that might be important to mediating tenogenic differentiation. We looked at the growth factors bFGF, IGF-1, GDF-5, GDF-7, TGF-β1, and BMP-2, factors that our group (Caliari and Harley 2013) as well as many others (Abrahamsson, Lundborg et al. 1991; Aspenberg and Forslund 1999; Lou, Tu et al. 2001; Costa, Wu et al. 2006; Pryce, Watson et al. 2009; Date, Furumatsu et al. 2010; Park, Hogan et al. 2010; Maeda, Sakabe et al. 2011) have shown to be beneficial for mediating a tenogenic phenotype. We also supplemented the growth factors with dexamethasone and ascorbic acid, two factors that are commonly used to help induce MSC differentiation down various lineages (Pittenger, Mackay et al. 1999). We cultured MSCs in 96-well plates for 14 days and used antibody-fluorophore conjugates to assess onset of a tenogenic phenotype. Representative calibration curves probing for cell number (Hoechst, **Figure A.7(a)**) and scleraxis expression (SCXB, **Figure A.7(b)**) validated the use of this 96-well platform with linear ($R^2 > 0.9$) increases in fluorescence corresponding to increasing cell number. Using this platform, we showed that all growth factors tested led to increased scleraxis expression compared to naïve MSCs (**Figure A.7(c)**). Scleraxis is a transcription factor that is a hallmark of developing and mature tendon (Schweitzer, Chyung et al. 2001). Moreover, the inclusion of differentiation agents dexamethasone and ascorbic acid appears to enhance the expression of scleraxis, in particular for the IGF-1 and GDF-7 groups.

We also examined gene expression profiles of tenocytes, MSCs indirectly co-cultured with tenocytes, and MSCs supplemented with one of several growth factors in the TGF-β superfamily. We quantified the expression of tenogenic genes encoding for type I collagen (the main protein constituent of tendon, **Figure A.8(a)**) and scleraxis (**Figure A.8(c)**) as well as COMP and tenascin-C (two proteins important in osteotendinous junctions and collagen fibrillogenesis, **Figure A.8(b,d)**). Not surprisingly, tenocytes expressed significantly higher levels of all four markers compared to naïve MSCs ($p < 0.03$). Interestingly, despite literature indicating that indirect co-culture with tenocytes promotes tenogenic differentiation of MSCs (Luo, Song et al. 2009) and amniotic epithelial cells (Barboni, Curini et al. 2012), we observed no beneficial effect of indirect co-culture on tenogenic MSC phenotype in our system. While TGF-β1 and BMP-2 also promoted type I collagen up-regulation ($p < 0.02$), the expression levels of other tenogenic markers by these groups did not come close to the levels found in native tenocytes, highlighting the limitations of using solely biochemical stimulation to drive tenogenic differentiation.

A.3.6 3D combinatorial screening of biophysical and biochemical factors to drive tenogenesis

Following completion of the 2D studies, we examined the combined effects of pore size, anisotropy, and growth factor presentation on MSC phenotype. Two conditions for each parameter were tested: "small" and "large" pores were created using the aluminum and polysulfone bases respectively, aligned and isotropic pores were induced by changing the freezing conditions, and immobilized GDF-5 and GDF-7 was added post-fabrication via carbodiimide crosslinking. In total, 8 groups probing every combination of these factors were examined over a 7 day culture period.

MSC metabolic activity was measured at the conclusion of the experiment using alamarBlue® reduction (**Figure A.9**). The highest metabolic activities were found in two of the larger pore groups, isotropic (-) and anisotropic (+). This is not surprising since pore size has previously been shown to be an important regulator of metabolic activity in CG scaffolds (Caliari and Harley 2011). GDF-5/7 incorporation did not appear to significantly improve cell metabolic activity, also consistent with previous results (Caliari and Harley 2013).

Next, the expression of various genes was measured (**Figure A.10**). In general, pore anisotropy (*a* significance markers) and pore size (*b* markers) had a greater effect on phenotype than GDF-5/7 incorporation (*c* markers). It is important to note that unlike in the screening studies discussed earlier, the growth factors were covalently immobilized to the scaffold instead of freely soluble. Growth factor sequestration is an important feature of the native ECM and allows factors to remain bioactive and localized to specific tissue regions. While growth factors immobilized in CG scaffolds, including GDF-5, have previously demonstrated maintenance of some level of bioactivity (Caliari and Harley 2013), it is possible that phenotypic effects may be dulled compared to soluble supplementation, or that the day 7 time point observed here is too late to resolve effects. Future studies will examine temporal expression profiles in response to various microenvironmental stimuli.

COLI levels were significantly higher in the anisotropic small pore scaffolds compared to the isotropic small pore groups ($p < 0.002$). Both groups also showed significantly higher expression levels compared to the anisotropic large pore groups ($p < 0.03$). In contrast to the COLI expression profile, COMP and TNC were significantly up-regulated in the large pore isotropic

groups compared to their anisotropic counterparts ($p < 0.03$). One possible explanation for the trends in COMP and TNC expression is that these two proteins are typically localized to the fibrocartilagenous insertion region of the tendon-bone junction (Liu, Aschbacher-Smith et al. 2012), an area of the tissue that is more geometrically isotropic compared to tendon proper. SCXB expression was elevated in two large pore groups: isotropic (+) and anisotropic (-). It is unclear why GDF incorporation led to significant up-regulation in the isotropic large pore group but significant down-regulation in the anisotropic large pore group. We observed no significant differences in the expression of THSP4 ($p = 0.74$) or OC ($p = 0.95$). This makes sense in the case of OC since it was included as a control to ensure that we were not inducing MSC differentiation down non-tenogenic (*e.g.* osteogenic) lineages. Together, the data from this 3D array trial highlight the complex interplay between various regulators of MSC fate.

A.4 Conclusions

Strategies for combinatorial evaluation of biophysical and biochemical regulators of cell behavior are needed to inform the design of new biomaterials. This chapter outlines an approach to fabricate arrays of CG scaffolds with variable pore size, anisotropy, and presentation of biomolecular cues. Arrays were created with the geometry of a 96-well plate to enable integration with standard well-plate assay technologies. As a proof of concept we used this scaffold array to assess combinations of microenvironmental cues to drive tenogenic MSC differentiation. 2D cell culture experiments demonstrate that biochemical supplementation alone is insufficient to drive tenogenic differentiation. 3D scaffold array experiments showed complex

interplay between pore size, alignment, and GDF presentation on modulating MSC metabolic activity and tenogenic phenotype.

A.5 Tables

Removable Base	Final Freezing Temperature	Average Pore Size	Aspect Ratio
Aluminum	-10ºC	77 ± 16 µm	0.944 ± 0.049
Polysulfone	-10ºC	126 ± 32 µm*	0.917 ± 0.065
Aluminum	-40ºC	88 ± 28 µm	0.949 ± 0.056
Polysulfone	-40ºC	157 ± 47 µm*	0.887 ± 0.106

Table A.1. Pore size/aspect ratio analysis obtained by stereology for scaffolds fabricated within the CG array mold. Pore size is indicated as average pore diameter ± standard deviation. *: significantly larger than aluminum group at that freezing temperature. Table courtesy of Emily Gonnerman.

A.6 Figures

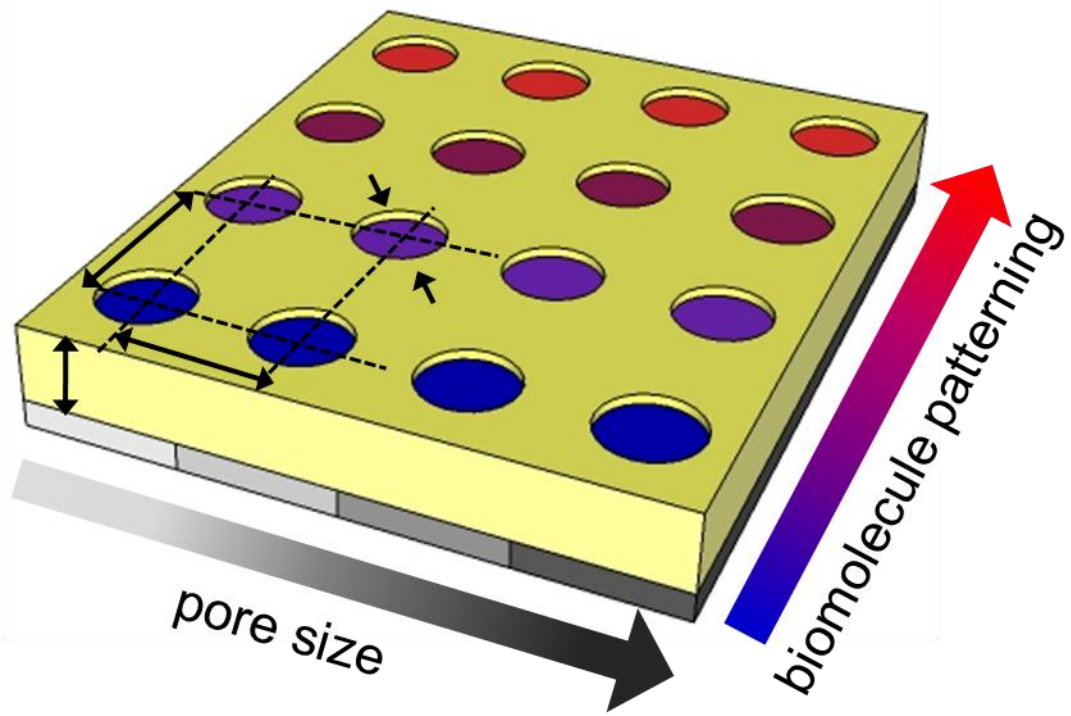

Figure A.1. Schematic of array mold concept with varied pore size in one direction due to changes in mold base conductivity during freezing. In the other direction, biomolecule immobilization is varied in a gradient fashion, as to create a homologous series of microenvironments. Image courtesy of Emily Gonnerman.

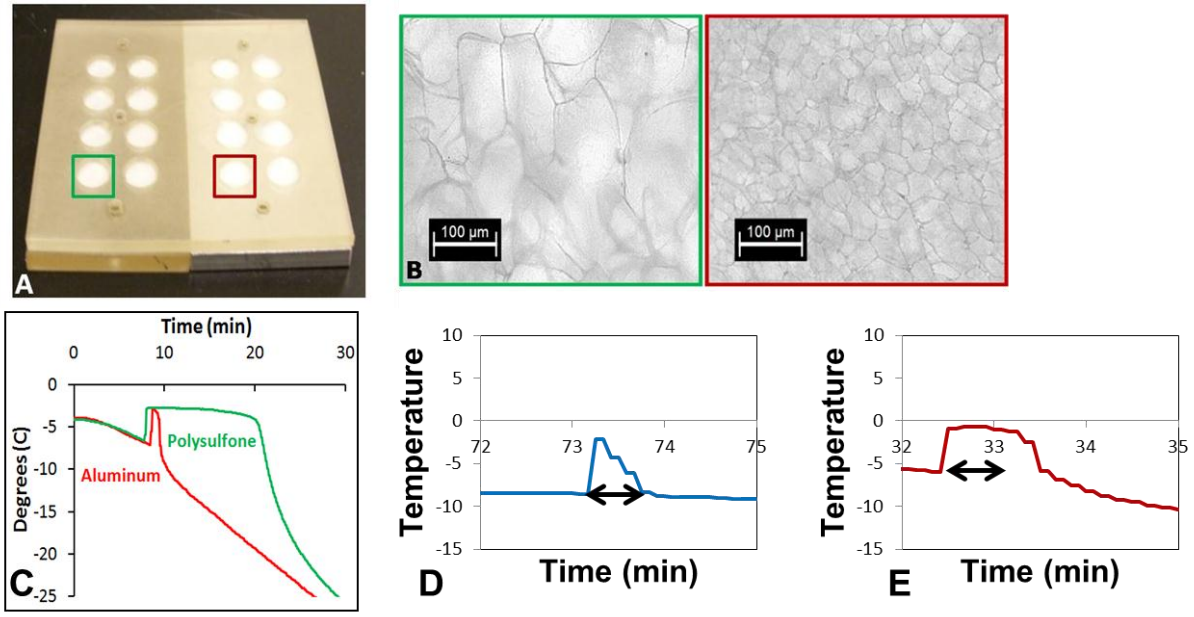

Figure A.2. Photograph of scaffold array mold with disparate base thermal conductivities ($k_{aluminum}/k_{polysulfone} \approx 850$) A) Freeze-dried suspensions of constant chemical composition but different local thermal conductivity yield scaffolds with differing average pore sizes (phase contrast microscopy images: polysulfone *green*, aluminum *red*). B) Representative light micrographs of CG scaffolds freeze-dried in molds with aluminum (*red*) and polysulfone (*green*) bases. C) The ice crystal growth phase period is markedly shorter for the scaffolds fabricated in the mold with a base with a higher heat transfer coefficient (aluminum). Representative solidification profiles for CG scaffolds in the aluminum section of the array mold for final freezing temperatures of D) -10ºC and E) -40ºC. The ice crystal growth phase is shorter for the -10ºC freezing treatment. *Scale bars*: 100 µm. Image courtesy of Emily Gonnerman.

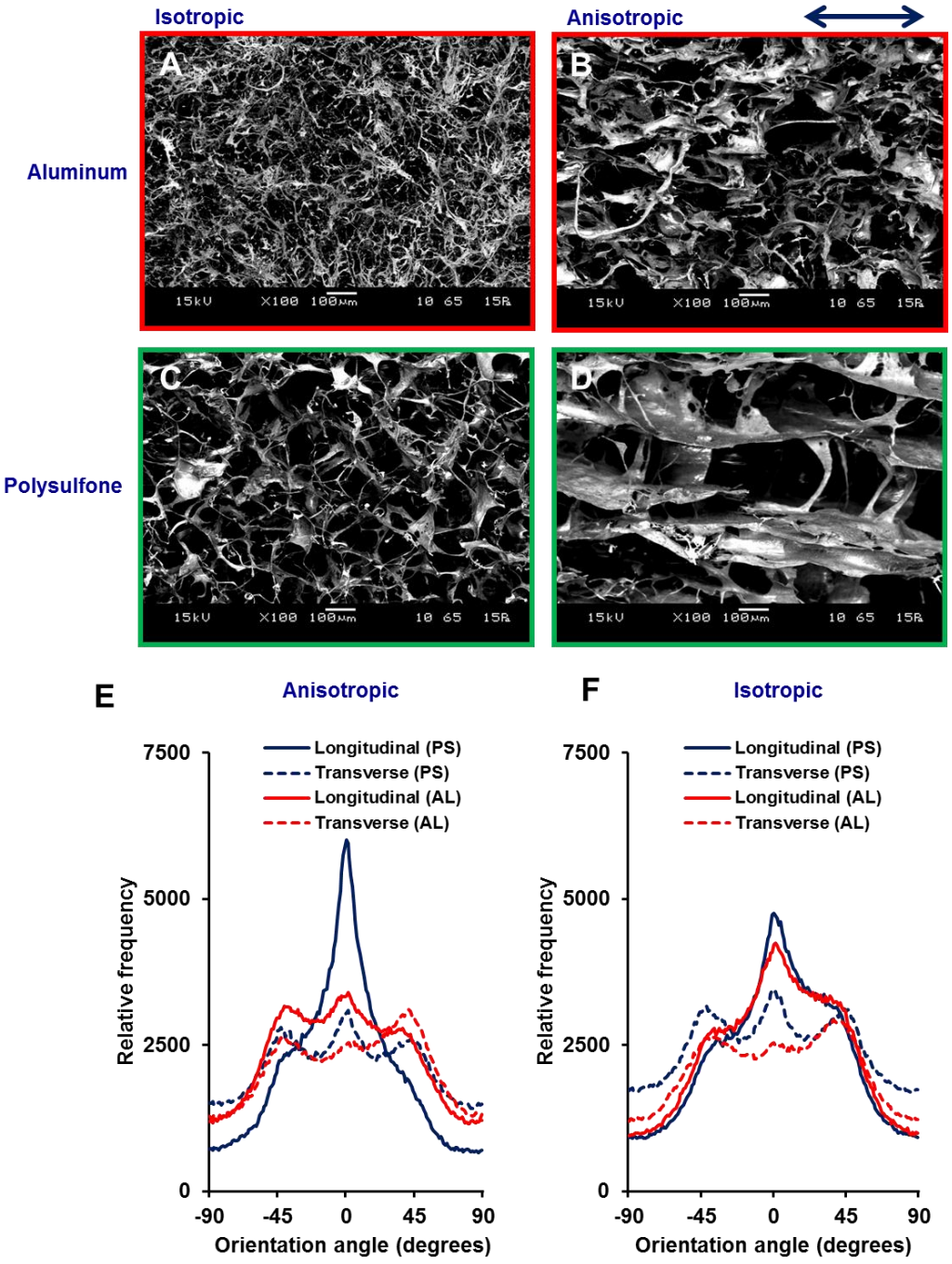

Figure A.3. SEM micrographs of array scaffold pore structure. Pores appear to be qualitatively smaller when frozen with the aluminum base (A, B) compared to the polysulfone base (C, D). Pores are also aligned when frozen on the pre-cooled freeze-dryer shelf compared to isotropic pores formed using the constant cooling technique as measured by OrientationJ analysis of SEM images (E,F). *Scale bars*: 100 µm.

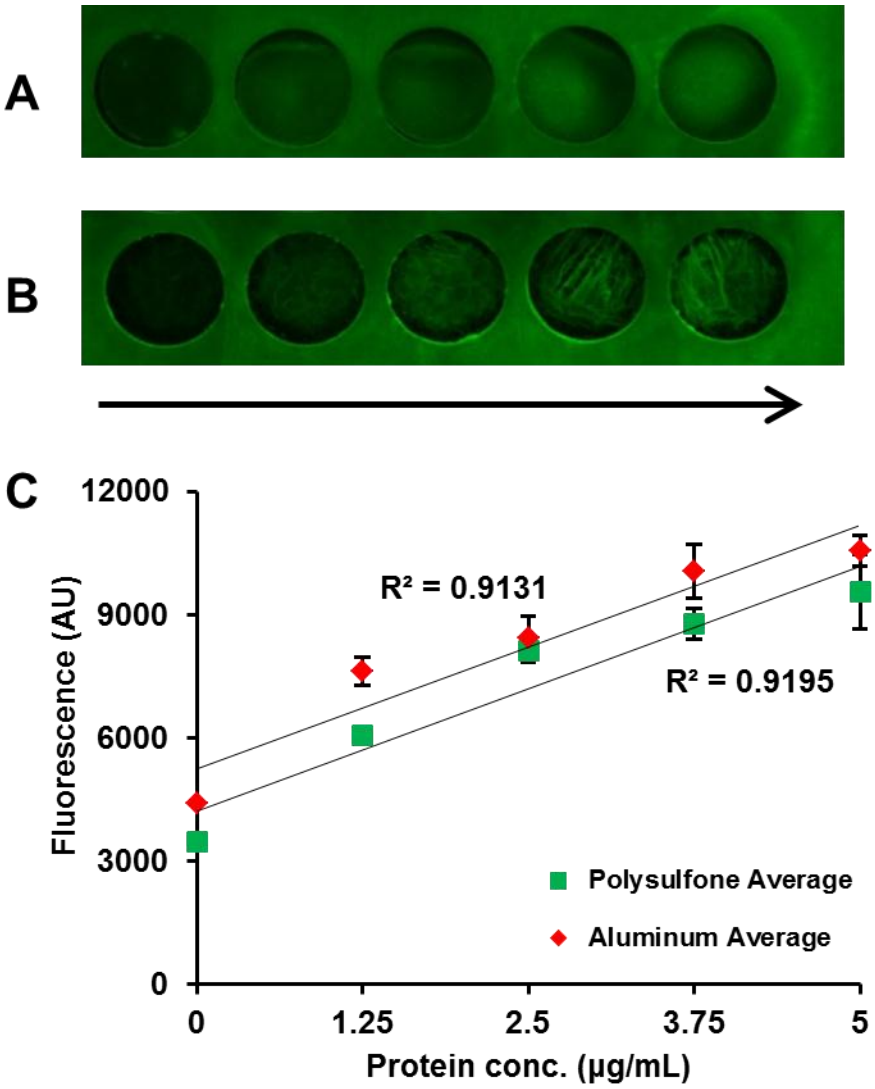

Figure A.4. Step-wise gradient of biotinylated concanavalin A covalently immobilized to scaffolds within the array chip. Image of representative rows from scaffolds with A) aluminum and B) polysulfone bases, with the arrow indicating increasing protein immobilization. C) Quantification of mean fluorescence for each step of the gradient. Red diamonds indicate average ± S.E.M. intensities for scaffolds fabricated with an aluminum base; green squares indicate average ± S.E.M. intensities for scaffolds fabricated with a polysulfone base. Image courtesy of Emily Gonnerman.

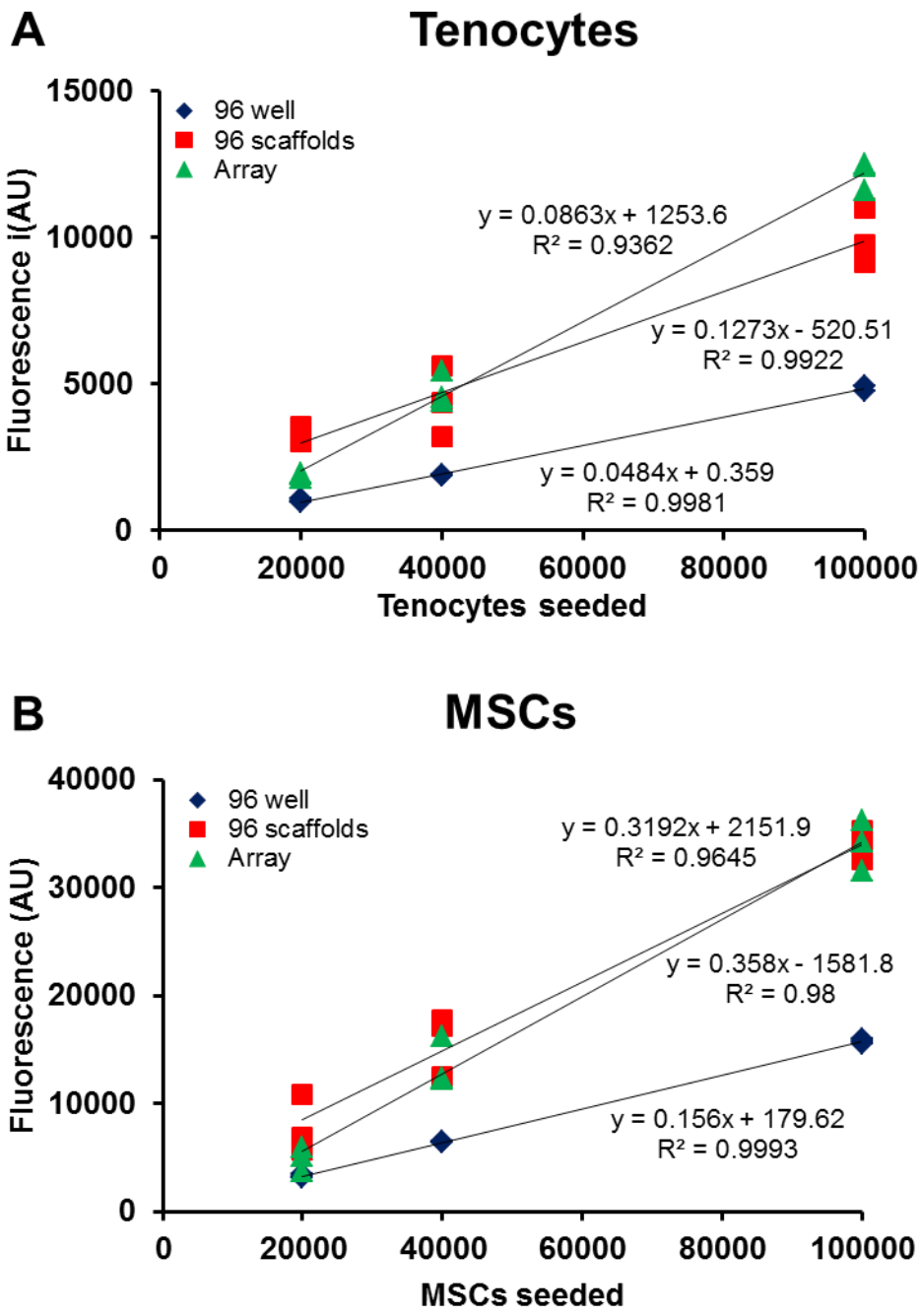

Figure A.5. Array cell number quantified directly on plate reader. Fluorescent intensity of A) tenocytes and B) MSCs stained with CellTracker Green CFMDA determined by plate reader analysis after 2 hours in culture: Cells cultured within a 96 well plate (blue diamonds); scaffolds cultured within 96 well plate (red squares); scaffolds cultured within CG array with 96-well plate geometry (green triangles).

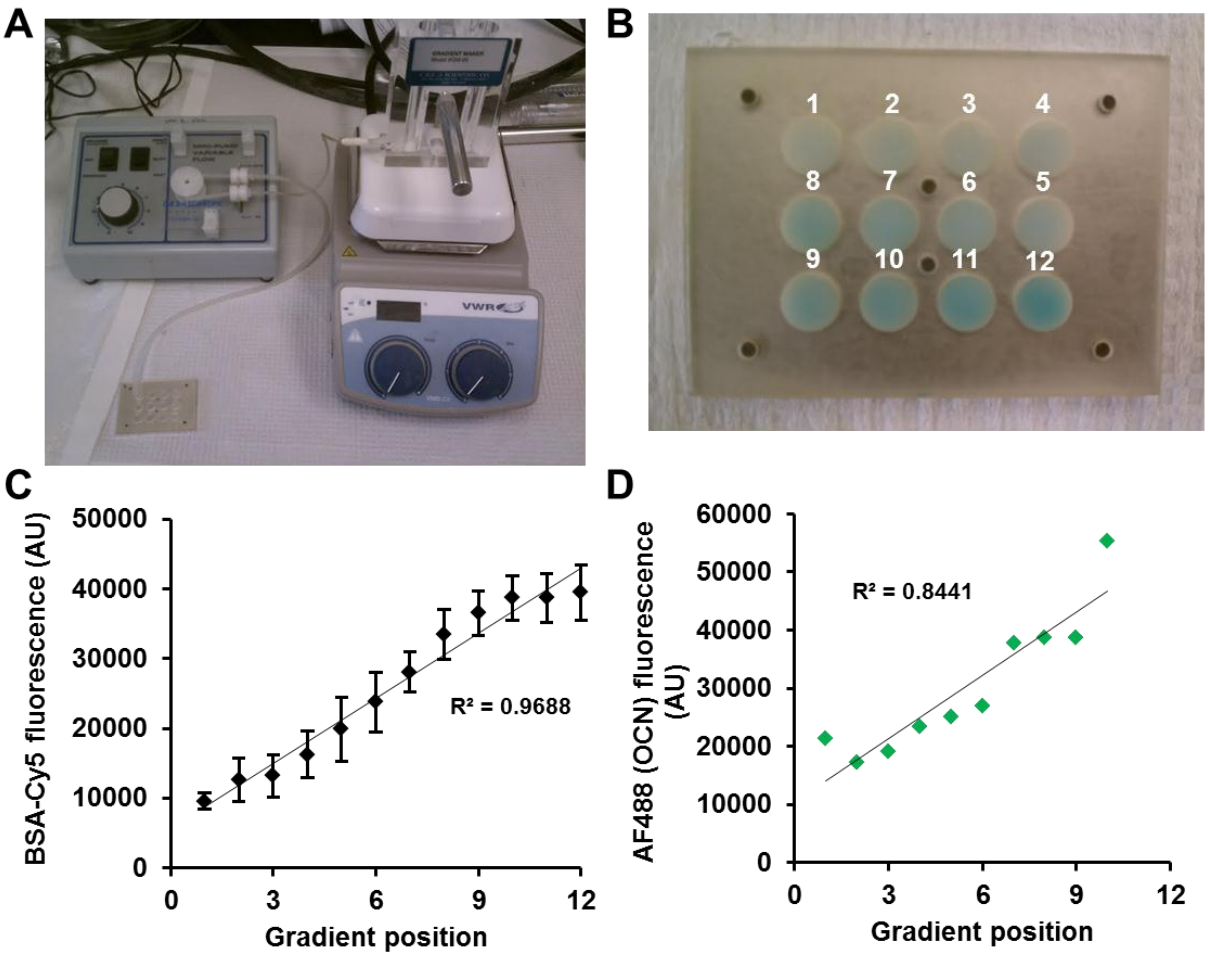

Figure A.6. Gradient maker integration with array setup to make linear biomolecular arrays. A) Gradient maker setup. Gradient maker is set on stir plate and connected to peristaltic pump to meter mixed CG suspension to array mold. B) Representative array of CG scaffold loaded with gradient of BSA-labeled Cy5. C) Direct plate reader quantification of Cy5 signal on scaffolds in arrays demonstrated the creation of a linear biomolecular gradient. D) A gradient of BMP peptide incorporated into CG scaffold array resulted in linear increase in osteocalcin expression.

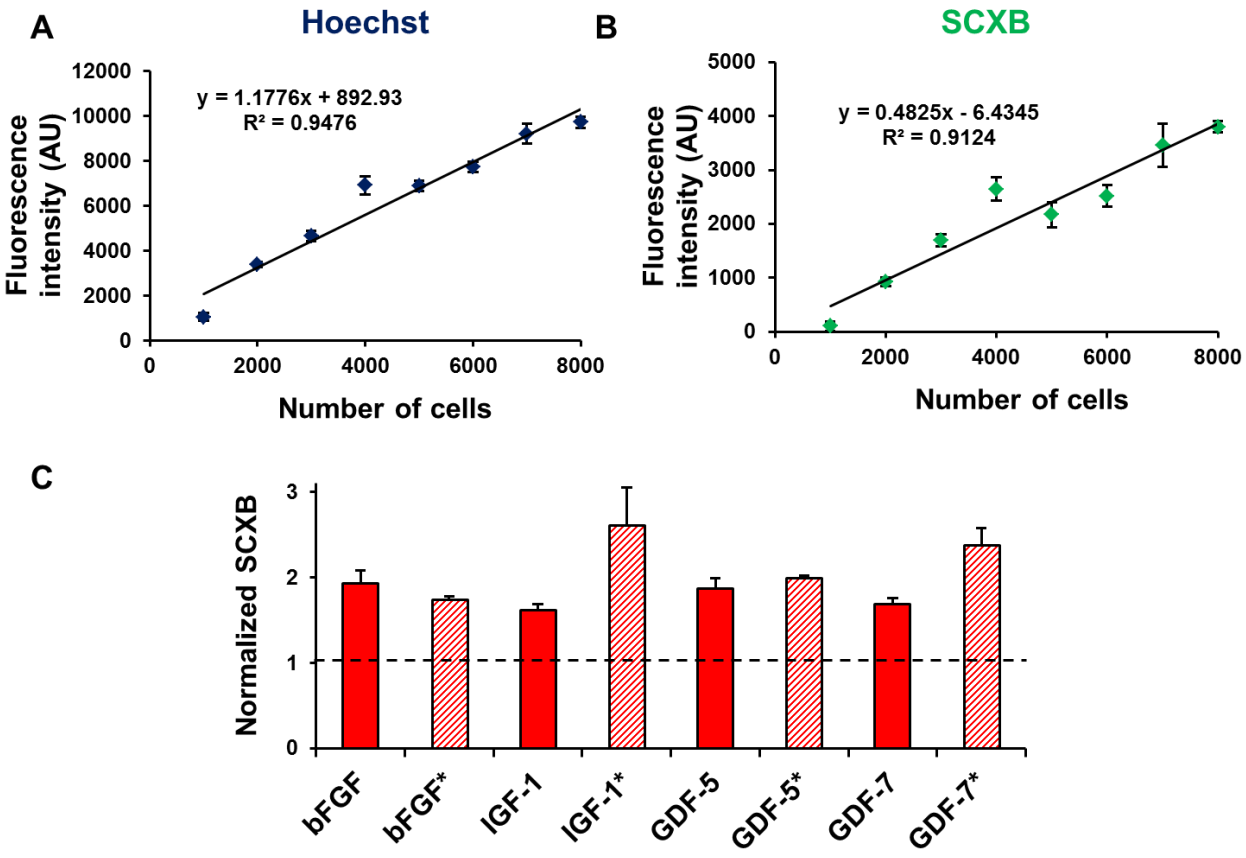

Figure A.7. 2D screening of soluble factors to drive tenogenic MSC differentiation *(n* = 3). Calibration curves validating the antibody-mediated fluorescent quantification of A) cell number via Hoechst nuclear staining and B) SCXB protein expression. C) Effect of soluble factor treatment on SCXB expression. *Dashed line*: expression level of naïve MSCs. * indicates growth factor supplemented groups that were additionally supplemented with differentiation agents dexamethasone (0.1 µM) and ascorbic acid (50 µM).

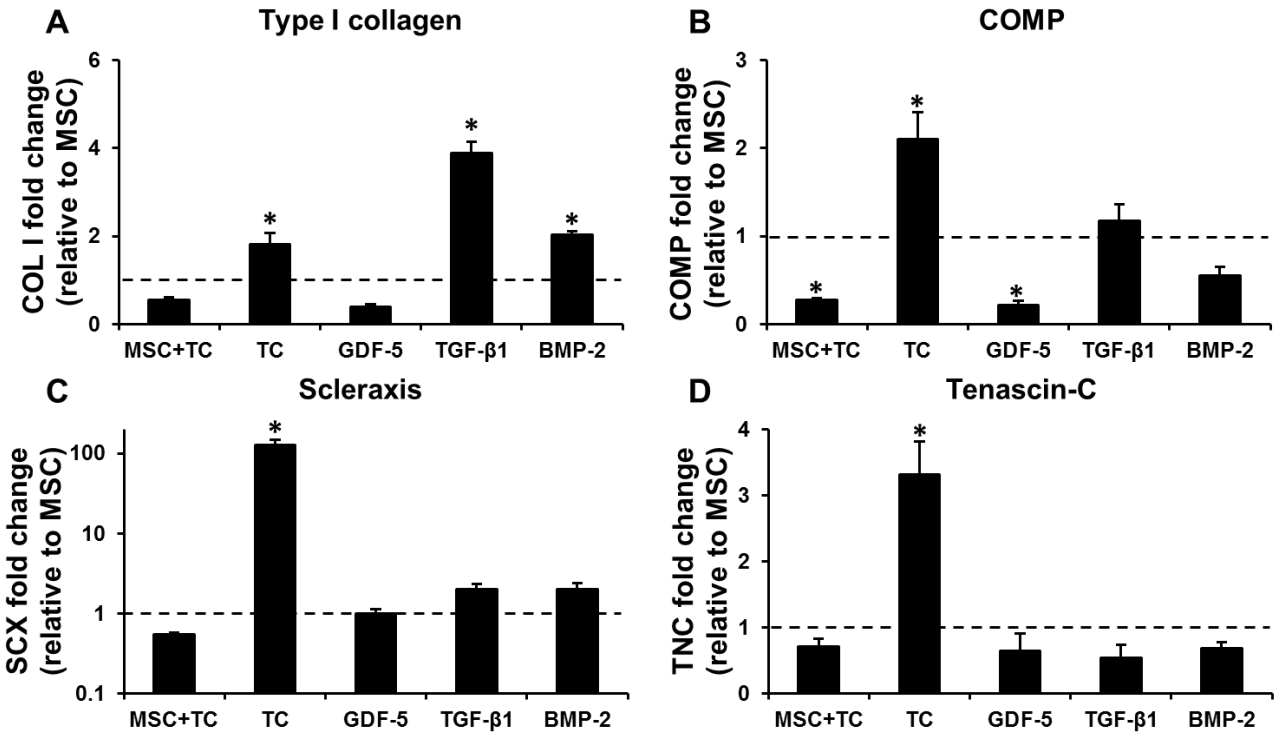

Figure A.8. Tenogenic gene expression of tenocytes and MSCs in 2D culture *(n* = 3). Experimental groups: MSC/tenocyte co-culture (MSC+TC), tenocytes (TC), MSCs+GDF-5 (GDF-5), MSCs+TGF-β1 (TGF-β1), and MSCs+BMP-2 (BMP-2). Expression levels were measured for tenogenic markers A) type I collagen, B) cartilage oligomeric matrix protein (COMP), C) scleraxis, and D) tenascin-C. *Dashed line*: expression level of naïve MSCs. * : significantly different from naïve MSCs.

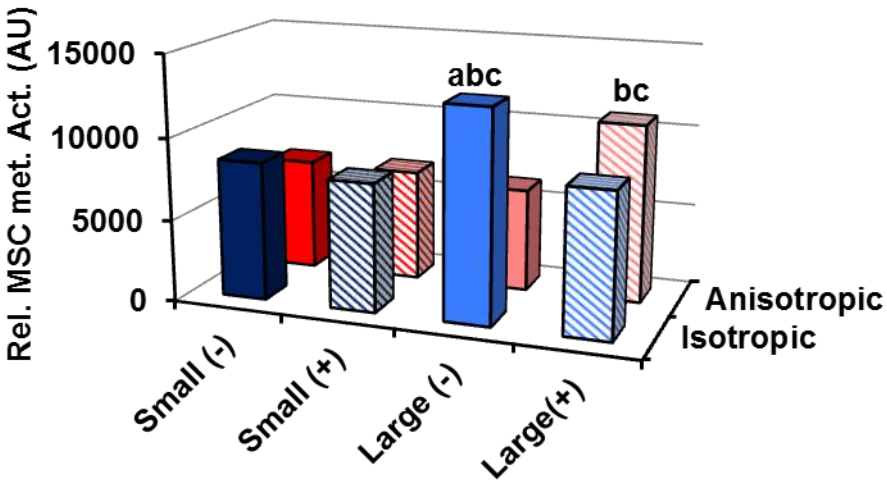

Figure A.9. MSC metabolic activity in CG scaffold arrays after 7 days *(n* = 3). Experimental groups: isotropic (small pores, with and without immobilized GDF-5/7; large pores, with and without immobilized GDF-5/7) and anisotropic (small pores, with and without immobilized GDF-5/7; large pores, with and without immobilized GDF-5/7). *a*: significantly higher than corresponding isotropic/anisotropic group, *b*: significantly higher than corresponding small/large pore group, *c*: significantly higher than corresponding no GDF-5/7 or GDF-5/7 group.

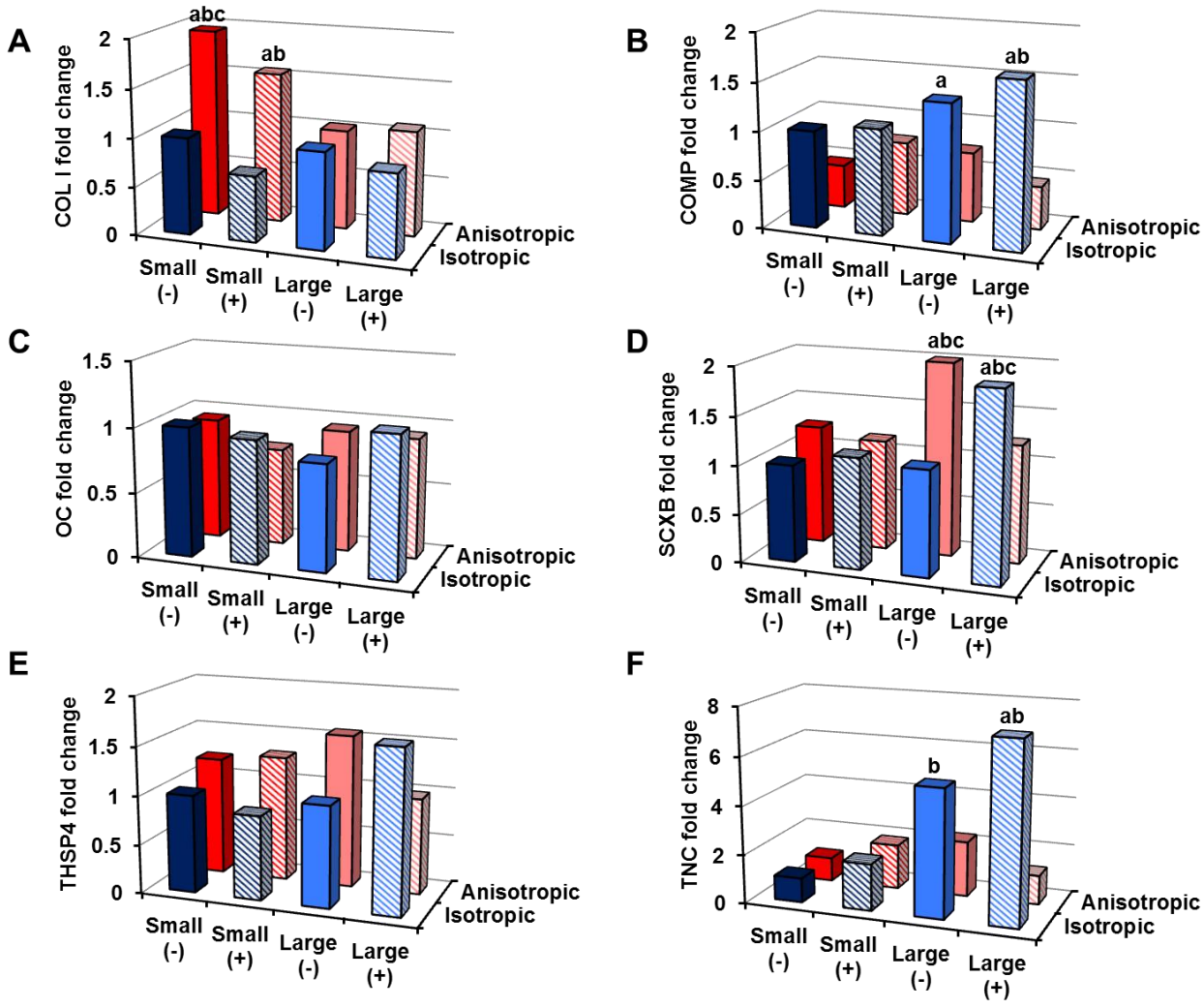

Figure A.10. MSC gene expression in CG scaffold arrays after 7 days *(n* = 3). Experimental groups: isotropic (small pores, with and without immobilized GDF-5/7; large pores, with and without immobilized GDF-5/7) and anisotropic (small pores, with and without immobilized GDF-5/7; large pores, with and without immobilized GDF-5/7). Expression levels were measured for markers A) type I collagen, B) cartilage oligomeric matrix protein (COMP), C) osteocalcin, D) scleraxis, E) thrombospondin 4, and F) tenascin-C. *a*: significantly higher than corresponding isotropic/anisotropic group, *b*: significantly higher than corresponding small/large pore group, *c*: significantly higher than corresponding no GDF-5/7 or GDF-5/7 group.

APPENDIX B: DESIGN AND CHARACTERIZATION OF PERFORATED COLLAGEN-GYCOSAMINOGLYCAN MEMBRANES FOR OPTIMIZING CELL INFILTRATION AND BIOACTIVITY[8]

B.1 Introduction

Membranes have been used in a variety of tissue engineering and surgical settings for decades. Periosteal grafts are commonly applied as membranes to help localize cells to the wound site during osteoarthritis repair procedures such as autologous chondrocyte implantation. Additionally, electrospun poly(caprolactone) (PCL) membranes have been applied as a substitute for periosteal grafts in osteochondral repair(Ho, Hutmacher et al. 2010). Silicone membranes are often implanted as artificial epidermal grafts during skin repair (Violas, Abid et al. 2005). In addition to synthetic materials, naturally-based membranes are also commonly used. Amniotic membranes can be used as wound dressings and even tissue engineering scaffolds (Chen, Chung et al. 2011) themselves. Collagen membranes have found utility in dental and synovial tissue engineering applications (Xu, Cao et al. 2010). Increasingly, collagen wraps have been used in orthopedic tissue engineering applications as surgical wraps to helps stabilize grafts and localize nutrients, cells, and other intrinsic factors to the wound site (Guda, Walker et al. 2012).

Recently, we described the development of collagen-glycosaminoglycan (CG) membranes for creating composites for tendon tissue engineering (Caliari, Ramirez et al. 2011). CG scaffolds are a class of naturally-derived biomaterials that have been applied to a variety of regenerative medicine challenges, including the repair of skin (Yannas, Lee et al. 1989) and peripheral nerves (Harley, Spilker et al. 2004). CG scaffolds possess many desirable characteristics for tissue engineering challenges, including biocompatibility, native ligands to support cell activity, high

[8] This chapter has been adapted from the following publication:
Caliari S.R., et al. (in preparation). "Design and characterization of perforated collagen-glycosaminoglycan membranes for optimizing cell infiltration and bioactivity."

specific surface area, and an open pore network for aiding cell infiltration as well as nutrient and waste transport (Harley and Gibson 2008). In addition to *in vivo* applications, CG scaffolds have found utility as *in vitro* analogs of the native extracellular matrix (ECM) to probe the role of microstructural, mechanical, and compositional cues on cellular behaviors including adhesion (O'Brien, Harley et al. 2005), motility (Harley, Kim et al. 2008), differentiation (Farrell, O'Brien et al. 2006), and phenotypic stability (Caliari, Weisgerber et al. 2012). Recently, CG scaffolds have been considered for a variety of orthopedic tissue engineering applications related to bone (Cunniffe, Dickson et al. 2010; Harley, Lynn et al. 2010; Curtin, Cunniffe et al. 2012), tendon (Caliari and Harley 2011; Caliari, Ramirez et al. 2011), and osteochondral (Harley, Lynn et al. 2010; Getgood, Kew et al. 2012) tissue engineering. In order to manufacture CG scaffolds for tendon tissue engineering, we coupled our high strength, low porosity CG membrane with a relatively low strength, high porosity CG scaffold to create CG scaffold-membrane composites (Caliari, Ramirez et al. 2011). These composites resembled core-shell composites in nature such as plant stems and porcupine quills, maintaining an open pore structure to support cellular activity while also increasing elastic modulus by a factor of 36 via membrane incorporation (Caliari, Ramirez et al. 2011).

While the membrane shell improved composite mechanics, it was not cell permeable. For *in vivo* applications this could have significant implications by excluding extrinsic mediators of wound healing. In some applications, such as peripheral nerve regeneration, designing CG scaffolds to preferentially exclude migration of extrinsic cells while keeping intrinsic cells from the wound site localized to the scaffold has proven to be beneficial (Harley, Hastings et al. 2006). For other tissues such as tendon this may not be the case; recent work has suggested that patellar tendon

healing is mediated primarily by extrinsically recruited cells (Kinneberg, Galloway et al. 2013). These data suggest that a method to design mechanically robust and yet highly porous scaffold composites that permit the migration of extrinsic cells may be optimal for tendon tissue engineering. Therefore, this chapter aims to address this clinically-relevant issue by describing a fabrication technique to make mechanically robust membranes with well-ordered arrays of microscale pores amenable to cell migration and nutrient transport. Additionally, this chapter will delve deeper into characterization of the biophysical and biochemical properties of CG membranes as we envision these materials may be useful, either on their own or in conjunction with scaffolds, for other tissue engineering and regenerative medicine studies.

B.2 Materials and methods

*All reagents were purchased from Sigma-Aldrich (St. Louis, MO) unless otherwise specified

B.2.1 CG suspension preparation

CG suspensions were prepared as previously described in great detail (Yannas, Lee et al. 1989; O'Brien, Harley et al. 2004; Caliari and Harley 2011). Briefly, type I microfibrillar collagen from bovine tendon and chondroitin sulfate derived from shark cartilage were mixed together at a 11.25:1 mass ratio and homogenized in 0.05 M acetic acid at 4°C to prevent collagen gelatinization. Suspension with collagen content of 0.5, 1, and 1.5 w/v% were created. 1.5% suspension was used to fabricate CG scaffolds while 0.5 and 1% suspension was used to synthesize CG membranes.

B.2.2 Fabrication of aligned CG scaffolds via freeze-drying

CG scaffolds with aligned tracks of elongated pores were fabricated using a directional solidification method as previously described (Caliari and Harley 2011; Caliari, Ramirez et al. 2011). Briefly, degassed CG suspension was added to thermally-mismatched molds consisting of a poly(tetrafluoroethylene) (PTFE) body and copper bottom. The more conductive copper promoted unidirectional heat transfer during freezing in the scaffold longitudinal direction, resulting in the formation of geometrically anisotropic pores in that plane. Scaffolds were frozen at -10°C for 2 h and then sublimated at 0°C and 200 mTorr until dry, resulting in dry, macroporous scaffolds that have previously been shown to support tenocyte adhesion, proliferation, alignment, and phenotypic stability (Caliari and Harley 2011; Caliari, Ramirez et al. 2011; Caliari, Weisgerber et al. 2012).

B.2.3 Membrane fabrication and integration into scaffold-membrane composites

CG membranes were fabricated by air-drying degassed CG suspension loaded in Petri dishes (Caliari, Ramirez et al. 2011). Previous work with these membranes identified correlations between membrane thickness and the amount/type of suspension added to the dish that was used to guide fabrication (Caliari, Ramirez et al. 2011). Perforated membranes were created by evaporating suspension in molds containing arrays of poly(dimethylsiloxane) (PDMS, MG Chemicals, Canada) microposts. PDMS micropost arrays were fabricated by layering PDMS (monomer: curing agent ratio 5:1) in a 3" diameter PTFE mold that contained 0.5 mm holes spaced 2.80 or 1.98 mm apart (corresponding to pore fractions of 2.5 and 5% respectively). Vacuum was pulled to degas PDMS and promote infiltration into the holes. PDMS was cured at

37°C overnight, cut out of the PTFE mold, and then adhered to a standard Petri dish using fresh PDMS. Scaffold-membrane composites were fabricated by cutting membrane pieces, rolling them, and placing them directly into wells of the PTFE-copper freeze-drying mold (Caliari, Ramirez et al. 2011). CG suspension was then pipetted into the membrane-loaded wells and allowed to hydrate the membrane for 15 min in order to promote integration. All scaffold-membrane composites were then freeze-dried at -10°C as already described.

B.2.4 SEM analysis

The microstructure of the perforated membranes was qualitatively assesses using scanning electron microscopy (SEM) on a JEOL JSM-6060LV Low Vacuum Scanning Electron Microscope (JEOL USA, Peabody, MA). As CG membranes are not conductive, they were imaged using both secondary and backscatter electron detection at low vacuum to avoid conductive coatings that may occlude features of the membranes (Harley, Lynn et al. 2010).

B.2.5 Scaffold and membrane hydration and crosslinking

Scaffolds, membranes, and scaffold-membrane composites first underwent physical crosslinking via dehydrothermal treatment in a vacuum oven (Welch, Niles, IL) at 105°C for 24 h. CG materials were then sterilized in ethanol for 1-2 h, rinsed repeatedly in phosphate-buffered saline (PBS), and then stored in PBS overnight at 4°C. Following hydration, CG materials underwent chemical crosslinking using carbodiimide chemistry as previously described (Olde Damink, Dijkstra et al. 1996; Harley, Leung et al. 2007) in a solution of 1-ethyl-3-[3-dimethylaminopropyl] carbodiimide hydrochloride (EDC) and *N*-hydroxysulfosuccinimide

(NHS) at a molar ratio of 5:2:1 EDC:NHS:COOH where COOH represents the molar amount of collagen (carboxyl) content for 1.5 h at room temperature under shaking.

B.2.6 Nanoindentation analysis of CG membranes

Nanoindentation of hydrated membranes was performed in distilled water with a Hysitron UBI nanoindenter in displacement control using a 250 μm spherical tip and a ramp-hold creep profile (Galli, Comley et al. 2009; Galli and Oyen 2009). Constitutive poroelastic parameters (hydraulic/intrinsic permeability, Poisson's ratio) were calculated via a poroelastic finite element (FE) model (Galli, Comley et al. 2009).

B.2.7 Tenocyte isolation and culture

Primary equine tendon cells were isolated from superficial digital flexor tendons of non-tendinopathic horses in a manner approved by the University of Illinois IACUC as previously described (Kapoor, Caporali et al. 2010). Tenocytes were cultured in high glucose Dulbecco's modified Eagle's medium (DMEM) supplemented with 10% fetal bovine serum (FBS, Invitrogen, Carlsbad, CA) and antibiotics (Invitrogen) in normoxic conditions at 37°C/5% CO_2 and used at passage 4 for all experiments

B.2.8 Tenocyte chemotaxis assay

Tenocyte chemotaxis into anisotropic CG scaffolds through the perforated membranes was evaluated using a modified Transwell membrane setup (Caliari and Harley 2011; Caliari and Harley 2013). Transwell membrane inserts (6.5 mm diameter) were purchased from Fisher Scientific (Pittsburgh, PA). Membranes were cut out with a scalpel and replaced with 8 mm

diameter punches of standard or perforated membranes (45 μm membrane thickness) adhered to the insert with a thin layer of PDMS. Modified inserts were sterilized via ultraviolet (UV) and ethanol treatment before use. Hydrated anisotropic CG scaffolds were placed in the bottom of 24-well plates in contact with modified membranes. Tenocytes were seeded in the top compartment, and migration was evaluated 24 h after cell seeding.

B.2.9 Membrane culture conditions

45 μm thick membranes were cut into 1" diameter pieces for tenocyte culture experiments. Tenocytes were diluted to 5 x 10^4, 1 x 10^5, or 2 x 10^5 cells per 400 μL media. Membranes were set in ultra-low attachment 6-well plates (Corning Life Sciences, Lowell, MA) and seeded with 400 μL of cell suspension. Tenocytes were allowed to attach for 3 h, after which 4 mL of culture media was added to cover the membranes. Media was switched out at days 2 and 5 of the 7 day experiment.

B.2.10 Mechanical testing

Hydrated, crosslinked scaffold-membrane composites (6 mm diameter, 20 mm gauge length) underwent tensile mechanical testing in an MTS Insight electromechanical load frame (Eden Prairie, MN). Composites were strained at a rate of 1 mm min^{-1} until failure. Elastic modulus was calculated as the slope of the stress-strain curve in the range of 5-10% strain (Gibson, Ashby et al. 2010; Caliari, Ramirez et al. 2011) while ultimate tensile strength was determined from the peak stress value.

B.2.11 Tenocyte metabolic activity quantification

Metabolic activity of tenocytes seeded on membranes or migrating into scaffolds was evaluated using the alamarBlue® assay (Tierney, Jaasma et al. 2009). Membranes and scaffolds were incubated in alamarBlue® dye solution for 5 h at 37°C under gentle shaking. Live, viable cells continuously reduce the dye to a fluorescent product (resorufin) whose fluorescence was read on a fluorescent spectrophotometer (540/580 nm ex/em, Tecan, Switzerland).

B.2.12 Statistical analysis

One-way analysis of variance (ANOVA) was performed on scaffold-membrane mechanics, tenocyte metabolic activity, and chemotaxis data sets followed by Tukey-HSD post-hoc tests. Significance was set at $p < 0.05$. Mechanical tests used $n = 6$ or 7 composites per group, chemotaxis experiments used $n = 6$ scaffolds per group, and tenocyte growth on membranes used $n = 3$ membranes per group. Error is reported in figures as the standard error of the mean unless otherwise noted.

B.3 Results and Discussion

B.3.1 Membrane characterization

Preliminary results of nanoindentation on the 240 μm membrane variant indicate a transverse compressive modulus of 50–60 kPa, two orders of magnitude below the in-plane tensile modulus (~5 MPa); ongoing methodological development will enable calculation of constitutive poroelastic parameters (hydraulic/intrinsic permeability, Poisson's ratio) via a poroelastic finite element model and further analysis of the effect of collagen-GAG ratio and fiber alignment (**Table B.1**). Results indicate that while CG membrane fluid mobility is several orders of

magnitude less than CG scaffolds, it is comparable to cartilage as well as small intestine submucosa (SIS).

B.3.2 Tenocyte culture on membranes

We assessed the suitability of CG membranes to support the attachment and proliferation of tenocytes. CG membranes are biochemically identical to 3D scaffolds, making them potentially appealing as 2D substrates to easily and efficiently screen culture conditions without some of the inherent difficulties involved in working with 3D materials. CG membrane pieces (1" diameter, 45 μm thick) supported robust tenocyte attachment and proliferation with all three seeding densities harboring more than 10 times the number of cells originally seeded after 7 days in culture (**Figure B.1(a)**). Tenocyte number significantly increased in each group at each successive time point except for the 50000-seeded tenocyte group at day 4 (**Figure B.1(b)**).

B.3.3 Mechanics of scaffold-membrane composites

We next evaluated the mechanical properties of a new class of scaffold-membrane composites. Previous work with these composites showed that incorporation of the membrane shell would increase the composite elastic modulus in a manner predictable by cellular solids theory (Caliari, Ramirez et al. 2011). However, the scaffold core for those composites had a relative density of 0.5%. Scaffold with this density have since been shown to be susceptible to tenocyte-mediated contraction at high cell numbers, which leads to loss of pore anisotropy and more importantly, down-regulation of characteristic tenogenic genes (Caliari, Weisgerber et al. 2012). In contrast, higher density scaffolds (relative density of 1.5%) were shown to resist contraction, maintain an open pore network, and promote elevated and sustained expression of tenogenic markers

(Caliari, Weisgerber et al. 2012). Here, we created a series of composites with the 1.5% scaffold core and membranes of varying thickness: 23 μm (0.5% 1x) through 155 μm (1% 2 2x) (Caliari, Ramirez et al. 2011). Increasing membrane thickness resulted in significant increases in elastic modulus (**Figure B.2(a)**) and ultimate tensile strength (**Figure B.2(b)**) for each successive data point ($p < 0.02$). There were no significant differences in collapse strain (**Figure B.2(c)**, $p = 0.35$) between the groups with most composites failing at strains of 8-12%.

B.3.4 Creation of perforated membranes

In order to create a scaffold that was mechanically robust and yet amenable to extrinsic cell migration, we aimed to create membranes with ordered microscale perforations. We used Teflon-based molds to create PDMS micropost arrays (**Figure B.3**). Micropost arrays were fabricated from PDMS at a high monomer: crosslink ratio (5:1) to withstand buckling during the evaporation process. Micropost integrity was maintained throughout the process with few posts collapsing. Moreover, 500 μm diameter posts lead to the creation of holes in the membranes that are very close in diameter to the posts (**Figure B.4**).

B.3.5 Tenocyte chemotaxis through membranes into CG scaffolds

We assessed the feasibility of our perforated membranes for supporting extrinsic cell migration by using a modified Transwell set up with our CG membranes (both standard non-perforated and perforated groups). Chemotaxis was evaluated after 24 h. While non-perforated membranes supported negligible tenocyte migration into CG scaffolds as expected, the perforated membrane groups enabled robust tenocyte chemotaxis with the 2.5% and 5% + PDGF groups supporting significantly greater tenocyte chemotaxis than the 0% per group ($p < 0.03$) (**Figure B.5**). Not

surprisingly, PDGF-BB supplementation supported the highest levels of tenocyte chemotaxis into CG scaffolds (Caliari and Harley 2011; Caliari and Harley 2013). Interestingly, the non-supplemented 2.5% group had increased tenocyte chemotaxis over the 5% group, although this difference was not significant (p = 0.27). This result may be due to the setup of the assay. The tenocyte seeding solution may have leaked through the more permeable 5% membrane faster than in the 2.5% group, reducing the efficiency of tenocyte migration and attachment on the CG scaffold.

Ongoing work is assessing the capacity of these perforated membranes to support cell infiltration, as extrinsic cells are thought to be critical to the tendon wound healing process (Kinneberg, Galloway et al. 2013). Additionally, there is an expected tradeoff between increased perforation density (leading to increased permeability and cell migration) and mechanical integrity of the composite. This tradeoff will be explored more extensively in future studies to optimize all parameters involved. Additionally, long-term cell studies will assay the capability of perforated scaffold-membrane composites to support sustained cell viability within the scaffold core without the presence of a hypoxic core.

B.4 Conclusions

Mechanically efficient materials are needed for orthopedic tissue engineering that can simultaneously support cellular activities while withstanding physiological loads. Building on the development of a core-shell composite for tendon tissue engineering, this chapter introduced a method to fabricate CG membranes with well-ordered arrays of microscale pores to facilitate

cell migration, a design parameter that is likely to be critical for the *in vivo* success of these composites. We also characterized the poroelastic behavior of these membranes and demonstrated that they could support tenocyte viability as 2D cell culture substrates that maintain CG biochemistry. Ongoing work is optimizing the capacity of scaffold-perforated membrane constructs to support cell migration while maintaining adequate permeability and mechanical integrity.

B.5 Tables

Physical property	Experimental value
Shear Modulus, G(0)	520 ± 130 kPa
$E_{compression}$ [$E_{tension}$]	~1 - 1.5 MPa [7.5 ± 0.64 MPa]
Permeability, k	$2.03 \pm 0.7 \times 10^{-18}$ m^2
Fluid Mobility, K	2×10^{-15} $m^4/N \cdot s$
$K_{scaffold}$	10^{-10} $m^4/N \cdot s$
$K_{cartilage}$	10^{-15} $m^4/N \cdot s$
K_{SIS}	$10^{-14} – 10^{-15}$ $m^4/N \cdot s$

Table B.1. Membrane physical properties. CG membranes are nearly an order of magnitude stiffer in tension than compression. Nanoindentation analyses indicate CG membranes, while displaying lower fluid mobility than CG scaffolds, are comparable to cartilage and SIS. Values are expressed as mean ± SD.

B.6 Figures

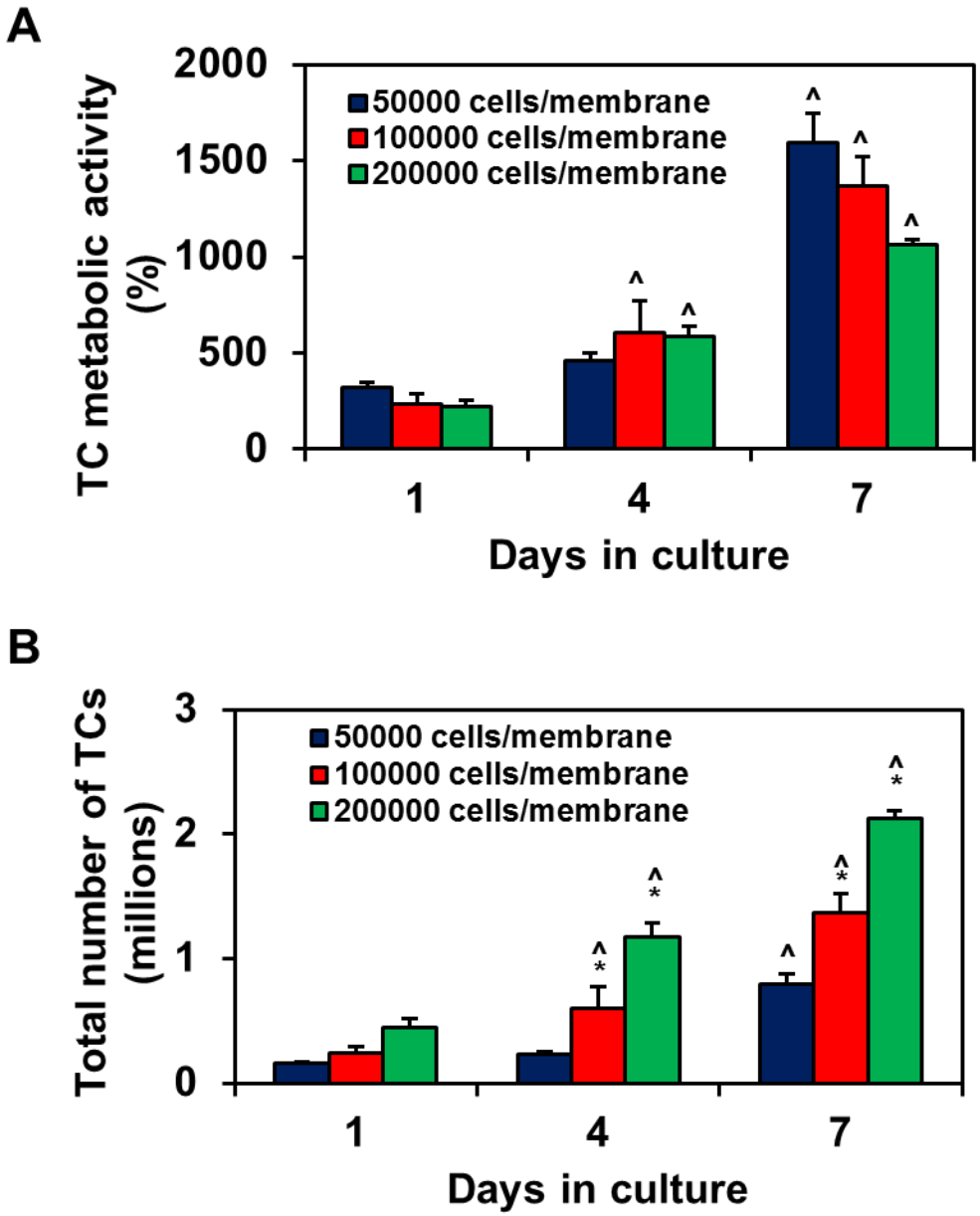

Figure B.1. Tenocyte adhesion and growth on CG membranes. A) CG membranes support sustained mitochondrial metabolic activity and B) proliferation over 7 days in culture when seeded at 50, 100, or 200 thousand cells per membrane (1 in diameter pieces, 45 µm thick). *: significantly higher at that time point compared to next lowest seeding density. ^: significant increase compared to previous time point.

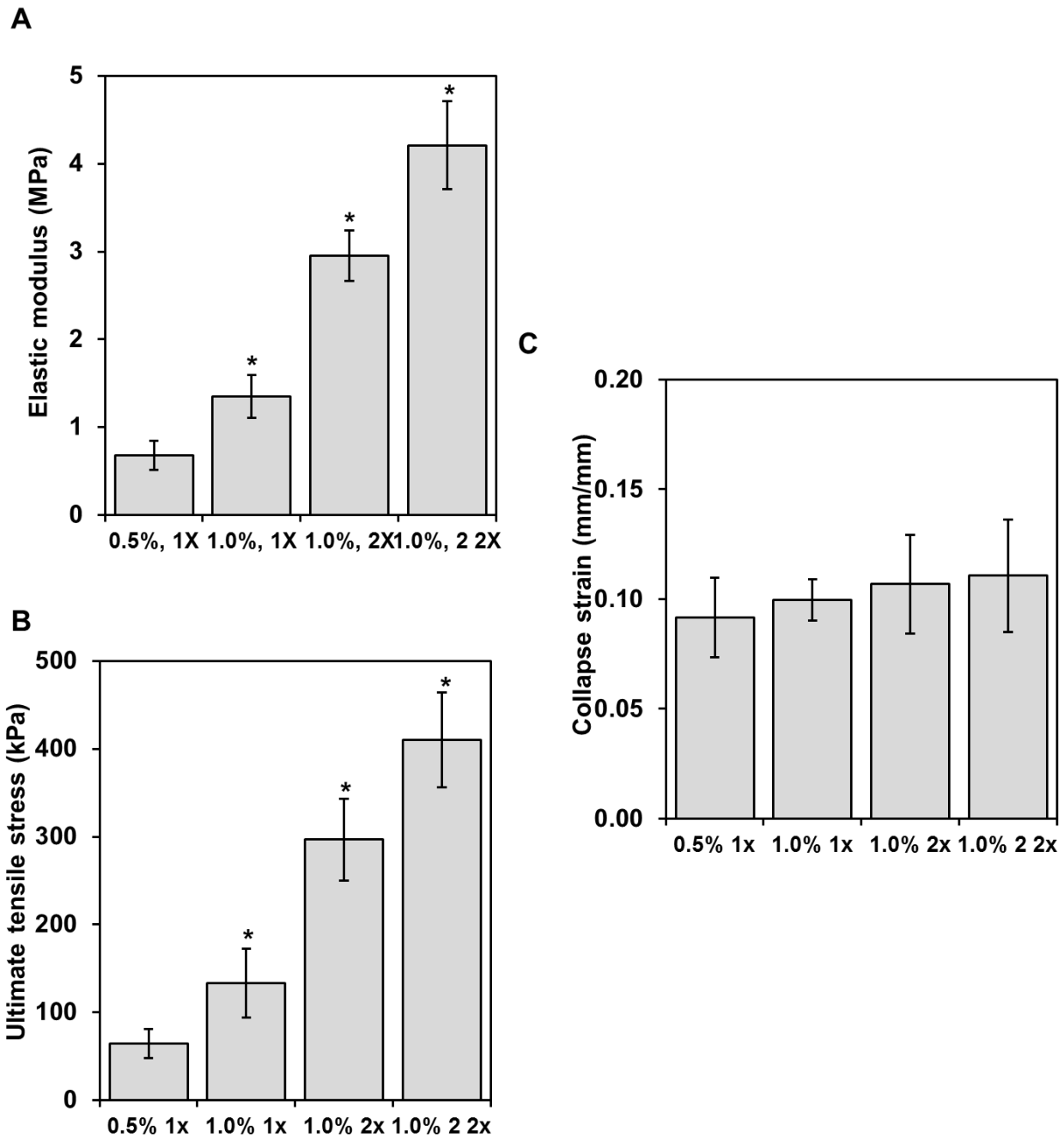

Figure B.2. CG scaffold-membrane composite mechanical properties. A) Composite tensile elastic modulus, B) Ultimate tensile stress, C) Collapse strain. *: significantly higher than the composite with the next thinnest membrane shell.

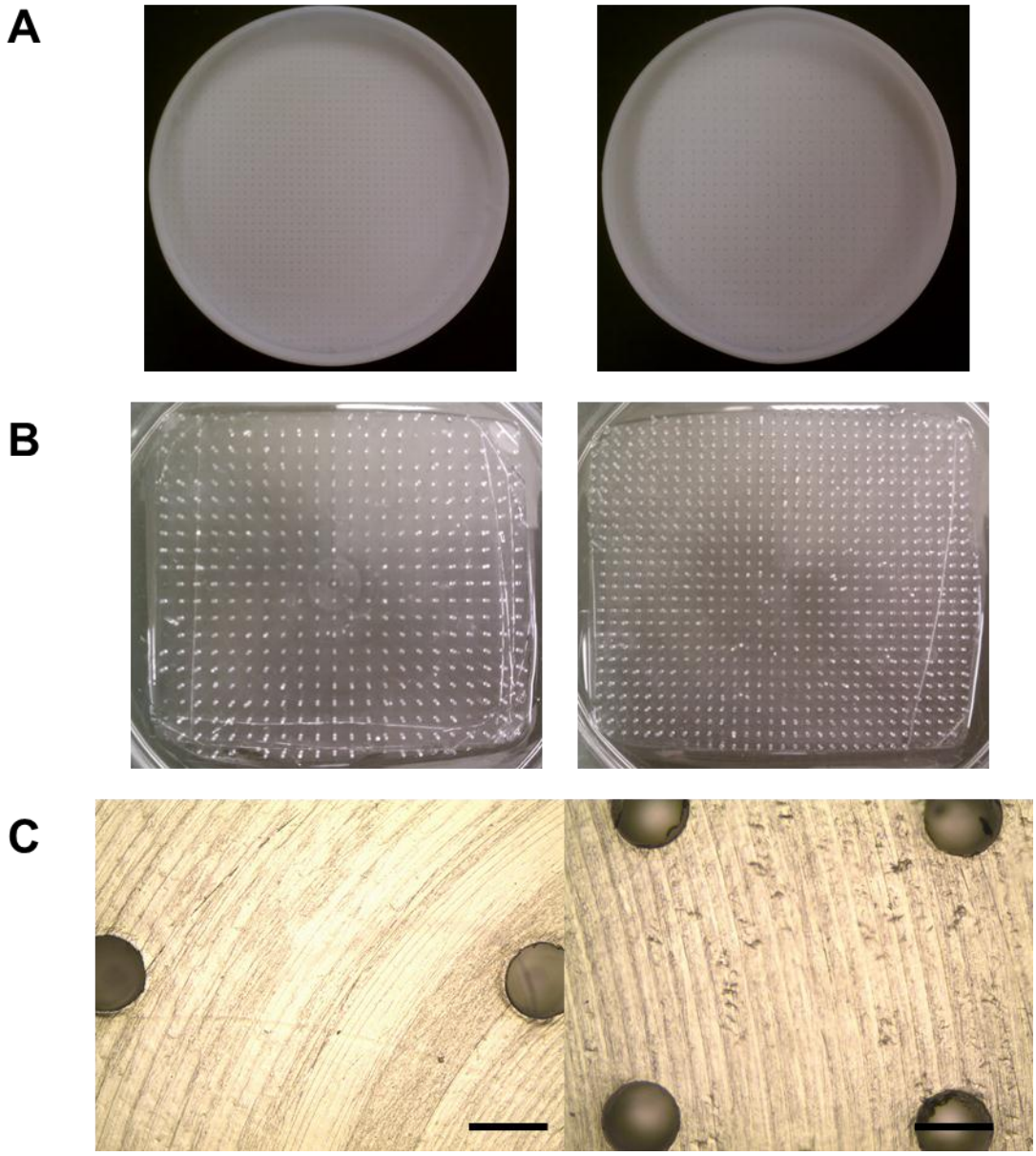

Figure B.3. Perforated membrane fabrication. A) Teflon molds used to create PDMS micropost arrays with 2.5% (left) and 5% (right) post coverage. B) Fabricated PDMS micropost arrays with 2.5% (left) and 5% (right) post coverage. C) Light microscope image of 500 μm diameter posts for 2.5% (left) and 5% (right) molds. *Scale bars*: 500 μm.

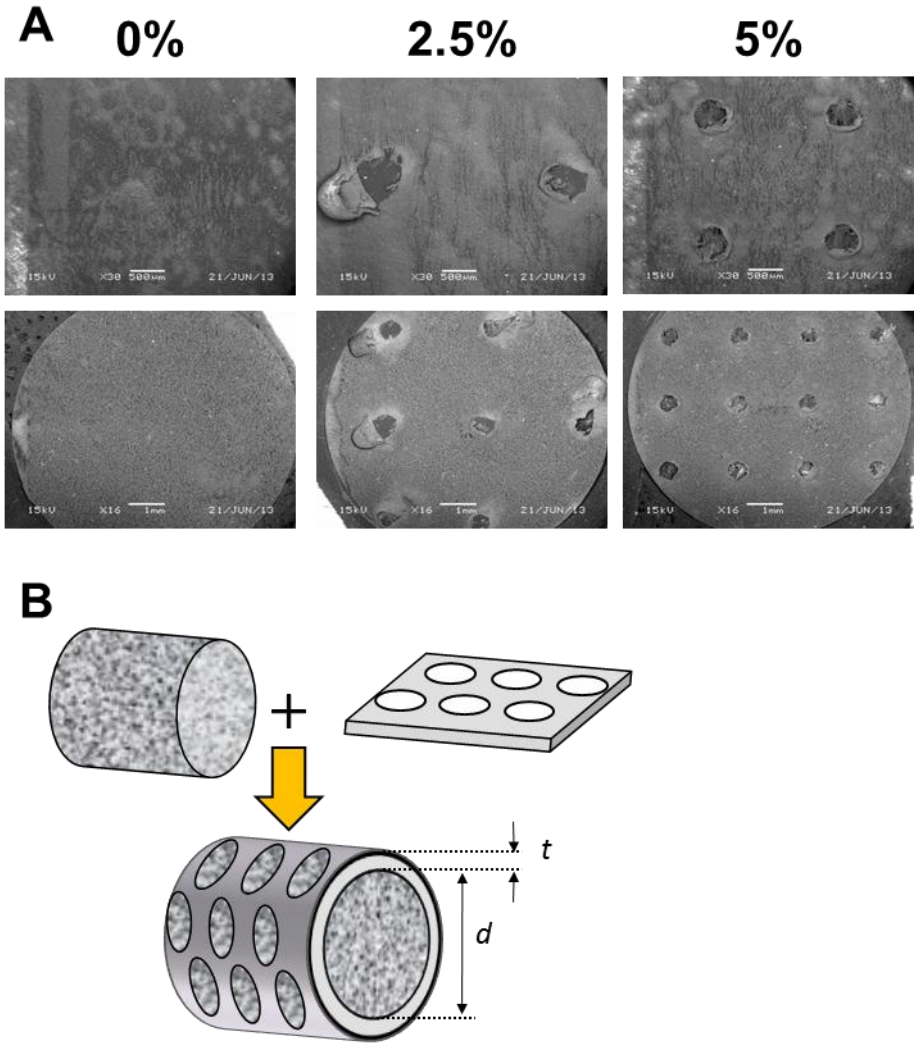

Figure B.4. Perforated membrane paradigm. A) SEM images of perforated membranes demonstrates the creation of holes in the 2.5% and 5% versions, while no holes are visible in the standard 0% membrane version. *Scale bars*: 500 µm (top row), 1 mm (bottom row). B) Core-shell composite design with perforated membrane.

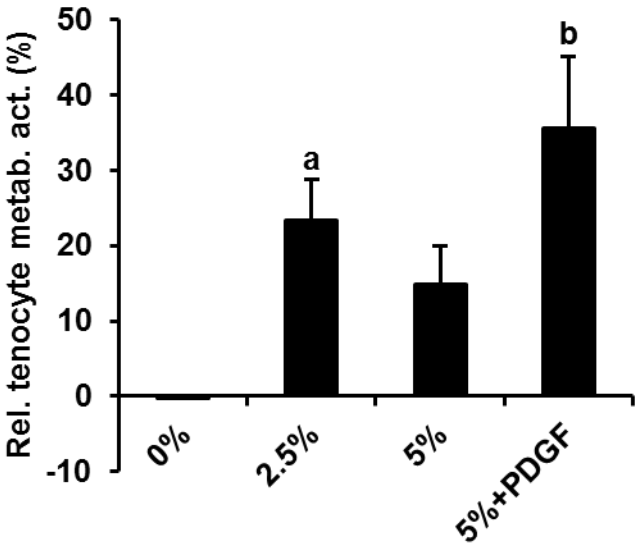

Figure B.5. Tenocyte chemotaxis through perforated membranes into CG scaffolds. Tenocytes are not able to penetrate standard non-perforated membranes while robust chemotaxis is observed in perforated groups. *a*: significantly greater than 0% group. *b*: significantly greater than 0% and 5% groups.

APPENDIX C: COLLAGEN-HYDROXYAPATITE SCAFFOLDS PRESENTING A MODULAR BMP-2 PEPTIDE FOR DRIVING MSC-MEDIATED OSTEOGENESIS[9]

C.1 Introduction

Biomaterial scaffolds have been designed as artificial analogs of natural extracellular matrices (ECMs) for a range of tissue engineering and regenerative medicine applications. One of the primary functions of the native ECM is to sequester and transiently present biomolecular regulators of cell activity such as growth factors. Therefore, scaffolds must be designed to present growth factor cues in a controllable and sustainable manner. However, there are significant challenges to this endeavor, including short factor half-lives in serum, diffusion out of the scaffold, and presenting the protein in its proper conformation so as to maintain activity. In order to overcome these limitations, biomimetic strategies to present growth factors within scaffolds in an immobilized, stable, and bioactive conformation would be tremendously useful for tissue engineering applications.

To this end, we recently developed a modular peptide that mimics features of multifunctional proteins containing motifs to bind tissue-specific ECM components as well as ligands to interact with cell surface receptors (Lee, Wagoner-Johnson et al. 2009; Lee, Wagoner Johnson et al. 2010). One of these peptides was designed with two functional peptide arms: one derived from the hydroxyapatite (HA)-binding peptide sequence encoded by osteocalcin and another from the knuckle epitope of bone morphogenetic protein-2 (BMP-2) that retains activity of the full-length protein (Saito, Suzuki et al. 2003; Lee, Wagoner-Johnson et al. 2009). 2D HA surfaces functionalized with this peptide were shown to promote osteogenic differentiation of

[9] This chapter has been adapted from the following publication:
Caliari S.R., et al. (in preparation). "Collagen-hydroxyapatite scaffolds presenting a modular BMP-2 peptide for driving MSC-mediated osteogenesis."

mesenchymal stem cells (MSCs), inducing robust mineralization, increased osteocalcin expression, and elevated alkaline phosphatase activity. While these results were promising, a 3D HA material to present the modular peptide would be preferred for regenerative medicine applications.

Many HA-containing materials have been developed in recent years for bone tissue engineering endeavors. One such class of materials is based on the collagen-glycosaminoglycan (CG) scaffolds system. CG scaffolds are highly porous 3D materials that are fabricated by freeze-drying. CG scaffolds have a tremendous history of *in vivo* success for soft tissue regeneration (Yannas, Lee et al. 1989; Harley, Spilker et al. 2004) and as *in vitro* templates to probe the influence of scaffold microarchitecture and mechanics on various cellular activities (Torres, Freyman et al. 2000; Samuel, Lee et al. 2002; O'Brien, Harley et al. 2005; Harley, Kim et al. 2008). Recently, a titrant-free concurrent mapping method was developed to incorporate controllable amounts of HA mineral content into the CG archetypical scaffold (Harley, Lynn et al. 2010; Lynn, Best et al. 2010). These CG-calcium phosphate (CGCaP) scaffolds have since been used to drive osteogenic MSC differentiation (Murphy, Matsiko et al. 2012), deliver genes (Curtin, Cunniffe et al. 2012), and as components of multi-phase scaffolds for osteochondral repair (Harley, Lynn et al. 2010; Getgood, Kew et al. 2012). In this chapter we describe the integration of a modular BMP-2 peptide with a collagen-HA scaffold to enhance the osteogenic potential of the material. We also discuss the influence of peptide and growth factor supplementation on driving osteogenesis in our scaffolds.

C.2 Materials and methods

*All reagents purchased from Sigma Aldrich (St Louis, MO) unless otherwise specified.

C.2.1 CG and CGCaP suspension preparation

CG and CGCaP suspensions were prepared via homogenization in a jacketed beaker (temperature: 4°C) to maintain the triple helical integrity of the collagen. CG suspension was composed of microfibrillar type I collagen from bovine tendon and chondroitin sulfate from shark cartilage in acetic acid as previously described (Yannas, Lee et al. 1989; Caliari, Weisgerber et al. 2012). Like the CG suspension, CGCaP suspension included type I collagen and chondroitin sulfate. Additionally, the suspension contained calcium salts (($Ca(OH)_2$, $Ca(NO_3)_2 \cdot 4H_2O$) with phosphoric acid as the solvent. Using a titrant-free concurrent mapping technique (Lynn, Best et al. 2010), suspension components were mixed to yield CGCaP that contained 40% calcium phosphate mineral by weight (Harley, Lynn et al. 2010; Lynn, Best et al. 2010).

C.2.2 Scaffold fabrication via freeze-drying

Isotropic CG and CGCaP scaffold sheets were fabricated via freeze-drying using a constant cooling method (O'Brien, Harley et al. 2004; O'Brien, Harley et al. 2005). Suspensions were degassed to remove air bubbles introduced during homogenization and added to 3” x 3” polysulfone molds. Suspension-loaded molds were placed in a VirTis freeze-dryer (Gardiner, NY) and cooled at a constant rate of 1°C/min to a final freezing temperature of -10°C. Suspensions were frozen at this temperature for 2 h and then ice crystals were sublimated at 0°C and 200 mTorr. Freeze-drying results in the formation of highly macroporous scaffolds (O'Brien, Harley et al. 2004; Harley, Lynn et al. 2010; Caliari and Harley 2011).

C.2.3 Scaffold hydration and crosslinking

Dry CG scaffolds were dehydrothermally crosslinked at 105°C for 24 h in a vacuum oven (Welch, Niles, IL) (Harley, Leung et al. 2007). CG and CGCaP scaffolds were also chemically crosslinking via carbodiimide treatment (Olde Damink, Dijkstra et al. 1996; Harley, Leung et al. 2007). Scaffolds were sterilized in ethanol for 1 h and then rinsed in phosphate-buffered saline (PBS) several times overnight. Hydrated scaffolds were then immersed in a solution of 1-ethyl-3-[3-dimethylaminopropyl] carbodiimide hydrochloride (EDC) and *N*-hydroxysulfosuccinimide (NHS) in PBS for 1.5 h at room temperature. Crosslinking was performed a molar ratio of 5:2:1 EDC:NHS:COOH where COOH represents the carboxyl groups in the collagen scaffold. Following crosslinking, scaffolds were rinsed thoroughly in PBS and stored in PBS at 4°C until use.

C.2.4 BMP-2 modular peptide synthesis

Modular peptides (**Table C.1**) were synthesized using solid-phase peptide synthesis as previously described (Lee, Wagoner-Johnson et al. 2009). Briefly, peptide synthesis was performed on Fmoc-Rink Amide MBHA resin with Fmoc-protected α-amino acids (Noviabiochem). Crude peptides were purified via high-performance liquid chromatography (HPLC). Some peptide was fluorescently-labeled with 5(6) carboxyfluorescein (FAM) for initial studies assessing peptide immobilization efficiency in scaffolds.

C.2.5 Peptide immobilization within scaffolds

FAM-conjugated BMP-2 peptide was used to assess peptide immobilization efficiency in CG and CGCaP scaffolds under various loading conditions. Peptide was diluted to the proper concentration in 40 µL of PBS with 20 µL added to each side of a dried scaffold disc (6-8 mm diameter, 3 mm thick). Peptide was allowed to attach for 2-24 h at 37°C, after which the peptide-loaded scaffolds were rinsed twice in PBS under moderate shaking for 1 h. Scaffolds were then digested in papain buffer at 60°C for 1-3 h to enable direct reading of fluorescent signal from the digest solution on a plate reader (Tecan, Switzerland). Immobilization efficiency was calculated by interpolating the fluorescent signal obtained on a standard curve created with FAM-labeled peptide that underwent identical thermal and enzymatic treatment to the peptide-loaded scaffolds (Caliari and Harley 2013)

C.2.6 ASC and MSC culture in scaffolds

Porcine adipose-derived stem cells (ASCs) were isolated from subcutaneous back fat of Yorkshire crossbred male pigs as previously described (Kim, Monaco et al. 2010). Human bone marrow-derived mesenchymal stem cells (MSCs) were purchased from Lonza (Walkersville, MD). Both cell types were cultured in low glucose DMEM supplemented with 10% FBS (Invitrogen, Carlsbad, CA) and antibiotics (Invitrogen) at 37°C and 5% CO_2. Media was switched twice a week and both cell types were used at passage 6 or 7 for all experiments.

C.2.7 Cell culture in scaffolds

In initial experiments, MSCs were cultured in 8 mm diameter x 3 mm thick scaffold punches. Four groups were examined: CG scaffolds in growth media, CGCaP scaffolds in growth media, CGCaP scaffolds in osteogenic induction media (growth media supplemented with 50 µM

ascorbic acid, 0.1 μM dexamethasone, and 10 mM β-glycerophosphate), and CGCaP scaffolds in growth media supplemented with 50 ng/mL full length BMP-2 (ProSpec, Israel, added fresh during each media change). A previously validated static seeding method was used to load scaffolds with cells (O'Brien, Harley et al. 2005). Scaffold pieces were set in ultra-low attachment 6-well plates (Corning Life Sciences) where excess scaffold moisture was removed to promote more efficient seeding. MSCs were re-suspended at a concentration of 1×10^5 cells per 20 μL with 10 μL of cell suspension added to each side of the scaffold discs. MSCs were allowed to attach for 2.5 h at 37°C and 5% CO_2 before media was added to well plates. MSC-seeded scaffolds were cultured for the duration of the experiment at 37°C and 5% CO_2 with media changes occurring twice a week. For 2D experiments, ASCs and MSCs were seeded in 24-well plates at a density of 5×10^3 cells per well. BMP-2 peptide (0, 1, 10, or 50 μg per well) was added fresh to the media at days 0 and 4 of the 8 day experiment.

C.2.8 Quantification of cell metabolic activity

ASC and MSC metabolic activity in both the 2D and 3D experiments was assayed using alamarBlue® (Invitrogen). Cells (2D) and cell-seeded scaffolds (3D) were incubated in alamarBlue® solution under gentle shaking at 37°C for 3 h, allowing viable cells to reduce the alamarBlue® dye to a by-product whose fluorescence could be read on a plate reader (Tecan) (Tierney, Jaasma et al. 2009).

C.2.9 RNA isolation, reverse transcription, and real-time PCR

RNA was isolated from MSC-seeded scaffolds at time points 2, 4, and 8 weeks using an RNeasy Plant Mini kit (Qiagen, Valencia, CA) (Duffy, McFadden et al. 2011; Caliari, Weisgerber et al.

2012) and reverse transcribed to cDNA with the QuantiTect Reverse Transcription kit (Qiagen). PCR reactions were performed in triplicate using SYBR green chemistry (Qiagen) on an Applied Biosystems 7900HT Fast Real-Time PCR system (Applied Biosystems, Carlsbad, CA). PCR primer sequences for alkaline phosphatase (ALP), bone sialoprotein (BSP), type I collagen (COL I), osteocalcin (OC), osteopontin (OP), runt-related transcription factor 2 (RUNX2), and GAPDH were acquired from literature (Frank, Heim et al. 2002; Pauly, Klatte et al. 2010; Zhou, Xu et al. 2011) and synthesized by Integrated DNA Technologies (Coralville, IA). Data were analyzed using Sequence Detection Systems software v2.4 (Applied Biosystems) with the delta-delta Ct method. GAPDH served as the housekeeping gene and results were presented as fold changes relative to expression levels in the CG group after 2 weeks.

C.2.10 Alizarin red staining

Following the 8 day 2D cell experiment, alizarin red staining was used to assess mineral deposition. Monolayers were rinsed in PBS and fixed with 10% neutral-buffered formalin for 30 min at room temperature. Formalin was removed and scaffolds were incubated in 2% alizarin red solution for 30 min at room temperature. Excess stain was rinsed with water and pictures were taken using a cell phone camera.

C.2.11 Statistical analysis

Two-way analysis of variance (ANOVA, independent variables time and scaffold/biomolecule treatment) was performed on metabolic activity and gene expression data sets with one-way ANOVA used for peptide immobilization studies. Pair-wise comparisons were made using the Tukey-HSD post-hoc test. Significance was set at $p < 0.05$. Metabolic activity experiments used

n = 3 (2D) or n = 6 (3D) samples per group. Gene expression and peptide immobilization experiments used n = 3 samples per group. Error is reported in figures as the standard error of the mean unless otherwise noted.

C.3 Results and Discussion

C.3.1 MSC metabolic activity in CG and CGCaP scaffolds

Initial studies focused on driving MSC osteogenic phenotype in CG and CGCaP scaffolds over the course of an 8 week *in vitro* experiment. We examined four experimental groups: CG scaffolds cultured in growth media, CGCaP scaffolds (growth media), CGCaP scaffolds (osteogenic media), and CGCaP scaffolds (growth media plus 50 ng/mL full length BMP-2 protein). Weekly assessment of MSC metabolic activity was performed using alamarBlue® (**Figure C.1**). Statistical analysis showed a significant effect of both culture time and scaffold treatment ($p < 0.0001$). Through the first two weeks of the experiment, CG scaffolds supported significantly higher metabolic activity than the CGCaP groups ($p < 0.02$). A likely contributor to this trend is that CG scaffolds are less dense and more permeable than CGCaP scaffolds. Additionally, the osteogenic group showed significantly lower metabolic activity than all other experimental groups starting at the day 14 time point ($p < 0.01$). This may be a sign that the MSCs are differentiating to osteoblasts in this group, as terminally-differentiated cells are known to be less metabolically active than stem cells. Although the CGCaP groups initially lagged behind the CG group, the two non-osteogenic CGCaP groups eventually caught up with and even exceeded the metabolic activity of the CG group at day 28 ($p < 0.05$). One explanation for this could be the higher specific surface area of the CGCaP scaffolds; although the increased density

may initially slow MSC growth kinetics, the greater availability of surface area for cells to attach and spread may help sustain long-term proliferation. MSC metabolic activity steadily increased over the course of the experiment in the non-osteogenic groups until around day 28 or 35, where it plateaued and remained relatively constant for the remainder of the 8 week experiment. This may be due remodeling or differentiation events occurring in these groups.

C.3.2 MSC osteogenic gene expression in CG and CGCaP scaffolds

Expression levels of the osteogenic genes encoding for alkaline phosphatase (ALP), bone sialoprotein (BSP), type I collagen (COL I), osteocalcin (OC), osteopontin (OP), and runt-related transcription factor 2 (RUNX2) were measured after 2, 4, and 8 weeks in culture (**Figure C.2**). These results revealed complex temporal trends in response to scaffold type (CG versus CGCaP) and media supplementation.

ALP expression was significantly influenced by scaffold treatment ($p = 0.004$), but not culture time ($p = 0.34$) (**Figure C.2(a)**). Although ALP expression was significantly up-regulated in the CG group compared to the other experimental groups at 4 weeks ($p < 0.02$), this effect was not sustained out to 8 weeks. At the conclusion of the experiment the osteogenic group had the highest level of expression, although this difference was not significant. BSP expression showed significant temporal effects ($p = 0.0009$), but no significant effect of scaffold treatment ($p = 0.46$) (**Figure C.2(b)**). Expression levels generally increased over time for all groups, with significant up-regulation in the CGCaP group from 4 to 8 weeks ($p = 0.03$). By the 8 week time point, all three CGCaP groups expressed BSP at least 4-fold higher than the CG group, although these effects were not significant.

Both culture time and scaffold treatment significantly affected the expression profiles of the COL I gene ($p < 0.0007$) (**Figure C.2(c)**). COL I expression was generally higher in the CG group over the course of the experiment and was significantly higher than the osteogenic group at all three time points ($p < 0.03$). By the conclusion of the experiment, both the CG and CGCaP groups expressed significantly higher levels of COL I than the osteogenic and BMP-2 groups ($p < 0.02$). For osteopontin expression, there was a significant effect of culture time only ($p = 0.01$) (**Figure C.2(e)**). CGCaP OP expression was up-regulated on the final time point ($p = 0.02$) with higher levels of expression in all three CGCaP groups by at least 2-fold compared to the CG group at the 8 week time point, although again this effect was not statistically significant. Finally, there were no significant differences ($p > 0.05$) in expression profiles for either OC (**Figure C.2(d)**) or RUNX2 (**Figure C.2(f)**), although the CGCaP groups displayed a trend of higher OC expression by at least 2-fold compared to the CG group at week 8.

C.3.3 BMP-2 peptide immobilization in CG and CGCaP scaffolds

While soluble supplementation of BMP-2 had some positive effects on driving osteogenesis in the previous experiments, it was done so in an inefficient manner as fresh BMP-2 was added during each media change (twice a week). Modular BMP-2 peptides have previously been shown to promote sustained osteogenesis on 2D HA surfaces (Lee, Wagoner-Johnson et al. 2009). In this set of experiments we sought to immobilize controllable levels of bioactive peptide within our 3D CG and CGCaP scaffolds. While CG scaffolds do not contain hydroxyapatite, it was thought that the peptide could still interact electrostatically with the negatively-charged GAG content as well as various functional groups in the collagen.

Calibration curves using FAM-conjugated BMP-2 peptide show that the peptide can be controllably immobilized in a linear manner on both CG and CGCaP scaffolds, although as expected this immobilization was more efficient in the CGCaP scaffolds (**Figure C.3(a)**). Tuning the immobilization time had no effect on immobilization efficiency in the CG scaffolds (p = 0.27) and only a relatively weak effect in the CGCaP scaffolds (p = 0.02) (**Figure C.3(b)**). For the CGCaP scaffolds, peak immobilization was observed at the 12 h time point with significantly more efficient peptide conjugation observed than the 2 and 4 h time points ($p < 0.04$). Based on the specific surface area of the CGCaP scaffold, the surface density of immobilized peptide was calculated to be in the range of 40-55 nmol/m^2. Maximal surface coverage on 2D HA surfaces was previously reported at 467 nmol/m^2 (Lee, Wagoner-Johnson et al. 2009). One explanation for this disparity is that our scaffold is only 40 wt% HA, which means that less peptide would be expected to adhere compared to a pure HA surface. Additionally, surface coverage data for the native osteocalcin protein reports levels of coverage six times lower on HA surfaces compared to the modular peptide (Dowd, Rosen et al. 2001). Given these points, we believe that the immobilization efficiency is high enough to elicit positive osteogenic effects in future cell experiments.

C.3.4 Effects of BMP-2 peptide on driving osteogenesis in 2D culture

We next assessed the ability of soluble, unbound BMP-2 peptide to drive osteogenesis, in our hands, in 2D ASC and MSC cultures over 8 days. This experiment was performed as a precursor to 3D cell experiments incorporating the peptide in scaffolds. We cultured ASCs and MSCs in either growth or osteogenic induction media supplemented with 0, 1, 10, or 50 µg of peptide.

Metabolic activity results after 8 days show significantly lower activity in the osteogenic media groups ($p < 0.0001$), indicative of differentiation to less metabolically active osteoblasts (**Figure C.4(a)**). Alizarin red mineral staining shows clear increases in osteogenic media groups compared to growth media groups, with the most robust mineral deposition occurring with the combination of osteogenic media and the 50 µg peptide dose for both cell types (**Figure C.4(b)**).

C.4 Conclusions

Strategies to present growth factor cues in a controllable, localized, and conformationally-active manner within 3D tissue engineering scaffolds are critically needed. This chapter discusses the evaluation of several culture conditions to drive MSC osteogenesis in 3D regulatory compliant CG and CGCaP scaffolds. We also validate the use of a modular peptide that mimics multifunctional proteins *in vivo* with an HA-binding motif on one end and a BMP-2 peptide fragment on the other end. We show that this peptide can be controllably bound to 3D CGCaP scaffolds and that the peptide can drive both ASC and MSC osteogenesis in 2D culture. Future studies will evaluate this effect in our 3D scaffolds. Moreover, strategies to bind modular growth factors to specific ECM components may be useful for the presentation of graded growth factor cues for complex tissue engineering applications such as orthopedic interface engineering.

C.5 Tables

Peptide	Amino acid sequence
Native BMP-2 (AAs 73-92)	KIPKACCVPTELSAISMLYL
Native OC (AAs 17-25)	γEPRRγEVCγEL
BMP-2 modular peptide	KIPKASSVPTELSAISTLYLAAAAγEPRRγEVAγEL

Table C.1. Amino acid sequences of native BMP-2 and OC sequences as well as BMP-2 modular peptide. Cysteine and methionine residues from the native BMP-2 sequence were replaced with serine and threonine groups respectively while the cysteine in the native OC sequence was replaced with alanine. This was done to avoid disulfide linkages between peptides. BMP-2 and OC-binding peptide arm were connected by a four alanine linker. Sequences based on references (Saito, Suzuki et al. 2003; Lee, Wagoner-Johnson et al. 2009).

C.6 Figures

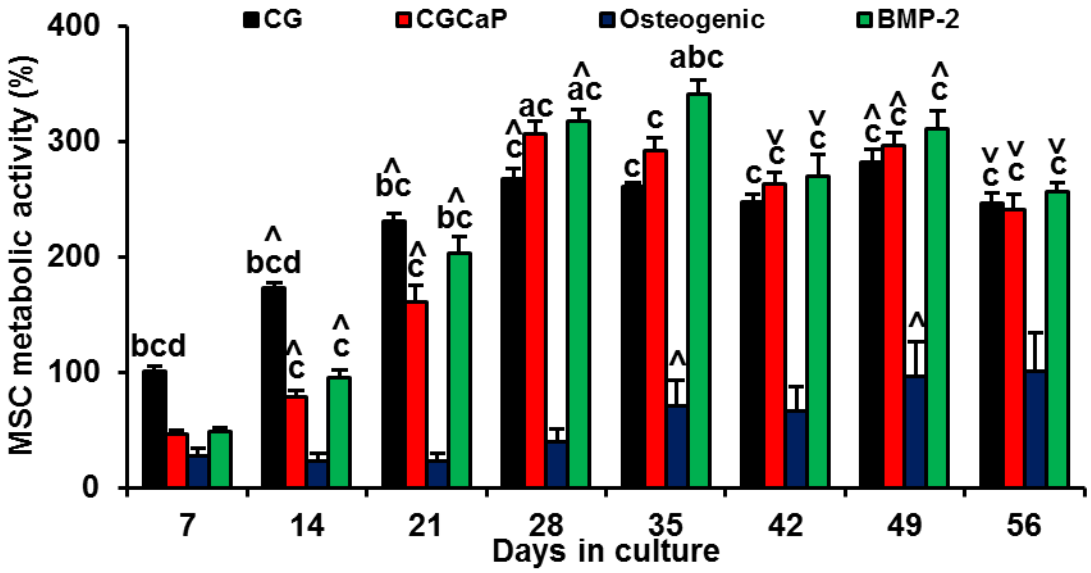

Figure C.1. MSC metabolic activity in response to osteogenic treatments *(n* = 6). MSC metabolic activity was measured over the course of 56 days on CG control scaffolds as well as non-supplemented CGCaP scaffolds and CGCaP scaffolds supplemented with osteogenic induction media and BMP-2 (50 ng/mL) respectively. *a*: significantly higher than CG group at that time point, *b*: significantly higher than CGCaP group at that time point, *c*: significantly higher than Osteogenic group at that time point, *d*: significantly higher than BMP-2 group at that time point, ∧: significantly higher than previous time point, ∨: significantly lower than previous time point.

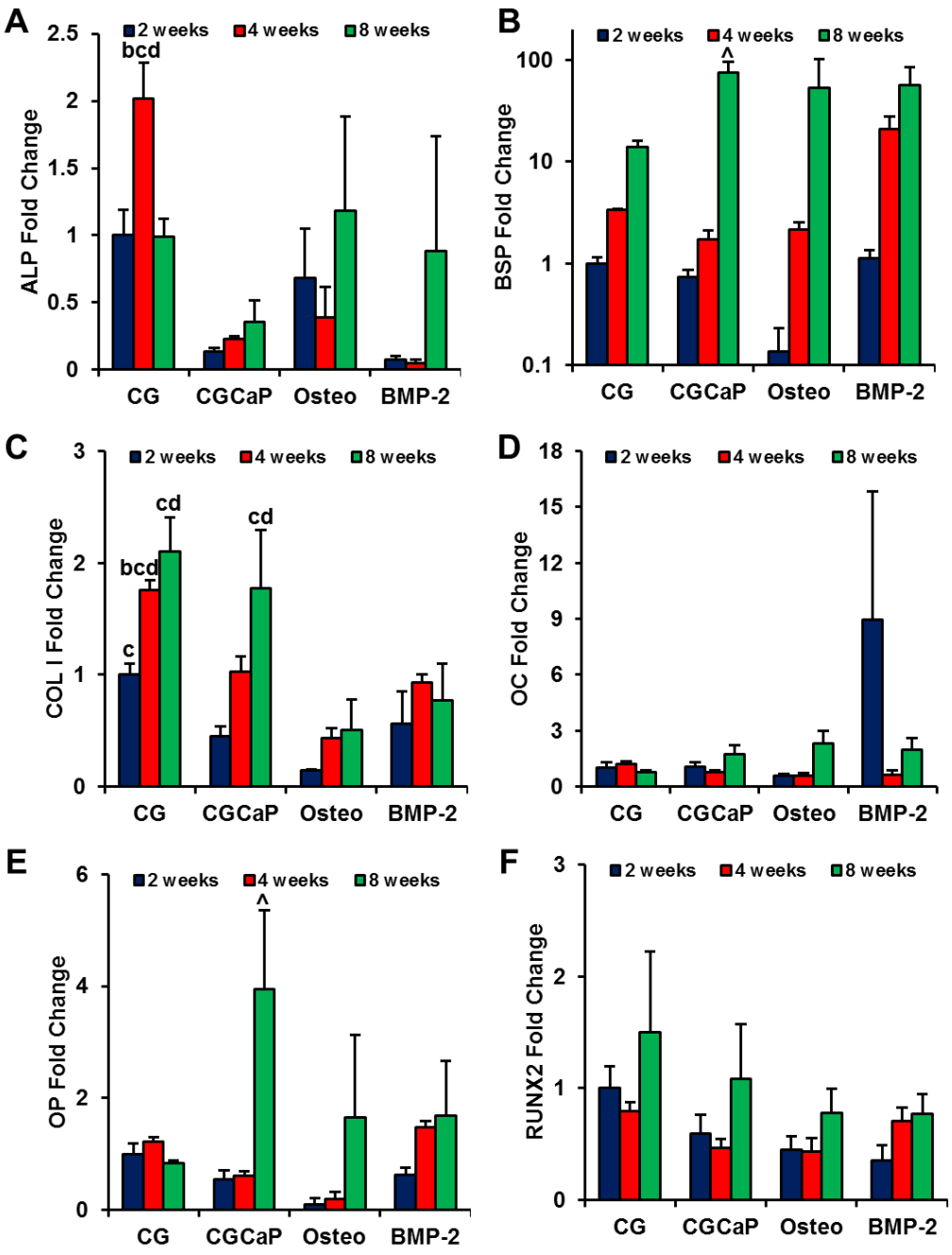

Figure C.2. MSC gene expression in response to osteogenic treatments *(n* = 3). MSC gene expression was measured over the course of 56 days on CG control scaffolds as well as non-supplemented CGCaP scaffolds and CGCaP scaffolds supplemented with osteogenic induction media and BMP-2 (50 ng/mL) respectively. A) alkaline phosphatase (ALP), B) bone sialoprotein (BSP), C) type I collagen (COL I), D) osteocalcin (OC), E) osteopontin (OP), and F) runt-related transcription factor 2 (RUNX2). *a*: significantly higher than CG group at that time point, *b*: significantly higher than CGCaP group at that time point, *c*: significantly higher than Osteogenic group at that time point, *d*: significantly higher than BMP-2 group at that time point, ∧: significantly higher than previous time point, ∨: significantly lower than previous time point.

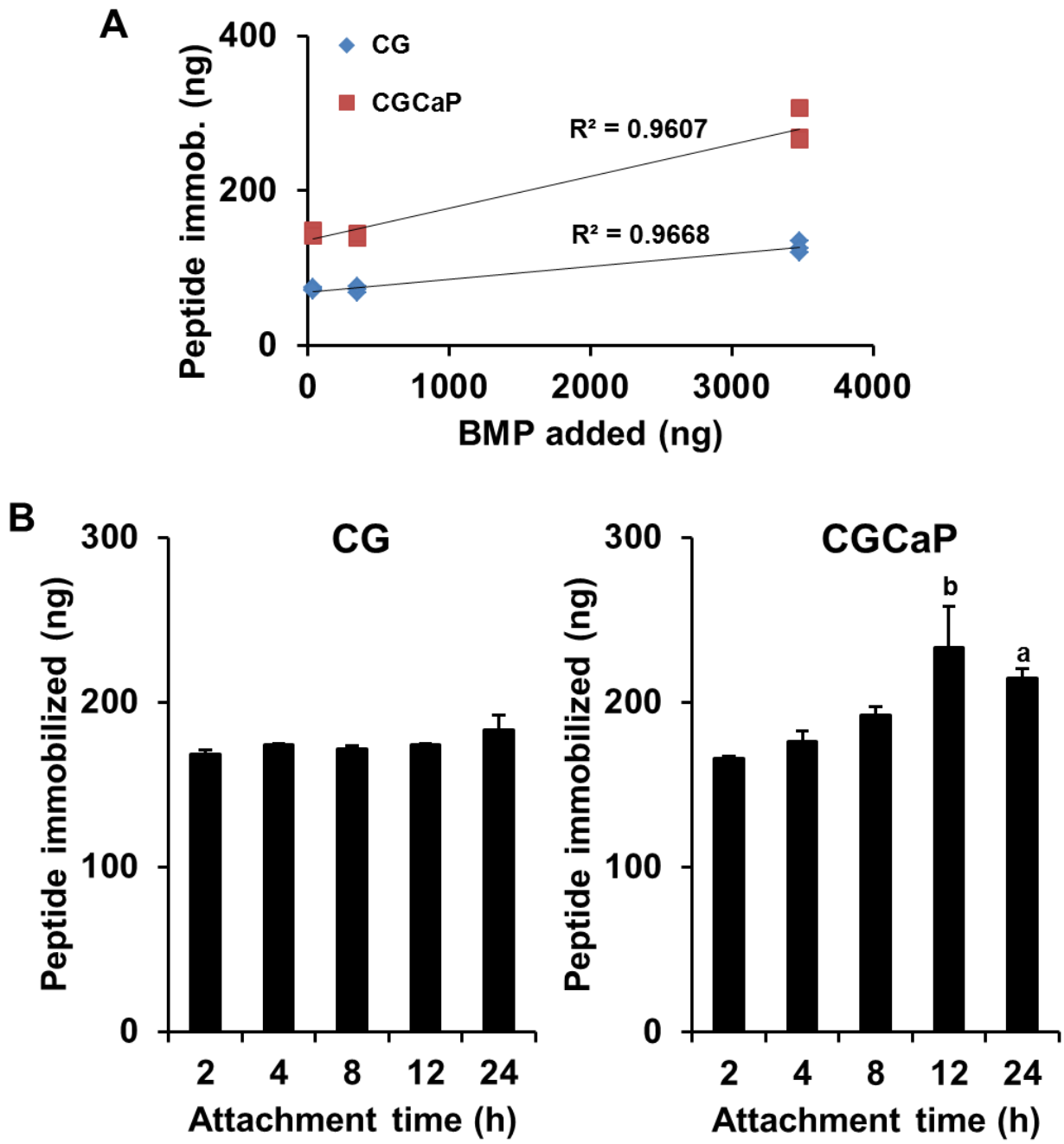

Figure C.3. BMP-2 peptide immobilization onto CG and CGCaP scaffolds *(n* = 3). A) BMP-2 peptide could be immobilized in both CG and CGCaP scaffolds, although the immobilization was more efficient in the HA-containing CGCaP group. B) Immobilization times of over 2 h did not significantly improve immobilization efficiency in CG, while minor improvement was seen in CGCaP scaffolds. *a*: significantly higher than 2 h group, *b*: significantly higher than 2 and 4 h groups.

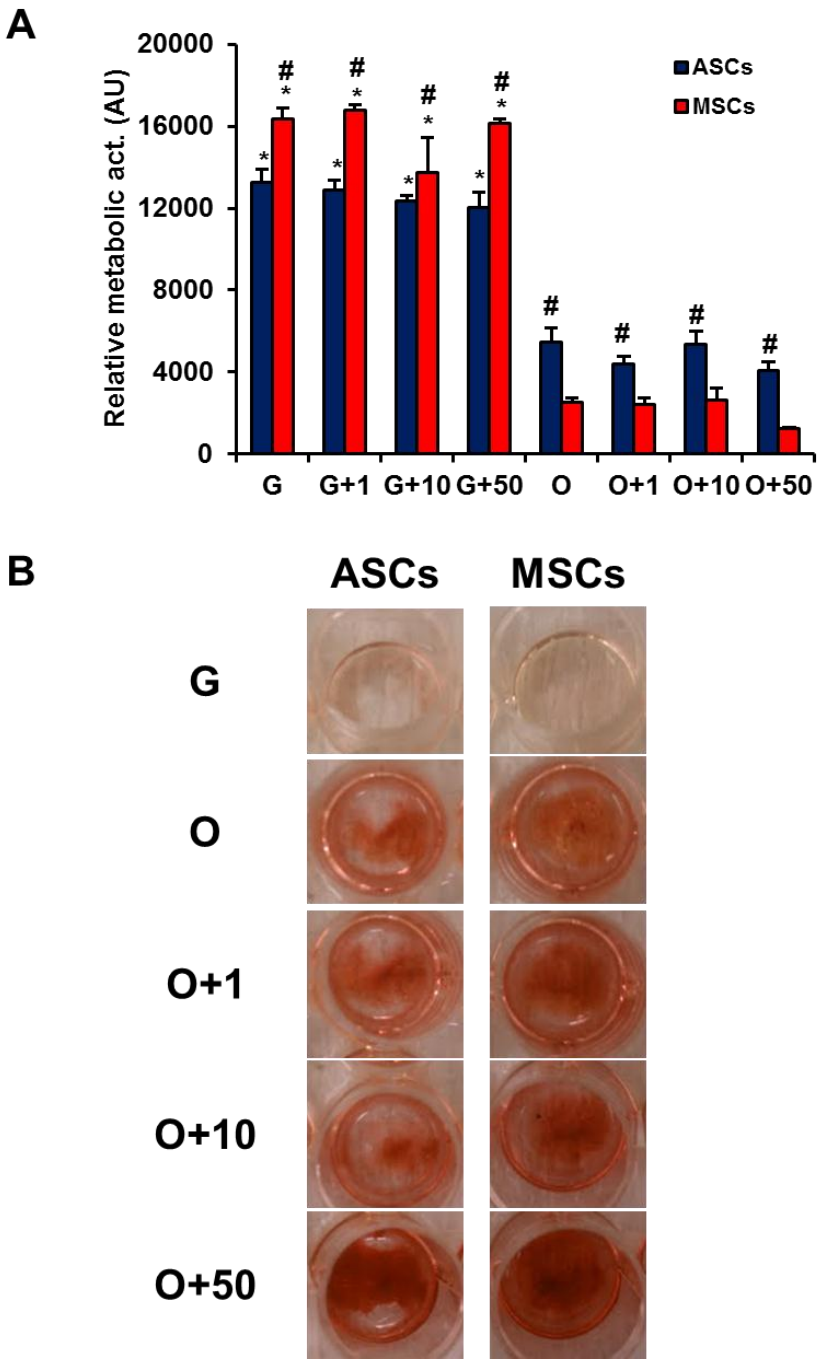

Figure C.4. Effect of BMP-2 peptide on osteogenic potential of ASCs and MSCs *(n* = 3). Cells were grown for 8 days in growth (G) or osteogenic (O) media with 0, 1, 10, or 50 μg of BMP-2 peptide added twice during the culture period. A) Metabolic activity of both ASCs and MSCs is lower in groups treated with osteogenic media, indicating onset of differentiation. B) Alizarin red staining illustrates increased mineral deposition by both ASCs and MSCs with increasing BMP-2 peptide dose. *: significantly higher than corresponding osteogenic group, #: significantly higher than ASC or MSC group for specific media treatment.

APPENDIX D: SCAFFOLD FABRICATION AND CHARACTERIZATION PROTOCOLS

D.1 CG suspension preparation protocol

Reference: (Yannas, Lee et al. 1989; O'Brien, Harley et al. 2004)

Reagents

- Collagen from bovine Achilles tendon (Sigma-Aldrich C9879); store at 4^{o}C
- Chondroitin sulfate sodium salt from shark cartilage (Sigma-Aldrich C4384); store at 4^{o}C
- Glacial acetic acid (Sigma-Aldrich 71251)
- Ethylene glycol (VWR BDH1125-4LP)
- Deionized water

Supplies and equipment

- Recirculating chiller (Fisher Isotemp Model 900)
- Rotor-stator (IKA 0593400)
- Disperser (IKA 3565001)
- Jacketed beaker (Ace Glass 5340-115)
- Freeze-dryer (VirTis Genesis)
- Dual range balance (Mettler Toledo XS105)
- Beakers
- Transfer pipets
- Parafilm

Procedure

*This procedure describes how to make 300 mL of 0.5% CG suspension. Scale collagen and GAG content appropriately to create different volumes of suspension.

1) Fill recirculating chiller with a 50/50 mix of ethylene glycol and deionized water, making sure that the cooling coils are completely immersed in the liquid. Set the recirculating chiller to 4^{o}C.

2) Attach recirculating chiller to jacketed beaker and give 20-30 min for temperature to equilibrate to 4^{o}C. Maintaining this temperature is important, as it will prevent the collagen from denaturing during the blending process.

3) Prepare a 0.05 M solution of acetic acid by adding 0.87 mL of glacial acetic acid to 300 mL of deionized water.

4) Weigh 1.5 g of collagen and add to the jacketed beaker.

5) Pour 250 mL of the 0.05 M acetic acid into the jacketed beaker.

6) Assemble the rotor-stator and attach it to the disperser. Lower the rotor-stator into the suspension. The rotor-stator should be vertical and centered in the beaker.

7) Blend the suspension at 15,000 rpm for 90 min at 4^{o}C. The height of the rotor-stator may need to be adjusted during the blending process: If the rotor-stator is positioned too high, the holes on its side will be visible; if it is too low, the suspension will bubble excessively. Periodically check to see if the rotor-stator is clogged with collagen; remove clogs with a spatula as needed.

8) Add 50 mL of 0.05 M acetic acid to a 50 mL centrifuge tube. Weigh out 0.133 g of chondroitin sulfate (GAG) and add to the centrifuge tube. Keep GAG solution in the refrigerator (4^{o}C) until next step.

9) Mix the GAG solution well and add it drop-wise with a transfer pipet to the collagen suspension while it is being mixed at 15,000 rpm at 4^{o}C. It may be necessary to stop and unclog the rotor-stator with a spatula during this process.

10) Once all of the GAG solution has been added, blend at 15,000 rpm for 90 min at 4^{o}C. Periodically check to ensure the rotor-stator is lowered to the correct depth, as the suspension will gradually become less viscous and creep up the sides of the jacketed beaker. Periodically check to see if the rotor-stator is clogged; remove clogs with a spatula as needed.

11) Store the suspension for 18-22 h at 4°C.

12) Degas the suspension in the freeze-dryer to remove any air bubbles prior to use. Make sure to run the 'Degas' program and let the condenser temperature reach < -50°C to prevent liquid from entering the vacuum pump. Degas suspension in a Parafilm-covered beaker until solution boils. Note that higher density suspensions typically have more trapped bubbles so adjust the degassing volume accordingly.

13) Store the suspension at 4^{o}C. Periodically check the CG suspension; if not homogenous, re-blend at 15,000 rpm for 30 min at 4^{o}C.

D.2 CGCaP suspension preparation protocol

Reference: (Harley, Lynn et al. 2010; Lynn, Best et al. 2010), Process Record No. PR OM-004 Preparation of Mineralized Slurry, BioUetikon and OrthoMimetics, Process Record No. PR OM-001 Preparation of 0.1456M Phosphoric Acid/0.037M Calcium Hydroxide, BioUetikon and OrthoMimetics.

Reagents

- Collagen from bovine Achilles tendon (Sigma-Aldrich C9879); store at 4^{o}C
- Chondroitin sulfate sodium salt from shark cartilage (Sigma-Aldrich C4384); store at 4^{o}C
- 0.1456M phosphoric acid / 0.037M calcium hydroxide buffer solution
    - 5.904 mL 85% phosphoric acid (Sigma-Aldrich P5811)
    - 570 mL deionized water
    - 1.644 g calcium hydroxide (Sigma-Aldrich 31219)
    - Add acid to water, then calcium hydroxide. Bring volume to 600 mL and adjust pH to 2.0-2.4. Solution is good for 3 months.
- Calcium hydroxide (Sigma-Aldrich, 31219)
- Calcium Nitrate Tetrahydrate (Sigma-Aldrich, 31218)
- Ethylene glycol (VWR BDH1125-4LP)
- Deionized water

Supplies and equipment

- Recirculating chiller (Fisher Isotemp Model 900)
- Rotor-stator (IKA 0593400)
- Disperser (IKA 3565001)
- Jacketed beaker (Ace Glass 5340-115)
- Freeze-dryer (VirTis Genesis)
- Dual range balance (Mettler Toledo XS105)
- pH meter
- Beakers
- Transfer pipets
- Centrifuge tubes
- Parafilm

Procedure

*This procedure describes how to make 300 mL of 40 wt% CGCaP suspension.

1) Setup the jacketed vessel, setting the water temperature to 4°C.

2) Add 5.7966 g collagen to the jacketed vessel. Then add 242.12mL of phosphate acid / calcium hydroxide buffer to the collagen. Set the blender to 15,000 rpm for 30 min, so that the collagen is submerged prior to hydration. Allow the collagen to hydrate for 18-22 h in the cooled jacketed vessel at 4°C. This mixture will become very viscous and difficult to blend.

3) Measure out 2.515 g of chondroitin sulfate and add it to 42.94mL of phosphate acid / calcium hydroxide buffer in a beaker. Then mix the buffer and the chondroitin (GAG solution), using a magnetic stirring bar, until fully dissolved.

4) Measure out 1.92 g calcium hydroxide and 1.17 g calcium nitrate tetrahydrate and place both in a 50 mL centrifuge tube. Add 15 mL of deionized water to the tube using a pipette. Then mix (vortex/shake) the solution to suspend the salts in the water.

5) Set the blender to 15,000 rpm and blend the hydrated collagen made in step 2 for 60 min.

6) Add the GAG solution prepared in step 3 to the hydrated collagen solution prepared in step 2 in 8 mL steps while mixing at 15,000 rpm. In between each 8 mL step, take care to prevent any clumping of the collagen/GAG with a spatula. With the additional volume, the slurry will mix better.

7) Blend this GAG / hydrated collagen solution at 15,000 rpm for 30 min.

8) Blend the collagen / GAG mixture at 200-800 rpm while adding the salts to maximize dispersion. Using a pipette, add the salt solution at a rate of 8mL/min to the collagen / GAG mixture, allowing time for blending after each volume. Then blend the slurry at 15,000 rpm for 30 min.

9) Stores the slurry for 18-22 h at 2-8°C before use. Periodically check the CG suspension; if not homogenous, re-blend at 15,000 rpm for 30 min at 4^{o}C.

D.3 CG membrane fabrication protocol

Reference: (Caliari, Ramirez et al. 2011)

Reagents

- CG suspension; store at 4^{o}C

Supplies and equipment

- Chemical fume hood (Lab Fabricators Company)
- Freeze-dryer (VirTis Genesis)
- Petri dishes (100 mm diameter)
- Beakers
- Parafilm
- Kimwipes

Procedure

*This procedure describes how to make 1x volume membranes. Scale suspension volume and solids content to adjust final membrane thickness.

1) Degas CG suspension in Parafilm-covered beaker by pulling vacuum inside freeze-dryer to remove all air bubbles. Make sure the condenser is at least -50°C or cooler before degassing.

2) Carefully pipette 25 mL of degassed suspension inside Petri dish. Wipe inside of Petri dish with Kimwipe before adding suspension to facilitate membrane removal from dish.

3) Leave open Petri dish to dry in chemical fume hood for 1-2 days. Cover Petri dish once the membrane is dry and store at room temperature until use.

D.4 Aligned CG scaffold fabrication protocol

Reference: (Caliari and Harley 2011; Caliari, Ramirez et al. 2011)

Reagents

- CG suspension; store at 4^{o}C
- Welch DirecTorr Gold synthetic pump oil (Fisher 01-184-105)

Supplies and equipment

- Freeze-dryer (VirTis Genesis)
- PTFE-copper freeze-drying mold
- Beakers
- Parafilm
- Aluminum foil

Procedure

*This procedure describes the fabrication of 15 mm tall aligned scaffolds (single and multi-compartment, with and without membrane shells). Check that oil is clean (not yellow) before and after each freeze-dryer run, replacing when necessary.

1) Degas CG suspension in Parafilm-covered beaker by pulling vacuum inside freeze-dryer to remove all air bubbles. Make sure the condenser is at least -50°C or cooler before degassing.

2) Begin to cool freeze-dryer shelves by running 'Tf = xx C shelf cool' program where xx is the desired freezing temperature (-10, -40, or -60°C).

3) If making scaffold-membrane composites, cut membranes to size, roll, and place in PTFE-copper freeze-drying mold holes.

4) Pipette 970 μL (8 mm diameter holes) or 540 μL (6 mm diameter holes) of suspension into each hole in PTFE-copper freeze-drying mold. For scaffold-membrane composites, allow suspension to hydrate membranes for 15-30 min at 4°C.

5) For multi-compartment scaffold fabrication, carefully pipet the first suspension (e.g. CG suspension, 360 μL) into mold wells. Then, add the second suspension (e.g. CGCaP suspension, 180 μL) carefully on top of the first suspension, taking care not to mix the two layers. Following pipetting, place entire mold on Kimwipe and allow to interdiffuse for 15-30 min at 4°C.

6) Cancel shelf cool program and place freeze-dryer mold on the pre-cooled shelf. Shut the freeze-dryer door and run program 'Aligned Tf = xx' where xx is the desired freezing temperature (-10, -40, or -60°C). A typical freeze-drying schedule is shown for the fabrication of an aligned -60°C scaffold:

Step	Temperature °C	Time, min	Ramp/Hold	Vacuum level, torr	PCM
Freezing hold	-60	60	H	~600	N/A
Drying ramp	0	60	R	0.2	150
Drying hold	0	5	H	0.2	1
Extra drying	0	60	H	0.2	0
Storage ramp	20	20	R	0.2	0
Storage hold	20	indefinite	H	0.2	0

PCM refers to the minimum reading difference between the Pirani and capacitance manometer pressure gauges that must be achieved before the program proceeds to the next step. In Pirani gauges, a filament in the gauge is heated so that it is at a constant temperature at a given pressure. As the pressure increases or decreases, the amount of gas molecule collisions with the filament will change accordingly. More collisions remove more heat from the filament, which lowers the temperature and changes the resistance of the filament. This change in resistance is converted to an output pressure. Pirani gauges are accurate to within around 7-8%. Capacitance manometers operate on the principle of a diaphragm held at a very low reference pressure (10^{-7} mbar) that is deflected by changing pressure. This deflection changes the capacitance between the diaphragm and an electrode. This change is converted to pressure. These gauges are extremely accurate (1%). These gauges will read different pressures because they operate on very different principles. The capacitance manometer is more accurate because it reads pressure independent of the type of gas present. In contrast, the temperature of the filament in the Pirani gauge is affected by the thermal conductivity of the colliding gas molecules. For example, the thermal conductivity of water vapor is higher than that of air, so for an equal number of water vapor and air molecules colliding with the filament the water vapor will remove more heat, causing the Pirani gauge to read a higher pressure than the true pressure. Once all of the water vapor is removed the differential between the two gauges should read about the same, indicating that the scaffolds are dry.

7) Once the program has reached the storage hold stage, the program can be cancelled and scaffolds can be removed from the freeze-dryer.

8) Allow scaffolds to sit in mold at room temperature for at least 1 h before carefully removing them with forceps and placing in an aluminum foil pouch. Label pouch with name, collagen type, collagen concentration, freeze date, freeze temperature, and any other relevant notes.

D.5 Isotropic CG scaffold fabrication protocol

Reference: (O'Brien, Harley et al. 2004)

Reagents

- CG suspension; store at 4°C
- Welch DirecTorr Gold synthetic pump oil (Fisher 01-184-105)

Supplies and equipment

- Freeze-dryer (VirTis Genesis)
- Aluminum, polysulfone tray molds (3" x 3")
- Beakers
- Parafilm
- Aluminum foil

Procedure

*This procedure describes the fabrication of 3 mm tall scaffold sheets. Check that oil is clean (clear, not yellowed) before and after each freeze-dryer run, replacing when necessary. It is easiest to replace the oil just after a run, when the oil is still warm.

1) Degas the CG suspension in a beaker (covered in Parafilm with small slits) by pulling vacuum inside freeze-dryer. Degas just to the boiling point to remove all air bubbles. Make sure the condenser is at least -50°C or cooler before degassing.

2) Add 24.25 mL of CG suspension to a 3" x 3" tray mold, ensuring that the suspension reaches the corners. Push any bubbles or unblended collagen to the edge using tweezers.

3) Open freeze- dryer door, place mold on center of shelf. Quickly close the freeze-dryer door and run the program 'Tf-xx No Hold' where xx is the desired freezing temperature (-10, -40, or -60°C). A typical schedule is shown below for the constant cooling fabrication method with a final freezing temperature of -10°C.

Step	**Temperature °C**	**Time, min**	**Ramp/Hold**	**Vacuum level, torr**	**PCM**
Freezing hold	20	5	H	~600	N/A
Freezing ramp	-10	30	R	~600	N/A
Freezing hold	-10	120	H	~600	N/A
Drying ramp	0	10	R	0.2	150
Drying hold	0	5	H	0.2	1
Extra drying	0	60	H	0.2	0
Storage ramp	20	20	R	0.2	0
Storage hold	20	indefinite	H	0.2	0

4) Once the program has reached the storage hold stage, the program can be cancelled and the array can be removed from the freeze-dryer.

5) Gently remove scaffold by lifting from corner with tweezers. Place scaffold in puffed aluminum pouch. Label pouch with name, collagen type, collagen concentration, freeze date, freeze temperature, and any other relevant notes. Clean mold by rubbing with soapy water; use 0.05 M acetic acid to remove collagen residue. Do not use cleaning brushes.

D.6 CG scaffold array fabrication protocol

Reference: (Caliari, Gonnerman et al. in preparation)

Reagents

- CG suspension; store at 4^{o}C
- Welch DirecTorr Gold synthetic pump oil (Fisher 01-184-105)

Supplies and equipment

- Freeze-dryer (VirTis Genesis)
- Macor array chip with removable aluminum and polysulfone bases
- Parafilm
- Aluminum foil
- Transfer pipets
- Glass and plastic Petri dishes

Procedure

*This procedure describes the fabrication of scaffold arrays. Check that oil is clean (clear, not yellowed) before and after each freeze-dryer run, replacing when necessary. It is easiest to replace the oil just after a run, when the oil is still warm.

1) Degas the CG suspension in a beaker (covered in Parafilm with small slits) by pulling vacuum inside freeze-dryer. Degas just to the boiling point to remove all air bubbles. Make sure the condenser is at least -50°C or cooler before degassing.

2) Run freeze-dryer using protocols described in either D.4 or D.5, depending on whether you are fabricating aligned or isotropic scaffolds.

3) Assemble scaffold array and tape down on freeze-dryer shelf, making sure that the entire mold bottom is contacting the shelf.

4) Add degassed CG suspension to the array using a transfer pipet, adding an excess layer on top connecting all of the nodes to promote easier post-fabrication handling and to account for any leaking during freeze-drying.

5) Run freeze-drying program as specified in protocols D.4 or D.5. Once the program has reached the storage hold stage, the program can be cancelled and the array can be removed from the freeze-dryer.

6) Carefully disassemble mold by unscrewing one base at a time, taking care not to unnecessarily tear the collagen film layer. Remove bases one at a time with a horizontal sliding motion. Place array mold in a glass Petri dish, and place scaffold array in a plastic Petri dish for storage. Label dish with name, collagen type, collagen concentration, freeze date, freeze temperature, and any other relevant notes.

7) Clean mold by rubbing with soapy water; use 0.05 M acetic acid to remove collagen residue. Do not use cleaning brushes.

D.7 Making CG scaffold arrays with gradient maker protocol

Reference: (Caliari, Gonnerman et al. in preparation)

Reagents

- CG suspension; store at 4^{o}C

Supplies and equipment

- Gradient maker (CBS Scientific GM-20)
- 'Medium' mini-peristaltic pump (CBS Scientific MPP-100)
- Freeze-dryer (VirTis Genesis)
- Stir plate
- Macor array chip with removable aluminum and polysulfone bases

Procedure

1) Set gradient maker on stir plate and connect to peristaltic pump. Make sure small stir bar is in place in left column.

2) Fill gradient maker with water, open valve, set stir plate on setting '1' and flush with water using 'Prime' pump setting, speed '0'.

3) Make sure all moisture is pumped out of gradient maker; wait some extra time but try not to run pump dry for very long. Turn off pump, turn off stir plate, and close valve.

4) Carefully mix degassed slurry with biomolecule of interest so as not to introduce bubbles. Load blank slurry on left (Column A) and mixed slurry on right (Column B). More slurry needs to be loaded into right column (1 mL on left, 1.5 mL on right for 12 point gradient, 0.65 mL and 1 mL for 8 point gradient.

5) Once slurries are loaded, open valve and turn on stir plate. Make sure that slurry on right has traveled through connecting channel and contacting column on left. If it isn't happening, lightly flick right side of gradient maker to encourage movement.

6) Run pump 'Forward' on speed '0', setting 'Prime' until slurry reaches close to end of tube. Change setting to 'Slow' and add 2 drops of slurry per gradient node.

7) Freeze-dry array as before.

8) Flush out gradient maker with copious amount of water.

9) Clean out gradient maker with rolled up paper towel, taking care to remove little pieces of slurry without losing stir bar.

D.8 Preparing scaffolds for Flexcell® bioreactor protocol

Reference: (Boerboom, Rubbens et al. 2008)

Reagents

- PBS
- Cell culture media; store at 4^{o}C

Supplies and equipment

- Poly(dimethylsiloxane) (PDMS)
- Flexcell® plates (Flexcell TT-4001U)
- 6-well plates (Fisher 08-772-1B)
- Dual range balance (Mettler Toledo XS105)
- Pipet tips

Procedure

* Note: all steps should be performed in the laminar flow hood unless otherwise noted.

1) Prepare PDMS for scaffold immobilization. Use a monomer: curing agent ratio of 10:1. About 2 g of PDMS is needed per 6-well plate.

2) Using a 1 mL pipet tip, carefully paint a thin rectangular strip of PDMS in the center of each well of plate.

3) UV irradiate PDMS-treated plates in laminar flow hood for 30 min.

4) Turn off UV and add two dry scaffold pieces (6 mm diameter by 10 mm length) to each well, being careful to maintain symmetry for multi-compartment scaffolds. Make sure that the full length of each scaffold is contacting the partially-cured PDMS.

5) Place scaffold-loaded plates in incubator and keep at 37°C under polymerization is complete (usually at least 2 h).

6) Hydrate, crosslink, and perform cell culture on scaffolds as normal.

D.9 DHT crosslinking protocol

Reference: (Yannas, Lee et al. 1989; Harley, Leung et al. 2007)

Supplies and equipment

- Sterile air filter (Millipore SLGP033RS)
- Vacuum oven (Welch Vacuum, Fisher 13-262-52)

Procedure

*Note: vacuum pump oil levels and integrity of vacuum fittings should be checked periodically. Also, change sterile air filter on 'Purge' line regularly. Remember that scaffolds containing CGCaP content should be oven treated as this will cause irreversible dehydration of the calcium phosphate phase from brushite to monetite.

1) Turn on vacuum oven and set desired temperature (usually 105°C).

2) Once vacuum oven has reached temperature set point, place CG scaffolds in opened aluminum pouches carefully inside the oven. Close the oven door.

3) Completely open the 'Vacuum' valve on the lower right front face of the vacuum oven while completely closing the 'Purge' valve.

4) Turn on the vacuum pump and make sure vacuum is pulled to a sufficiently low level (< 1 in Hg). Allow scaffolds to crosslink for 24 h.

5) After crosslinking is complete turn off the vacuum pump, close the 'Vacuum' valve, open the 'Purge' valve, carefully remove scaffolds from the oven, and seal the aluminum pouches. Store sealed scaffolds (now sterile) in desiccator until time of use.

D.10 EDAC crosslinking protocol

Reference: (Olde Damink, Dijkstra et al. 1996; Harley, Leung et al. 2007; Caliari, Ramirez et al. 2011)

Reagents

- 1-ethyl-3-[3-dimethylaminopropyl]carbodiimide hydrochloride (EDAC, Sigma-Aldrich E7750); store at -20^{o}C
- N-hydroxysulfosuccinimide (NHS, Sigma-Aldrich H7377); store in desiccator
- Sterile phosphate-buffered saline (PBS)
- 100% ethanol

Supplies and equipment

- 6-well plates (Fisher 08-772-1B)
- 50 mL centrifuge tubes (Fisher 14-432-22)
- Syringe and syringe filter (Fisher 148232A)
- MTS 2/4 digital microtiter shaker (IKA 3208001)
- Dual range balance (Mettler Toledo XS105)
- Razor blades

Procedure

* Note: all steps should be performed in the laminar flow hood unless otherwise noted.

1) Cut scaffold or membrane samples to be crosslinked using a razor blade.

2) Transfer scaffold or membrane pieces to sterile centrifuge tube, remove from laminar flow hood, and weigh pieces on dual range balance.

3) Hydrate pieces in 100% ethanol overnight.

4) Rinse pieces several times in PBS and then let soak in PBS for 24 h before crosslinking.

5) Determine the EDAC and NHS concentrations to be used in crosslinking solution. The sample calculations in this protocol are done with a 5:2:1 EDAC:NHS:COOH molar ratio where COOH is carboxylic acid groups in CG material based on a conversion factor of 1.2 mmol COOH per gram of collagen (Olde Damink, Dijkstra et al. 1996). The mass of EDAC and NHS required can be calculated as follows:

$$M_{EDAC} = M_{scaffold}\left(0.0012\frac{mol_{COOH}}{g_{collagen}}\right)\left(\frac{5mol_{EDAC}}{1mol_{COOH}}\right)\left(\frac{191.7g_{EDAC}}{1mol_{EDAC}}\right) \quad \textbf{(Equation D.1)}$$

$$M_{NHS} = M_{scaffold}\left(0.0012\frac{mol_{COOH}}{g_{collagen}}\right)\left(\frac{2mol_{NHS}}{1mol_{COOH}}\right)\left(\frac{116.0g_{NHS}}{1mol_{NHS}}\right) \quad \textbf{(Equation D.2)}$$

6) Mix the EDAC and NHS in sterile PBS. Approximately 1 mL of solution will be needed per scaffold piece (6-8 mm diameter, 3-5 mm thick).

7) In the laminar flow hood, sterile filter the solution and add to 6-well plates.

8) Add scaffolds in crosslinking solution and place well plate on shaker on bench 6. Allow scaffolds to crosslink under moderate shaking for 1.5 h. Crosslinking time should be increased for less permeable constructs such as membranes and high solids content scaffolds.

9) Remove EDAC/NHS solution and rinse scaffolds in sterile PBS under moderate shaking for 10-15 min.

10) Remove first PBS wash solution and rinse scaffolds in fresh PBS under moderate shaking for an additional 30-45 min. Store in fresh sterile PBS at 4°C until use.

D.11 Scaffold glycolmethacrylate embedding protocol

Reference: (O'Brien, Harley et al. 2004; O'Brien, Harley et al. 2005; Caliari and Harley 2011)

Reagents

- JB-4 embedding solution A (100 mL); store at 4^{o}C for up to 1 week
    - 100 mL JB-4 embedding solution A (monomer) (Polysciences 0226A-800)
    - 1.25 g JB-4 catalyst (benzoyl peroxide, plasticized) (Polysciences 02618-12); store at 4^{o}C
- JB-4 embedding solution B (accelerator) (Polysciences 0226B-30)
- 100% ethanol

Supplies and equipment

- Polyethylene molding cup trays (Polysciences 16643A-1)
- JB-4 plastic block holders (Polysciences 15899-50)
- DryFast vacuum pump (Welch Vacuum 2014B-01)
- Pyrex desiccator (Fisher 08-626B)
- Serological pipettes (Fisher 13-678-14B)
- 6-well plates (08-772-1B)
- Chemical fume hood (Lab Fabricators Company)
- Razor blades

Procedure

1) Cut scaffold pieces to be analyzed using a razor blade. 15 mm aligned scaffolds are typically cut in thirds. Both transverse and longitudinal sections should be cut for analysis.

2) Place samples in 6-well plates and hydrate in 100% ethanol under vacuum inside desiccator for 24 h.

3) Add hydrated samples to JB-4 embedding solution A under vacuum inside desiccator at 4^{o}C. After 24 h, replace with fresh JB-4 embedding solution A and hold under vacuum inside desiccator at 4^{o}C for an additional 48 h.

4) Mix 25 mL of JB-4 embedding solution A with 1 mL of JB-4 B solution and pipette ~3.5 mL into each well of the plastic embedding mold.

5) Place each sample into a well. The JB-4 mixture will polymerize quickly (~30 min) so make sure the samples stay in the proper orientation.

6) Place one labeled plastic stub in each well once the JB-4 mixture has become sufficiently viscous that the stubs don't completely sink.

7) Keep embedding mold at 4^{o}C overnight to allow polymerization to complete. Store samples at 4^{o}C until use.

D.12 Scaffold pore size analysis: aniline blue staining, image acquisition, and linear intercept analysis protocol

Reference: (O'Brien, Harley et al. 2004; O'Brien, Harley et al. 2005; Caliari and Harley 2011)

Reagents

- Aniline blue solution (100 mL)
    - 2.5 g aniline blue (Fisher AC40118-0250)
    - 2 mL glacial acetic acid (Sigma-Aldrich 71251)
    - 100 mL deionized water
    - Mix well, filter before use
- 1% Acetic acid (100 mL)
    - 1 mL glacial acetic acid (Sigma-Aldrich 71251)
    - 99 mL deionized water
- Permount mounting medium (Fisher SP15-100)
- 95%, 100% ethanol

Supplies and equipment

- Optical microscope with camera (Leica Microsystems DMIL LED with DFC295 camera)
- Scion Image analysis software (Scion Co)
- Beakers
- Cover slips

Aniline blue staining procedure

1) Obtain slides of serially sectioned embedded scaffolds from histologist.

2) Dip slides in aniline blue solution for 2-4 min. Analyze in groups of 12-18 slides.

3) Place slides in 1% acetic acid for 1 min.

4) Dip each slide several times in 95% ethanol until most of background staining goes away.

5) Dip each slide several times in 100% ethanol to complete rinse and allow slides to dry.

6) Mount each sample with 1 drop of Permount per slide section. Firmly press cover slip onto slide so as not to introduce any air bubbles. Allow slides to dry for 24 h before further analysis.

Image acquisition procedure

1) Visualize embedded, sectioned, and stained scaffold samples using optical microscope.

2) Acquire three tiff images for each transverse section and two images for each smaller longitudinal section using camera.

Linear intercept analysis procedure

1) Transfer images for analysis to a folder with a short path length from C.

2) Open Scion Image. Under 'Special' menu select 'Load macros' and open the 'pore characterization macros Steven' file.

3) Open tiff file in Scion Image. Under 'Edit' menu, select 'Invert,' then under 'Options' menu select 'Threshold.' Adjust the threshold values to optimize the visualization of the scaffold strut network. Any extraneous spots can be cleaned with eraser tool although no artifacts under 5 pixels will be detected by the pore analysis macro.

4) Under the 'Process' menu select 'Make Binary' under 'Binary' sub-menu. Save the edited tiff file.

5) Under the 'Analysis' menu select 'Set Scale.' For images taken at 4x magnification the correct scale is 347 pixels per mm. At 10x magnification the scale is 867 pixels per mm.

6) Select an area of the image to be analyzed with the oval drawing tool. Try to select as much of the viable image as possible.

7) Under the 'Special' menu, run the 'Linear Intercept' macro. The distance between the pore walls along lines at five degree angle increments from the center of the selected region are calculated. Next, run the 'Plot Intercepts' macro. This macro transforms the average distance between struts to a best-fit ellipse and calculates linear intercept coefficients C0, C1, and C2 for the ellipse.

8) Transfer C0, C1, and C2 data to spreadsheet to calculate minor (*a*) and major (*b*) axes of best-fit ellipse using the following equations:

$$a = \frac{1}{\sqrt{C_0 + \sqrt{C_1^2 + C_2^2}}} \qquad \textbf{(Equation D.3)}$$

$$b = \sqrt{\frac{\sqrt{C_1^2 + C_2^2}}{C_0\sqrt{C_1^2 + C_2^2} + C_2^2 - C_1^2}} \qquad \textbf{(Equation D.4)}$$

$$AspectRatio = \frac{b}{a} \qquad \textbf{(Equation D.5)}$$

9) Calculate the mean pore size (*d*) from values of the major and minor axes of the best-fit ellipse. To account for the fact that pores were not sectioned through their maximal cross-section the mean pore size is corrected by a factor of 1.5. To convert the pore radius to diameter the mean pore size is additionally multiplied by 2 for a total correction factor of 3:

$$d = 3\sqrt{\frac{a^2 + b^2}{2}}$$ (**Equation D.6**)

Linear intercept macro code

```
macro 'Linear Draw'
{This macro is used for testing different line drawing routines for use
with the macro 'Linear Intercept'}
var
  left,top,width,height,MinDim,nx,ny,i,j,k:integer;
                    ThetaStep,NSteps,PI,x1,x2,y1,y2,dy,dx:real;
  Theta,valx,valy,plength,scale,AspectRatio:real;
   IntLength,LineSum:real;
  Intercepts:integer;
   switch,indicator:boolean;
   unit:string;
begin
   GetRoi(left,top,width,height);
   if width=0 then begin
      PutMessage('Selection required.');
      exit;
   end;
   if width<height  then MinDim:=width
      else MinDim:=height;
   PI:=3.141592654;
   GetScale(scale,unit,AspectRatio);
   NSteps:=GetNumber('Enter theta steps between 0 and 90 deg.',3,0);
   ThetaStep:=PI/(2*NSteps);
   for j:=0 to 2*NSteps-1 do begin
      x1:=left;
      y1:=top;
                              Theta:=j*ThetaStep;
     nx:=5*sin(Theta)*width/height;
     ny:=5*abs(cos(Theta));
     for i:=0 to nx do begin
       if Theta=0 then begin
                  x1:=left;
                  x2:=x1+width;
       end  else begin
                  x1:=left+(width*i/(nx+1))+width/(2*(nx+1));
                  x2:=x1+(height*cos(Theta)/sin(Theta));
                end;
                                        y2:=top+height;
                                                                  if x2>=left+width then begin
         x2:=left+width;
         y2:=y1+(x2-x1)*sin(Theta)/cos(Theta);
```

```
      end  else if x2<left then begin
                     x2:=left;
                    if Theta>PI/2 then y2:=y1+(x2-x1)*sin(Theta)/cos(Theta);
                   end;
       {plength is the length of the line to be drawn in pixels}
                                                          plength:=sqrt(sqr(x2-x1)+sqr((y2-
y1)/AspectRatio));
      valx:=x1;
                                                          valy:=y1;
      dx:=(x2-x1)/plength;
      dy:=(y2-y1)/plength;
      switch:=true;
      if plength>=MinDim then begin
                                                          for k:=0 to plength do
           PutPixel(x1+k*dx,y1+k*dy,255);
       end;
    end;
    for i:=1 to ny do begin
      if Theta<=PI/2 then begin
              x1:=left;
              x2:=left+width
        end  else begin
              x1:=left+width;
              x2:=left;
       end;
      y1:=top+height*i/(ny+1);
      y2:=y1+(width*sin(Theta)/abs(cos(Theta)));
                                                          if y2>top+height then begin
        y2:=top+height;
        x2:=x1+((y2-y1)*cos(Theta)/sin(Theta));
       end;
       {plength is the length of the line to be drawn in pixels}
                                                          plength:=sqrt(sqr(x2-x1)+sqr((y2-
y1)/AspectRatio));
      valx:=x1;
                                                          valy:=y1;
      dx:=(x2-x1)/plength;
      dy:=(y2-y1)/plength;
      switch:=true;
      if plength>=MinDim then begin
                                                          for k:=0 to plength do
          PutPixel(x1+k*dx,y1+k*dy,255);
      end;  {if}
    end;{i}
  end; {j}
end;
```

```
macro 'Linear Intercept'
{This macro measures the linear intercept distance over a giver ROI
at intervals of angle}
var
  left,top,width,height,MinDim,nx,ny,i,j,k:integer;
                    ThetaStep,NSteps,PI,x1,x2,y1,y2,dy,dx:real;
  Theta,valx,valy,plength,scale,AspectRatio:real;
   IntLength,LineSum,dummy:real;
  Intercepts:integer;
   switch,indicator:boolean;
   unit:string;
begin
   SetOptions('User1;User2');
   GetRoi(left,top,width,height);
   if width=0 then begin
      PutMessage('Selection required.');
      exit;
   end;
   if width<height  then MinDim:=width
      else MinDim:=height;
   PI:=3.141592654;
   GetScale(scale,unit,AspectRatio);
   NSteps:=18;{GetNumber('Enter # steps between 0 and 90 deg.',3,0);}
   ThetaStep:=PI/(2*NSteps);

{block out next line when doing cumulative measurements}

   SetCounter(2*NSteps);
   SetUser1Label('Theta(rad)');
   SetUser2Label('Lx10^3');
   for j:=0 to 2*NSteps-1 do begin
      LineSum:=0;
      Intercepts:=0;
      x1:=left;
      y1:=top;
                              Theta:=j*ThetaStep;
     nx:=10*sin(Theta)*width/height;
     ny:=10*abs(cos(Theta));
      for i:=0 to nx do begin
        if Theta=0 then begin
                  x1:=left;
                  x2:=x1+width;
        end  else begin
```

```
            x1:=left+(width*i/(nx+1))+width/(2*(nx+1));
            x2:=x1+(height*cos(Theta)/sin(Theta));
          end;
                                    y2:=top+height;
                                                        if x2>=left+width then begin
      x2:=left+width;
      y2:=y1+(x2-x1)*sin(Theta)/cos(Theta);
    end  else if x2<left then begin
                 x2:=left;
                 if Theta>PI/2 then   y2:=y1+(x2-x1)*sin(Theta)/cos(Theta);
                end;
     {plength is the length of the line to be drawn in pixels}
                                                        plength:=sqrt(sqr(x2-x1)+sqr((y2-
y1)/AspectRatio));
    valx:=x1;
                                                        valy:=y1;
    dx:=(x2-x1)/plength;
    dy:=(y2-y1)/plength;
    switch:=true;
    if plength>=MinDim then begin
    LineSum:=LineSum+(plength/scale);
                                                        for k:=0 to plength do begin
        if GetPixel(x1+k*dx,y1+k*dy)>0
            then indicator:=true
            else indicator:=false;
        if (switch=true) and (indicator=true) then begin
           Intercepts:=Intercepts+1;
           switch:=false;
        end;
        if  (indicator=false) then switch:=true;
      end;
   end;
  end;
 for i:=1 to ny do begin
    if Theta<=PI/2 then begin
            x1:=left;
            x2:=left+width
      end  else begin
            x1:=left+width;
            x2:=left;
      end;
    y1:=top+height*i/(ny+1);
    y2:=y1+(width*sin(Theta)/abs(cos(Theta)));
                                                        if y2>top+height then begin
      y2:=top+height;
      x2:=x1+((y2-y1)*cos(Theta)/sin(Theta));
```

```
        end;
        {plength is the length of the line to be drawn in pixels}
                                                        plength:=sqrt(sqr(x2-x1)+sqr((y2-
y1)/AspectRatio));
        valx:=x1;
                                                        valy:=y1;
        dx:=(x2-x1)/plength;
        dy:=(y2-y1)/plength;
        switch:=true;
        if plength>=MinDim then begin
        LineSum:=LineSum+(plength/scale);
                                                        for k:=0 to plength do begin
             if GetPixel(x1+k*dx,y1+k*dy)>0
                  then indicator:=true
                  else indicator:=false;
             if (switch=true) and (indicator=true) then begin
                Intercepts:=Intercepts+1;
                switch:=false;
             end;
             if  (indicator=false) then switch:=true;
          end;
       end;
     end;{i}
    IntLength:=LineSum/Intercepts;
   dummy:=rUser2[j+1];
    rUser1[j+1]:=180*Theta/PI;

{to do cumulative measurements, type in 'dummy+ before Intlength in the next line}

    rUser2[j+1]:=IntLength*1000;
   end; {j}
   ShowResults;
end;

macro 'Linear Intercept +'
{This macro measures the linear intercept distance over a giver ROI
at intervals of angle}
var
  left,top,width,height,MinDim,nx,ny,i,j,k:integer;
                    ThetaStep,NSteps,PI,x1,x2,y1,y2,dy,dx:real;
  Theta,valx,valy,plength,scale,AspectRatio:real;
    IntLength,LineSum,dummy:real;
  Intercepts:integer;
    switch,indicator:boolean;
    unit:string;
begin
```

```
  SetOptions('User1;User2');
  GetRoi(left,top,width,height);
  if width=0 then begin
    PutMessage('Selection required.');
    exit;
  end;
  if width<height  then MinDim:=width
    else MinDim:=height;
  PI:=3.141592654;
  GetScale(scale,unit,AspectRatio);
  NSteps:=18;{GetNumber('Enter # steps between 0 and 90 deg.',3,0);}
  ThetaStep:=PI/(2*NSteps);

{block out next line when doing cumulative measurements}

  {SetCounter(2*NSteps);}
  SetUser1Label('Theta(rad)');
  SetUser2Label('Lx10^3');
  for j:=0 to 2*NSteps-1 do begin
    LineSum:=0;
    Intercepts:=0;
    x1:=left;
    y1:=top;
                          Theta:=j*ThetaStep;
   nx:=10*sin(Theta)*width/height;
   ny:=10*abs(cos(Theta));
    for i:=0 to nx do begin
      if Theta=0 then begin
               x1:=left;
               x2:=x1+width;
      end  else begin
               x1:=left+(width*i/(nx+1))+width/(2*(nx+1));
               x2:=x1+(height*cos(Theta)/sin(Theta));
             end;
                                    y2:=top+height;
                                                        if x2>=left+width then begin
        x2:=left+width;
        y2:=y1+(x2-x1)*sin(Theta)/cos(Theta);
      end  else if x2<left then begin
                  x2:=left;
                 if Theta>PI/2 then   y2:=y1+(x2-x1)*sin(Theta)/cos(Theta);
                end;
       {plength is the length of the line to be drawn in pixels}
                                                        plength:=sqrt(sqr(x2-x1)+sqr((y2-
y1)/AspectRatio));
      valx:=x1;
```

```
                                                        valy:=y1;
      dx:=(x2-x1)/plength;
      dy:=(y2-y1)/plength;
      switch:=true;
      if plength>=MinDim then begin
      LineSum:=LineSum+(plength/scale);
                                                        for k:=0 to plength do begin
           if GetPixel(x1+k*dx,y1+k*dy)>0
               then indicator:=true
               else indicator:=false;
           if (switch=true) and (indicator=true) then begin
              Intercepts:=Intercepts+1;
              switch:=false;
           end;
           if  (indicator=false) then switch:=true;
         end;
       end;
     end;
    for i:=1 to ny do begin
      if Theta<=PI/2 then begin
              x1:=left;
              x2:=left+width
        end  else begin
              x1:=left+width;
              x2:=left;
        end;
      y1:=top+height*i/(ny+1);
      y2:=y1+(width*sin(Theta)/abs(cos(Theta)));
                                                        if y2>top+height then begin
        y2:=top+height;
        x2:=x1+((y2-y1)*cos(Theta)/sin(Theta));
       end;
       {plength is the length of the line to be drawn in pixels}
                                                        plength:=sqrt(sqr(x2-x1)+sqr((y2-
y1)/AspectRatio));
      valx:=x1;
                                                        valy:=y1;
      dx:=(x2-x1)/plength;
      dy:=(y2-y1)/plength;
      switch:=true;
      if plength>=MinDim then begin
      LineSum:=LineSum+(plength/scale);
                                                        for k:=0 to plength do begin
           if GetPixel(x1+k*dx,y1+k*dy)>0
               then indicator:=true
               else indicator:=false;
```

```
            if (switch=true) and (indicator=true) then begin
               Intercepts:=Intercepts+1;
               switch:=false;
            end;
            if  (indicator=false) then switch:=true;
          end;
       end;
     end;{i}
    IntLength:=LineSum/Intercepts;
   dummy:=rUser2[j+1];
    rUser1[j+1]:=180*Theta/PI;

{to do cumulative measurements, type in 'dummy+ before Intlength in the next line}

    rUser2[j+1]:=dummy+IntLength*1000;
   end; {j}
   ShowResults;
end;

Macro 'Plot Intercepts'
{This macro plots the linear intercept distance as a function of angle
in cylindrical coordinates
It then finds the best-fit ellipse to a set of linear intercept distance vs. angle data
using multiple linear regression of the equation Y=C0+C1*X+C2*Z, where
Y=1/L^2 ,  where L is one half  the linear intercept distance at Theta
X=cosine(2*Theta),    Z=sine(2*Theta)
C0=(Mii+Mjj)/2 , C1=(Mii-Mjj)/2 , C2=Mij.
The objective is to solve for M11, Mjj, and Mij
The best-fit ellipse it then plotted on top of the linear intercept measurements}

var
   left,top,width,height,X0,Y0,X1,Y1,i,n:integer;
   pscale,aspectRatio,dx1,dx2,dy1,dy2,maxdim:real;
   unit:string;
  sumX,sumY,sumZ,sumXZ,sumXY,sumYZ,sumZsqr,sumXsqr:real;
  C0,C1,C2,Mii,Mjj,Mij,Y,X,Z,PI,Theta1,Theta2,L1,L2:real;

begin
  PI:=3.141592654;
 SaveState;
  SetForegroundColor(255);
  SetBackgroundColor(0);
  width:=400;
  height:=400;
  maxdim:=0;
  for i:=1 to rCount do begin
```

```
   if rUser2[i]>maxdim then maxdim:=rUser2[i];
end;
pscale:=.8*(width+height)/(2*maxdim);
SetNewSize(width,height);
MakeNewWindow('Linear Intercepts vs. Theta');
SetLineWidth(1);
X0:=(width/2);
Y0:=(height/2);
MakeLineROI(0,Y0,width,Y0);
Fill;
MakeLineROI(X0,0,X0,height);
Fill;
 for i:=1 to rCount do begin
   dx1:=pscale*0.5*rUser2[i]*cos(rUser1[i]*PI/180);
   dy1:=pscale*0.5*rUser2[i]*sin(rUser1[i]*PI/180);
   if i<rCount then begin
      dx2:=pscale*0.5*rUser2[i+1]*cos(rUser1[i+1]*PI/180);
      dy2:=pscale*0.5*rUser2[i+1]*sin(rUser1[i+1]*PI/180);
   end else begin
      dx2:=-pscale*0.5*rUser2[1]*cos(rUser1[1]*PI/180);
      dy2:=-pscale*0.5*rUser2[1]*sin(rUser1[1]*PI/180);
   end;
   MoveTo(X0+dx1,Y0+dy1);
   LineTo(X0+dx2,Y0+dy2);
   MoveTo(X0-dx1,Y0-dy1);
   LineTo(X0-dx2,Y0-dy2);
end;
n:=rCount;
sumX:=0;
sumY:=0;
sumZ:=0;
sumXY:=0;
sumYZ:=0;
sumXZ:=0;
sumZsqr:=0;
sumXsqr:=0;
for i:=1 to n do begin
   Y:=1/(sqr(rUser2[i]/2));
   X:=cos(2*PI*rUser1[i]/180);
   Z:=sin(2*PI*rUser1[i]/180);
   sumX:=sumX+X;
   sumY:=sumY+Y;
   sumZ:=sumZ+Z;
   sumXY:=sumXY+(X*Y);
   sumYZ:=sumYZ+(Y*Z);
   sumXZ:=sumXZ+(X*Z);
```

```
    sumZsqr:=sumZsqr+sqr(Z);
    sumXsqr:=sumXsqr+sqr(X);
  end;
  C1:=((sumXY*sumZsqr)-(sumXZ*sumYZ))/((sumXsqr*sumZsqr)-sqr(sumXZ));
  C2:=((sumYZ*sumXsqr)-(sumXY*sumXZ))/((sumXsqr*sumZsqr)-sqr(sumXZ));
  C0:=(sumY/n)-C1*(sumX/n)-C2*(sumZ/n);
  for i:=1 to rCount do begin
    Theta1:=rUser1[i]*PI/180;
    if i<rCount then Theta2:=rUser1[i+1]*PI/180
     else Theta2:=rUser1[1]*PI/180;
    L1:=1/sqrt(C0+C1*cos(2*Theta1)+C2*sin(2*Theta1));
    L2:=1/sqrt(C0+C1*cos(2*Theta2)+C2*sin(2*Theta2));
    dx1:=pscale*L1*cos(Theta1);
    dy1:=pscale*L1*sin(Theta1);
    if i<rCount then begin
       dx2:=pscale*L2*cos(Theta2);
       dy2:=pscale*L2*sin(Theta2);
     end else begin
       dx2:=-pscale*L2*cos(Theta2);
       dy2:=-pscale*L2*sin(Theta2);
    end;
    MoveTo(X0+dx1,Y0+dy1);
    LineTo(X0+dx2,Y0+dy2);
    MoveTo(X0-dx1,Y0-dy1);
    LineTo(X0-dx2,Y0-dy2);
  end;
NewTextWindow('Results');
write(C0:8:8', ');
write(C1:8:8', ');
write(C2:8:8);
end;


macro 'Count Black and White Pixels [B]';
{
Counts the number of black and white pixels in the current
selection and stores the counts in the User1 and User2 columns.
}
begin
  RequiresVersion(1.44);
  SetUser1Label('Black');
  SetUser2Label('White');
  Measure;
  rUser1[rCount]:=histogram[255];
  rUser2[rCount]:=histogram[0];
  UpdateResults;
```

```
end;


macro 'Compute Percent Black and White';
{
Computes the percentage of back and white pixels in the
current selection. This macro only works with binary images.
}
var
  nPixels,mean,mode,min,max:real;
begin
  RequiresVersion(1.44);
  SetUser1Label('Black');
  SetUser2Label('White');
  Measure;
  GetResults(nPixels,mean,mode,min,max);
  rUser1[rCount]:=histogram[255]/nPixels;
  rUser2[rCount]:=histogram[0]/nPixels;
  UpdateResults;
  if (histogram[0]+histogram[255])<>nPixels
    then PutMessage('This macro requires a binary image.');
end;


macro 'Compute Area Percentage [P]';
{
Computes the percentage of foreground
pixels in the current selection.
}
var
  mean,mode,min,max:real;
  i,lower,upper,fPixels,nPixels,count:integer;
begin
  RequiresVersion(1.50);
  SetUser1Label('%');
  Measure;
  GetResults(nPixels,mean,mode,min,max);
  GetThresholds(lower,upper);
  if (lower=0) and (upper=0) and
     ((histogram[0]+histogram[255])<>nPixels)
     then begin
       PutMessage('This macro requires a binary or thresholded image.');
       exit;
     end;
  if nPixels=0 then begin
  end;
```

```
  if (lower=0) and (upper=0) then begin
    if nPixels=0
      then rUser1[rCount]:=0
      else rUser1[rCount]:=(histogram[255]/nPixels)*100;
    UpdateResults;
    exit;
  end;
  fPixels:=0;
  nPixels:=0;
  for i:=0 to 255 do begin
    count:=histogram[i];
    nPixels:=nPixels+count;
    if (i>=lower) and (i<=upper)
      then fPixels:=fPixels+count;
  end;
  rUser1[rCount]:=(fPixels/nPixels)*100;
  UpdateResults;
end;
```

APPENDIX E: CELL CULTURE, ASSAY, AND IMAGING PROTOCOLS

E.1 Incubator disinfection protocol

Reagents

- Steris staphene spray (Fisher 14-415-15)
- 70% ethanol

Procedure

1) Shut off the CO_2 tanks and turn off the incubator.

2) Prepare the sterile hood by covering the inside with bench-coat.

3) Cover the chemical fume hood with fresh bench-coat.

4) Disassemble all removable parts from the incubator chamber. Spray all pieces from the incubator inside the chemical fume hood with staphene. Spray the inside of the inside of the incubator with staphene. Let stand for 15 min with the incubator door cracked open ~2 in.

5) Spray the inside of the incubator with 70% ethanol. Wipe off the excess staphene with paper towels.

6) Spray all internal pieces of the incubator in the chemical fume hood with 70% ethanol and wipe off the excess staphene. Spray each part generously with ethanol again and place into the sterile hood to dry. Do not wipe anything down. Allow all parts to air dry for 15-30 min.

7) Spray the inside of the incubator with 70% ethanol and allow all parts to dry for 15-30 min; do not wipe anything down.

8) Reassemble all internal pieces of the incubator, taking care to move each piece from the sterile hood to the incubator as quickly as possible.

9) Spray the inside of incubator again with 70% ethanol. Shut the foot and allow all parts to dry; do not wipe anything down.

10) Turn on the incubator power and open the valves on the CO_2 tanks. Allow the incubator to ventilate with the CO_2 on for 24 h before using again.

E.2 Tenocyte culture protocol

Reference: (Kapoor, Caporali et al. 2010; Caliari and Harley 2011; Caliari, Ramirez et al. 2011)

Reagents

- Complete tenocyte media (500 mL); store at 4^{o}C
    - 445 mL high glucose DMEM (Based on Fisher SH30022.FS, order from Sandy at SCS Media Facility); store at 4^{o}C
    - 50 mL fetal bovine serum (Invitrogen 16140-071); store at -20^{o}C
    - 5 mL antibiotic-antimyotic (Invitrogen 15140-122); store at -20^{o}C
    - 25 mg ascorbic acid (Wako 014-04801)
    - Sterile filter before use
- Trypsin-EDTA (Invitrogen 25300-062); store at -20^{o}C
- Trypan blue (Sigma-Aldrich T8154)
- DMSO (Fisher D128-500)
- Sterile phosphate-buffered saline without Ca^{2+} or Mg^{2+} (PBS)

Supplies and equipment

- Hausser phase contrast hemacytometer (Fisher 02-671-5)
- Tabletop centrifuge (VWR 53513-812)
- Optical microscope (Leica Microsystems DMIL LED)
- Water bath (37^{o}C, Fisher 15-474-35)
- Sterile filters
- Sterile pipettes (5, 10, 25 mL)
- T75 tissue culture flasks

*Note: all steps should be performed in the laminar flow hood unless otherwise noted.

Tenocyte thawing procedure

1) Place complete tenocyte media in water bath and warm to 37^{o}C.

2) Thaw frozen cell vials in 37^{o}C water bath for about 2 min.

3) Transfer the thawed cells and freezing media to a 15 mL centrifuge tube. Add complete tenocyte media until the cerulean effect has dissipated, then bring the volume up to 9 mL.

4) Remove a 10 μL cell suspension aliquot for counting. Gently re-suspend the cells in the diluted media and pellet the cells at 1000 rpm for 7 min.

5) While cells are spinning down, mix the 10 μL cell suspension aliquot with 10 μL of Trypan blue. Pipette several times to mix the stain and cell suspension.

6) Place a cover slip on the hemacytometer and pipette 10 μL of the stain/cell suspension into the hemacytometer.

7) Cell counts are performed in as many of the nine separate regions of the hemacytometer as is feasible. Average number of cells per region is used to calculate the total cell population. For this calculation, the dilution factor is typically 2 (1:1 ratio of cell suspension to Trypan blue).

*Total Cell Population = (Mean Cells per Region) * Dilution * 10,000 * (Cell Suspension Volume)*

8) Seed the cells at the required density (usually 10,000 cells/cm^2). Use around 10-12 mL media for a 100 mm dish, 12-14 mL for a T75, or 7-8 mL for a T25.

9) Place the flask(s) into the incubator. Check the confluence every 24 h and feed cells twice a week. Cells are usually confluent after 5 days. Do not use past passage 4.

Tenocyte feeding procedure

1) Warm complete tenocyte media in water bath to 37^{o}C.

2) When the media is warm, wipe dry with paper towel and spray with 70% ethanol before placing in the sterile hood.

3) Remove all old media from each T75 flask, taking care not to scrape the cells with the pipette tip.

4) Add 12-14 mL of complete tenocyte media. Return the T75 flasks to the incubator and feed every twice a week. Adjust volume of media accordingly for different sized flasks.

Tenocyte passaging procedure

1) Warm complete tenocyte media, sterile PBS, and 3 mL trypsin-EDTA per T75 flask to be passaged in water bath to 37^{o}C.

2) When the media, PBS and trypsin are warm, wipe them dry with paper towel and spray with 70% ethanol before placing in the sterile hood.

3) Remove all old media from each T75 flask, taking care not to scrape the cells with the pipette tip.

4) Add 10 mL of PBS per T75 flask and leave the PBS in the flask to rinse the cells for 30 s. Swirl gently to remove any excess media from the cells. Adjust volumes of PBS, media, and trypsin accordingly for different sized flasks.

5) Remove the PBS and add 3 mL of trypsin per T75 flask. Return the flasks to the incubator for 6 min to allow for the cells to detach from the tissue culture plastic (allow the cells to sit for 3-4 additional min in the incubator if they do not detach after 6 min). Slap flasks a few times to detach cells.

6) Add 6 mL of complete tenocyte media to each flask to neutralize the trypsin and to flush cells off of the tissue culture plastic.

7) Remove the trypsin, additional media, and cells from the flask and put into a conical tube. Remove a 10 μL cell suspension aliquot for counting. Centrifuge the cells at 1000 rpm for 7 min.

8) While cells are spinning down, mix the 10 μL cell suspension aliquot with 10 μL of Trypan blue. Pipette several times to mix the stain and cell suspension.

9) Place a cover slip on the hemacytometer and pipette 10 μL of the stain/cell suspension into the hemacytometer.

10) Cell counts are performed in as many of the nine separate regions of the hemacytometer as is feasible. Average number of cells per region is used to calculate the total cell population. For this calculation, the dilution factor is typically 2 (1:1 ratio of cell suspension to Trypan blue).

*Total Cell Population = (Mean Cells per Region) * Dilution * 10,000 * (Cell Suspension Volume)*

11) Aspirate off the media supernatant and add new media to dilute cells to desired concentration.

12) Seed the cells at the required density (usually 10,000-50,000 cells/cm^2). Use around 10-12 mL media for a 100 mm dish, 12-14 mL for a T75, or 7-8 mL for a T25.

13) Place the flask(s) into the incubator. Check the confluence every 24 h and feed cells every 48-72 h.

Tenocyte freezing procedure

1) Grow cells to confluence and replace media the day before freezing.

2) Warm complete tenocyte media, sterile PBS, and 3 mL trypsin-EDTA per T75 flask to be passaged in water bath to 37^{o}C.

3) When the media, PBS and trypsin are warm, wipe them dry with paper towel and spray with 70% ethanol before placing in the sterile hood.

4) Remove all old media from each flask, taking care not to scrape the cells with the pipette tip.

5) Add 10 mL of PBS per T75 flask and leave the PBS in the flask to rinse the cells for 30 s. Swirl gently to remove any excess media from the cells. Adjust volumes of PBS, media , and trypsin accordingly for different sized flasks.

6) Remove the PBS and add 3 mL of trypsin per T75 flask. Return the flasks to the incubator for 6 min to allow for the cells to detach from the tissue culture plastic (allow the cells to sit for 3-4

additional min in the incubator if they do not detach after 6 min). Slap flasks a few times to detach cells.

7) Add 6 mL of complete tenocyte media to each flask to neutralize the trypsin and to flush cells off of the tissue culture plastic.

8) Remove the trypsin, additional media, and cells from the flask and put into a conical tube. Remove a 10 μL cell suspension aliquot for counting. Centrifuge the cells at 1000 rpm for 7 min.

9) While cells are spinning down, mix the 10 μL cell suspension aliquot with 10 μL of Trypan blue. Pipette several times to mix the stain and cell suspension.

10) Place a cover slip on the hemacytometer and pipette 10 μL of the stain/cell suspension into the hemacytometer.

11) Cell counts are performed in as many of the nine separate regions of the hemacytometer as is feasible. Average number of cells per region is used to calculate the total cell population. For this calculation, the dilution factor is typically 2 (1:1 ratio of cell suspension to Trypan blue).

*Total Cell Population = (Mean Cells per Region) * Dilution * 10,000 * (Cell Suspension Volume)*

12) Aspirate off the media supernatant and calculate volume of freezing media needed to re-suspend 1-10 x 10^6 cells per mL (freezing media: 50% complete tenocyte, 40% FBS, 10% DMSO).

13) Aliquot cells into 1 mL cryogenic tubes and place in -20^{o}C freezer for 1 h.

14) Place cryogenic tubes in -80^{o}C freezer. Cells can be stored here for up to 6 months. For longer-term storage, keep cells at -80^{o}C for at least 24 h and then carefully move to liquid nitrogen storage in IGB.

E.3 hMSC culture and differentiation protocol

Reference: Protocols from Matt Wheeler group and Jennie P. Mather

Reagents

- Complete hMSC media (500 mL); store at 4°C
    - 445 mL low glucose DMEM (Based on Fisher SH30022.FS, order from Sandy at SCS Media Facility); store at 4°C
    - 50 mL MSC-validated fetal bovine serum (Invitrogen 12662-029); store at -20°C
    - 5 mL antibiotic-antimyotic (Invitrogen 15140-122); store at -20°C
- Osteogenic induction media (500 mL); store at 4°C
    - 445 mL low glucose DMEM (Based on Fisher SH30022.FS, order from Sandy at SCS Media Facility); store at 4°C
    - 50 mL MSC-validated fetal bovine serum (Invitrogen 12662-029); store at -20°C
    - 5 mL antibiotic-antimyotic (Invitrogen 15140-122); store at -20°C
    - 0.1 µM dexamethasone (Sigma D4902-100MG); store at -20°C
    - 10 mM beta-glycerophosphate (Sigma G9422-10G)
    - 50 µM ascorbic acid (Sigma A4403-100MG)
    - Sterile filter before use
- Chondrogenic induction media (500 mL); store at 4°C
    - 490 mL low glucose DMEM (Based on Fisher SH30022.FS, order from Sandy at SCS Media Facility); store at 4°C
    - 5 mL antibiotic-antimyotic (Invitrogen 15140-122); store at -20°C
    - 0.1 µM dexamethasone (Sigma D4902-100MG); store at -20°C
    - 1 mM sodium pyruvate (Sigma P5280-25G); store at 4°C
    - ITS+ supplement (Sigma I3146-5ML); store at 4°C
    - 40 µg/mL proline (Sigma, P5607-25G); store at 4°C
    - 10 ng/mL TGF-β3 (ProSpec CYT-368); aliquot and store at -20°C
    - Sterile filter before use
- Adipogenic induction media (500 mL); store at 4°C
    - 445 mL low glucose DMEM (Based on Fisher SH30022.FS, order from Sandy at SCS Media Facility); store at 4°C
    - 50 mL MSC-validated fetal bovine serum (Invitrogen 12662-029); store at -20°C
    - 5 mL antibiotic-antimyotic (Invitrogen 15140-122); store at -20°C
    - 1 µM dexamethasone (Sigma D4902-100MG); store at -20°C
    - 100 µM indomethacin (Sigma I7378-5G)
    - 500 µM IBMX (Sigma I5879-250MG); store at -20°C
    - 10 µg/mL insulin (Sigma I9278-5ML); store at 4°C
    - Sterile filter before use
- Trypsin-EDTA (Invitrogen 25300-062); store at -20°C
- Trypan blue (Sigma-Aldrich T8154)
- DMSO (Fisher D128-500)
- Sterile phosphate-buffered saline without Ca^{2+} or Mg^{2+} (PBS)

Supplies and equipment

- Hausser phase contrast hemacytometer (Fisher 02-671-5)

- Tabletop centrifuge (VWR 53513-812)
- Optical microscope (Leica Microsystems DMIL LED)
- Water bath (37^{o}C, Fisher 15-474-35)
- Sterile filters
- Sterile pipettes (5, 10, 25 mL)
- T75 tissue culture flasks

*Note: all steps should be performed in the laminar flow hood unless otherwise noted.

MSC thawing procedure

1) Place complete MSC media in water bath and warm to 37^{o}C.

2) Thaw frozen cell vials in 37^{o}C water bath for about 2 min.

3) Transfer the thawed cells and freezing media to a 15 mL centrifuge tube. Add complete MSC media until the cerulean effect has dissipated, then bring the volume up to 9 mL.

4) Remove a 10 μL cell suspension aliquot for counting. Gently re-suspend the cells in the diluted media and pellet the cells at 600 g for 5 min.

5) While cells are spinning down, mix the 10 μL cell suspension aliquot with 10 μL of Trypan blue. Pipette several times to mix the stain and cell suspension.

6) Place a cover slip on the hemacytometer and pipette 10 μL of the stain/cell suspension into the hemacytometer.

7) Cell counts are performed in as many of the nine separate regions of the hemacytometer as is feasible. Average number of cells per region is used to calculate the total cell population. For this calculation, the dilution factor is typically 2 (1:1 ratio of cell suspension to Trypan blue).

*Total Cell Population = (Mean Cells per Region) * Dilution * 10,000 * (Cell Suspension Volume)*

8) Seed the cells at the required density (usually 5,000-6,000 cells/cm^{2}). Use around 10-12 mL media for a 100 mm dish, 12-14 mL for a T75, or 7-8 mL for a T25.

9) Place the flask(s) into the incubator. Check the confluence every 24 h and feed cells twice a week. Cells are usually confluent after 7-9 days. Do not use past passage 6.

MSC feeding procedure

1) Warm complete MSC or lineage-specific induction media in water bath to 37^{o}C.

2) When the media is warm, wipe dry with paper towel and spray with 70% ethanol before placing in the sterile hood.

3) Remove all old media from each flask or well plate, taking care not to scrape the cells with the pipette tip.

4) Add appropriate volume of media. Return the flasks or well plates to the incubator and feed every twice a week. Adjust volume of media accordingly for different sized containers.

MSC passaging procedure

1) Warm complete MSC media, sterile PBS, and 3 mL trypsin-EDTA per T75 flask to be passaged in water bath to 37^{o}C.

2) When the media, PBS and trypsin are warm, wipe them dry with paper towel and spray with 70% ethanol before placing in the sterile hood.

3) Remove all old media from each T75 flask, taking care not to scrape the cells with the pipette tip.

4) Add 10 mL of PBS per T75 flask and leave the PBS in the flask to rinse the cells for 30 s. Swirl gently to remove any excess media from the cells. Adjust volumes of PBS, media, and trypsin accordingly for different sized flasks.

5) Remove the PBS and add 3 mL of trypsin per T75 flask. Return the flasks to the incubator for 8 min to allow for the cells to detach from the tissue culture plastic (allow the cells to sit for 3-4 additional min in the incubator if they do not detach after 6 min). Slap flasks a few times to detach cells.

6) Add 6 mL of complete MSC media to each flask to neutralize the trypsin and to flush cells off of the tissue culture plastic.

7) Remove the trypsin, additional media, and cells from the flask and put into a conical tube. Remove a 10 μL cell suspension aliquot for counting. Centrifuge the cells at 600 g for 5 min.

8) While cells are spinning down, mix the 10 μL cell suspension aliquot with 10 μL of Trypan blue. Pipette several times to mix the stain and cell suspension.

9) Place a cover slip on the hemacytometer and pipette 10 μL of the stain/cell suspension into the hemacytometer.

10) Cell counts are performed in as many of the nine separate regions of the hemacytometer as is feasible. Average number of cells per region is used to calculate the total cell population. For this calculation, the dilution factor is typically 2 (1:1 ratio of cell suspension to Trypan blue).

*Total Cell Population = (Mean Cells per Region) * Dilution * 10,000 * (Cell Suspension Volume)*

11) Aspirate off the media supernatant and add new media to dilute cells to desired concentration.

12) Seed the cells at the required density (usually 5,000-6,000 cells/cm^2). Use around 10-12 mL media for a 100 mm dish, 12-14 mL for a T75, or 7-8 mL for a T25.

13) Place the flask(s) into the incubator. Check the confluence every 24 h and feed cells twice a week.

MSC freezing procedure

1) Grow cells to confluence and replace media the day before freezing.

2) Warm complete MSC media, sterile PBS, and 3 mL trypsin-EDTA per T75 flask to be passaged in water bath to 37^oC.

3) When the media, PBS and trypsin are warm, wipe them dry with paper towel and spray with 70% ethanol before placing in the sterile hood.

4) Remove all old media from each flask, taking care not to scrape the cells with the pipette tip.

5) Add 10 mL of PBS per T75 flask and leave the PBS in the flask to rinse the cells for 30 s. Swirl gently to remove any excess media from the cells. Adjust volumes of PBS, media , and trypsin accordingly for different sized flasks.

6) Remove the PBS and add 3 mL of trypsin per T75 flask. Return the flasks to the incubator for 8 min to allow for the cells to detach from the tissue culture plastic (allow the cells to sit for 3-4 additional min in the incubator if they do not detach after 6 min). Slap flasks a few times to detach cells.

7) Add 6 mL of complete tenocyte media to each flask to neutralize the trypsin and to flush cells off of the tissue culture plastic.

8) Remove the trypsin, additional media, and cells from the flask and put into a conical tube. Remove a 10 μL cell suspension aliquot for counting. Centrifuge the cells at 600 g for 5 min.

9) While cells are spinning down, mix the 10 μL cell suspension aliquot with 10 μL of Trypan blue. Pipette several times to mix the stain and cell suspension.

10) Place a cover slip on the hemacytometer and pipette 10 μL of the stain/cell suspension into the hemacytometer.

11) Cell counts are performed in as many of the nine separate regions of the hemacytometer as is feasible. Average number of cells per region is used to calculate the total cell population. For this calculation, the dilution factor is typically 2 (1:1 ratio of cell suspension to Trypan blue).

*Total Cell Population = (Mean Cells per Region) * Dilution * 10,000 * (Cell Suspension Volume)*

12) Aspirate off the media supernatant and calculate volume of freezing media needed to re-suspend 1-10 x 10^6 cells per mL (freezing media: 50% complete MSC media, 40% FBS, 10% DMSO).

13) Aliquot cells into 1 mL cryogenic tubes and place in -20^{o}C freezer for 1 h.

14) Place cryogenic tubes in -80^{o}C freezer. Cells can be stored here for up to 6 months. For longer-term storage, keep cells at -80^{o}C for at least 24 h and then carefully move to liquid nitrogen storage in IGB.

E.4 Cell chemotaxis protocol

Reference: (Caliari and Harley 2011)

Reagents

- Cell culture media (see E.2 and E.3 for recipes); store at 4°C
- Trypsin-EDTA (Invitrogen 25300-062); store at -20°C
- Trypan blue (Sigma-Aldrich T8154)
- Human recombinant PDGF-BB (R&D Systems 220-BB-010); store at -20°C
- Human recombinant IGF-1 (R&D Systems 291-G1-050); store at -20°C
- Human recombinant SDF-1α (R&D Systems 350-NS-050); store at -20°C
- Human recombinant bFGF (R&D Systems 233-FB-025); store at -20°C
- Human recombinant GDF-5 (Peprotech 120-01); store at -20°C
- Human recombinant GDF-6 (Peprotech 120-04); store at -20°C
- Human recombinant GDF-7 (Peprotech 120-37); store at -20°C
- Sterile phosphate-buffered saline without Ca^{2+} or Mg^{2+} (PBS)

Supplies and equipment

- 24-well plates with Transwell inserts (Fisher 07-200-150)
- Hausser phase contrast hemacytometer (Fisher 02-671-5)
- Tabletop centrifuge (VWR 53513-812)
- Optical microscope (Leica Microsystems DMIL LED)
- Water bath (37°C, Fisher 15-474-35)
- Sterile pipettes (5, 10, 25 mL)

*Note: all steps should be performed in the laminar flow hood unless otherwise noted.

Procedure

1) Warm media, sterile PBS, and 3 mL trypsin-EDTA per T75 flask to be passaged in water bath to 37°C.

2) Place hydrated scaffold pieces in fresh media to hydrate for at least 30 min.

3) Prepare aliquots of growth factor supplemented media at required concentrations for experiment. Remember to include a control group with media containing no supplemented growth factors. Pipette 600 μL of media into each well in the plate (without inserts) and place 1 scaffold piece in each well. Place Transwell inserts in wells so that scaffold is maximally contacted with membrane.

4) When the media, PBS and trypsin are warm, wipe them dry with paper towel and spray with 70% ethanol before placing in the sterile hood.

5) Remove all old media from each flask, taking care not to scrape the cells with the pipette tip.

6) Add 10 mL of PBS per T75 flask and leave the PBS in the flask to rinse the cells for 30 s. Swirl gently to remove any excess media from the cells. Adjust volumes of PBS, media , and trypsin accordingly for different sized flasks.

7) Remove the PBS and add 3 mL of trypsin per flask. Return the flasks to the incubator for 6-8 min to allow for the cells to detach from the tissue culture plastic (allow the cells to sit for 3-4 additional min in the incubator if they do not detach after 6 min). Slap flasks a few times to detach cells.

8) Add 6 mL of complete media to each flask to neutralize the trypsin and to flush cells off of the tissue culture plastic.

9) Remove the trypsin, additional media, and cells from the flask and put into a conical tube. Remove a 10 μL cell suspension aliquot for counting. Centrifuge the cells at appropriate speed and time.

10) While cells are spinning down, mix the 10 μL cell suspension aliquot with 10 μL of Trypan blue. Pipette several times to mix the stain and cell suspension.

11) Place a cover slip on the hemacytometer and pipette 10 μL of the stain/cell suspension into the hemacytometer.

12) Cell counts are performed in as many of the nine separate regions of the hemacytometer as is feasible. Average number of cells per region is used to calculate the total cell population. For this calculation, the dilution factor is typically 2 (1:1 ratio of cell suspension to Trypan blue).

*Total Cell Population = (Mean Cells per Region) * Dilution * 10,000 * (Cell Suspension Volume)*

13) Aspirate off the media supernatant and add new media to dilute to 1-5 x 10^5 cells per 100 μL media.

14) Check that scaffolds are properly positioned under membranes. Add 100 μL of cell suspension to the upper compartment of each Transwell insert.

15) Incubate at 37^{o}C for 24 h.

E.5 Cell seeding on CG scaffolds protocol

Reference: (Caliari and Harley 2011; Caliari, Ramirez et al. 2011)

Reagents

- Complete media (see E.2 and E.3 protocols for cell recipes); store at 4^{o}C
- Trypsin-EDTA (Invitrogen 25300-062); store at -20^{o}C
- Trypan blue (Sigma-Aldrich T8154)
- Human recombinant PDGF-BB (R&D Systems 220-BB-010); store at -20^{o}C
- Human recombinant IGF-1 (R&D Systems 291-G1-050); store at -20^{o}C
- Human recombinant SDF-1α (R&D Systems 350-NS-050); store at -20^{o}C
- Human recombinant bFGF (R&D Systems 233-FB-025); store at -20^{o}C
- Human recombinant GDF-5 (Peprotech 120-01); store at -20^{o}C
- Human recombinant GDF-6 (Peprotech 120-04); store at -20^{o}C
- Human recombinant GDF-7 (Peprotech 120-37); store at -20^{o}C
- Human recombinant BMP-2 (ProSpec CYT-261); store at -20°C
- Human recombinant BMP-7 (ProSpec CYT-333); store at -20°C
- Human recombinant TGF-β1 (ProSpec CYT-761); store at -20°C
- Human recombinant TGF-β3 (ProSpec CYT-368); store at -20°C
- Sterile phosphate-buffered saline without Ca^{2+} or Mg^{2+} (PBS)

Supplies and equipment

- Ultra-low attachment 6-well plates (Fisher 07-200-601)
- Hausser phase contrast hemacytometer (Fisher 02-671-5)
- Tabletop centrifuge (VWR 53513-812)
- Optical microscope (Leica Microsystems DMIL LED)
- Water bath (37^{o}C, Fisher 15-474-35)
- Sterile pipettes (5, 10, 25 mL)
- Kimwipes

*Note: all steps should be performed in the laminar flow hood unless otherwise noted. For growth factor supplemented studies, use tendon cell media without serum.

Procedure

1) Warm complete media, sterile PBS, and 3 mL trypsin-EDTA per T75 flask to be passaged in water bath to 37^{o}C.

2) Place hydrated scaffold pieces in fresh media for at least 30 min.

3) Carefully remove excess media from scaffolds with a Kimwipe and place 3-4 scaffold pieces in each well of Ultra-low attachment 6-well plates. Do not overdry scaffolds (especially CGCaP scaffolds) as this will lead to reduced viability.

4) When the media, PBS and trypsin are warm, wipe them dry with paper towel and spray with 70% ethanol before placing in the sterile hood.

5) Remove all old media from each flask, taking care not to scrape the cells with the pipette tip.

6) Add 10 mL of PBS per T75 flask and leave the PBS in the flask to rinse the cells for 30 s. Swirl gently to remove any excess media from the cells. Adjust volumes of PBS, media, and trypsin accordingly for different sized flasks.

7) Remove the PBS and add 3 mL of trypsin per flask. Return the flasks to the incubator for 6-8 min to allow for the cells to detach from the tissue culture plastic (allow the cells to sit for 3-4 additional min in the incubator if they do not detach after 6 min). Slap flasks a few times to detach cells.

8) Add 6 mL of complete tendon cell media to each flask to neutralize the trypsin and to flush cells off of the tissue culture plastic.

9) Remove the trypsin, additional media, and cells from the flask and put into a conical tube. Remove a 10 μL cell suspension aliquot for counting. Centrifuge the cells at appropriate speed and time.

10) While cells are spinning down, mix the 10 μL cell suspension aliquot with 10 μL of Trypan blue. Pipette several times to mix the stain and cell suspension.

11) Place a cover slip on the hemacytometer and pipette 10 μL of the stain/cell suspension into the hemacytometer.

12) Cell counts are performed in as many of the nine separate regions of the hemacytometer as is feasible. Average number of cells per region is used to calculate the total cell population. For this calculation, the dilution factor is typically 2 (1:1 ratio of cell suspension to Trypan blue).

*Total Cell Population = (Mean Cells per Region) * Dilution * 10,000 * (Cell Suspension Volume)*

13) Aspirate off the media supernatant and add new media to dilute cells to desired concentration. For 8 mm diameter, 5 mm thick scaffold pieces dilute to 1-5 x 10^5 cells per 20-40 μL media.

14) Add 10-20 μL of cell suspension to each scaffold piece. Place scaffolds in incubator for 15-30 min.

15) Remove scaffolds from incubator, flip over, add additional 10-20 μL of cell suspension to the other side of each scaffold, and return to incubate for additional 2-3 h.

16) Carefully add 6 mL complete media (or media with growth factors but without serum) to each well. Change media every 3 days over the course of the experiment.

E.6 AlamarBlue metabolic activity protocol

Reference: (Tierney, Jaasma et al. 2009; Caliari and Harley 2011; Caliari, Ramirez et al. 2011)

Reagents

- Complete media (see E.2 and E.3 for recipes); store at 4^{o}C
- AlamarBlue (Invitrogen DAL1100); store at 4^{o}C

Supplies and equipment

- 24-well plates (Fisher 08-772-1)
- 96-well plates (Fisher 12-565-369)
- MTS 2/4 digital microtiter shaker (IKA 3208001)
- Water bath (37^{o}C, Fisher 15-474-35)
- Fluorescence spectrophotometer (Tecan, Room 299 RAL)

*Note: all steps should be performed in the laminar flow hood unless otherwise noted. The volumes of reagents used are correct for 8 mm diameter, 5 mm thick scaffold pieces. Use identical media to that being used for experiment.

Generating standard curve procedure

1) Warm media and alamarBlue in water bath to 37^{o}C.

2) Before starting an experiment, generate a standard curve with a known number of cells. The standard should have at least eight sample points: one well with just media, one well with media and alamarBlue, and six wells with media, alamarBlue, and a different number of cells. An example standard setup is shown:

	Well 1	**Well 2**	**Well 3**	**Well 4**	**Well 5**	**Well 6**	**Well 7**	**Well 8**
Media	1000 μL	900 μL	895 μL	890 μL	885 μL	880 μL	860 μL	840 μL
Cell suspension	0 μL	0 μL	5 μL	10 μL	15 μL	20 μL	40 μL	60 μL
AlamarBlue	0 μL	100 μL	100 μL	100 μL	100 μL	100 μL	100 μL	100 μL

Well 1 is a negative control, well 2 is a background control, and the other wells are used to make the standard curve.

3) Incubate at 37^{o}C under gentle (~50 rpm) shaking for 1.5-5.5 h. During this time healthy cells convert the active ingredient in alamarBlue (resazurin) to the highly fluorescent resorufin. Longer incubation times are necessary for smaller cell concentrations, but make sure not to incubate cells too long or all of the resazurin will be reduced to resorufin.

4) After incubation, pipette 100 μL in triplicate from each sample well into a clear 96-well plate.

5) Measure fluorescence (excitation: 540 nm, emission: 580 nm) on the spectrophotometer in RAL 299 using the program 'AlamarBlue F200'. Remember to reserve the F200 machine on the Google Calendar prior to use. For each data point, adjust the fluorescence reading by subtracting the reading from well 2 (background control). The standard curve is created by plotting cell number as a function of adjusted fluorescent intensity.

Quantifying metabolic activity on scaffolds procedure

1) For measuring cell metabolic activity on scaffolds, pipette 900 μL media into each well (one well for each scaffold piece plus the two control wells). Add 100 μL alamarBlue to each well except for one negative control well. Adjust volumes for smaller/larger materials accordingly, keeping the 9:1 media: alamarBlue® ratio constant.

2) Remove scaffolds to be assayed and rinse in sterile PBS to remove excess media and unattached/dead cells. Add scaffolds to experimental wells and incubate at 37^{o}C under gentle (~50 rpm) shaking for 1.5-5.5 h. The incubation time should be identical to the time used to make the standard curve.

3) After incubation, pipette 100 μL in triplicate from each sample well into a 96-well plate.

4) Measure fluorescence (excitation: 540 nm, emission: 580 nm) on the spectrophotometer in RAL 299 using the program 'AlamarBlue F200'. Remember to reserve the F200 machine on the Google Calendar prior to use. Subtract the background control from the data points and extrapolate adjusted fluorescent intensity on the standard curve to give metabolic activity.

5) This assay is non-destructive, so scaffolds can continue to be cultured and analyzed at later time points.

E.7 Hoechst DNA quantification protocol

Reference: (Kim, Sah et al. 1988; Caliari and Harley 2011; Caliari, Ramirez et al. 2011)

Reagents

- Hoechst dye buffer (500 mL); store at 4°C for up to 3 months
  - 400 mL deionized water
  - 58.44 g sodium chloride (RAL storeroom)
  - 0.605 g Tris base (RAL storeroom)
  - 0.185 g disodium EDTA (Sigma-Aldrich E5134)
  - Adjust pH to 7.4, bring total volume to 500 mL, sterile filter before use
- Papain buffer (100 mL); store at 4°C
  - 100 mL PBS
  - 1 mL 0.5 M EDTA (pH = 8.0, Sigma-Aldrich EDS); store at 4°C
  - 79 mg cysteine-HCl (Sigma-Aldrich 00320)
- Hoechst 33258 dye solution (1 mL); store at 4°C for up to 6 months
  - 1 mL sterile water
  - 1 mg Hoechst 33258 dye (Invitrogen H1398); store at 4°C
- Papain from Carica papaya (Sigma-Aldrich 76218); store at -20°C
- Sterile phosphate-buffered saline without Ca^{2+} or Mg^{2+} (PBS)

Supplies and equipment

- 96-well plates (Fisher 12-565-369)
- Vortex (Fisher 02-215-365)
- Water bath (60°C, Fisher 15-460-2SQ)
- Fluorescence spectrophotometer (Tecan, Room 299 RAL)
- Microcentrifuge tubes (1.5 mL)

Generating standard curve procedure

*Note: steps 1-2 should be performed in the laminar flow hood.

1) At the beginning of each experiment, a standard curve should be generated with a known number of cells. To make a standard curve spanning 5×10^3 to 1.5×10^6 million cells, make up active papain enzyme solution by dissolving 18-20 mg papain in 15 mL papain buffer in the 60°C water bath.

2) Spin down two aliquots of 2 million cells each. Remove supernatant and add 12 mL papain enzyme solution to one tube and 400 μL to the other tube. Allow to digest for 24 h in the 60°C water bath.

3) After 24 h, vortex tubes thoroughly. For the 12 mL tube, add cell lysate to labeled microcentrifuge tubes in 30 μL intervals (starting from a blank control) up to 300 μL. Bring all volumes to 300 μL with blank papain buffer. For the 400 μL tube, add cell lysate to labeled microcentrifuge tubes in 2 μL intervals (starting from a blank control) up to 30 μL. Bring all volumes to 30 μL with blank papain buffer.

4) Prepare Hoechst working dye solution by adding 1 μL dye solution to 10 mL Hoechst dye buffer. Vortex thoroughly. Add working dye solution to each tube to bring total volume to 630 μL. Vortex thoroughly. The Hoechst dye fluorescently binds to double-stranded DNA from the lysed cells, allowing quantification of DNA and thus cell number.

5) Pipette 200 μL from each tube in triplicate into a black 96-well plate.

6) Measure fluorescence (excitation: 360 nm, emission: 465 nm) on the spectrophotometer in RAL 299. Use the 'DNA F200' program and remember to reserve the F200 machine on the Google Calendar prior to use. For each data point, adjust the fluorescence reading by subtracting the reading from the blank control. The standard curve is created by plotting cell number as a function of adjusted fluorescent intensity.

Quantifying cell number on scaffolds procedure
*Note: step 2 should be performed in the laminar flow hood.

1) For measuring cell number on scaffolds, pipette 300 μL of papain enzyme solution into microcentrifuge tubes (one for each scaffold plus two controls: one tube with just papain enzyme solution as a negative control and one tube containing a blank scaffold with no seeded cells as a background control).

2) Remove scaffolds to be assayed and rinse in sterile PBS to remove excess media and unattached/dead cells. Add scaffolds to microcentrifuge tubes and incubate in 60^{o}C water bath for 24 h. Vortex occasionally to facilitate digestion of scaffold.

3) After incubation, pipette 600 μL Hoechst working dye solution in microcentrifuge tubes.

4) Remove samples from water bath and vortex thoroughly. Add 30 μL from each tube to its corresponding tube containing working dye solution. Vortex thoroughly.

5) Pipette 200 μL from each tube in triplicate from each sample well into a 96-well plate.

6) Measure fluorescence (excitation: 360 nm, emission: 465 nm) on the spectrophotometer in RAL 299. Use the 'DNA F200' program and remember to reserve the F200 machine on the Google Calendar prior to use. For each data point, adjust the fluorescence reading by subtracting the reading from the background control. Adjusted fluorescent intensity can be extrapolated on the standard curve to give a cell number.

E.8 Scaffold contraction protocol

References: (Spilker, Asano et al. 2001; Caliari and Harley 2011)

Supplies and equipment

- Drafting template

Procedure

* Note: all steps should be performed in the laminar flow hood unless otherwise noted.

1) On day 0, measure the diameter of the fully hydrated scaffolds before cell seeding. This can be done several ways:

- Place drafting template over well plate containing scaffolds and move template until finding the hole that most closely approximates the diameter of the scaffold.
- Remove scaffolds from solution and measure using template as before.

Scaffolds can be measured either in or out of solution, but the key is consistency; the same method should be used for all samples and time points.

2) Repeat step 1 for subsequent time points in experiment. Normalize measurements to results from day 0.

E.9 Soluble collagen assay protocol

Reference: (Sahoo, Ouyang et al. 2006; Lareu, Zeugolis et al. 2010; Sahoo, Toh et al. 2010)

Supplies and equipment

- Sircol assay kit
- 2x pepsin/acetic acid solution (0.2 mg/mL 1 M acetic acid, make up fresh)
- Pipettes
- Low protein binding or regular microcentrifuge tubes
- Amicon Ultra centrifugal filter units (Fisher: UFC510024)
- Vortex (Fisher 02-215-365)
- Cotton swabs
- Microcentrifuge
- 96-well plates
- Fluorescence spectrophotometer (Tecan, Room 299 RAL)

Procedure

Serum-containing sample:

Day 1 (0.5 h)

1) Label a set of low protein binding microcentrifuge tubes for standards (0, 5, 10, and 15 µg) as well as samples.

2) Make up standards and samples to 1000 µL in media used in experiments.

3) Add 100 µL of 2x pepsin/acetic acid solution to each tube, bringing final concentration to 0.1 mg pepsin/mL 0.5 M acetic acid.

4) Incubate tubes overnight at 4 C.

Day 2 (1.5 h)

5) Add 200 µL of each sample to centrifugal filter unit and place in provided collection tube. Centrifuge tubes at 14000 g for 10 min.

6) Wash retentate and filter by adding 200 µL of 1 mM acetic acid and spinning down at 14000 g for 3 min. Repeat twice for a total of 3 washes.

7) Turn filter unit upside down and place in clean tube. Centrifuge at 1000 g for 2 min.

8) Add 1 mL 'Sircol Dye Reagent' to each tube. Mix by inverting tubes.

9) Mix for 30 min on gentle shaker (vortex at setting 2 or 3).

10) Centrifuge tubes at 12000 rpm for 10 min. Carefully remove supernatant by inversion or by using a micropipette. Pellet should be visible; do not disturb!

11) Gently layer 750 µL ice cold 'Acid-Salt Wash Reagent' on collagen-dye pellet to remove excess dye on pellet and tube surface. Try to remove pellet from bottom of tube without breaking it up.

12) Centrifuge at 12000 rpm for 10 min. Remove supernatant and remove excess liquid with cotton swab.

13) Add 1 mL 'Alkali Reagent' to all tubes. Vortex tubes thoroughly.

14) Read standard and samples in clear 96-well plate (200 µL per well, absorbance at 555 nm) on the M200 machine in RAL 299. Be sure to reserve time on the Google Calendar before using.

Non serum-containing sample:

1) Label a set of regular microcentrifuge tubes for standards (0, 10, 20, 30, 40, and 50 µg) as well as samples.

2) Make up standards and samples to 100 µL in media used in experiments.

3) Add 1 mL 'Sircol Dye Reagent' to each tube. Mix by inverting tubes.

4) Mix for 30 min on gentle shaker (vortex at setting 2 or 3).

5) Centrifuge tubes at 12000 rpm for 10 min. Carefully remove supernatant by inversion or by using a micropipette. Pellet should be visible; do not disturb!

6) Gently layer 750 µL ice cold 'Acid-Salt Wash Reagent' on collagen-dye pellet to remove excess dye on pellet and tube surface. Try to remove pellet from bottom of tube without breaking it up.

7) Centrifuge at 12000 rpm for 10 min. Remove supernatant and remove excess liquid with cotton swab.

8) Add 1 mL 'Alkali Reagent' to all tubes. Vortex tubes thoroughly.

9) Read standard and samples in 96 well plate (200 µL per well, absorbance at 555 nm) on the M200 machine in RAL 299. Be sure to reserve time on the Google Calendar before using.

E.10 RNA isolation protocol

Reference: (Duffy, McFadden et al. 2011; Caliari, Weisgerber et al. 2012)

Reagents

- RNeasy Plant Mini Kit (Qiagen 74904)
- β-mercaptoethanol (Sigma M7522-100ML)
- 70% ethanol (use RNase free water when making solution)
- Sterile phosphate-buffered saline without Ca^{2+} or Mg^{2+} (PBS)
- RNase-free water
- Ice

Supplies and equipment

- 2 mL RNase free non-graduated microcentrifuge tubes
- RNase free pipette tips
- Ice bucket
- Kimwipes
- Microcentrifuge

Procedure

Reagent prep (before starting)

1) Lysis buffer: Add 10 µL β-mercaptoethanol (14.3 M) per 1 mL of Buffer RLT supplied with Qiagen kit. This solution can be stored at room temperature for 1 month.

2) Buffer RPE: Add 4 volumes of 100% ethanol to the bottle of Buffer RPE supplied with Qiagen kit.

RNA Extraction

*All steps are performed at room temperature. Work quickly; limit the number of samples for RNA extraction to 18-24 in each sitting. RNase free tips should be used throughout.

1) Label one microcentrifuge tube for each sample.

2) Put some ice (2^{nd} floor RAL) in an ice bucket.

3) Wash scaffolds in PBS three times, cut in half with razor blade, and then place in labeled tubes.

4) Add ~ 500 µL of ice-cold lysis buffer to each tube and keep on ice for ~ 5 min, shaking tubes periodically to help the buffer infiltrate the scaffolds. Scale amount of lysis buffer appropriately.

5) Pipette lysate into a labeled QIAShredder column. Place scaffold pieces in column as well. Spin at 14,000 rpm for 2.5 min.

6) Add equal volume of 70% ethanol to each sample and mix by pipetting up and down.

7) Add half of the lysate + ethanol to labeled RNeasy column (with 2-mL collection tube).

8) Centrifuge at 12,000 rpm for 30 s. Discard flow-through and replace column.

9) Add the remaining lysate + ethanol to the column.

10) Centrifuge at 12,000 rpm for 30 s. Discard flow-through and replace column.

11) Add 700 µL Buffer RW1 to the column.

12) Centrifuge at 12,000 rpm for 30 s. Discard flow-through and replace column.

13) Pipet 500 µL Buffer RPE into the column.

14) Centrifuge at 12,000 rpm for 30 s. Discard flow-through and replace column.

15) Add another 500 µL Buffer RPE into the column.

16) Centrifuge at 12,000 rpm for 2.5 min. Discard flow-through and place the column in a new 2 mL collection tube (supplied with kit).

17) Centrifuge at 12,000 rpm for 2.0 min.

18) Transfer the column to a new labeled, 1.5-mL collection tube.

19) Pipet 30 µL RNase-free water into the column and wait 5 min.

20) Centrifuge the RNeasy column at 12,000 rpm for 1.5 min.

21) Store RNA at -80°C for later use or put on ice if directly proceeding to quantification, reverse transcription, and RT-PCR.

E.11 Quantification of RNA and reverse transcription protocol

Reference: (Duffy, McFadden et al. 2011; Caliari, Weisgerber et al. 2012)

Reagents

- QuantiTect Reverse Transcription Kit (Qiagen 205313); store at -20°C although individual kit aliquots may be stored at 4°C once opened.
- TE buffer (pH = 8.0)
- DTT (100 mM stock); store at -20°C
- RNase-free water
- RNase H; store at -20°C
- Ice

Supplies and equipment

- Cuvettes
- Thermocycler (BioRad 185-2196**)**
- RNase-free pipette tips
- RNase-free PCR tubes (100 µL, CLSL stockroom)
- Ice bucket
- Kimwipes
- Ambion DNase I removal kit
- Vortex (Fisher 02-215-365)

Procedure

RNA quantification

1) Gather pipettes, RNase-free tips, TE buffer, cuvettes, and samples in an ice bucket.

2) Proceed to the spectrophotometer in the IGB 2nd floor (shared equipment).

3) Remove piece of tape covering the cuvette opening and turn the machine on. Make sure it is in 'RNA' mode (button 9).

4) Pipet 50 µL TE buffer into a clean cuvette and blank the machine.

5) For each RNA sample, pipet 10 µL of RNA into 40 µL of TE buffer in cuvette. Lightly flick the cuvette several times to mix and then read absorbance. Record the A260 and A260/280 ratio readings.

6) Empty the cuvette on a pile of Kimwipes, getting the cuvette relatively dry. Repeat step 5 for subsequent samples.

7) RNA amount (µg) can be calculated using the following equation:

$$[RNA] = A_{260} * \left(40\ \frac{\mu g}{mL}\right) * dilution\ factor * \ RNA\ volume\ (mL)$$ (**Equation E.1**)

Normal procedure for reverse transcription with hexameric primers

1) Label PCR tubes for number of reactions needed and defrost reverse transcription kit components on ice if needed. Keep kit components and RNA samples on ice. Turn on thermocycler so it can warm up.

2) Calculate the amount of RNA needed for each reaction. Typically, > 10 ng of cDNA will be desired per well for subsequent RT-PCR experiment.

3) For 10 µL reactions, add 1 µL gDNA wipeout buffer (orange tubes) to each PCR tube.

4) Add RNase-free water to each PCR tube so that the total reaction volume (when RNA is added) will be 7 µL. If RNA quantification was low do not add water.

5) Add RNA to each tube. Add up to 10 µL per tube if RNA amount is very low.

6) Close tubes and place in thermocycler. Close lid with extra quarter turn of tightness.

7) Run the 'CAV1' program. This will begin by incubating the samples at 42°C for 2 min.

8) While the first step is running, prepare reaction buffer. Note that the RT buffer (green tubes) and the Primer Mix (purple tubes) can be combined in one tube. If you do this, place a check mark on the lid of the green tube. Combine 2.5 µL of RT buffer/primer mix plus 0.33-0.5 µL reverse transcriptase (red tubes) per sample into a single tube and vortex well.

9) Pipet 2.83-3 µL of reaction buffer mix into each PCR tube once the 2 min initial incubation is complete. Close tubes, lid, and then press enter to skip to the next step, which is a 15 min incubation at 42°C followed by 95°C incubation for 3 min.

10) Once the cycle is complete, place samples in a labeled box or Petri dish and put on ice if proceeding directly to RT-PCR, or store at -20°C (short term) or -80°C (long term).

Procedure for generating gene-specific cDNA

1) Label PCR tubes for number of reactions needed and defrost reverse transcription kit components on ice if needed. Keep kit components and RNA samples on ice. Turn on thermocycler so it can warm up.

2) DNA removal 1: incubate 1 µL gDNA wipeout buffer (orange tubes) with up to 100 ng RNA. Bring total volume to 7 µL with RNase-free water.

3) Run the 'ScxGFP' program, which begins by incubating mix at 42°C for 2 min.

4) DNA removal 2: add 1 µL of 10x DNase I buffer, 1 µL DNase I, and 1 µL RNase-free water to bring total volume to 10 µL. Incubate at RT for 15 min.

5) Inactivate DNase I by adding 1 µL of EDTA solution. Heat at 65°C for 10 min.

6) Add 1 µL of reverse primer (20 µM stock), 1 µL reverse transcriptase (red tubes), 1 µL DTT (100 mM stock), 2 µL RNase-free water, and 4 µL RT buffer (green tube WITHOUT primers added) to each tube to bring total volume to 20 µL.

7) Set up a reverse transcriptase-free control to test for the presence of genomic DNA contamination.

8) Incubate mix at 42°C for 15 min.

9) Incubate mix at 95°C for 3 min to inactivate reverse transcriptase.

10) Dilute RNase H so that 2 U are added to each reaction and then add 1 µL of the diluted RNase H to mix and incubate at 37°C for 20 min.

11) Freeze down cDNA for later use or dilute reaction 10 times in 179 µL RNase-free water to perform regular PCR using primers specific to the coding sequence of the scleraxis gene and encoding restriction sites to facilitate cloning in pEGFP-N1 and pEGFP-C1.

E.12 PCR protocol

Reference: (Duffy, McFadden et al. 2011; Caliari, Weisgerber et al. 2012)

Reagents

- QuantiTect SYBR Green Kit (Qiagen 204145); store at -20°C although individual kit aliquots may be stored at 4°C once opened.
- Primers (Integrated DNA Technologies)
    - Dilute to 30 µM in TE buffer (pH = 8.0)
    - Aliquot and store at -20°C or keep at 4°C
- Ice
- DNase removal buffer

Supplies and equipment

- Rainier multi-pipettes
- 384-well plates (Invitrogen 4309849)
- Plate covers (Invitrogen 4311971)
- Sealing tool
- Rainier pipette tips (VWR)
- RNase-free PCR tubes (500 µL, CLSL stockroom)
- Ice bucket
- Vortex (Fisher 02-215-365)
- Applied Biosystems 7900HT Fast Real-Time PCR system (Applied Biosystems)
- Sequence Detection Systems software v2.4 (Applied Biosystems)

Procedure

*Note: keep PCR area as clean as possible and remember to wipe down area with DNase removal buffer following each plate prep. Remember to reserve time on the PCR system on the IGB website (each plate takes 1 h 55 min to run).

1) Diagram plate layout and determine the amount of water, SYBR green, and primers you will need. Master mix 1 consists of SYBR green and primers, and is added at 5.2 µL per well for 10 µL reactions. Master mix 2 is RNase-free water and cDNA, and is added at 4.8 µL per well for 10 µL reactions. Make up ~ 10% excess reagent for each mix.

2) Make up master mixes. Vortex each tube of master mix 1 thoroughly and pipet into wells.

3) Vortex each tube of master mix 2 thoroughly and pipet into wells.

4) Place cover on plate. Make sure the plate is sealed tightly on all edges with the sealing tool.

5) Keep plate protected from light at 4°C until ready to analyze.

6) Transport to IGB 124A and set up plate on PCR machine. Follow instructions obtained during training on machine, making sure to add extra stage to determining product melting point. SYBR

green dye non-specifically binds to all DNA, so the melting curve must be obtained to confirm the presence of a single product.

7) Analyze results using the Sequence Detection Systems software to obtain Ct values. For multiple plates, make sure the threshold is set at the same number for each primer pair. Calculate fold changes in expression using the delta-delta Ct method.

E.13 Protein isolation protocol

Reference: (Caliari and Harley in preparation)

Reagents

- RIPA buffer (500 mL)
    - 495 mL deionized water
    - 4.38 g sodium chloride (150 mM, RAL storeroom)
    - 5 mL Triton X-100 (1%, Sigma 93443-100ML)
    - 2.5 g sodium deoxycholate (0.5%, Sigma D6750-10G)
    - 0.5 g SDS (0.1%, Sigma L3771-25G)
    - 3.03 g Tris base (50 mM, RAL storeroom)
    - Adjust pH to 8.0 and store at 4°C
- Protease inhibitor cocktail (Sigma P8340-1ML)
- Phosphatase inhibitor cocktail 2 (Sigma P5726-1ML)
- Phosphatase inhibitor cocktail 3 (Sigma P0044-1ML)
- Ice
- Sterile phosphate-buffered saline without Ca^{2+} or Mg^{2+} (PBS)

Supplies and equipment

- Ice bucket
- Microcentrifuge tubes
- Vortex (Fisher 02-215-365)

Procedure

*Note: steps 2-3 should be performed in the laminar flow hood.

1) Label microcentrifuge tubes for each sample. Prepare ~ 200 µL of ice-cold RIPA buffer per sample and add protease and phosphatase inhibitors (100x stocks) fresh to the buffer.

2) Rinse scaffold pieces in PBS to remove dead and unattached cells. Place scaffolds in empty, labeled microcentrifuge tubes.

3) Pipet 150-200 µL complete RIPA buffer onto each scaffold piece.

4) Keep scaffolds on ice for 30 min, agitating with a pipet tip occasionally to aid buffer infiltration.

5) After 30 min, remove scaffold from tubes, squeeze out excess liquid, and store lysates at -80°C until use.

E.14 Western blotting protocol

Reference: (Caliari and Harley in preparation)

Reagents

- Running buffer (1L, 10x); store at 4°C
    - 30.3 g Tris base (0.25 M, RAL storeroom)
    - 144 g glycine (1.92 M, RAL storeroom)
    - 10 g SDS (1%, Sigma L3771-25G)
    - Bring volume to 1 L in deionized water, sterile filter
- Running buffer: Need ~700 mL per gel (when running 1-2 gels), can re-use several times
    - 10% 10x running buffer
    - 90% deionized water
    - Final concentrations:25 mM Tris base, 192 mM glycine, 0.1% SDS. pH will be ~ 8.3.Store at 4°C.
- Towbin's electrotransfer buffer (1 L, 10x); store at 4°C
    - 30.3 g Tris base (0.25 M, RAL storeroom)
    - 144 g glycine (1.92 M, RAL storeroom)
    - Bring volume to 1 L in deionized water, sterile filter
- Transfer buffer: Need ~1 L per gel, can re-use several times
    - 20% Methanol (RAL storeroom)
    - 10% 10x Towbin's electrotransfer buffer
    - 70% Water
    - Store at 4°C
- TBS-T (1 L, 10x); store at 4°C
    - 24.2 g Tris base (0.2 M, RAL storeroom)
    - 80 g NaCl (RAL storeroom)
    - 10 mL Tween 20 (1% v/v, RAL storeroom)
- TBS-T (1x); store at 4°C
    - 10% 10x TBS-T
    - 90% deionized water
    - Final concentrations:20 mM Tris base, 0.8% w/v NaCl, 0.1 % v/v Tween 20, pH will be ~ 7.5
- 4x Laemlii buffer (CLSL stockroom): Need ~ 12 µL per sample
- Blocking Buffer (TBS-T + 5% non-fat milk)
    - 100 mL TBS-T
    - 5 g non-fat milk powder
    - Mix for ~ 15 min before use
- Ponceau S stain (Fisher Scientific, K793-500mL)
- Ice
- Deionized water
- β-mercaptoethanol (Sigma M7522-100ML)
- Stripping buffer (CLSL stockroom)

Supplies and equipment

- IGB shared equipment

    - Glass container
    - Biorad Mini-Protein apparatus
- Rainbow ladder (GE Healthcare, CLSL stockroom); store at -20°C
- Microcentrifuge tubes
- Gel-loading pipet tips
- Nitrocellulose membrane (Fisher Scientific, RPN303E)
- Whatman paper
- SuperSignal West Pico Chemiluminescence substrate (ECL reagents, CLSL stockroom); store at 4°C
- 10% polyacrylamide gels (CLSL stockroom); store at 4°C
- Plastic forceps
- Ice bucket
- Kimwipes
- Image Quant gel reader (GE Healthcare, IGB 124A)

Procedure

<u>Day 1: Protein lysate gel electrophoresis, transfer, primary antibody</u>

1) Have buffers and gels ready.

2) Thaw lysates on ice while walking to IGB.

3) Upon arrival, turn on heating block to 95°C on Schook's bench.

4) Label microcentrifuge tubes and prepare 4x Laemlii buffer by adding 0.5 µL β-mercaptoethanol for every 12 µL of buffer.

5) Add 37.5µL of lysate and 12.5 µL of Laemlii + β-mercaptoethanol per tube,

6) Heat tubes at 95°C in heating block for 5-10 min.

7) While tubes are heating, remove gels from fridge and rinse with water.

8) Take strip off bottom and place it to the front of electrophoresis apparatus.

9) Place a blank plastic cassette or another gel on the back side. Make sure everything is clamped in properly. (Red-red; black-black).

10) Pour running buffer between cassettes until gel is immersed. Fill container with running buffer to 2-gallon mark.

11) Take sample tubes. Spin down for a few seconds if you have solid pieces from hydrogels/scaffolds.

12) Carefully load 50 µL lysate/Laemlii mix into each lane (behind plate) using gel-loading tips.

Don’t use first or last lane. Load 5 µL rainbow ladder to one lane for reference.

13) Run at 80 V for 5-10 min until lysates become thin bands in stacking gel. This step can be run at RT but running at 4°C may reduce “smiley face effect.” There is a power supply available in the back 4°C cold room.

14) Run gel at 100 V for ~ 1.5 h until all lysates (blue line) arrive at the bottom black line. Check progress after 1 h to make sure proteins don’t run off the gel.

15) Prepare nitrocellulose membranes, filter papers, and transfer buffer ~ 15 min before gel is finished running. Cut membranes to match gel size.

16) Kill power and rinse gel cartridge thoroughly with DI water. Carefully open gel cartridge using opening lever by cracking open at 4 sides marked by arrowheads.

17) Remove stacking gel and rinse with water. Cut lane borders on top with green cutting tool.

18) Pour transfer buffer to the glass container. Then, prepare the transfer cassette assembly by stacking in the following order then soak it in transfer buffer in the glass container.

- Case (clear side)
- Sponge
- Whatman paper
- Membrane
- Gel
- Whatman paper
- Sponge
- Case (black side; negative terminal)

19) Use plastic forceps and/or green cutting tool to carefully maneuver the gel so that the entire area lays on the membrane.

20) Remove air bubbles by rolling with plastic pipet and then close cassette.

21) Place assembly in plastic module then into electrophoresis apparatus. Remember to match colors (e.g. black faces black).

22) Fill apparatus completely with transfer buffer, using big beaker to transfer buffer from glass container to the apparatus.

23) Place cooling unit (stored in far -20°C freezer) in buffer and transfer at 300 mA for 2 h at 4°C in far cold room.

24) After 2 h, take apart assembly. Discard filter paper and gel (nothing should be left in the gel, indicating the transfer was successful). Nick membrane edge (top left corner) with scissors so you know which side the protein is on (this is the side of the membrane that faced the gel!)

25) Stain with Ponceau S (1x) to check protein bands. Bands may not appear. Ponceau stain can be re-used. Cut bands according to molecular weight of desired targets while Ponceau stain is still visible. Rinse with TBS-T to remove stain.

26) Place membrane in mini plastic container (old microscope slide boxes) and pour in 10-15 mL blocking buffer. Incubate for 30 min on a shaker (~ 50 rpm).

27) While waiting, prepare primary antibody solution in ~ 5mL blocking buffer. Typical dilution is 1:2000, but optimize for each antibody. Note that primary antibodies diluted in blocking buffer can be used again. Store at -20°C or at 4°C for short times (< 2 weeks).

28) Incubate membranes in primary antibody solution overnight at 4°C on shaker.

Day 2 Secondary antibody, read blot using ECL reagents (enhanced chemiluminescence)

1) Wash membranes with TBS-T for 5 min on shaker at RT (3x).

2) While waiting, prepare 5 mL secondary antibody solution (1:2500 dilution) in blocking buffer from fridge. Make sure you use matching (anti-rabbit; anti-mouse, etc) secondary antibody.

3) Incubate in secondary antibody solution for 1 hr at RT under gentle shaking.

4) Wash membranes with TBS-T for 5 min on shaker at RT (3x).

5) While waiting, gather supplies for ECL detection: gloves, 15 mL conical tube, 1 mL pipette with tips, plastic forceps, and ECL reagents. Once membranes are finished rinsing add them to box of supplies.

6) Go down to IGB 124A. There should already be Kimwipes and saran wrap in this room.

7) Once in basement, log onto computer and start up the ImageQuant program.

8) Mix ECL reagents (1:1; make ~ 2 mL per full membrane).

9) Place saran wrap on a flat surface. Pick up your membrane with forceps then gently blot using Kimwipes. Quickly do this for all membranes and pipette mixed ECL solution onto the membranes.

10) Wrap membranes in saran wrap and keep in drawer for 2 min.

11) Take membranes from the drawer, blot, and place on clean saran wrap with forceps.

12) Place membranes in the detection chamber and focus to ensure membrane is in viewing window. Make sure the black tray is in the chamber and set at level 2 for chemiluminescence. Expose for 1 min first then adjust according to the output intensity.

13) Save image and perform post-analysis of band intensity using Gel Image Analyzer or ImageJ.

Stripping for re-probing

1) It may be desirable to strip the antibodies and re-probe for another protein that is close in molecular weight. To do this, begin by washing the membranes in TBS-T for 5 min (1x).

2) Cover membranes in stripping buffer and incubate under gentle shaking for 15 min.

3) Wash membranes in TBS-T for 5 min (3x).

4) Re-block membranes in blocking buffer for 30 min at RT under gentle shaking (see day 1 step 26). Repeat steps from here to completion.

E.15 Histology preparation protocol

Reference: (Caliari and Harley in preparation; Caliari and Harley submitted)

Reagents

- Formalin solution, 10% formaldehyde in neutral buffer (Polysciences 08379-3.75)
- Sterile phosphate-buffered saline without Ca^{2+} or Mg^{2+} (PBS)

Supplies and equipment

- Microcentrifuge or conical tubes
- Paraffin infiltration machine
- Embedding machine
- Microtome (Leica)
- Microscope slides

Procedure

1) Rinse samples in PBS to remove dead/unattached cells and then place samples in formalin. Store at 4°C overnight, replace formalin, and store at 4°C until next step.

2) Place samples in labeled plastic cages complete with blue foam dividers. Be sure to note orientation if trying to look at transverse versus longitudinal scaffold planes.

3) In the afternoon follow instructions on paraffin wax infiltrator to run samples overnight (until 10 am next day).

4) Next day: Take 10-15 min to warm up water bath (40°F), turn on embedding machine on left.

5) Fill metal mold with wax, insert sample face down and hold down with forceps on cooling block as paraffin solidifies.

6) Add on top part of cage (with sample ID) and backfill with paraffin wax, pushing out bubbles on top with forceps on hot part. Then place on cooling block to solidify for 10-15 min. Make sure to trim edges before mounting.

7) Turn on microtome. Make sure locks are in place while manipulating things.

8) Face the block, and turn crank (remember to turn towards wall) to obtain slices. Brush waste up and out with big brush. Start at left of blade and bring to sample. Slices can be obtained automatically by pushing the two blue buttons on the control panel simultaneously. Adjust speed accordingly.

9) Slice thickness: 5-7 µm. Use small brush to lift end of section trail. After 50-75 µm, grab ribbon edge with right hand and use small brush with left hand to separate carefully.

10) Place sections in water bath splaying out left to right, anchoring on side.

11) Dip slide into water under sections and use micropunch tool to cut between sections. Set aside slides to dry.

12) To change cutting blade: open lever on right, push guard pin over. The old blade goes in the bottom of the blade box; the new blade slides in place on the microtome same way.

E.16 Histological staining protocol

Reference: (Caliari and Harley in preparation; Caliari and Harley submitted)

Reagents

- Xylene (RAL storeroom)
- 95%, 100% ethanol (RAL storeroom)
- Acetone
- Deionized water
- Alizarin red solution (100 mL)
    - 2 g alizarin red (Sigma A5533-25G)
    - 100 mL deionized water, adjust pH to 4.1-4.3 with 2 drops 1M HCl
- Alcian blue solution (100 mL)
    - 1 g alcian blue (Sigma A3157-10G)
    - 97 mL deionized water
    - 3 mL glacial acetic acid (Sigma-Aldrich 71251)
- Hematoxylin
- Eosin
- Ammonium hydroxide
- Sterile phosphate-buffered saline without Ca^{2+} or Mg^{2+} (PBS)
- Deionized water

Supplies and equipment

- Histology stations (keep in fume hood)
- Microscope slides
- Cover slips
- Permount mounting medium (Fisher SP15-100)
- Vacuum oven (Welch Vacuum, Fisher 13-262-52)

Procedure

1) Cook slides in oven for ~ 1 h at 60°C to complete drying.

2) Set up stations in fume hood for depariffinization and do the following washes:

- Xylene 10 min x 2
- 100% ethanol 2 min x 2
- 95% ethanol 2 min
- 85% ethanol 2 min
- 70% ethanol 2 min
- PBS 2 min x 2

3) H&E staining:

- Stain in hematoxylin for 5-10 min
- Lightly wash several times with deionized water

- Blue in 0.2% ammonium water (0.2 mL ammonium hydroxide in 100 mL water) or pH 9.0 buffered solution for 30 s to 1 min.
- Lightly wash in water
- 70% ethanol 1 min
- 85% ethanol 1 min
- 95% ethanol 1 min
- 100% ethanol 1 min
- 100% ethanol 1 min
- Counterstain in eosin for 30 s to 1 min
- Differentiate in 95% ethanol, 1 min.
- 100% ethanol 5 min
- 100% ethanol 5 min
- Clear in xylene x2, 5 min each
- Mount on slides with Permount and coverslip

4) Alcian Blue staining:

- Stain in alcian blue solution for 30 min
- Lightly rinse with water
- Dehydrate through 95% alcohol, 100% alcohol 5 min each
- Clear in xylene x2, 5 min each
- Mount on slides with Permount and coverslip

5) Alizarin Red staining:

- Stain in alizarin red solution for 5 min
- Shake off, blot excess dye
- Dehydrate in acetone (20 dips), 50/50 mix of acetone/xylene (20 dips)
- Clear in xylene x2, 5 min each
- Mount on slides with Permount and coverslip

E.17 Immunohistochemisty protocol

Reference: Abcam, Cell Signaling websites

Reagents

- Xylene
- 100% ethanol
- 95% ethanol
- PBS w/0.1% Tween
- PBS w/3% BSA (blocking solution); store at 4°C
- Citrate buffer (500 mL)
    - 1.47 g sodium citrate dihydrate (Sigma W302600-1KG-K)
    - 500 mL deionized water
- Antibodies (dilute in blocking buffer)
    - Primary: Rabbit anti-SCX, rabbit anti-Patched1, mouse anti-β-catenin, typical dilution 1:1000
    - Secondary: Goat anti-rabbit AlexaFluor® 568, rabbit anti-mouse AlexaFluor® 488, typical dilution 1:1000
    - DAPI: 1:1000 dilution
- ProLong Gold; store at -20°C

Supplies and equipment

- Fume hood
- Washing station
- Humidity chamber
- Hot plate
- Parafilm
- Kimwipes
- Cover glasses
- Permount mounting medium (Fisher SP15-100)
- Hydrophobic pen
- Razor

Procedure

1) Cook slides in oven for ~ 1 h at 60°C to complete drying.

2) Set up stations in fume hood for depariffinization and do the following washes:

- Xylene 10 min x 2
- 100% ethanol 2 min x 2
- 95% ethanol 2 min
- 85% ethanol 2 min
- 70% ethanol 2 min
- PBS 2 min x 2

3) If HIER needed, put the sections in citrate buffer and cook at 105°C for 10 min (bring to boil).

4) Wash in deionized water 3 times.

5) Outline sections with hydrophobic pen and block sections in 3% BSA in PBS for at least 30 min at RT.

6) Carefully dry each slide with a Kimwipe, leaving a small amount of liquid over each sample section.

7) Add 30-50 µL of primary antibody on each slide. Add section of Parafilm onto slide to lock in moisture and place in black humidity chamber. Place chamber in refrigerator and store overnight.

8) Wash in PBS/Tween, 5 min (3x).

9) Repeat steps 6-7, replacing primary antibody with secondary antibody. Incubate slides at room temperature for 30 min.

10) Wash in PBS/Tween, 5 min (3x) in dark using wash station.

11) Repeat steps 6-7, replacing primary antibody with DAPI. Parafilm is not necessary here. Incubate slides at room temperature for 5 min.

12) Wash in PBS/Tween, 5 min (3x).

13) Repeat step 6 and add one drop of ProLong Gold onto each scaffold section. Press cover glass firmly onto slide and clean up excess liquid.

14) Allow to dry at room temperature in the dark and then store at 4°C in the dark until visualization.

E.18 Confocal imaging protocol

Reference: Invitrogen website, personal communication with Shiv Sivaguru

Reagents

- Formalin solution, 10% formaldehyde in neutral buffer (Polysciences 08379-3.75)
- Sterile phosphate-buffered saline without Ca^{2+} or Mg^{2+} (PBS)
- ITsignal FX (Invitrogen I36933); store at 4°C
- AlexaFluor® 488-phallodin (Invitrogen A12379); store at -20°C
- DAPI and Hoechst stocks; store at 4°C

Supplies and equipment

- 6-well plates
- Kimwipes
- Glass round bottom dishes
- Forceps
- Leica LSM 710 confocal microscope (IGB core facilities)
- ZEN analysis software

Procedure

<u>Example sample prep for imaging actin/nuclei and second harmonic generation (SHG) imaging</u>

1) Rinse samples in PBS to remove dead/unattached cells and then place samples in formalin. Store at 4°C overnight, replace formalin, and store at 4°C until next step.

2) Wash scaffolds in PBS for 1 min (3x).

3) Incubate scaffolds in 0.1% Triton X100 in PBS for 15 min.

4) Wash scaffolds in PBS for 1 min (3x).

5) Add 8 drops (~ 400 µL) of ITsignal FX per 1.6 mL PBS and incubate scaffolds for 30 min.

6) Dilute 25 µL of AlexaFluor® 488-phallodin dye methanolic stock solution per 1 mL PBS/ITSignal FX (800 µL PBS plus 5 drops of ITSignal FX).

7) Incubate scaffolds in solution for 30 min. Keep samples in the dark.

8) Wash scaffolds in PBS for 1 min (3x).

9) Dilute 1 µL of DAPI or Hoechst stock per 800 µL PBS and incubate scaffolds in solution for 5 min. Note: omit this step for SHG imaging or use alternative nuclear stain such as propidium iodide (PI).

10) Wash scaffolds in PBS for 1 min (3x).

11) Store scaffolds in PBS in the dark at 4°C until imaging.

Confocal and SHG imaging

1) Reserve time on confocal microscope (LSM 710) using calendar on IGB core website. The training contact is Mayandi (Shiv) Sivaguru.

2) Log on to computer and double click on MaiTai icon, make sure 'Comport 4' is selected, and click OK.

3) Press and hold 'ON' button until you see emission.

4) Wait until the bar reaches ~ 2.4-2.8 W IR power to proceed further.

5) While waiting, prepare first sample on glass bottom well dishes, making sure sample is adequately hydrated but not sitting on top of a puddle.

6) Press and hold 'SHUTTER' until button turns yellow.

7) Click file > exit and select 'close shutter and exit'.

8) Open ZEN program and start system.

9) Set rear to green and objective to 10x, then select online.

10) Carefully load sample dish onto microscope.

11) Select 'load position' and hit up arrow with bar on the left.

12) Bring sample into focus on the microscope.

13) Load personal settings file and select 're-use' on bottom screen. Note that Shiv will help set this file up for each unique staining combination needed.

14) Starting with a scaffold that has a lot of cells, center laser on scaffold and find scaffold surface.

15) Tune laser power and gains on respective channels accordingly so that there are a few red pixels after pressing ch1 and ch2 buttons. Do not set gains above 900 or laser power above 5%.

16) Once these settings have been optimized, proceed to imaging and do not change sample to sample. Note that the door should be shut with the computer monitors turned off while taking SHG images.

17) Zoomed out overview image settings: Zoom 2, frame size 512 x 512, speed 9, line average 4. Zoomed in image settings: Zoom 3.5, frame size 1024 x 1024, speed 8, line average 4.

18) Remember to transfer files from D drive to U drive at the end of every session before logging off.

19) Analyze images on personal computer using ZEN software.

E.19 Fluorescence imaging protocol

Supplies and equipment

- Leica fluorescence microscope (IGB 2nd floor)
- ImagePro software
- ImageJ

Procedure

Image acquisition

1) Turn on three boxes on bottom left.

2) Log in to IGB, password is 'rebterebte'.

3) Open ImagePro and click on camera icon.

4) Focus sample in brightfield using coarse focus on left.

5) Push 'TL/IL' button on left of scope to switch to fluorescence.

6) Channels include blue, red, green, and orange.

7) Use camera and view buttons on front of scope to toggle back and forth between channels.

8) Press preview button and adjust exposure time accordingly until image is visible. Once exposure time is set, keep constant for subsequent samples.

Image analysis

1) Perform analysis in ImageJ. Images will be in black and white.

2) Create a color image by doing the following:

- File > Open [filename.tif]
- Image > Look-Up Tables > (select any color).
- Save image as jpg.

3) Create a composite image by opening images to be merged and doing the following:

- Image > Color > Merge Channels. Select the individual files desired for each channel, check 'Create Composite', and click 'Ok'.
- Save new composite image as a tiff.

E.20 Orientation analysis protocol

Reference: (Caliari and Harley 2011; Gonnerman, McGregor et al. 2011)

Supplies and equipment

- Microcentrifuge tubes
- Leica Contrast-Phase Microscope
- ImageJ Software
- Microsoft Excel

Procedure

*This procedure requires the use of the "OrientationJ" plugin for ImageJ. It can be downloaded from the following website: http://bigwww.epfl.ch/demo/orientation/ under "Installation for final users."

Cell orientation analysis

1) Prepare samples for histology (see protocol E.15), making sure to note the orientation of the samples.

2) Stain slides using H&E protocol (see protocol E.16).

3) Using the contrast-phase microscope on the open filter (to get the maximum color contrast for the H&E stain, with cells appearing purple and scaffold pink), capture ~ 3 images per slide (9 per sample) for a total of 400-500 cells per sample. Save images as TIF files.

4) Use the OrientationJ plugin for ImageJ to analyze each cell's orientation angle:

- File > Open [filename.tif]
- Image > Color > Channels Tool.
- Select "Color" from dropdown menu.
- Select the "OK" button.
- Plugins > OrientationJ > OrientationJ Measure.
- Highlight the cell to analyze using the oval drawing tool.
- Press the "Measure" button. (Note: Make sure that the oval drawn encapsulates the entire cell.)

5) Analyzing each cell will give three orientation angles (one for each color channel), but the values should be similar. Copy and paste data into Excel.

6) Create a histogram of the data using Excel.

Scaffold strut orientation analysis

1) Obtain SEM images of longitudinal and transverse scaffold planes. 30x magnification is ideal, and remember to save images without the image data written onto the tiff file.

2) Use the OrientationJ plugin for ImageJ to analyze the overall orientation of the scaffold struts:

- File > Open [filename.tif]
- Plugins > OrientationJ > OrientationJ Distribution.
- Set Min. Coherency to 10%, Min. Energy to 1%, and click 'Run'.
- A graph of the distribution of the image feature orientation angles will appear. Click on 'List' and copy the data to Excel.

3) Create a histogram of the data using Excel. Typically, three images of each section (bottom, middle, top) of each plane of the scaffold are used to calculate the orientation distribution.

Collagen orientation analysis

1) Prepare samples for confocal imaging and obtain SHG images of collagen organization (see protocol E.18).

2) Use the OrientationJ plugin for ImageJ to analyze collagen fiber orientation angles:

- File > Open [filename.tif]
- Image > Color > Split Channels. Perform analysis on image from green (collagen) channel.
- Process > Binary > Make Binary.
- Plugins > OrientationJ > OrientationJ Measure.
- Highlight the collagen fiber to analyze using the oval drawing tool.
- Press the "Measure" button.

3) Copy and paste data into Excel and create a histogram of the data. Typically, at least 100 collagen fibers should be measured per group.

REFERENCES

Abrahamsson, S. O., G. Lundborg, et al. (1991). "Recombinant human insulin-like growth factor-I stimulates in vitro matrix synthesis and cell proliferation in rabbit flexor tendon." J Orthop Res **9**(4): 495-502.

Agrawal, C. M., J. S. McKinney, et al. (2000). "Effects of fluid flow on the in vitro degradation kinetics of biodegradable scaffolds for tissue engineering." Biomaterials **21**(23): 2443-2452.

Ahearne, M., P. O. Bagnaninchi, et al. (2008). "Online monitoring of collagen fibre alignment in tissue-engineered tendon by PSOCT." Journal of Tissue Engineering and Regenerative Medicine **2**(8): 521-524.

Aizawa, Y., R. Wylie, et al. (2010). "Endothelial Cell Guidance in 3D Patterned Scaffolds." Advanced Materials **22**(43): 4831-+.

Akizuki, S., V. C. Mow, et al. (1986). "Tensile properties of human knee joint cartilage: I. Influence of ionic conditions, weight bearing, and fibrillation on the tensile modulus." J Orthop Res **4**(4): 379-392.

Al-Munajjed, A. A. and F. J. O'Brien (2009). "Influence of a novel calcium-phosphate coating on the mechanical properties of highly porous collagen scaffolds for bone repair." J Mech Behav Biomed Mater **2**(2): 138-146.

Alhadlaq, A. and J. J. Mao (2005). "Tissue-engineered osteochondral constructs in the shape of an articular condyle." Journal of Bone and Joint Surgery-American Volume **87A**(5): 936-944.

Allan, K. S., R. M. Pilliar, et al. (2007). "Formation of biphasic constructs containing cartilage with a calcified zone interface." Tissue Engineering **13**(1): 167-177.

Allen, J. L., M. E. Cooke, et al. (2012). "ECM stiffness primes the TGFβ pathway to promote chondrocyte differentiation." Molecular Biology of the Cell **23**(18): 3731-3742.

Almodovar, J., T. Crouzier, et al. (2013). "Gradients of physical and biochemical cues on polyelectrolyte multilayer films generated via microfluidics." Lab on a Chip.

Altman, G. H., R. L. Horan, et al. (2002). "Silk matrix for tissue engineered anterior cruciate ligaments." Biomaterials **23**(20): 4131-4141.

Altman, G. H., R. L. Horan, et al. (2002). "Cell differentiation by mechanical stress." Faseb J **16**(2): 270-272.

Andalib, M. N., J. S. Lee, et al. "The role of RhoA kinase (ROCK) in cell alignment on nanofibers." Acta Biomaterialia(0).

Anderson, D. G., S. Levenberg, et al. (2004). "Nanoliter-scale synthesis of arrayed biomaterials and application to human embryonic stem cells." Nature Biotechnology **22**(7): 863-866.

Anderson, S. M., T. T. Chen, et al. (2009). "The phosphorylation of vascular endothelial growth factor receptor-2 (VEGFR-2) by engineered surfaces with electrostatically or covalently immobilized VEGF." Biomaterials **30**(27): 4618-4628.

Aspenberg, P. and C. Forslund (1999). "Enhanced tendon healing with GDF 5 and 6." Acta Orthop Scand **70**(1): 51-54.

Barboni, B., V. Curini, et al. (2012). "Indirect Co-Culture with Tendons or Tenocytes Can Program Amniotic Epithelial Cells towards Stepwise Tenogenic Differentiation." PLoS ONE **7**(2).

Beck, G. R., B. Zerler, et al. (2000). "Phosphate is a specific signal for induction of osteopontin gene expression." Proceedings of the National Academy of Sciences of the United States of America **97**(15): 8352-8357.

Bencherif, S. A., R. W. Sands, et al. (2012). "Injectable preformed scaffolds with shape-memory properties." Proc Natl Acad Sci U S A.

Benjamin, M. and J. R. Ralphs (2000). "The cell and developmental biology of tendons and ligaments." Int Rev Cytol **196**: 85-130.

Berendsen, A. D., L. W. Fisher, et al. (2011). "Modulation of canonical Wnt signaling by the extracellular matrix component biglycan." Proc Natl Acad Sci U S A.

Berthet, E., C. Chen, et al. (2013). "Smad3 Binds Scleraxis and Mohawk and Regulates Tendon Matrix Organization." J Orthop Res.

Birk, D. E. and R. Mayne (1997). "Localization of collagen types I, III and V during tendon development. Changes in collagen types I and III are correlated with changes in fibril diameter." Eur J Cell Biol **72**(4): 352-361.

Boerboom, R. A., M. P. Rubbens, et al. (2008). "Effect of strain magnitude on the tissue properties of engineered cardiovascular constructs." Ann Biomed Eng **36**(2): 244-253.

Boileau, P., N. Brassart, et al. (2005). "Arthroscopic repair of full-thickness tears of the supraspinatus: does the tendon really heal?" J Bone Joint Surg Am **87**(6): 1229-1240.

Brehm, W., B. Aklin, et al. (2006). "Repair of superficial osteochondral defects with an autologous scaffold-free cartilage construct in a caprine model: implantation method and short-term results." Osteoarthritis and Cartilage **14**(12): 1214-1226.

Brent, A. E., R. Schweitzer, et al. (2003). "A somitic compartment of tendon progenitors." Cell **113**(2): 235-248.

Burdick, J. A., A. Khademhosseini, et al. (2004). "Fabrication of gradient hydrogels using a microfluidics/photopolymerization process." Langmuir **20**(13): 5153-5156.

Butler, D. L., N. Juncosa-Melvin, et al. (2008). "Functional tissue engineering for tendon repair: A multidisciplinary strategy using mesenchymal stem cells, bioscaffolds, and mechanical stimulation." J Orthop Res **26**(1): 1-9.

Caceres, M., C. Suwyn, et al. (2007). "Increased cortical expression of two synaptogenic thrombospondins in human brain evolution." Cereb Cortex **17**(10): 2312-2321.

Caliari, S. R., E. A. Gonnerman, et al. (in preparation). "Macroporous collagen scaffold gradient arrays for parallel identification of biophysical and biochemical regulators of cell activity."

Caliari, S. R. and B. A. Harley (2013). "Composite Growth Factor Supplementation Strategies to Enhance Tenocyte Bioactivity in Aligned Collagen-GAG Scaffolds." Tissue Eng Part A **19**(9-10): 1100-1112.

Caliari, S. R. and B. A. C. Harley (2011). "The effect of anisotropic collagen-GAG scaffolds and growth factor supplementation on tendon cell recruitment, alignment, and metabolic activity." Biomaterials **32**(23): 5330-5340.

Caliari, S. R. and B. A. C. Harley (in preparation). "Selective modification of collagen-GAG scaffold structural and biochemical properties to enhance tenogenic, chondrogenic, and osteogenic MSC differentiation."

Caliari, S. R. and B. A. C. Harley (submitted). "Collagen-GAG scaffold biophysical properties bias MSC lineage selection in the presence of mixed soluble signals."

Caliari, S. R., M. A. Ramirez, et al. (2011). "The development of collagen-GAG scaffold-membrane composites for tendon tissue engineering." Biomaterials **32**(34): 8990-8998.

Caliari, S. R., D. W. Weisgerber, et al. (2012). "The influence of collagen-glycosaminoglycan scaffold relative density and microstructural anisotropy on tenocyte bioactivity and transcriptomic stability." J Mech Behav Biomed Mater **11**: 27-40.

Camper, L., D. Heinegård, et al. (1997). "Integrin α2β1 Is a Receptor for the Cartilage Matrix Protein Chondroadherin." The Journal of Cell Biology **138**(5): 1159-1167.

Canseco, J. A., K. Kojima, et al. (2012). "Effect on Ligament Marker Expression by Direct-Contact Co-Culture of Mesenchymal Stem Cells and Anterior Cruciate Ligament Cells." Tissue Eng Part A.

Capito, R. M. and M. Spector (2007). "Collagen scaffolds for nonviral IGF-1 gene delivery in articular cartilage tissue engineering." Gene Ther **14**(9): 721-732.

Castro, N. J., S. A. Hacking, et al. (2012). "Recent progress in interfacial tissue engineering approaches for osteochondral defects." Ann Biomed Eng **40**(8): 1628-1640.

Cha, C., W. B. Liechty, et al. (2012). "Designing Biomaterials To Direct Stem Cell Fate." ACS Nano **6**(11): 9353-9358.

Chamberlain, L. J., I. V. Yannas, et al. (1998). "Collagen-GAG substrate enhances the quality of nerve regeneration through collagen tubes up to level of autograft." Exp Neurol **154**(2): 315-329.

Chatterjee, K., S. Lin-Gibson, et al. (2010). "The effect of 3D hydrogel scaffold modulus on osteoblast differentiation and mineralization revealed by combinatorial screening." Biomaterials **31**(19): 5051-5062.

Chen, J., H. Chen, et al. (2011). "Simultaneous regeneration of articular cartilage and subchondral bone in vivo using MSCs induced by a spatially controlled gene delivery system in bilayered integrated scaffolds." Biomaterials **32**(21): 4793-4805.

Chen, K., P. Shi, et al. (2013). "In vitro generation of a multilayered osteochondral construct with an osteochondral interface using rabbit bone marrow stromal cells and a silk peptide-based scaffold." Journal of Tissue Engineering and Regenerative Medicine: n/a-n/a.

Chen, Y. J., M. C. Chung, et al. (2011). "The effects of acellular amniotic membrane matrix on osteogenic differentiation and ERK1/2 signaling in human dental apical papilla cells." Biomaterials.

Cheng, X., U. A. Gurkan, et al. (2008). "An electrochemical fabrication process for the assembly of anisotropically oriented collagen bundles." Biomaterials **29**(22): 3278-3288.

Cho, W. K., J. A. Ankrum, et al. (2012). "Microstructured barbs on the North American porcupine quill enable easy tissue penetration and difficult removal." Proc Natl Acad Sci U S A.

Choi, J. S. and B. A. Harley (2012). "The combined influence of substrate elasticity and ligand density on the viability and biophysical properties of hematopoietic stem and progenitor cells." Biomaterials **33**(18): 4460-4468.

Clegg, P. D., S. Strassburg, et al. (2007). "Cell phenotypic variation in normal and damaged tendons." International Journal of Experimental Pathology **88**(4): 227-235.

Coburn, J. M., M. Gibson, et al. (2012). "Bioinspired nanofibers support chondrogenesis for articular cartilage repair." Proc Natl Acad Sci U S A **109**(25): 10012-10017.

Cole, D. W., T. A. Ginn, et al. (2005). "Cost comparison of anterior cruciate ligament reconstruction: autograft versus allograft." Arthroscopy **21**(7): 786-790.

Cooper, J. A., Jr., J. S. Sahota, et al. (2007). "Biomimetic tissue-engineered anterior cruciate ligament replacement." Proc Natl Acad Sci U S A **104**(9): 3049-3054.

Cosson, S., S. Allazetta, et al. (2013). "Patterning of cell-instructive hydrogels by hydrodynamic flow focusing." Lab Chip.

Costa, M. A., C. Wu, et al. (2006). "Tissue engineering of flexor tendons: Optimization of tenocyte proliferation using growth factor supplementation." Tissue Engineering **12**(7): 1937-1943.

Crouzier, T., L. Fourel, et al. (2011). "Presentation of BMP-2 from a Soft Biopolymeric Film Unveils its Activity on Cell Adhesion and Migration." Advanced Materials **23**(12): H111-H118.

Crouzier, T., K. Ren, et al. (2009). "Layer-By-Layer Films as a Biomimetic Reservoir for rhBMP-2 Delivery: Controlled Differentiation of Myoblasts to Osteoblasts." Small **5**(5): 598-608.

Cunniffe, G. M., G. R. Dickson, et al. (2010). "Development and characterisation of a collagen nano-hydroxyapatite composite scaffold for bone tissue engineering." Journal of Materials Science-Materials in Medicine **21**(8): 2293-2298.

Curtin, C. M., G. M. Cunniffe, et al. (2012). "Innovative collagen nano-hydroxyapatite scaffolds offer a highly efficient non-viral gene delivery platform for stem cell-mediated bone formation." Adv Mater **24**(6): 749-754.

Date, H., T. Furumatsu, et al. (2010). "GDF-5/7 and bFGF activate integrin alpha2-mediated cellular migration in rabbit ligament fibroblasts." J Orthop Res **28**(2): 225-231.

Day, T. F., X. Z. Guo, et al. (2005). "Wnt/beta-catenin signaling in mesenchymal progenitors controls osteoblast and chondrocyte differentiation during vertebrate skeletogenesis." Developmental Cell **8**(5): 739-750.

DeForest, C. A. and K. S. Anseth (2011). "Cytocompatible click-based hydrogels with dynamically tunable properties through orthogonal photoconjugation and photocleavage reactions." Nature Chemistry **3**(12): 925-931.

DeForest, C. A., B. D. Polizzotti, et al. (2009). "Sequential click reactions for synthesizing and patterning three-dimensional cell microenvironments." Nat Mater **8**(8): 659-664.

Derwin, K. A., A. R. Baker, et al. (2006). "Commercial extracellular matrix scaffolds for rotator cuff tendon repair - Biomechanical, biochemical, and cellular properties." Journal of Bone and Joint Surgery-American Volume **88A**(12): 2665-2672.

Dormer, N. H., M. Singh, et al. (2011). "Osteochondral interface regeneration of the rabbit knee with macroscopic gradients of bioactive signals." J Biomed Mater Res A.

Doroski, D. M., M. E. Levenston, et al. (2010). "Cyclic tensile culture promotes fibroblastic differentiation of marrow stromal cells encapsulated in poly(ethylene glycol)-based hydrogels." Tissue Eng Part A **16**(11): 3457-3466.

Dowd, T. L., J. F. Rosen, et al. (2001). "The effect of Pb(2+) on the structure and hydroxyapatite binding properties of osteocalcin." Biochim Biophys Acta **1535**(2): 153-163.

Du, L., P. Yang, et al. (2012). "Stromal cell-derived factor-1 significantly induces proliferation, migration, and collagen type I expression in a human periodontal ligament stem cell subpopulation." J Periodontol **83**(3): 379-388.

Duan, P., Z. Pan, et al. (2013). "The effects of pore size in bilayered poly(lactide-co-glycolide) scaffolds on restoring osteochondral defects in rabbits." Journal of Biomedical Materials Research Part A: n/a-n/a.

Duance, V. C., D. J. Restall, et al. (1977). "The location of three collagen types in skeletal muscle." FEBS Lett **79**(2): 248-252.

Duffy, G. P., T. M. McFadden, et al. (2011). "Towards in vitro vascularisation of collagen-GAG scaffolds." Eur Cell Mater **21**: 15-30.
Engler, A., L. Bacakova, et al. (2004). "Substrate compliance versus ligand density in cell on gel responses." Biophys. J. **86**: 617-628.
Engler, A. J., S. Sen, et al. (2006). "Matrix elasticity directs stem cell lineage specification." Cell **126**(4): 677-689.
Erisken, C., D. M. Kalyon, et al. (2008). "Functionally graded electrospun polycaprolactone and beta-tricalcium phosphate nanocomposites for tissue engineering applications." Biomaterials **29**(30): 4065-4073.
Farrell, E., F. J. O'Brien, et al. (2006). "A collagen-glycosaminoglycan scaffold supports adult rat mesenchymal stem cell differentiation along osteogenic and chondrogenic routes." Tissue Engineering **12**(3): 459-468.
Favata, M., P. K. Beredjiklian, et al. (2006). "Regenerative properties of fetal sheep tendon are not adversely affected by transplantation into an adult environment." J Orthop Res **24**(11): 2124-2132.
Felson, D. T. (2006). "Clinical practice. Osteoarthritis of the knee." N Engl J Med **354**(8): 841-848.
Fisher, O. Z., A. Khademhosseini, et al. (2010). "Bioinspired materials for controlling stem cell fate." Acc Chem Res **43**(3): 419-428.
Flaim, C. J., D. Teng, et al. (2008). "Combinatorial signaling microenvironments for studying stem cell fate." Stem Cells Dev **17**(1): 29-39.
Fonck, E., G. G. Feigl, et al. (2009). "Effect of aging on elastin functionality in human cerebral arteries." Stroke **40**(7): 2552-2556.
Fox, A. J. S., A. Bedi, et al. (2011). "Diabetes Mellitus Alters the Mechanical Properties of the Native Tendon in an Experimental Rat Model." Journal of Orthopaedic Research **29**(6): 880-885.
Frank, O., M. Heim, et al. (2002). "Real-time quantitative RT-PCR analysis of human bone marrow stromal cells during osteogenic differentiation in vitro." Journal of Cellular Biochemistry **85**(4): 737-746.
Freyman, T. M. (2001). Development of an In Vitro Model of Contraction by Fibroblasts. Dept. of Materials Science and Engineering. Cambridge, Massachusetts Institute of Technology.
Freyman, T. M., I. V. Yannas, et al. (2001). "Cellular materials as porous scaffolds for tissue engineering." Prog Mater Sci **46**(3-4): 273-282.
Freyman, T. M., I. V. Yannas, et al. (2001). "Micromechanics of fibroblast contraction of a collagen-GAG matrix." Exp Cell Res **269**: 140-153.
Freyman, T. M., I. V. Yannas, et al. (2001). "Fibroblast contraction of a collagen-GAG matrix." Biomaterials **22**(21): 2883-2891.
Galatz, L., S. Rothermich, et al. (2007). "Development of the supraspinatus tendon-to-bone insertion: localized expression of extracellular matrix and growth factor genes." J Orthop Res **25**(12): 1621-1628.
Galatz, L. M., L. J. Sandell, et al. (2006). "Characteristics of the rat supraspinatus tendon during tendon-to-bone healing after acute injury." J Orthop Res **24**(3): 541-550.
Galli, M., K. S. C. Comley, et al. (2009). "Viscoelastic and poroelastic mechanical characterization of hydrated gels." Journal of Materials Research **24**(3): 973-979.

Galli, M. and M. L. Oyen (2009). "Fast Identification of Poroelastic Parameters from Indentation Tests." Cmes-Computer Modeling in Engineering & Sciences **48**(3): 241-269.
Galperin, A., R. A. Oldinski, et al. (2012). "Integrated Bi-Layered Scaffold for Osteochondral Tissue Engineering." Advanced Healthcare Materials: n/a-n/a.
Gao, J. Z., J. E. Dennis, et al. (2001). "Tissue-engineered fabrication of an osteochondral composite graft using rat bone marrow-derived mesenchymal stem cells." Tissue Engineering **7**(4): 363-371.
Gao, J. Z., D. Knaack, et al. (2004). "Osteochondral defect repair by demineralized cortical bone matrix." Clinical Orthopaedics and Related Research(427): S62-S66.
Gao, L., R. McBeath, et al. (2010). "Stem Cell Shape Regulates a Chondrogenic Versus Myogenic Fate Through Rac1 and N-Cadherin." Stem Cells **28**(3): 564-572.
Gao, R. Z., J. E. Dennis, et al. (2002). "Repair of osteochondral defect with tissue-engineered two-phase composite material of injectable calcium phosphate and hyaluronan sponge." Tissue Engineering **8**(5): 827-837.
Garvican, E. R., A. Vaughan-Thomas, et al. (2008). "Chondrocytes harvested from osteochondritis dissecans cartilage are able to undergo limited in vitro chondrogenesis despite having perturbations of cell phenotype in vivo." J Orthop Res **26**(8): 1133-1140.
Genin, G. M., A. Kent, et al. (2009). "Functional grading of mineral and collagen in the attachment of tendon to bone." Biophys J **97**(4): 976-985.
Getgood, A. M. J., S. J. Kew, et al. (2012). "Evaluation of early-stage osteochondral defect repair using a biphasic scaffold based on a collagen–glycosaminoglycan biopolymer in a caprine model." The Knee **19**(4): 422-430.
Gibson, L. J., M. F. Ashby, et al. (2010). Cellular materials in nature and medicine. Cambridge, U.K., Cambridge University Press.
Gobaa, S., S. Hoehnel, et al. (2011). "Artificial niche microarrays for probing single stem cell fate in high throughput." Nat Methods **8**(11): 949-955.
Gonnerman, E. A., D. O. Kelkhoff, et al. (2012). "The promotion of HL-1 cardiomyocyte beating using anisotropic collagen-GAG scaffolds." Biomaterials **33**(34): 8812-8821.
Gotoh, M., K. Hamada, et al. (1997). "Significance of granulation tissue in torn supraspinatus insertions: an immunohistochemical study with antibodies against interleukin-1 beta, cathepsin D, and matrix metalloprotease-1." J Orthop Res **15**(1): 33-39.
Grinnell, F., C. H. Ho, et al. (2003). "Dendritic fibroblasts in three-dimensional collagen matrices." Mol Biol Cell **14**(2): 384-395.
Gross, G. and A. Hoffmann (2013). "Therapeutic strategies for tendon healing based on novel biomaterials, factors and cells." Pathobiology **80**(4): 203-210.
Guda, T., J. A. Walker, et al. (2012). "Guided Bone Regeneration in Long-Bone Defects with a Structural Hydroxyapatite Graft and Collagen Membrane." Tissue Eng Part A.
Gulotta, L. V. and S. A. Rodeo (2009). "Growth factors for rotator cuff repair." Clin Sports Med **28**(1): 13-23.
Gulotta, L. V. and S. A. Rodeo (2011). "Emerging ideas: Evaluation of stem cells genetically modified with scleraxis to improve rotator cuff healing." Clin Orthop Relat Res **469**(10): 2977-2980.
Guo, X. Z., T. F. Day, et al. (2004). "Wnt/beta-catenin signaling is sufficient and necessary for synovial joint formation." Genes & Development **18**(19): 2404-2417.
Guvendiren, M. and J. A. Burdick (2012). "Stiffening hydrogels to probe short- and long-term cellular responses to dynamic mechanics." Nat Commun **3**: 792.

Hagerty, P., A. Lee, et al. (2012). "The effect of growth factors on both collagen synthesis and tensile strength of engineered human ligaments." Biomaterials **33**(27): 6355-6361.
Halasz, K., A. Kassner, et al. (2007). "COMP acts as a catalyst in collagen fibrillogenesis." J Biol Chem **282**(43): 31166-31173.
Harley, B. A., T. M. Freyman, et al. (2007). "A new technique for calculating individual dermal fibroblast contractile forces generated within collagen-GAG scaffolds." Biophysical Journal **93**(8): 2911-2922.
Harley, B. A., A. Z. Hastings, et al. (2006). "Fabricating tubular scaffolds with a radial pore size gradient by a spinning technique." Biomaterials **27**(6): 866-874.
Harley, B. A., H. D. Kim, et al. (2008). "Microarchitecture of three-dimensional scaffolds influences cell migration behavior via junction interactions." Biophys J **95**(8): 4013-4024.
Harley, B. A., J. H. Leung, et al. (2007). "Mechanical characterization of collagen-glycosaminoglycan scaffolds." Acta Biomater **3**(4): 463-474.
Harley, B. A., A. K. Lynn, et al. (2010). "Design of a multiphase osteochondral scaffold III: Fabrication of layered scaffolds with continuous interfaces." J Biomed Mater Res A **92**(3): 1078-1093.
Harley, B. A., A. K. Lynn, et al. (2010). "Design of a multiphase osteochondral scaffold. II. Fabrication of a mineralized collagen-glycosaminoglycan scaffold." J Biomed Mater Res A **92**(3): 1066-1077.
Harley, B. A., M. H. Spilker, et al. (2004). "Optimal degradation rate for collagen chambers used for regeneration of peripheral nerves over long gaps." Cells Tissues Organs **176**(1-3): 153-165.
Harley, B. A. C. and L. J. Gibson (2008). "In vivo and in vitro applications of collagen-GAG scaffolds." Chem Eng J **137**(1): 102-121.
Harley, B. A. C., H. D. Kim, et al. (2008). "Microarchitecture of three-dimensional scaffolds influences cell migration behavior via junction interactions." Biophysical Journal **95**(8): 4013-4024.
Hartmann, C. and C. J. Tabin (2001). "Wnt-14 plays a pivotal role in inducing synovial joint formation in the developing appendicular skeleton." Cell **104**(3): 341-351.
Haugh, M. G., C. M. Murphy, et al. (2010). "Novel freeze-drying methods to produce a range of collagen-glycosaminoglycan scaffolds with tailored mean pore sizes." Tissue Eng Part C Methods **16**(5): 887-894.
He, J., Y. Du, et al. (2010). "Rapid generation of biologically relevant hydrogels containing long-range chemical gradients." Adv Funct Mater **20**(1): 131-137.
He, P. F., K. S. Ng, et al. (2012). "In Vitro Ligament-Bone Interface Regeneration Using a Trilineage Coculture System on a Hybrid Silk Scaffold." Biomacromolecules **13**(9): 2692-2703.
Ho, S. T., D. W. Hutmacher, et al. (2010). "The evaluation of a biphasic osteochondral implant coupled with an electrospun membrane in a large animal model." Tissue Eng Part A **16**(4): 1123-1141.
Hodge, W. A., R. S. Fijan, et al. (1986). "Contact pressures in the human hip joint measured in vivo." Proc Natl Acad Sci U S A **83**(9): 2879-2883.
Hoffmann, A., G. Pelled, et al. (2006). "Neotendon formation induced by manipulation of the Smad8 signalling pathway in mesenchymal stem cells." J Clin Invest **116**(4): 940-952.

Huang, K. F., W. C. Hsu, et al. (2012). "Functional improvement and neurogenesis after collagen-GAG matrix implantation into surgical brain trauma." Biomaterials **33**(7): 2067-2075.

Huangfu, X. Q. and J. Z. Zhao (2007). "Tendon-bone healing enhancement using injectable tricalcium phosphate in a dog anterior cruciate ligament reconstruction model." Arthroscopy-the Journal of Arthroscopic and Related Surgery **23**(5): 455-462.

Hudalla, G. A., J. T. Koepsel, et al. (2011). "Surfaces That Sequester Serum-Borne Heparin Amplify Growth Factor Activity." Advanced Materials **23**(45): 5415-5418.

Hudalla, G. A., N. A. Kouris, et al. (2011). "Harnessing endogenous growth factor activity modulates stem cell behavior." Integr Biol (Camb) **3**(8): 832-842.

Huebsch, N., P. R. Arany, et al. (2010). "Harnessing traction-mediated manipulation of the cell/matrix interface to control stem-cell fate." Nat Mater **9**(6): 518-526.

Istrate, O. M. and B. Chen (2011). "Relative modulus-relative density relationships in low density polymer-clay nanocomposite foams." Soft Matter.

James, R., G. Kesturu, et al. (2008). "Tendon: Biology, biomechanics, repair, growth factors, and evolving treatment options." J Hand Surg-Am **33A**(1): 102-112.

James, R., S. G. Kumbar, et al. (2011). "Tendon tissue engineering: adipose-derived stem cell and GDF-5 mediated regeneration using electrospun matrix systems." Biomedical Materials **6**(2).

Jarvinen, T. A., L. Jozsa, et al. (2003). "Mechanical loading regulates the expression of tenascin-C in the myotendinous junction and tendon but does not induce de novo synthesis in the skeletal muscle." J Cell Sci **116**(Pt 5): 857-866.

Jiang, C. C., H. Chiang, et al. (2007). "Repair of porcine articular cartilage defect with a biphasic osteochondral composite." J Orthop Res **25**(10): 1277-1290.

Jiang, J., A. Tang, et al. (2010). "Bioactive stratified polymer ceramic-hydrogel scaffold for integrative osteochondral repair." Ann Biomed Eng **38**(6): 2183-2196.

Jones, G. C., A. N. Corps, et al. (2006). "Expression profiling of metalloproteinases and tissue inhibitors of metalloproteinases in normal and degenerate human achilles tendon." Arthritis Rheum **54**(3): 832-842.

Juncosa-Melvin, N., K. S. Matlin, et al. (2007). "Mechanical stimulation increases collagen type I and collagen type III gene expression of stem cell-collagen sponge constructs for patellar tendon repair." Tissue Eng **13**(6): 1219-1226.

Juncosa-Melvin, N., J. T. Shearn, et al. (2006). "Effects of mechanical stimulation on the biomechanics and histology of stem cell-collagen sponge constructs for rabbit patellar tendon repair." Tissue Engineering **12**(8): 2291-2300.

Kang, Y., S. Kim, et al. (2011). "Creation of bony microenvironment with CaP and cell-derived ECM to enhance human bone-marrow MSC behavior and delivery of BMP-2." Biomaterials.

Kanungo, B. P. and L. J. Gibson (2009). "Density-property relationships in mineralized collagen-glycosaminoglycan scaffolds." Acta Biomater **5**(4): 1006-1018.

Kanungo, B. P. and L. J. Gibson (2010). "Density-property relationships in collagen-glycosaminoglycan scaffolds." Acta Biomater **6**(2): 344-353.

Kapoor, A., E. H. Caporali, et al. (2010). "Microtopographically patterned surfaces promote the alignment of tenocytes and extracellular collagen." Acta Biomater **6**(7): 2580-2589.

Keller, T. C., M. V. Hogan, et al. (2011). "Growth/differentiation factor-5 modulates the synthesis and expression of extracellular matrix and cell-adhesion-related molecules of rat Achilles tendon fibroblasts." Connect Tissue Res **52**(4): 353-364.

Kempson, G. E., H. Muir, et al. (1973). "The tensile properties of the cartilage of human femoral condyles related to the content of collagen and glycosaminoglycans." Biochim Biophys Acta **297**(2): 456-472.

Keogh, M. B., F. J. O'Brien, et al. (2010). "Substrate stiffness and contractile behaviour modulate the functional maturation of osteoblasts on a collagen-GAG scaffold." Acta Biomater **6**(11): 4305-4313.

Ker, E. D., A. S. Nain, et al. (2011). "Bioprinting of growth factors onto aligned sub-micron fibrous scaffolds for simultaneous control of cell differentiation and alignment." Biomaterials **32**(32): 8097-8107.

Ker, E. D. F., B. Chu, et al. (2011). "Engineering spatial control of multiple differentiation fates within a stem cell population." Biomaterials **32**(13): 3413-3422.

Khanarian, N. T., N. M. Haney, et al. (2012). "A functional agarose-hydroxyapatite scaffold for osteochondral interface regeneration." Biomaterials **33**(21): 5247-5258.

Khanarian, N. T., J. Jiang, et al. (2012). "A hydrogel-mineral composite scaffold for osteochondral interface tissue engineering." Tissue Eng Part A **18**(5-6): 533-545.

Khetan, S. and J. A. Burdick (2010). "Patterning network structure to spatially control cellular remodeling and stem cell fate within 3-dimensional hydrogels." Biomaterials **31**(32): 8228-8234.

Khetan, S., M. Guvendiren, et al. (2013). "Degradation-mediated cellular traction directs stem cell fate in covalently crosslinked three-dimensional hydrogels." Nat Mater **advance online publication**.

Khoroshkov, Y. A. (1975). "Ultrastructural elements of the strength of the muscle-tendon junction." Polymer Mechanics **11**(4): 535-537.

Kilian, K. A., B. Bugarija, et al. (2010). "Geometric cues for directing the differentiation of mesenchymal stem cells." Proc Natl Acad Sci U S A **107**(11): 4872-4877.

Kilian, K. A. and M. Mrksich (2012). "Directing Stem Cell Fate by Controlling the Affinity and Density of Ligand-Receptor Interactions at the Biomaterials Interface." Angewandte Chemie-International Edition **51**(20): 4891-4895.

Kim, D., E. Monaco, et al. (2010). "Morphologic and transcriptomic comparison of adipose- and bone-marrow-derived porcine stem cells cultured in alginate hydrogels." Cell Tissue Res **341**(3): 359-370.

Kim, K., J. Lam, et al. (2013). "Osteochondral tissue regeneration using a bilayered composite hydrogel with modulating dual growth factor release kinetics in a rabbit model." J Control Release **168**(2): 166-178.

Kim, Y. J., R. L. Sah, et al. (1988). "Fluorometric assay of DNA in cartilage explants using Hoechst 33258." Anal Biochem **174**(1): 168-176.

Kinneberg, K. R., V. S. Nirmalanandhan, et al. (2010). "Chondroitin-6-sulfate incorporation and mechanical stimulation increase MSC-collagen sponge construct stiffness." J Orthop Res.

Kinneberg, K. R. C., M. T. Galloway, et al. (2013). "The native cell population does not contribute to central-third graft healing at 6, 12, or 26 weeks in the rabbit patellar tendon." Journal of Orthopaedic Research **31**(4): 638-644.

Klepps, S., J. Bishop, et al. (2004). "Prospective evaluation of the effect of rotator cuff integrity on the outcome of open rotator cuff repairs." American Journal of Sports Medicine **32**(7): 1716-1722.

Kloxin, A. M., A. M. Kasko, et al. (2009). "Photodegradable hydrogels for dynamic tuning of physical and chemical properties." Science **324**(5923): 59-63.

Kloxin, A. M., K. J. R. Lewis, et al. (2012). "Responsive culture platform to examine the influence of microenvironmental geometry on cell function in 3D." Integrative Biology.

Kloxin, A. M., M. W. Tibbitt, et al. (2010). "Synthesis of photodegradable hydrogels as dynamically tunable cell culture platforms." Nat Protoc **5**(12): 1867-1887.

Kon, E., M. Delcogliano, et al. (2011). "Novel Nano-composite Multilayered Biomaterial for Osteochondral Regeneration A Pilot Clinical Trial." American Journal of Sports Medicine **39**(6): 1180-1190.

Kuo, C. K., B. C. Petersen, et al. (2008). "Spatiotemporal protein distribution of TGF-betas, their receptors, and extracellular matrix molecules during embryonic tendon development." Dev Dyn **237**(5): 1477-1489.

Kuo, C. K. and R. S. Tuan (2008). "Mechanoactive tenogenic differentiation of human mesenchymal stem cells." Tissue Eng Part A **14**(10): 1615-1627.

Ladd, M. R., S. J. Lee, et al. (2011). "Co-electrospun dual scaffolding system with potential for muscle-tendon junction tissue engineering." Biomaterials **32**(6): 1549-1559.

Lan Levengood, S. K., S. J. Polak, et al. (2010). "The effect of BMP-2 on micro and macroscale osteointegration of biphasic calcium phosphate scaffolds with multiscale porosity." Acta Biomaterialia **In Press, Accepted Manuscript**.

Langer, R. and J. P. Vacanti (1993). "Tissue engineering." Science **260**(5110): 920-926.

Lareu, R. R., D. I. Zeugolis, et al. (2010). "Essential modification of the Sircol Collagen Assay for the accurate quantification of collagen content in complex protein solutions." Acta Biomater **6**(8): 3146-3151.

Larkin, L. M., S. Calve, et al. (2006). "Structure and functional evaluation of tendon-skeletal muscle constructs engineered in vitro." Tissue Eng **12**(11): 3149-3158.

Lee, J. S., A. Wagoner-Johnson, et al. (2009). "Modular peptide growth factors for substrate-mediated stem cell differentiation." Angew Chem Int Ed Engl **48**(34): 6266-6269.

Lee, J. S., A. J. Wagoner Johnson, et al. (2010). "A modular, hydroxyapatite-binding version of vascular endothelial growth factor." Adv Mater **22**(48): 5494-5498.

Li, X., J. Xie, et al. (2009). "Nanofiber scaffolds with gradations in mineral content for mimicking the tendon-to-bone insertion site." Nano Lett **9**(7): 2763-2768.

Li, X. D., L. Jin, et al. (2006). "Demineralized bone matrix gelatin as scaffold for osteochondral tissue engineering." Biomaterials **27**(11): 2426-2433.

Li, Y., X. Yu, et al. (2007). "Insulin-like growth factor 1 enhances the migratory capacity of mesenchymal stem cells." Biochem Biophys Res Commun **356**(3): 780-784.

Liu, C. F., L. Aschbacher-Smith, et al. (2012). "Spatial and temporal expression of molecular markers and cell signals during normal development of the mouse patellar tendon." Tissue Eng Part A **18**(5-6): 598-608.

Liu, C. F., L. Aschbacher-Smith, et al. (2011). "Spatial and temporal expression of molecular markers and cell signals during normal development of the mouse patellar tendon." Tissue Eng Part A.

Liu, H. W., C. H. Chen, et al. (2006). "Targeted delivery system for juxtacrine signaling growth factor based on rhBMP-2-mediated carrier-protein conjugation." Bone **39**(4): 825-836.

Liu, W., Y. Zhang, et al. (2012). "Generation of Controllable Gradients in Cell Density." Angew Chem Int Ed Engl.
Liu, Y., H. S. Ramanath, et al. (2008). "Tendon tissue engineering using scaffold enhancing strategies." Trends in Biotechnology **26**(4): 201-209.
Lo, I. K., L. L. Marchuk, et al. (2004). "Matrix metalloproteinase and tissue inhibitor of matrix metalloproteinase mRNA levels are specifically altered in torn rotator cuff tendons." Am J Sports Med **32**(5): 1223-1229.
Lou, J. R., Y. Z. Tu, et al. (2001). "BMP-12 gene transfer augmentation of lacerated tendon repair." Journal of Orthopaedic Research **19**(6): 1199-1202.
Lovati, A. B., B. Corradetti, et al. (2012). "Tenogenic differentiation of equine mesenchymal progenitor cells under indirect co-culture." Int J Artif Organs: 0.
Lu, H. H., S. D. Subramony, et al. (2010). "Tissue engineering strategies for the regeneration of orthopedic interfaces." Ann Biomed Eng **38**(6): 2142-2154.
Luo, Q., G. Song, et al. (2009). "Indirect co-culture with tenocytes promotes proliferation and mRNA expression of tendon/ligament related genes in rat bone marrow mesenchymal stem cells." Cytotechnology **61**(1-2): 1-10.
Luo, Y. and M. S. Shoichet (2004). "A photolabile hydrogel for guided three-dimensional cell growth and migration." Nat Mater **3**(4): 249-253.
Lynn, A. K., S. M. Best, et al. (2010). "Design of a multiphase osteochondral scaffold. I. Control of chemical composition." J Biomed Mater Res A **92**(3): 1057-1065.
Ma, J., K. Goble, et al. (2009). "Morphological and functional characteristics of three-dimensional engineered bone-ligament-bone constructs following implantation." J Biomech Eng **131**(10): 101017.
Ma, J., M. J. Smietana, et al. (2012). "Three-dimensional engineered bone-ligament-bone constructs for anterior cruciate ligament replacement." Tissue Eng Part A **18**(1-2): 103-116.
Ma, M., L. Guo, et al. (2013). "Bio-Inspired Polymer Composite Actuator and Generator Driven by Water Gradients." Science **339**(6116): 186-189.
Maeda, T., T. Sakabe, et al. (2011). "Conversion of Mechanical Force into TGF-beta-Mediated Biochemical Signals." Current Biology **21**(11): 933-941.
Manning, C. N., H. M. Kim, et al. (2011). "Sustained delivery of transforming growth factor beta three enhances tendon-to-bone healing in a rat model." J Orthop Res.
Martin, R. B., D. B. Burr, et al., Eds. (1998). Skeletal Tissue Mechanics. New York, Springer.
Martin, T. A., S. R. Caliari, et al. (2011). "The generation of biomolecular patterns in highly porous collagen-GAG scaffolds using direct photolithography." Biomaterials **32**(16): 3949-3957.
McBeath, R., D. M. Pirone, et al. (2004). "Cell shape, cytoskeletal tension, and RhoA regulate stem cell lineage commitment." Developmental Cell **6**(4): 483-495.
McCarrel, T. and L. Fortier (2009). "Temporal Growth Factor Release from Platelet-Rich Plasma, Trehalose Lyophilized Platelets, and Bone Marrow Aspirate and Their Effect on Tendon and Ligament Gene Expression." Journal of Orthopaedic Research **27**(8): 1033-1042.
McNeilly, C. M., A. J. Banes, et al. (1996). "Tendon cells in vivo form a three dimensional network of cell processes linked by gap junctions." Journal of Anatomy **189**: 593-600.
Melvin, A., A. Litsky, et al. (2010). "An artificial tendon with durable muscle interface." J Orthop Res **28**(2): 218-224.

Mikos, A. G., S. W. Herring, et al. (2006). "Engineering complex tissues." Tissue Eng **12**(12): 3307-3339.
Millar, N. L., X. Wu, et al. (2009). "Open versus two forms of arthroscopic rotator cuff repair." Clin Orthop Relat Res **467**(4): 966-978.
Mishra, A., J. Woodall, Jr., et al. (2009). "Treatment of tendon and muscle using platelet-rich plasma." Clin Sports Med **28**(1): 113-125.
Mitrovic, D., M. Quintero, et al. (1983). "Cell density of adult human femoral condylar articular cartilage. Joints with normal and fibrillated surfaces." Lab Invest **49**(3): 309-316.
Moffat, K. L., A. S. Kwei, et al. (2009). "Novel nanofiber-based scaffold for rotator cuff repair and augmentation." Tissue Eng Part A **15**(1): 115-126.
Moffat, K. L., W. H. Sun, et al. (2008). "Characterization of the structure-function relationship at the ligament-to-bone interface." Proc Natl Acad Sci U S A **105**(23): 7947-7952.
Moffat, K. L., I. N. Wang, et al. (2009). "Orthopedic interface tissue engineering for the biological fixation of soft tissue grafts." Clin Sports Med **28**(1): 157-176.
Mohan, N., N. H. Dormer, et al. (2011). "Continuous Gradients of Material Composition and Growth Factors for Effective Regeneration of the Osteochondral Interface." Tissue Eng Part A.
Molloy, T., Y. Wang, et al. (2003). "The roles of growth factors in tendon and ligament healing." Sports Med **33**(5): 381-394.
Muller, P., U. Bulnheim, et al. (2008). "Calcium phosphate surfaces promote osteogenic differentiation of mesenchymal stem cells." J Cell Mol Med **12**(1): 281-291.
Murphy, C. M., M. G. Haugh, et al. (2010). "The effect of mean pore size on cell attachment, proliferation and migration in collagen-glycosaminoglycan scaffolds for bone tissue engineering." Biomaterials **31**(3): 461-466.
Murphy, C. M., A. Matsiko, et al. (2012). "Mesenchymal stem cell fate is regulated by the composition and mechanical properties of collagen-glycosaminoglycan scaffolds." J Mech Behav Biomed Mater **11**: 53-62.
Mutsuzaki, H., M. Sakane, et al. (2011). "Effect of Calcium Phosphate-Hybridized Tendon Graft on Biomechanical Behavior in Anterior Cruciate Ligament Reconstruction in a Goat Model: Novel Technique for Improving Tendon-Bone Healing." Am J Sports Med.
Nakajima, M., T. Ishimuro, et al. (2007). "Combinatorial protein display for the cell-based screening of biomaterials that direct neural stem cell differentiation." Biomaterials **28**(6): 1048-1060.
O'Brien, F. J., B. A. Harley, et al. (2007). "The effect of pore size on permeability and cell attachment in collagen scaffolds for tissue engineering." Technol Health Care **15**(1): 3-17.
O'Brien, F. J., B. A. Harley, et al. (2004). "Influence of freezing rate on pore structure in freeze-dried collagen-GAG scaffolds." Biomaterials **25**(6): 1077-1086.
O'Brien, F. J., B. A. Harley, et al. (2005). "The effect of pore size on cell adhesion in collagen-GAG scaffolds." Biomaterials **26**(4): 433-441.
Odedra, D., L. L. Chiu, et al. (2011). "Endothelial cells guided by immobilized gradients of vascular endothelial growth factor on porous collagen scaffolds." Acta Biomater **7**(8): 3027-3035.
Oh, S. H., T. H. Kim, et al. (2011). "Creating growth factor gradients in three dimensional porous matrix by centrifugation and surface immobilization." Biomaterials **32**(32): 8254-8260.

Olde Damink, L. H., P. J. Dijkstra, et al. (1996). "Cross-linking of dermal sheep collagen using a water-soluble carbodiimide." Biomaterials **17**(8): 765-773.
Ozaki, Y., M. Nishimura, et al. (2007). "Comprehensive analysis of chemotactic factors for bone marrow mesenchymal stem cells." Stem Cells Dev **16**(1): 119-129.
Park, A., M. V. Hogan, et al. (2010). "Adipose-derived mesenchymal stem cells treated with growth differentiation factor-5 express tendon-specific markers." Tissue Eng Part A **16**(9): 2941-2951.
Park, C. H., H. F. Rios, et al. (2010). "Biomimetic hybrid scaffolds for engineering human tooth-ligament interfaces." Biomaterials **31**(23): 5945-5952.
Park, C. H., H. F. Rios, et al. (2012). "Tissue engineering bone-ligament complexes using fiber-guiding scaffolds." Biomaterials **33**(1): 137-145.
Pauly, S., F. Klatte, et al. (2010). "Characterization of tendon cell cultures of the human rotator cuff." Eur Cell Mater **20**: 84-97.
Paxton, J. Z., K. Donnelly, et al. (2009). "Engineering the Bone-Ligament Interface Using Polyethylene Glycol Diacrylate Incorporated with Hydroxyapatite." Tissue Engineering Part A **15**(6): 1201-1209.
Paxton, J. Z., L. M. Grover, et al. (2010). "Engineering an in vitro model of a functional ligament from bone to bone." Tissue Eng Part A **16**(11): 3515-3525.
Paxton, J. Z., P. Hagerty, et al. (2012). "Optimizing an Intermittent Stretch Paradigm Using ERK1/2 Phosphorylation Results in Increased Collagen Synthesis in Engineered Ligaments." Tissue Engineering Part A **18**(3-4): 277-284.
Pek, Y. S., M. Spector, et al. (2004). "Degradation of a collagen-chondroitin-6-sulfate matrix by collagenase and by chondroitinase." Biomaterials **25**(3): 473-482.
Pelham, J., Robert J. and Y.-L. Wang (1997). "Cell locomotion and focal adhesions are regulated by substrate flexibility." Proc Natl Acad Sci USA **9**: 13661-13665.
Peyton, S. R. and A. J. Putnam (2005). "Extracellular matrix rigidity governs smooth muscle cell motility in a biphasic fashion." J. Cell Physiol. **204**(1): 198-209.
Phillippi, J. A., E. Miller, et al. (2008). "Microenvironments engineered by inkjet bioprinting spatially direct adult stem cells toward muscle- and bone-like subpopulations." Stem Cells **26**(1): 127-134.
Phillips, J. E., K. L. Burns, et al. (2008). "Engineering graded tissue interfaces." Proc Natl Acad Sci U S A **105**(34): 12170-12175.
Pittenger, M. F., A. M. Mackay, et al. (1999). "Multilineage potential of adult human mesenchymal stem cells." Science **284**(5411): 143-147.
Ponte, A. L., E. Marais, et al. (2007). "The in vitro migration capacity of human bone marrow mesenchymal stem cells: comparison of chemokine and growth factor chemotactic activities." Stem Cells **25**(7): 1737-1745.
Poole, A. R., T. Kojima, et al. (2001). "Composition and structure of articular cartilage - A template for tissue repair." Clinical Orthopaedics and Related Research(391): S26-S33.
Poole, A. R., L. C. Rosenberg, et al. (1996). "Contents and distributions of the proteoglycans decorin and biglycan in normal and osteoarthritic human articular cartilage." J Orthop Res **14**(5): 681-689.
Prendergast, P. J., R. Huiskes, et al. (1997). "ESB Research Award 1996. Biophysical stimuli on cells during tissue differentiation at implant interfaces." J Biomech **30**(6): 539-548.
Pryce, B. A., S. S. Watson, et al. (2009). "Recruitment and maintenance of tendon progenitors by TGFbeta signaling are essential for tendon formation." Development **136**(8): 1351-1361.

Qi, H., Y. Du, et al. (2010). "Patterned differentiation of individual embryoid bodies in spatially organized 3D hybrid microgels." Adv Mater **22**(46): 5276-5281.
Quapp, K. M. and J. A. Weiss (1998). "Material characterization of human medial collateral ligament." J Biomech Eng **120**(6): 757-763.
Ramalingam, M., M. F. Young, et al. (2012). "Nanofiber scaffold gradients for interfacial tissue engineering." J Biomater Appl.
Re'em, T., F. Witte, et al. (2012). "Simultaneous regeneration of articular cartilage and subchondral bone induced by spatially presented TGF-beta and BMP-4 in a bilayer affinity binding system." Acta Biomater **8**(9): 3283-3293.
Ren, K. F., T. Crouzier, et al. (2008). "Polyelectrolyte multilayer films of controlled stiffness modulate myoblast cell differentiation." Advanced Functional Materials **18**(9): 1378-1389.
Retting, K. N., B. Song, et al. (2009). "BMP canonical Smad signaling through Smad1 and Smad5 is required for endochondral bone formation." Development **136**(7): 1093-1104.
Reyes, R., A. Delgado, et al. (2013). "Cartilage repair by local delivery of TGF-beta1 or BMP-2 from a novel, segmented polyurethane/polylactic-co-glycolic bilayered scaffold." J Biomed Mater Res A.
Riley, G. P., R. L. Harrall, et al. (1996). "Tenascin-C and human tendon degeneration." Am J Pathol **149**(3): 933-943.
Rodeo, S. A., K. Suzuki, et al. (1999). "Use of recombinant human bone morphogenetic protein-2 to enhance tendon healing in a bone tunnel." American Journal of Sports Medicine **27**(4): 476-488.
Rowland, C. R., D. P. Lennon, et al. (2013). "The effects of crosslinking of scaffolds engineered from cartilage ECM on the chondrogenic differentiation of MSCs." Biomaterials.
Sahoo, S., H. Ouyang, et al. (2006). "Characterization of a novel polymeric scaffold for potential application in tendon/ligament tissue engineering." Tissue Eng **12**(1): 91-99.
Sahoo, S., T. Teh, et al. (2011). "Interface tissue engineering: next phase in musculoskeletal tissue repair." Ann Acad Med Singapore **40**(5): 245-251.
Sahoo, S., S. L. Toh, et al. (2010). "A bFGF-releasing silk/PLGA-based biohybrid scaffold for ligament/tendon tissue engineering using mesenchymal progenitor cells." Biomaterials **31**(11): 2990-2998.
Saito, A., Y. Suzuki, et al. (2003). "Activation of osteo-progenitor cells by a novel synthetic peptide derived from the bone morphogenetic protein-2 knuckle epitope." Biochim Biophys Acta **1651**(1-2): 60-67.
Samavedi, S., S. A. Guelcher, et al. (2012). "Response of bone marrow stromal cells to graded co-electrospun scaffolds and its implications for engineering the ligament-bone interface." Biomaterials **33**(31): 7727-7735.
Samuel, R. E., C. R. Lee, et al. (2002). "Delivery of plasmid DNA to articular chondrocytes via novel collagen-glycosaminoglycan matrices." Hum Gene Ther **13**(7): 791-802.
Schinagl, R. M., D. Gurskis, et al. (1997). "Depth-dependent confined compression modulus of full-thickness bovine articular cartilage." Journal of Orthopaedic Research **15**(4): 499-506.
Schmidt, A., D. Ladage, et al. (2006). "Basic fibroblast growth factor controls migration in human mesenchymal stem cells." Stem Cells **24**(7): 1750-1758.
Schneider, A., G. Francius, et al. (2006). "Polyelectrolyte multilayers with a tunable Young's modulus: Influence of film stiffness on cell adhesion." Langmuir **22**(3): 1193-1200.

Schoen, D. C. (2005). "Injuries of the wrist." Orthop Nurs **24**(4): 304-307.
Schweitzer, R., J. H. Chyung, et al. (2001). "Analysis of the tendon cell fate using Scleraxis, a specific marker for tendons and ligaments." Development **128**(19): 3855-3866.
Seidi, A., M. Ramalingam, et al. (2011). "Gradient biomaterials for soft-to-hard interface tissue engineering." Acta Biomater **7**(4): 1441-1451.
Shahab-Osterloh, S., F. Witte, et al. (2010). "Mesenchymal stem cell-dependent formation of heterotopic tendon-bone insertions (osteotendinous junctions)." Stem Cells **28**(9): 1590-1601.
Shao, X. X., J. C. H. Goh, et al. (2006). "Repair of large articular osteochondral defects using hybrid scaffolds and bone marrow-derived mesenchymal stem cells in a rabbit model." Tissue Engineering **12**(6): 1539-1551.
Sheehy, E. J., T. Vinardell, et al. (2013). "Engineering osteochondral constructs through spatial regulation of endochondral ossification." Acta Biomaterialia **9**(3): 5484-5492.
Shen, W., X. Chen, et al. (2010). "The effect of incorporation of exogenous stromal cell-derived factor-1 alpha within a knitted silk-collagen sponge scaffold on tendon regeneration." Biomaterials **31**(28): 7239-7249.
Shen, Y. H., M. S. Shoichet, et al. (2008). "Vascular endothelial growth factor immobilized in collagen scaffold promotes penetration and proliferation of endothelial cells." Acta Biomater **4**(3): 477-489.
Singh, M., N. Dormer, et al. (2010). "Three-dimensional macroscopic scaffolds with a gradient in stiffness for functional regeneration of interfacial tissues." J Biomed Mater Res A **94**(3): 870-876.
Singh, M., C. P. Morris, et al. (2008). "Microsphere-based seamless scaffolds containing macroscopic gradients of encapsulated factors for tissue engineering." Tissue Eng Part C Methods **14**(4): 299-309.
Soller, E. C., D. S. Tzeranis, et al. (2012). "Common features of optimal collagen scaffolds that disrupt wound contraction and enhance regeneration both in peripheral nerves and in skin." Biomaterials **33**(19): 4783-4791.
Son, B. R., L. A. Marquez-Curtis, et al. (2006). "Migration of bone marrow and cord blood mesenchymal stem cells in vitro is regulated by stromal-derived factor-1-CXCR4 and hepatocyte growth factor-c-met axes and involves matrix metalloproteinases." Stem Cells **24**(5): 1254-1264.
Spalazzi, J. P., E. Dagher, et al. (2008). "In vivo evaluation of a multiphased scaffold designed for orthopaedic interface tissue engineering and soft tissue-to-bone integration." J Biomed Mater Res A **86**(1): 1-12.
Spalazzi, J. P., S. B. Doty, et al. (2006). "Development of controlled matrix heterogeneity on a triphasic scaffold for orthopedic interface tissue engineering." Tissue Eng **12**(12): 3497-3508.
Spalazzi, J. P., M. C. Vyner, et al. (2008). "Mechanoactive scaffold induces tendon remodeling and expression of fibrocartilage markers." Clin Orthop Relat Res **466**(8): 1938-1948.
Spilker, M. H., K. Asano, et al. (2001). "Contraction of collagen-glycosaminoglycan matrices by peripheral nerve cells in vitro." Biomaterials **22**(10): 1085-1093.
Steward, R. L., Jr., C. M. Cheng, et al. (2011). "Mechanical stretch and shear flow induced reorganization and recruitment of fibronectin in fibroblasts." Sci Rep **1**: 147.
Subramony, S. D., B. R. Dargis, et al. (2012). "The guidance of stem cell differentiation by substrate alignment and mechanical stimulation." Biomaterials.

Sullivan, J. and T. Best (2005). Injury of the Musculotendinous Junction. Tendon Injuries. N. Maffulli, P. Renström and W. Leadbetter, Springer London**:** 63-69.

Swasdison, S. and R. Mayne (1991). "In vitro attachment of skeletal muscle fibers to a collagen gel duplicates the structure of the myotendinous junction." Exp Cell Res **193**(1): 227-231.

Swasdison, S. and R. Mayne (1992). "Formation of highly organized skeletal muscle fibers in vitro. Comparison with muscle development in vivo." J Cell Sci **102 (Pt 3)**: 643-652.

Tampieri, A., M. Sandri, et al. (2008). "Design of graded biomimetic osteochondral composite scaffolds." Biomaterials **29**(26): 3539-3546.

Tang, S. Q. and M. Spector (2007). "Incorporation of hyaluronic acid into collagen scaffolds for the control of chondrocyte-mediated contraction and chondrogenesis." Biomedical Materials **2**(3): S135-S141.

Taylor, S. E., A. Vaughan-Thomas, et al. (2009). "Gene expression markers of tendon fibroblasts in normal and diseased tissue compared to monolayer and three dimensional culture systems." BMC Musculoskelet Disord **10**: 27.

ten Dijke, P. and H. M. Arthur (2007). "Extracellular control of TGF beta signalling in vascular development and disease." Nature Reviews Molecular Cell Biology **8**(11): 857-869.

Thomopoulos, S., G. M. Genin, et al. (2010). "The development and morphogenesis of the tendon-to-bone insertion - what development can teach us about healing." J Musculoskelet Neuronal Interact **10**(1): 35-45.

Thomopoulos, S., F. L. Harwood, et al. (2005). "Effect of several growth factors on canine flexor tendon fibroblast proliferation and collagen synthesis in vitro." J Hand Surg Am **30A**(3): 441-447.

Thomopoulos, S., J. P. Marquez, et al. (2006). "Collagen fiber orientation at the tendon to bone insertion and its influence on stress concentrations." J Biomech **39**(10): 1842-1851.

Thomopoulos, S., G. R. Williams, et al. (2003). "Variation of biomechanical, structural, and compositional properties along the tendon to bone insertion site." J Orthop Res **21**(3): 413-419.

Tidball, J. G., G. Salem, et al. (1993). "Site and mechanical conditions for failure of skeletal muscle in experimental strain injuries." J Appl Physiol **74**(3): 1280-1286.

Tien, Y. C., T. T. Chih, et al. (2004). "Augmentation of tendon-bone healing by the use of calcium-phosphate cement." Journal of Bone and Joint Surgery-British Volume **86B**(7): 1072-1076.

Tierney, C. M., M. J. Jaasma, et al. (2009). "Osteoblast activity on collagen-GAG scaffolds is affected by collagen and GAG concentrations." J Biomed Mater Res A **91**(1): 92-101.

Torres, D. S., T. M. Freyman, et al. (2000). "Tendon cell contraction of collagen-GAG matrices in vitro: effect of cross-linking." Biomaterials **21**(15): 1607-1619.

Trappmann, B., J. E. Gautrot, et al. (2012). "Extracellular-matrix tethering regulates stem-cell fate." Nat Mater **11**(7): 642-649.

Trotter, J. A. (2002). "Structure-function considerations of muscle-tendon junctions." Comparative Biochemistry and Physiology a-Molecular and Integrative Physiology **133**(4): 1127-1133.

Turner, C. E., N. Kramarcy, et al. (1991). "Localization of paxillin, a focal adhesion protein, to smooth muscle dense plaques, and the myotendinous and neuromuscular junctions of skeletal muscle." Exp Cell Res **192**(2): 651-655.

Vaquette, C., W. Fan, et al. (2012). "A biphasic scaffold design combined with cell sheet technology for simultaneous regeneration of alveolar bone/periodontal ligament complex." Biomaterials.

Venn, M. F. (1978). "Variation of chemical composition with age in human femoral head cartilage." Ann Rheum Dis **37**(2): 168-174.

Vickers, S. M., T. Gotterbarm, et al. (2010). "Cross-Linking Affects Cellular Condensation and Chondrogenesis in Type II Collagen-GAG Scaffolds Seeded with Bone Marrow-Derived Mesenchymal Stem Cells." Journal of Orthopaedic Research **28**(9): 1184-1192.

Vickers, S. M., L. S. Squitieri, et al. (2006). "Effects of cross-linking type II collagen-GAG scaffolds on chondrogenesis in vitro: dynamic pore reduction promotes cartilage formation." Tissue Eng **12**(5): 1345-1355.

Violas, P., A. Abid, et al. (2005). "Integra artificial skin in the management of severe tissue defects, including bone exposure, in injured children." Journal of Pediatric Orthopaedics-Part B **14**(5): 381-384.

Vitale, M. A., M. G. Vitale, et al. (2007). "Rotator cuff repair: an analysis of utility scores and cost-effectiveness." J Shoulder Elbow Surg **16**(2): 181-187.

Vos, T., A. D. Flaxman, et al. (2012). "Years lived with disability (YLDs) for 1160 sequelae of 289 diseases and injuries 1990-2010: a systematic analysis for the Global Burden of Disease Study 2010." Lancet **380**(9859): 2163-2196.

Wagenhauser, M. U., M. F. Pietschmann, et al. (2012). "Collagen type I and decorin expression in tenocytes depend on the cell isolation method." BMC Musculoskelet Disord **13**(1): 140.

Waggett, A. D., J. R. Ralphs, et al. (1998). "Characterization of collagens and proteoglycans at the insertion of the human Achilles tendon." Matrix Biol **16**(8): 457-470.

Wagner, D. R., D. P. Lindsey, et al. (2008). "Hydrostatic pressure enhances chondrogenic differentiation of human bone marrow stromal cells in osteochondrogenic medium." Ann Biomed Eng **36**(5): 813-820.

Wang, J. H. C. (2006). "Mechanobiology of tendon." Journal of Biomechanics **39**(9): 1563-1582.

Wang, X., E. Wenk, et al. (2009). "Growth factor gradients via microsphere delivery in biopolymer scaffolds for osteochondral tissue engineering." J Control Release **134**(2): 81-90.

Weisgerber, D. W., D. O. Kelkhoff, et al. (in review). "The impact of discrete compartments of a multi-compartment collagen-GAG scaffold on biophysical properties."

Wolfman, N. M., G. Hattersley, et al. (1997). "Ectopic induction of tendon and ligament in rats by growth and differentiation factors 5, 6, and 7, members of the TGF-beta gene family." J Clin Invest **100**(2): 321-330.

Woo, S. L., R. E. Debski, et al. (2000). "Injury and repair of ligaments and tendons." Annu Rev Biomed Eng **2**: 83-118.

Woodruff, K., L. M. Fidalgo, et al. (2013). "Live mammalian cell arrays." Nat Methods.

Wopenka, B., A. Kent, et al. (2008). "The tendon-to-bone transition of the rotator cuff: a preliminary Raman spectroscopic study documenting the gradual mineralization across the insertion in rat tissue samples." Appl Spectrosc **62**(12): 1285-1294.

Wylie, R. G., S. Ahsan, et al. (2011). "Spatially controlled simultaneous patterning of multiple growth factors in three-dimensional hydrogels." Nature Materials **10**(10): 799-806.

Wynn, R. F., C. A. Hart, et al. (2004). "A small proportion of mesenchymal stem cells strongly expresses functionally active CXCR4 receptor capable of promoting migration to bone marrow." Blood **104**(9): 2643-2645.
Xie, J., X. Li, et al. (2010). ""Aligned-to-random" nanofiber scaffolds for mimicking the structure of the tendon-to-bone insertion site." Nanoscale **2**(6): 923-926.
Xu, B., G. Song, et al. (2012). "RhoA/ROCK, cytoskeletal dynamics, and focal adhesion kinase are required for mechanical stretch-induced tenogenic differentiation of human mesenchymal stem cells." Journal of Cellular Physiology **227**(6): 2722-2729.
Xu, L., D. Cao, et al. (2010). "In vivo engineering of a functional tendon sheath in a hen model." Biomaterials **31**(14): 3894-3902.
Xu, Y. and G. A. Murrell (2008). "The basic science of tendinopathy." Clin Orthop Relat Res **466**(7): 1528-1538.
Xu, Y. H. and G. A. C. Murrell (2008). "The basic science of tendinopathy." Clinical Orthopaedics and Related Research **466**(7): 1528-1538.
Yang, P. J. and J. S. Temenoff (2009). "Engineering orthopedic tissue interfaces." Tissue Eng Part B Rev **15**(2): 127-141.
Yang, Y., D. Bolikal, et al. (2008). "Combinatorial polymer scaffold libraries for screening cell-biomaterial interactions in 3D." Advanced Materials **20**(11): 2037-+.
Yannas, I. V. (2001). Tissue and organ regeneration in adults. New York, Springer.
Yannas, I. V., J. F. Burke, et al. (1980). "Design of an artificial skin. II. Control of chemical composition." J Biomed Mater Res **14**(2): 107-132.
Yannas, I. V., M. D. Kwan, et al. (2007). "Early fetal healing as a model for adult organ regeneration." Tissue Eng **13**(8): 1789-1798.
Yannas, I. V., E. Lee, et al. (1989). "Synthesis and characterization of a model extracellular matrix that induces partial regeneration of adult mammalian skin." Proc Natl Acad Sci USA **86**(3): 933-937.
Yannas, I. V. and A. V. Tobolsky (1967). "Cross-linking of gelatine by dehydration." Nature **215**(5100): 509-510.
Yeung, T., P. C. Georges, et al. (2005). "Effects of substrate stiffness on cell morphology, cytoskeletal structure, and adhesion." Cell Motil. Cytoskeleton **60**: 24-34.
Yilgor, P., K. Tuzlakoglu, et al. (2009). "Incorporation of a sequential BMP-2/BMP-7 delivery system into chitosan-based scaffolds for bone tissue engineering." Biomaterials **30**(21): 3551-3559.
Yin, Z., X. Chen, et al. (2010). "The regulation of tendon stem cell differentiation by the alignment of nanofibers." Biomaterials **31**(8): 2163-2175.
Yoon, J. H. and J. Halper (2005). "Tendon proteoglycans: biochemistry and function." J Musculoskelet Neuronal Interact **5**(1): 22-34.
Yoshikawa, Y. and S. O. Abrahamsson (2001). "Dose-related cellular effects of platelet-derived growth factor-BB differ in various types of rabbit tendons in vitro." Acta Orthop Scand **72**(3): 287-292.
Zaman, M. H., L. M. Trapani, et al. (2006). "Migration of tumor cells in 3D matrices is governed by matrix stiffness along with cell-matrix adhesion and proteolysis." Proc Natl Acad Sci U S A **103**(29): 10889-10894.
Zhang, S., L. Chen, et al. (2013). "Bi-layer collagen/microporous electrospun nanofiber scaffold improves the osteochondral regeneration." Acta Biomater.

Zhang, W. B., W. M. Pan, et al. (2011). "In vivo evaluation of two types of bioactive scaffold used for tendon-bone interface healing in the reconstruction of anterior cruciate ligament." Biotechnology Letters **33**(4): 837-844.

Zhou, J., C. Xu, et al. (2011). "In vitro generation of osteochondral differentiation of human marrow mesenchymal stem cells in novel collagen-hydroxyapatite layered scaffolds." Acta Biomater **7**(11): 3999-4006.

Zhu, J., J. Li, et al. (2010). "The regulation of phenotype of cultured tenocytes by microgrooved surface structure." Biomaterials **31**(27): 6952-6958.